IChF
Institute of Physical Chemistry PAS

PhD Dissertation

New materials for studies on nanostructures and spatio-temporal patterns self-organized by surface phenomena

Richard Julius Gotthard Löffler

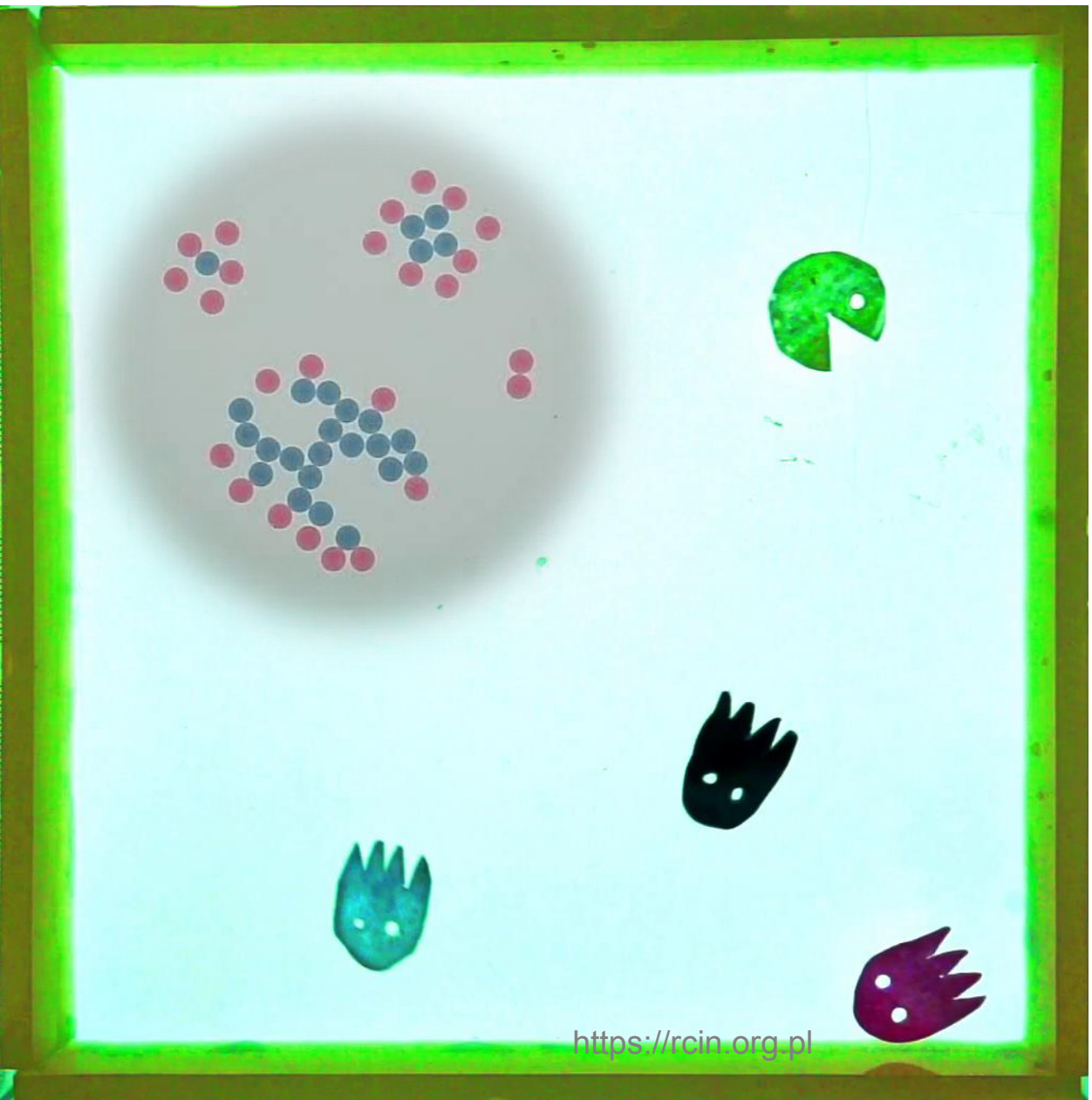

IChF
Institute of Physical Chemistry PAS

UNIVERSITÀ
DI TRENTO

Thesis submitted for the degree

of

Doctor of Philosophy

in the field

Chemical Sciences

prepared within the

International PhD Studies

of the

Institute of Physical Chemistry of the Polish Academy of Sciences in Warsaw

presented by

Richard Julius Gotthard Löffler

New materials for studies on nanostructures and spatio-temporal patterns self-organized by surface phenomena

Supervised by

Prof. dr. hab. Jerzy Gorecki

&

Assoc. Prof. dr. Martin M. Hanczyc

Institute of Physical Chemistry of the Polish Academy of Sciences
ul. Kasprzaka 44/52, 01-224 Warszawa

Warsaw, May 2021

Acknowledgements

Working on this project was one of the most rewarding times I have had thus far in my education as the project framework allowed me to conduct research in a way that truly could satisfy my curiosity. Furthermore, I had the great luck to really expand my network through the mobility funding that was part of the project, attending several conferences, week-long research visits and a 12-month secondment. This had the result that I came into contact with a large abundance of incredibly gifted and helpful colleagues, collaborators, fellow conference attendees and supervisors who all contributed to this work in some way or form. Therefore, I'd like to take this opportunity to thank all of them and some individuals in particular.

First, I would like to thank my supervisor Jerzy Gorecki for constantly being ready with valuable advice and always the right questions while also giving me almost completely free rains to conduct my research in the direction it naturally was taking me. I am thankful for being able to meet with Jerzy almost at any time to have a relaxing chat about the latest results and on those occasions also learning a wealth of historical anecdotes. He created an encouraging and inspiring atmosphere in which I could realize my potential for discovery. Another big thank you goes out to my second supervisor Martin Hanczyc who in the first place pointed out this opportunity to me so without him I would not even have started on this journey. He also created a welcoming atmosphere and a stimulating working environment during my 12-month secondment in his laboratory at the University of Trento, where I, despite a devastating first wave of COVID-19 closing everything down for several months, was able to gather valuable knowledge and results for my thesis. Martin has the ability to spread a good mood even on dark days which has an immense motivational effect. I would also like to thank Dr. Shinpei Tanaka from Hiroshima University who, not for the first time, almost coincidentally has become a vital contributor to my scientific career with helpful advice and challenging work. I hope it keeps happening! Special thanks also go out to Dr. Yuki Koyano, Dr. Hiroyuki Kitahata, Prof. Satoshi Nakata and Yuta Yamaguchi for helpful advice and access to equipment during several research visits to Japan, supported by the Japan Society for the Promotion of Science. To Lorenzo Moschini for helping me use the SEM in Trento. Next up, I'd like to thank some of the colleagues, turned friends from both Warsaw and Trento in no particular order – Janek, Gabriel, Dusan, Silvia, Matteo, Federica, Andrea, Alexandre, Daniele, Luca, Lorena, Leilah, Reginald and Marco along with all of the other PhD students at the IChF for good companionship and listening to my video-filled, presentations.

I would also like to thank my friends from Denmark: Lasse, Martin, Simon, Søren, Christian, Pall, Henrik, Troels, Ian, Vladimir, Gediminas, Sabine, Lars, Rene, Kristoffer, Daniel, Jesper, Alexander, Alex E., Gleb, Marijn, Christina, Yuki, Esben and everyone else I could not think of right now.
My family deserve immense gratitude for getting me to the point I am now and making me the person I am. My three amazing, always supportive, super intelligent siblings, Philipp, Anne and Lea as well as my parents, without whom, none of this would have been possible.
Finally, I cannot find the words that express my gratitude for my amazing partner in crime Elizaveta who makes me feel loved, gives me strength, confidence and energy throughout all this time including several months of strict lockdown and the stressful writing period during which I was not easy to be around. Thank you for being in my life!

Funding

This research is part of a project that has received funding from the European Union's Horizon 2020 research and innovation programme under the Marie Skłodowska-Curie grant agreement No. 711859.

,

Scientific work funded from the financial resources for science in the years 2017-2022 awarded by the Polish Ministry of Science and Higher Education for the implementation of an international co-financed project.

,

Additional funding for exchange trip accommodation and diets was provided by Bilateral Joint Research Program "Spatio-temporal patterns of elements driven by self-generated, geometrically constrained flows" between Japan Society for the promotion of Science and the Polish Academy of Sciences

Ministry of Science and Higher Education
Republic of Poland

Declaration of originality

I hereby declare that the research included within this thesis was carried out by myself or with support by others included in acknowledgments.

I state that I have exercised care to ensure that the work is original and contains no previously published material or written by another person, except where citations have been made in the text. To the best of my knowledge, the content provided here does not violate any copyrights.

I accept that the Polish Academy of Sciences has the right to use plagiarism detection software to ensure the thesis's legitimacy.

I certify that no part of my thesis has been or will be submitted for obtaining a degree or diploma by the Institute of Physical Chemistry, Polish Academy of Science, or any other educational institution.

This thesis's copyright rests with the author, and no information derived from it may be published without the author's consent.

Warsaw, 10 May 2021 .....

(signature)

List of publications

1. Löffler, R.J.G.; Gorecki, J.; Hanczyc, M. Better red than dead: On the influence of Oil Red O dye on complexity of evolution of a camphor-paraffin droplet on the water surface. In Proceedings of the 2018 Conference on Artificial Life; MIT Press: Cambridge, MA, 2018; pp. 574–579, doi: https://doi.org/10.1162/isal_a_00106
2. Löffler, R.J.G.; Hanczyc, M.M.; Gorecki, J. A hybrid camphor-camphene wax material for studies on self-propelled motion. *Phys. Chem. Chem. Phys.* **2019**, *21*, 24852–24856, doi:10.1039/c9cp04722k.
3. Löffler, R.J.G.; Hanczyc, M.M.; Gorecki, J. A Perfect Plastic Material for Studies on Self-Propelled Motion on the Water Surface. *Molecules* **2021**, *26*, 3116, doi:10.3390/molecules26113116.

List of abbreviations

CN – camphene

$cos\ (\alpha)$ – cosine of the angle between the velocity and the bisector of the angle, defined by the three markers on a crescent shape -> defines direction of movement

CR – camphor

D – diameter of Petri dish

d – distance between right (as seen from below) CR boat edge and closest CR pill perimeter

d – self-propelled disk diameter

ES – ethyl salicylate

fps – frames per second

$g(r)$ – radial distribution function of self-propelled disk locations

H_2O_2 – Dihydrogen Peroxide

IT – Interfacial tension in mN/m

L – CR boat length

m – frame number

M – number of frames

N – number of droplets

$n_0(S)$ - number of frames in which the pill center is observed within the fragment S of the water surface

OrO – Oil red O

p – diffusion distance: distance between CR boat edge and closest CR pill perimeter regardless of side

$P(v)$ – Speed/velocity probability distribution

PF – paraffin

PP – polypropylene

R – Petri dish radius

S – fragment of the water surface $n_0(S)$

SbB – Sudan black B

SDS – sodium dodecyl sulfate

SEM – scanning electron microscopy

ST – Surface tension in mN/m

TIPS – thermally induced phase separation

$u(r)$ – camphor surface conc. as a function of position

$U[r, r + \Delta r]$ – Ring around the dish center with with inner radius r and outer radius $r + \Delta r$.

$v(t_m)$ – pill speed at time t_m

w – camphor mass fraction of camphor-camphene wax

w_{CN} – mass ratio of camphene in camphene-camphor-polypropylene plastic

w_{CR} – mass ratio of camphor in camphene-camphor-polypropylene plastic

w_{PP} – mass ratio of polypropylene in camphene-camphor-polypropylene plastic

(x_m, y_m) – coordinates for center of marker on self-propelled disk

Δt – change in time

γ – surface tension in mN/m

γ_C – surface tension at center of ES-droplet ring

γ_O – surface tension outside as ES-droplet ring

γ_R – surface tension near ES-droplet ring inside and outside

Streszczenie

Przedstawiona rozprawa doktorska opisuje nowe materiały i układy eksperymentalne, które mogą znaleźć zastosowania w badaniach na złożoną ewolucją czasową obiektów samoporuszających się na powierzchni wody. Ruch takich obiektów jest efektem oddziaływań międzyfazowych i powierzchniowych, modyfikowanych koncentracją substancji czynnych. Badania ekseprymentalne nad samoporuszającymi się obiektami są ważne dla zrozumienia warunków w których ruch obiektów naśladuje organizmy żywe oraz dla testowania modeli teoretycznych opisujących ewolucję czasową aktywnej materii. Przyczynią się one do lepszego zrozumienia przemiany energii chemicznej w mechaniczną w układach dyssypatywnych, dalekich od równowagi. Myślę, że moje badania wniosą wkład do rozwoju takich dziedzin jak chemia nieliniowa, sztuczne życie i pochodzenie życia. Spodziewam się, że uzyskane wyniki zostaną zastosowane w nowych technologiach robotyki miękkiej.

Opisane zjawiska spowodowane są zmianami napięcia powierzchniowego wody oraz napięć międzyfazowych między obiektem (w formie stałej lub kropli cieczy niemieszającej się z wodą), a fazą wodnej. Są one powiązane z rozpuszczaniem, parowaniem oraz reakcjami substancji powierzchniowo czynnej i generują konwekcję Marangoniego. Badane układy obejmują zarówno łódki kamforowe poruszane na powierzchni wody przez krystaliczną kamforę w stanie stałym, obiekty o różnych kształtach uformowane z miękkiego materiału kompozytowego złożonego z kamfory, kamfenu i polipropylenu, oraz krople substancji organicznej z rozpuszczonym czynnikiem aktywnym.

Dla badań na ruchem łodzi kamforowej (Rozdział 1) zaprojektowano nowy typ eksperymentu w którym łódka obraca się wokół ustalonej osi. Układ taki umożliwia badanie różnych typów ruchu przez długi czas bez kontaktu ze ściankami naczynia. Zbadano typy ruchu łódki (ruch ciągły, ruch przerywany, ruch oscylujący) oraz przejścia między różnymi typami ruchu rozpatrując odległość pomiędzy środkiem pigułki kamforowej napędzającej łódź, a środkiem łodzi jako parametr kontrolny.

Odkrycie miękkich materiałów hybrydowych zwierających kamforę, kamfen i polipropylen o własnościach mechanicznych podobnych do wosku, jest ważnym rezultatem rozprawy (Rozdział 2). Stanowią one doskonały materiał do badania zależności między kształtem, a trajektorią samoporuszających obiektów. Ponadto jako "produkt uboczny" mojej pracy, odkryłem mikroporowatą, superhydrofobową piankę polimerową, która może znaleźć wiele zastosowań. Na przykład może ona bardzo skutecznie absorbować zanieczyszczenia takie jak oleje z powierzchni wody.

Trzecim tematem poruszanym w rozprawie jest wpływ barwników na zachowanie samoporuszających kropel zawierających roztwór kamfory w parafinie oraz na ewolucję czasową układów kropli w układzie salicylan etylu - środek powierzchniowo czynny (Rozdział 3). Odkryłem, że powszechny stosowany barwnik, Czerwień olejowa O (Oil Red O), zmniejszał napięcie międzyfazowe między olejem a wodą i, w zależności od jego stężenia, jakościowo zmieniał się typ ewolucji takich kropel. Wobec tego stężenie barwnika jest dodatkowym parametrem kontrolnym, który wpływa na zachowanie się kropli. Wykazano przy użyciu dwóch podobnych barwników (Czerwień olejowa O oraz Czernią Sudanu B - Sudan Black B), że ich obecność w różny sposób wpływa na ewolucję czasowo-przestrzenną zarówno pojedynczych kropli jak też układów wielu kropli. Badania nad układem salicylan etylu - środek powierzchniowo czynny doprowadziły do odkrycia oddziaływań typu drapieżnik-ofiara między dekanolem i kroplami salicylanu etylu na powierzchni czystej wody.

Abstract

My Ph.D. project was concerned with new materials and experimental systems that show interesting and complex self-propelled motion resulting from interfacial and surface phenomena. The experiments are of great use to study life-like behavior and test theoretical models for the active matter. They are a vital part of understanding the conversion of chemical energy into mechanical in dissipative, far-from-equilibrium systems and certain aspects of behavior observed in living systems. Therefore, the research on self-propelled motion advances fields such as non-linear chemistry, artificial life, and origins of life. The results can be applied to new technologies within the field of soft robotics.

In this thesis, I describe multiple new materials and improved experimental setups based on the physicochemical interaction between condensed- or soft-matter- and interfaces of the aqueous phase combined with dissolution, reactions or evaporation effects that cause and support Marangoni convection. The investigated systems range from boats actuated on a water surface by solid-state crystalline camphor, hybrid, wax-like materials containing camphor, camphene, and polypropylene that are self-propelled on a water surface to soft droplets of organic oil that release the surface-active agent.

For the research on camphor boats, a new type of experiment was designed in which the boat is on a forced circular trajectory along the edge of a Petri dish (Part 1). Such an arrangement allows to study various types of boat motion over a long period of time in a stationary regime, without contact between the boat and the dish walls. The types of boat motion (continuous motion, intermittent motion, inversive motion) were investigated. Transitions between different types of boat motion were examined considering the location of the camphor pill driving the boat with respect to the boat center as the control parameter.

Malleable semi-soft-matter hybrid materials containing camphor, camphene, and polypropylene are important new discoveries described in the thesis (Part 2). They provide the perfect material for the investigation of the relationship between the shape and trajectory of self-propelled objects. Furthermore, a potentially useful, microporous, superhydrophobic polymer foam that very effectively can absorb pollutants such as oils was discovered as a side product of this project.

The effect of dyes on the behavior of the self-propelled camphor-paraffin droplets and on the time evolution of ethyl salicylate – surfactant system is the third subject discussed in the thesis (Part 3). I discovered that a common dye, Oil red O, decreased the interfacial tension between oil and water and, depending on its concentration, the time evolution of such droplets was qualitatively changed. Therefore, the dye concentration is an additional control parameter that

influences droplet behavior. It has been demonstrated using two similar dyes (Oil red O vs. Sudan black B) that both the individual and collective spatio-temporal evolution of such droplets can be affected by the presence of a dye in different ways. Work on the ethyl salicylate system ultimately yielded a previously unknown predator-prey interaction between a decanol and ethyl salicylate droplet on a clean water surface.

Table of Contents

I **Preamble**

I. 1 Introduction

Complexity, as a concept and consequence of modern research, is becoming an ever more unavoidable subject to study [1–3]. Learning more about complexity can help us better understand systems which are governed by non-linear processes with a potential multitude of unknown parameters. Artificial self-propelled and stimuli-responsive systems based on dissipative conversion of chemical into mechanical energy can act as a model system for such complexity. This area of science requires a strong collaboration between theoreticians and experimentalists. Theoreticians can be limited by the experimental systems available to them to verify existing mathematical models or to discover new kinds of behavior that can be modeled. Therefore, it is crucial that we search for new materials and combinations thereof with interesting self-propelled or otherwise complex properties that can be set up easily and inexpensively. Furthermore, the search for such materials is simultaneously a search for functional materials with interesting properties that have great potential for real world application. The work done for this thesis aims at exactly that: to develop new setups and materials for the study of complex self-propelled and possibly responsive behavior.

One of the most important examples of complex systems is Life, which provides a source of inspiration in the search for new artificial complex systems. The concept of Life relies on a complex network of processes that are dependent on each other[4]. The function and dysfunction of the human body, or any biological system for that matter, is only broadly understood. We can describe and explain the function of most of the organs and are aware of most of the fundamental mechanisms at the cellular and molecular level, but the complex interactions of those processes that make a biological system a living and possibly even conscious entity are too complex for the human mind to envelope. Therefore, studying the origin of life by for example pursuing the creation of the least complex living system (such as protocells [5]) as well as understanding the principles of complexity may lead us to the point where we can imitate such systems and use them to create new technologies. Furthermore, as complexity plays an important role at every level of the scale of the universe, unexpected analogies could potentially further the understanding of seemingly unrelated topics.
Exactly such analogous systems are of interest to us because, similarly to how a mathematical

model describes a certain system by reducing it to its most essential parameters, systems that share essential mechanisms help us to understand a system (or at least aspects of it) by observing a potentially less complex one. This can be the case, even across sizescales of several orders of magnitude for example in the case of self-organization which can be seen on a mesoscopic scale[6].

In the pursuit to define and understand complex concepts such as Life it is helpful to split it into several aspects. These may in the case of Life, among many others, include: the boundary between the living entity and the world, the metabolism of the entity, displacement of the entity and evolution/procreation of the entity. The distinction between the entity and its surrounding is very important for not only philosophical considerations as for example displacement could not occur if no such distinction exists. A very crude definition of this distinction could be an area that is thermodynamically different from its surroundings by being far from chemical equilibrium. A metabolism is a process that maintains that distinction of the entity and its surroundings by keeping it away from equilibrium by chemical conversion of a nutrient that is found in the surroundings. The concept of displacement is important for the entity to follow the substances it needs to maintain the metabolism (and at a higher level to prevent it from becoming part of another metabolism). Finally, the procreation/evolution ensures to maintain this entity as a process for much longer timescales by splitting it up into generations. Furthermore, the evolution comes from small changes that, potentially, can increase the process-sustainability. It is obvious that each of these aspects already contains complex mechanisms and are highly codependent. The higher order complexity becomes evident when multiple of such entities interact and even start to cooperate.

The work done for this thesis is the development and phenomenological description of new far-from-equilibrium systems, that display complex spatio-temporal changes. In particular, the systems presented in later parts, have one thing in common: physicochemical interactions at the interface between the studies material and the aqueous phase. Such systems fit under the umbrella term "active matter" and in the following introductory part the reader can find a short review of the scientific field that deals with such systems and summarizes the origin of the inspiration for the work done in this thesis.

I. 2 Active matter

The term active matter encompasses a wide range of systems that have one thing in common: Dissipation of energy due to a state far away from equilibrium. Real-world examples include

self-organizing systems such as animal swarms, bacteria colony growth or even the spontaneous assembly of biological cell components[2,7–10].

Usually, a system is composed of many particles or entities that dissipate energy by, for example, converting chemical energy into kinetic energy. Due to the interactions between particles the spatiotemporal evolution of the system is highly complex and non-reversible. In order to describe and understand such systems it is useful to start at the individual level, as already the trajectory of a single particle can be based on a complex mechanism. Once that is understood and predictable it enables further understanding of collective behavior. Synthetic analogues of living organisms, also called life-like or self-propelled systems, are very useful in this regard. They are composed of chemical ensembles, which mimic certain aspects of real behaviors. This can include complex trajectories due to the dissipation of chemical energy[11,12], responsiveness to the environment[13] and change of the environment[14].

Just like Life, the systems of most interest to this work, are active due to the interactions between an object and its surroundings. The interaction occurs either at the air-water interface or the interface between the water and the object. Movement of most self-propelled objects is based on liquid flows that are driven by a dissipative physicochemical process. Highly relevant to this thesis' work is the so-called Marangoni effect in which a convective flow is triggered in the aqueous bulk and/or along the interface between the object and the water due to a chemical gradient that is proportional to changes of water-surface and/or object-water interfacial tensions caused by said chemical[15,16].

From a chemical and biological viewpoint, many self-propelled systems include substances that influence surfaces and/or interfaces, also called surfactants. What such substances have in common is their ability to decrease interfacial potentials due to a varying degree of amphiphilicity. This means that they have an asymmetric electronic structure such that one part is polar, while the other is not (See Figure I.1).

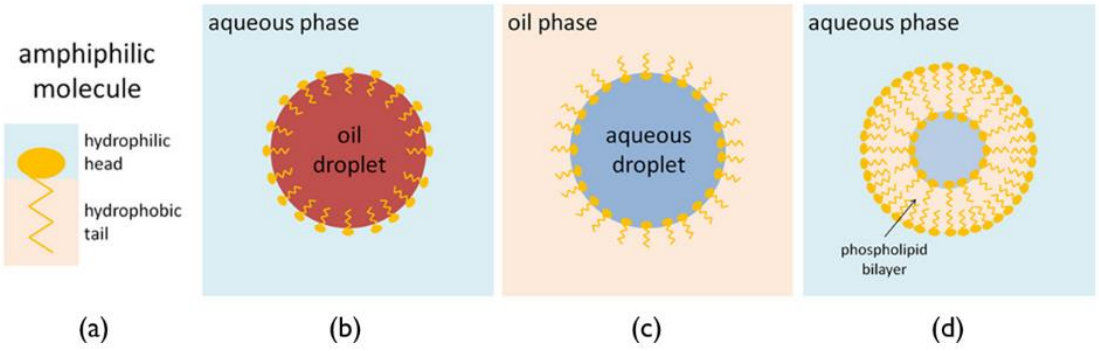

Figure I.1: (a) Graphical representation of an amphiphilic molecule. (b) involvement of amphiphilic molecules in the stabilization of an oil droplet suspended in aqueous solution. (c) Amphiphilic molecules stabilizing an aqueous droplet in oil phase. (c) Bilayer of amphiphiles, sequestering an aqueous phase inside another. Figure from Čejková et. al. 2017[13]

Amphiphilic molecules are mostly known from biology where highly amphiphilic phospholipids make up the main building blocks for biological cell membranes due to their thermodynamically driven self-assembly into bilayer structures at physiological conditions[17]. Some systems that will be presented in this introduction are responsive to their environment through what is commonly termed as artificial taxis i.e., the mimicking of directional displacement of organisms as a response to stimuli.

The artificial self-propelled systems, found in the literature, which fit this description can be divided into two sub-categories: Condensed matter and soft matter. In the following sections, selected examples of such systems, some of which inspired the work in this thesis, will be presented.

I. 3 Condensed systems

Self-propelled objects made of condensed matter are in general less complex and easier to work with, as they are less likely to be changed by their surroundings but rather interact with or change their surroundings triggering motion. Therefore, these experimental systems are very powerful tools for the understanding of basic underlying principles of self-displacement inside a fluid and interaction with substrates. The most basic principles of interest here are symmetry breaking, interfacial interactions and hydrodynamics One of the most studied type of artificially self-propelled particles in a fluid are self-propelled colloidal particles such as spherical or rod-shaped Janus particles. Such particles were first introduced by C. Casagrande et al. in the 1980's as amphiphilic glass spheres[18]. They are based on structures that have a broken symmetry by consisting of areas with different chemical or physical properties that interact with the surrounding medium. As an example, when micrometer sized polystyrene spheres of which half is plated with Platinum are suspended in hydrogen peroxide (H_2O_2), they will actively diffuse as the platinum catalyzes the decomposition of H_2O_2, which creates a chemical gradient of H_2O_2 and O_2[19]. Such systems can act as powerful analogues to for example individual or collective behaviors of similarly shaped bacteria [2,7,8].

Another experimental system that is of great interest to researchers studying complex systems and hydrodynamics is based on the interaction between terpenes such as the white crystalline substance camphor (see structure in Figure I.2) and a water surface. Already in the late 19th century it was discovered that a scraping of the crystalline substance, camphor, placed on a water surface expressed complex motion, that could almost be considered life-like [20,21].

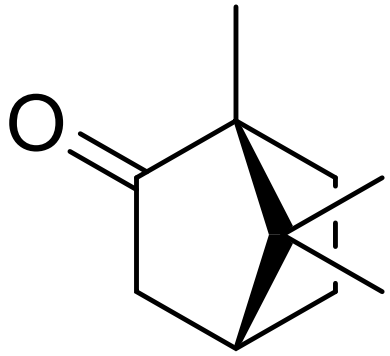

Figure I.2: Structure of a camphor molecule. Made in Chembiodraw [22]

The motion of camphor particles is due to the deposition of a thin film of camphor on the water surface. Camphor acts as a weak surfactant and lowers the surface tension depending on its surface concentration by more than ca. 20 $mN \cdot m^{-1}$[23–25]. As camphor is sublimating at room temperature, this film evaporates from the surface rapidly, creating a concentration gradient as a function of the distance from the camphor source. The proportionally equivalent surface tension gradient results in a surface Marangoni flow that propels the camphor particle towards an area with higher surface tension. As the source starts moving, the surface tension gradients become more and more asymmetric which results in a complex motion[9,12,26–28]. The dissolution of camphor does not play a significant role as it is only weakly soluble in water (1.2 $g \cdot dm^{-3}$ [29]). The crystalline granules of camphor can easily be pressed into simple shapes – most commonly round – using a pill press. A typical trajectory of a round camphor pill on a water surface in a Petri dish can be seen in Figure I.3.

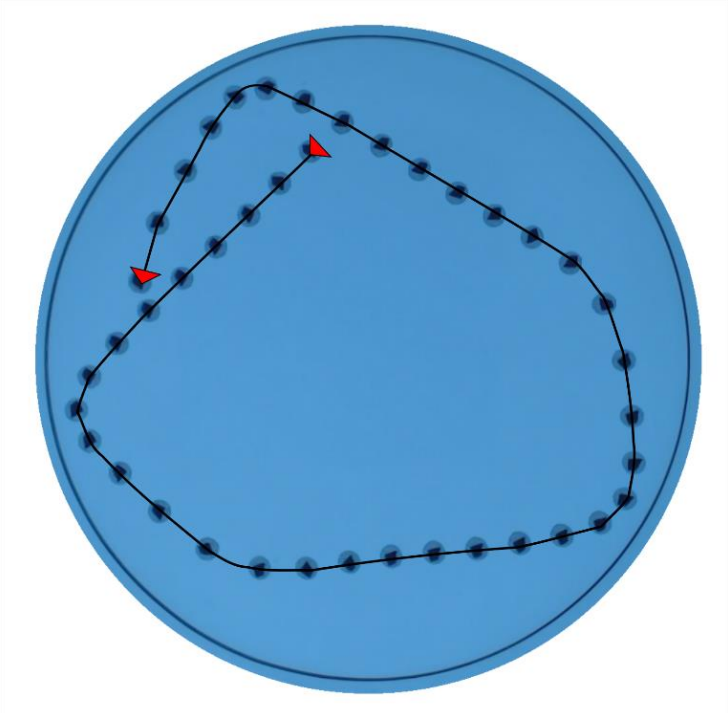

Figure I.3: Typical short-term (ca. 3s) trajectory of a circular 4mm diameter camphor pill.

The initial trajectories vary depending on the initial conditions which include the initial position of the pill and small imperfections in the shape of the pill. These initial conditions along with stochastic fluctuations in the diffusion and evaporation rate determine how the symmetry is broken[30]. Since this free movement already is quite complex and challenging to theoretically describe and at this point it is not possible to properly visualize or measure the distribution of surface tension or chemical gradients, there are methods to limit the freedom of the system in such a way that the breaking of symmetry becomes a controllable variable. This has been done by changing the geometry of the system, using one-dimensional channels that can be either circular (Example in Figure I.4) to obtain periodic boundary conditions[31] or linear (example in Figure I.5) which results in reciprocal motion[32,33]. In these cases, the speed and weight of the particle along with localized surface tension measurements provide important clues about the diffusion and evaporation mechanics of the camphor.

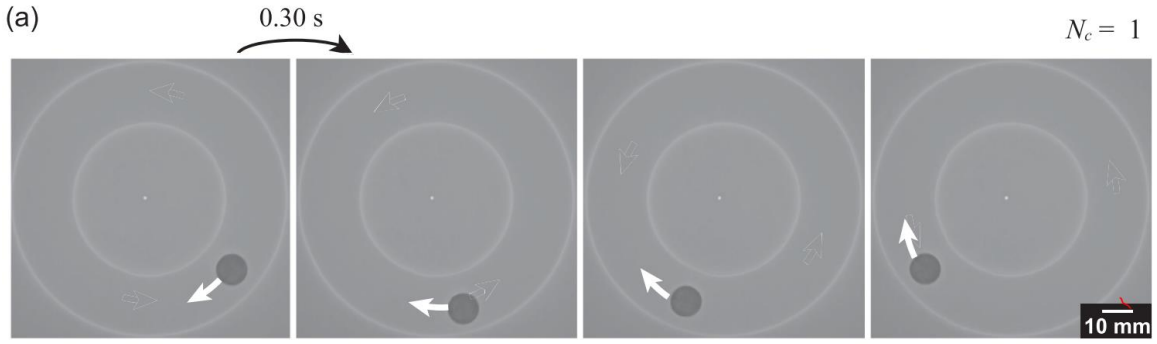

Figure I.4: Circular motion of circular filter paper saturated with camphor expressing a continuous unidirectional motion. Figure from Ikura et. al. 2013[31].

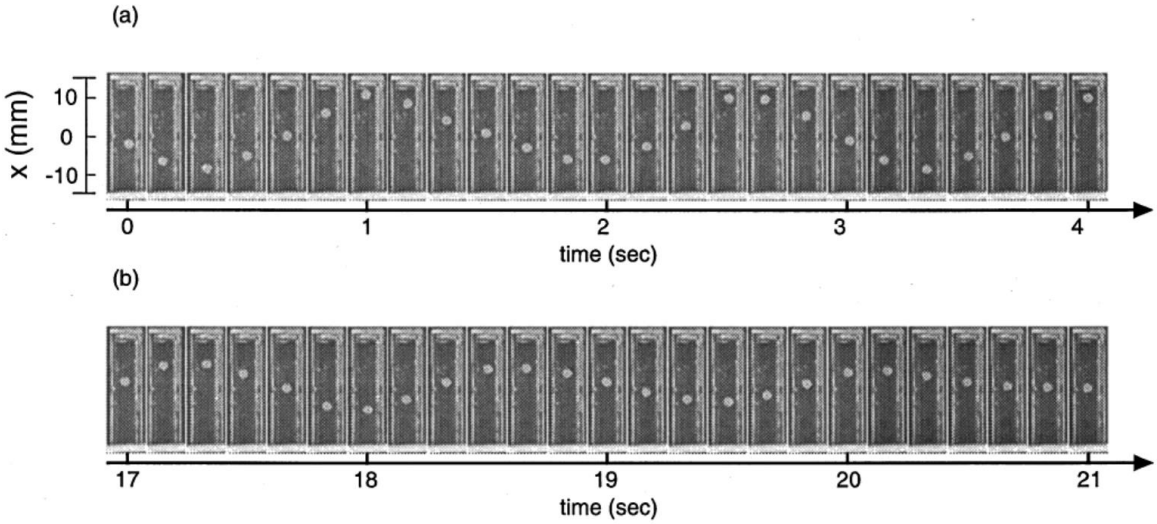

Figure I.5: Snapshots of a pressed camphor pill in a linear channel, expressing reciprocal motion between the two edges. a) and b) distinguish between two different time intervals 0-4 and 17-21s after placement of pill respectively. Figure from Hayashima et. al. 2001[32].

Another way of limiting the complexity and controlling the breaking of symmetry is to attach the camphor particle underneath a boat made of folded plastic or metal that limits the direction

of diffusion[34–36]. In such a setup the camphor particles have: 1. Limited diffusion depending on direction and 2. Depending on the pill position the symmetry can be broken in two different directions. A graphical representation of such a boat can be seen in Figure I.6. For instance, if the camphor source is closer to one side of the boat than the other, the shorter diffusion distance on one side results in a higher camphor concentration than on the other side. The resulting difference in surface tensions on each side of the boat with trigger a flow with a force proportional to the surface tension gradient. Just like a pill the movement itself changes the situation.

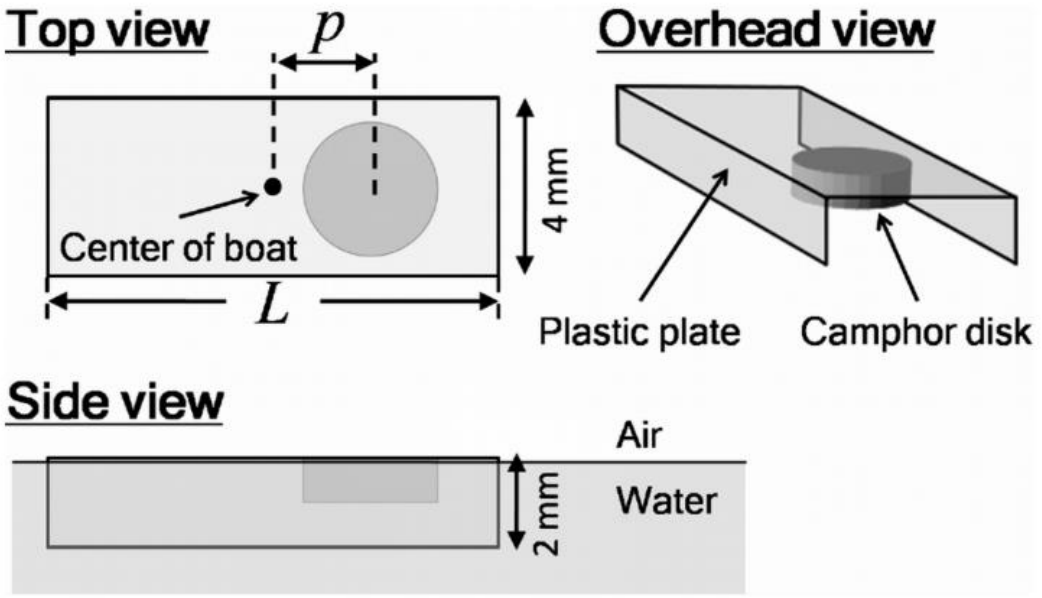

Figure I.6: A graphical representation of a camphor boat used in literature. The different parameters can be adjusted as necessary. Figure from Suematsu et. al. 2010[36].

Results have shown that such so-called camphor boats express different modes of motion depending on the pill position[36]. These include low activity for unbroken symmetry, intermittent motion of slightly broken symmetry and continuous motion of strongly broken symmetry (see Figure I.7). The shortcomings of such systems are that initial conditions/positions still have a strong effect on the behavior as well as boundary conditions preventing longer term observation of a specific behavior as the interaction with a boundary would influence the current behavior of a camphor boat. Nonetheless, boats are a useful self-propelled system as they can be hybridized to fulfil a certain function as for example in the research area of chemobrionics where camphor boats have been used to facilitate a random deposition of the chemicals that are involved in the growth of chemical gardens[37].

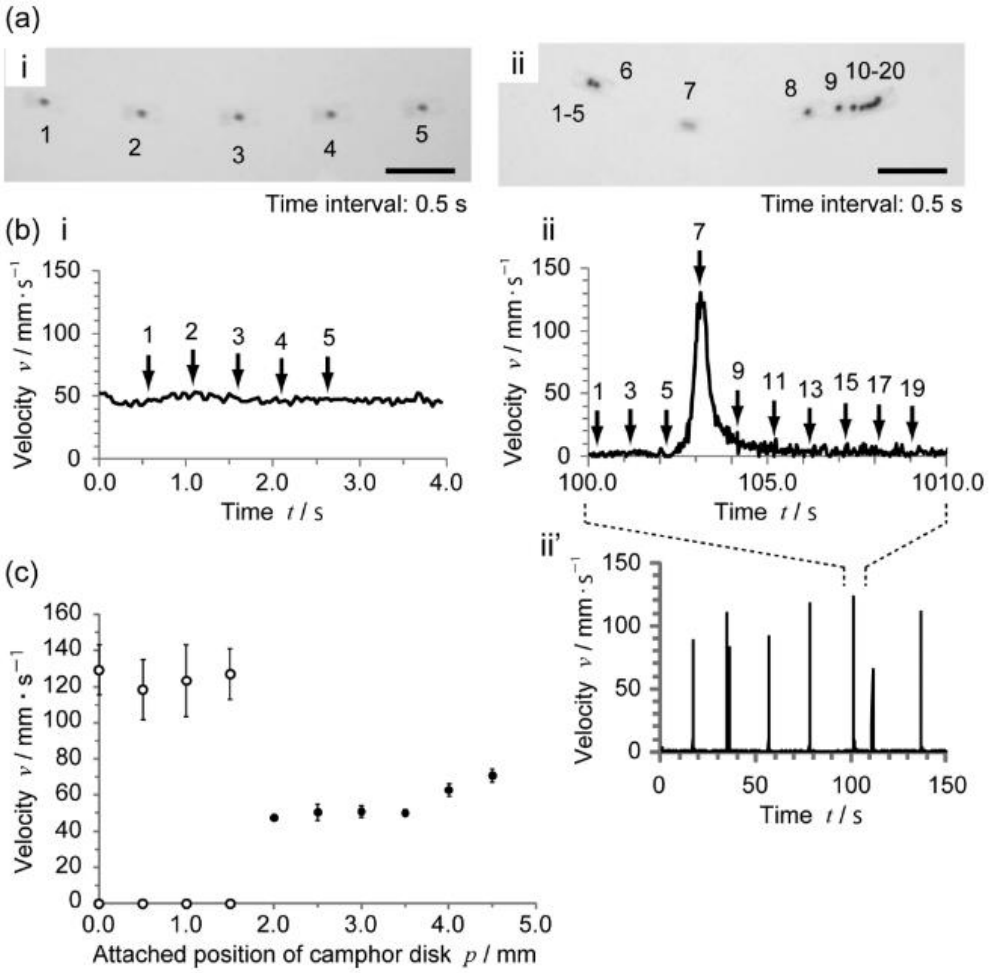

Figure I.7: Figure illustrating continuous and intermittent motion of a camphor boat. In (a) snapshots of boat motion is superimposed at a time interval of 0.5s (scale bar = 20mm) to illustrate the motion. In (b), the time series of (i) continuous and (ii) intermittent motion, which is a short time interval of the full intermittent motion shown in (ii') are displayed. (c) shows the average velocities as a function of the pill center distance from the boat center. Filled circles indicate continuous motion while empty circles show the minimum and maximum velocities of intermittent bursts of motion. Figure from Nakata et. al. 2010[36].

Attaching camphor particles as "motors" to different geometric shapes that are free to rotate on an axis can be further useful for the modelling of hydrodynamic drag forces and theorizing the diffusive flow of camphor on a water surface[38–40]. An additional advantage of condensed systems is that they maintain their shape which enables study hydrodynamics and deposition geometry dependence on shape of self-propelled objects [23,41–45].However, controlling the shape of camphor as a solid crystalline material is by the precise machining required for the production of a pill press that has more non-trivial geometry. This limitation has been circumvented in several ways. One of them is to prepare a porous medium such as agar gel[46] or absorbent filter papers[31] in the required shape and load them with camphor via camphor solutions in volatile solvents such as methanol or acetone.

Furthermore, other terpenes such as camphene[47] or camphoric acid[26,48,49] also express

self-motion and open up new possibilities. These substances are limited on other ways however as camphoric acid is not evaporating but dissolves in the water phase instead. Therefore, the duration of motion is limited by the solubility in the water phase. Camphene is very difficult to work with as it is a soft, wax and very sticky substance and creates a smaller surface tension gradient which results in reduced motion[47]. It depends however, on the ingenuity of the experimenter, as such properties can be useful instead of hindering. Thus, complex shapes can be obtained by manipulating the shape of camphene by hand or preparing hydrogels rich in camphoric acid or other water-soluble surface-active substances such as ethanol[50].

While these terpene-based systems are very useful for the study of simple self-propelled motion on a water surface, they are unresponsive towards their environment (apart from their self-induced change of the environment). Hence, artificial taxis is difficult to achieve with condensed matter systems. For the investigation of such aspects, systems involving liquid-liquid interface are much more useful.

I. 4 Soft-matter systems

Self-propelled soft-matter systems consist of phase separated liquid droplets that are propelled due to an internal mechanism that creates a flow at the phase boundary or an interaction with surface active substances that are dissolved in the droplet or the opposite phase. Life-like complex behavior is often seen in self-propelled liquid systems. This could be because life as we know it itself is consists of soft matter and the scientific consensus appears to be that life emerged in a liquid environment. This is also quite intuitive, since life cannot exist without flows, changes and interactions across phase boundaries as well as having a phase boundary that prevents miscibility in the first place. These are much more likely to occur at a liquid-liquid phase boundary as opposed to boundaries with solid phases.

Another aspect is the ability of liquids to easily mix or to act as solvents for solids. This provides an incredibly large reservoir of possible systems that can be designed in the expectation of a certain behavior. Since there are almost infinite possible ways to compose a system, the chemical and physical intuition of the experimentalist plays an important role in finding new systems with interesting behaviors by recognizing/predicting compositions that are far away from equilibrium in a way that may lead to interesting behavior. For that purpose, it is advantageous to look at actually living systems and recognize certain mechanisms. One important aspect is to look at the type of chemicals that are involved in living processes and investigate whether similar but simpler chemical compositions can imitate them.

The behavior of droplet systems can, depending on the type of system, be in response to many possible external or internal stimuli, but the mechanism of the response most often occurs at the phase boundary of the system[13,51]. Therefore, one can categorize droplet systems depending on their phase boundaries and what processes occur at which interface.
The first type are droplets which float, phase separated, on another liquid and is the most relevant to some of the work done for this thesis. They are most commonly composed of low-density oils that are either completely inert but acting as solvents for surface active substances or are composed of oils stabilized by a surfactant. There are examples of systems in which interactions and flows occur at the liquid-liquid interface as a response to internal chemical processes that trigger interfacial flows and internal convections or as a reaction with other chemicals situated in the adjacent liquid phase[52–54]. In other cases, the flow occurs at the liquid-gas interface, usually of the higher density phase and is a result of the droplet depositing or removing surface active chemicals on the liquid surface[10,55].

In other systems the droplet is situated in the bulk of the opposite phase and has no liquid-gas phase boundary. Depending on the ratio of densities, the droplet can be floating in the bulk or be in contact with a solid substrate at the bottom. In the first case, any interaction can only occur at the liquid-liquid boundary, where concentration gradients result in Marangoni flows along the interface, which in turn triggers an internal convection of the droplet. Thus, the breaking of the droplet's symmetry along with the surface flow leads to a displacement[51,53,56]. This kind of interaction has been demonstrated in several setups and the internal convections have been visualized as is depicted in Figure I.8.

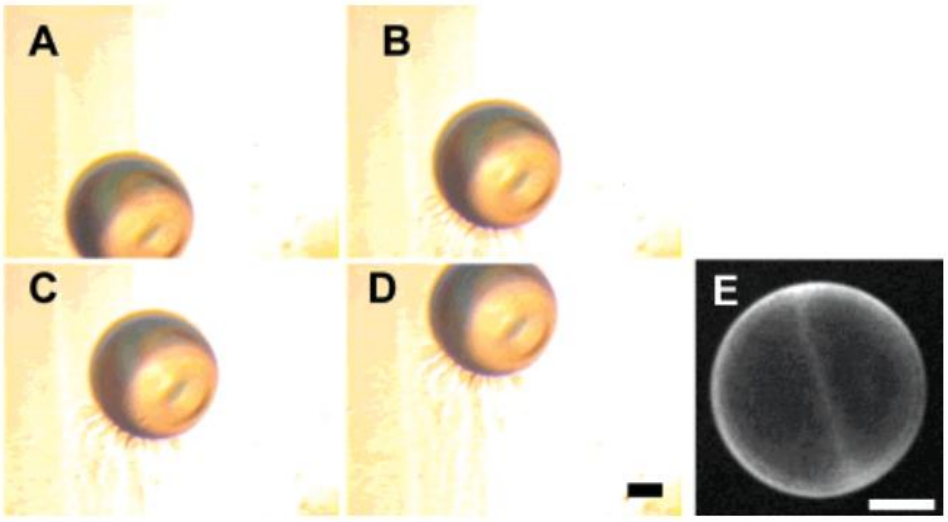

Figure I.8: Observation of microscopic moving droplet, visualized by phase contrast microscopy. In (A-D) it can be seen how the droplet has a tail of lipid material which is transported from one end to the other during motion as the droplet has an internal convection due to a chemical gradient across its surface. The internal convection is visualized via fluorescence microscopy in (E). Scale bar: 100 μm. Figure from [56].

It is either due to an internal reaction or due to an interaction with a surface-active substance in the bulk [57,58]. When the droplet is in contact with a solid substrate inside another liquid phase, the interaction is still most commonly occurring at the liquid-liquid interface[59,60], however there are examples of droplets interacting with a solid substrate without any other liquid phase present. Examples of this are droplets containing liquids of different evaporation rates, which can cause an internal convection and a modification of the contact-angle [61] or Leidenfrost-type droplets on a structured surface [62,63]. It would appear though, that most self-propelled systems on solid surfaces interact with a liquid phase through interfacial flows or through evaporation of components to a gas phase.

There is one more type of droplet system in which the droplet is situated on a solid substrate but in contact with both a thin liquid film and a gas phase. In such cases it is observed how droplets can both move or change their morphology due to both interfacial flows as well as evaporation induced changes[64,65].

An additional life-like property of many self-propelled droplet systems is artificial taxis i.e., the directional displacement reaction to external stimuli. There are many examples of which are propelled along a chemical gradient[66] and even are able to find their way towards a source of such a gradient through a maze, such as for instance decanol droplets following a chemical gradient of added decanoate [13,53,59,67]. Other droplet systems have been found to react to a light source which triggers phototactic movement[68]. Since droplets are soft matter, movement is not the only possible behavior. Droplets are also able to divide, fuse change their shape and interact with other objects similarly to amoeba that change their shape and move in response to physical or chemical stimuli[69,70] (see Figure I.9).

(i)

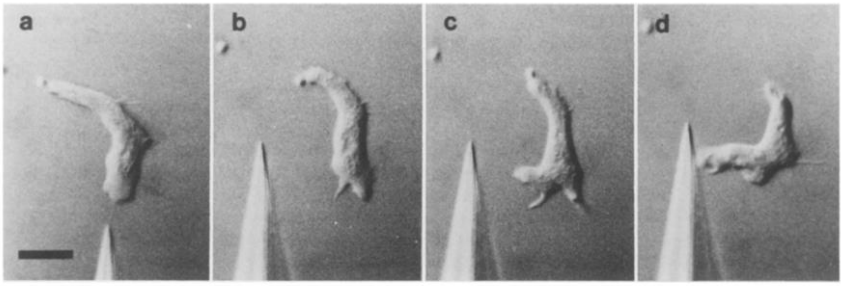

(ii)

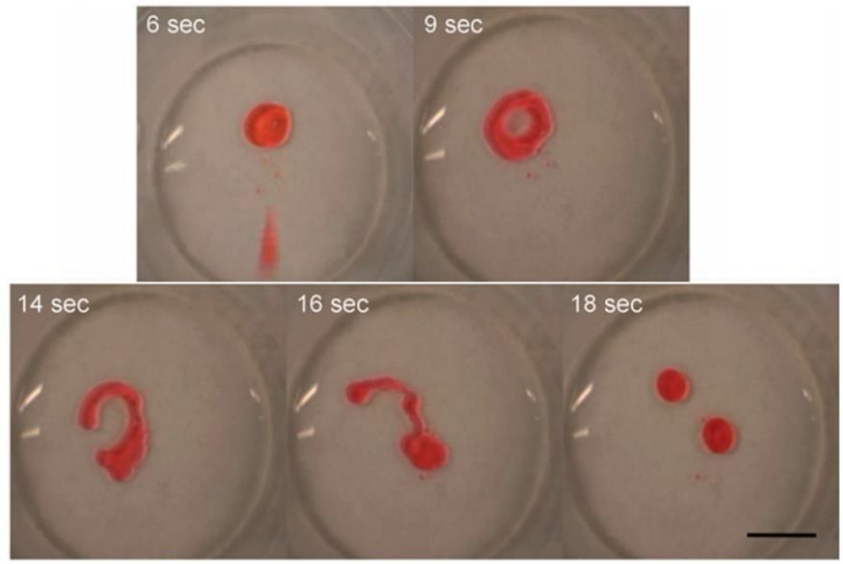

Figure I.9: (i) Chemoresponse of Dictyostelium discoideum amoeba to cyclic adenosine monophosphate (cAMP) delivered by a microneedle. It can be seen how the amoeba changes it's shape and moves towards the source of cAMP (scale bar= 10μm). Figure from Swanson et. al. 1982 [69] *(ii) spontaneous shape change anf fission of a 5μl droplet of nitrobenzene with Oil red O impregnated with 20mM CTAB added to a decanoate solution (scale bar= 5mm). Figure from Caschera et. al. 2013* [70].

It is rather simple to control, the behavior of droplets by addition of some chemistry that changes the interaction of the droplet with its surroundings. With this it is possible to induce division of droplets or coalescence by modification of one or several interfacial tensions in the system. That chemistry can be directly added to the droplet or be combined with artificial chemotaxis. Division is usually triggered by a change oil-water interfacial tension along with a surface flow that will disturb the droplet to divide [55,70]. In the absence of strong surface flows and especially with high-viscosity oils it is possible to observe a change of the droplet morphology which is very reminiscent of the change in morphology that can be seen for certain biological systems such as white blood cells. A system of this kind will be presented as part of this thesis.

All of these examples emphasize what was stated earlier, namely that there are endless possible combinations for soft-matter systems. In this environment it requires chemical intuition and imagination to come up with new chemistries and behaviors. However, another

way is to take advantage of automation. The development of pipetting robots[71,72] or microfluidics in combination with machine learning and image recognition have enabled the possibility to search for new behaviors by creating setups in which thousands of combinations of droplet components can be tested while even using evolutionary algorithms to search for specific behaviors within the given parameters[73,74].

While exploring new behaviors of droplet systems it is also necessary to consider possible applications for such systems. The potential is there for them to be employed in the field of soft robotics which recently has been garnering increased attention [13,75–77]. Since self-propelled droplets can be designed in a way where it is possible to control their behavior and response to external stimuli, they are an obvious candidate for applications in this field. For that it is necessary to come up with protocols that enable us to control the behavior and response by addition of chemistry to the system. It has been reported that it is possible to use decanol droplets as a vessel for targeted transport and release of cargo such as alginate capsules that can be functionalized[78].

I. 5 Collective behavior

Another important aspect of life-like systems and active matter is the collective behavior. In this case, droplets have the advantage that they are easy to produce and can be quickly deposited to their respective reactive environment in larger numbers. Many droplet systems, such as for example the decanol droplets mentioned earlier, that have interesting individual behaviors, express even more interesting evolutions when interacting with several others[79]. Another interesting system, which will be further explored in a later part, is the collective behavior of ethyl salicylate droplets on a surfactant solution which is expressed as a periodical formation and collapse of ordered arrangements[10].

But also, the condensed matter systems presented earlier, are very useful to study collective behaviors. Their advantage is that it is possible to explore the effect of shapes and asymmetries in the interaction of self-moving objects. A good example of this are bristle bots[80,81] which are small oblong robots that propel themselves in random directions by vibrating bristles on their bottom sides. When large numbers are located in a confined area, they arrange themselves into ordered structures as can be seen in Figure I.10.

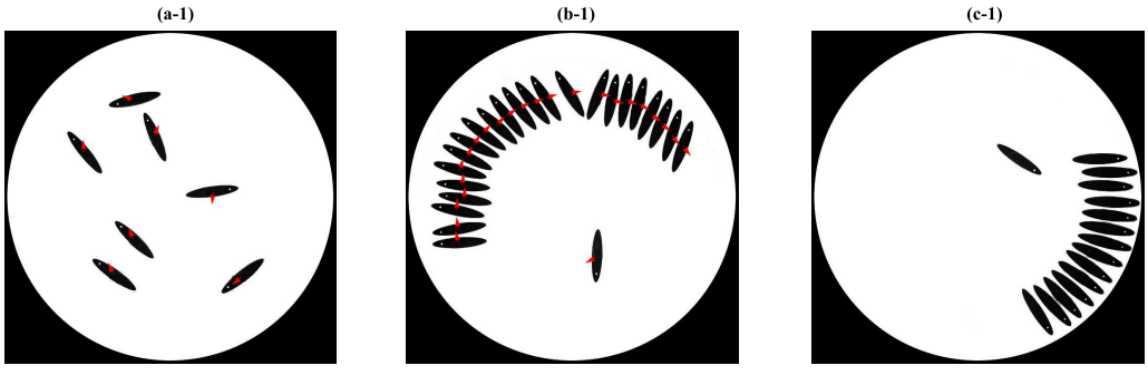

Figure I.10: Snapshots from experiments showing three different behaviors of spinning bristle-bots: (a) disordered (random) motion at low density, (b) swirling motion of spinners at high density and (c) stasis of bots at high density. self-organizing over time. Illustration from[80]

Using self-propelled materials on a water surface it is much cheaper and faster to recreate similar behaviors for further study. However, many of these materials have a consistency that makes the easy production of many shapes challenging. A new material will be presented in this thesis which enables the easy production of non-trivial geometric shapes for such purposes.

I. 6 Modeling and theoretical experiments

Although it was not applied in this thesis, it is important to mention that cooperation with skilled theoreticians is hugely beneficial, as the mathematical modeling of the complex phenomena observed in the previously presented systems enables us to truly understand the underlying mechanisms. The validity of such mathematical models can then be tested by performing theoretical experiments in the form of computer simulations in which the goal is initially to reproduce the behaviors seen in situ. However, once a mathematical model is good enough, it can be used to predict new behaviors, as it is much easier to change parameters.
Some of the most important types of models used to describe the behavior of active matter include reaction-diffusion models, the hydrodynamical model and more recently agent-based models.
Reaction-diffusion models are useful for the description of periodic pattern formations and can be traced back to a paper by Alan Turing entitled "The Chemical Basis of Morphogenesis"[82]. The reaction-diffusion equations can describe spatio-temporal patterns and wave-like phenomena that are formed due to local chemistry coupled with the differing diffusion coefficients of the reagents and products. Therefore, it is a very powerful tool for the description of complex behavior. A general way to express the reaction diffusion model is:

$$\frac{\partial q}{\partial t} = D\nabla^2 q + R(q) \qquad (1)$$

Where $q(x,t)$ is a vector describing spatio-temporal distribution of components, D is a matrix containing the information of different diffusion coefficients in the system and R accounts for all reactions. This general form can be representing a one component system in which it most commonly results in a traveling wave or in the case of multiple components can form complex patterns. For example, in the case of camphor particles moving on a water surface this general form can be applied by the following expression taken from [83]:

$$\frac{\partial u}{\partial t} = D\nabla^2 u - au + S\big(\boldsymbol{x}, \boldsymbol{x}_c(t),\, \Omega_s(t)\big),\ \boldsymbol{x} \in \Omega,\ \mathrm{t} > 0 \qquad (2)$$

where $u(x,t)$ describes the surface concentration of camphor, D describes the diffusion rate of camphor molecules on the water surface, a represents the sum of possible reactions, namely sublimation and dissolution of camphor from the water surface, S describes the supply of camphor molecules from the particle to the air-water interface and contains information about the geometry of the water bath ($\boldsymbol{x}_c(t) = (x_c(t), y_c(t))$) as well as the camphor particle ($\Omega_S(t)$). This equation contains the information about the surface concentration field of camphor on the water surface over time and can thus be used to determine the equation of motion for the particle which depends on the camphor induced surface tension gradients ($\gamma(u)$ -> surface tension is a function of surface camphor concentration). This model can then also be modified to describe droplets, where one has to consider that the geometric description of the droplet will depend on several factors such as the speed and the drag[84] or one can modify it to include more complex chemistry at any of the interfaces or in the bulk of either the medium or a droplet[54].

The hydrodynamical model, which was introduced by Vicsek et. al in 1995[85] is generally used for the description of collective behavior in active matter[2]. It expresses the tendency of multiple self-propelled particles of similar characteristics to align their orientation and speed with that of their neighbors. It considers that multiple equivalent objects that have some velocity which is determined by some fixed and simple rule along with random fluctuations. The main rule of the model is: *"at each time step a given particle driven with a constant absolute velocity assumes the average direction of motion of the particles in its neighborhood of radius r with some random perturbation added."*[85]. Theoretical systems based on such a simple model can express clustering, transport and phase transitions.

Agent-based models can be traced back to the early 20th century when the first steps were done by people like Stanislaw Ulam and John von Neumann in the form of the first cellular automata[86], which consist of a regular grid of squares that can have either an on or off state. Starting from an initial distribution of states, the new states of each cell at every consecutive time step depend on set rules. These rules determine the new state based on the

current state and neighborhood of each cell. Since the 1970's, agent-based models have steadily moved into closer focus, as they are based on simple rules than can serve as efficient approximates of higher order complex systems that involve "agents" changing themselves and/or their environment. Thus, they are also useful tools in the description of active matter and life-like behaviors.

I. 7 Goals of this thesis

The main goal of this thesis is to find new materials with self-propelled behaviors and to demonstrate their use in simple and inexpensive experiments for the investigation of the complex spatio-temporal dynamics of single- and multibody self-propelled systems. Despite the apparent abundance of self-propelled and life-like systems, the challenge for theoreticians is to find new types of behaviors and chemistries to generate new experimental data as inputs for improving theoretical models on non-linear dissipative systems. Therefore, it is important to improve the methodology of existing experimental systems and develop entirely novel ones to enable simple experiments that can be robustly reproduced *in silico*. We also look for potentially previously undiscovered types of behavior in biology and/or experimental active matter. With such systems we can widen our horizon of phenomena in regards to, life-like systems. Nano-, life- and artificial life sciences are some of the most promising scientific fields at the moment because Life is one of the most advanced technologies, which we are still barely able to apply for human innovation. My contribution, in the form of this thesis will be presented in the following three parts. The parts are presented in the order of a phase transition from condensed, over semi-soft to soft-matter. In the first part the development of an improved experimental setup for an existing self-propelled camphor boat system[36] will be presented. Following that, in Part 2, the development of a whole new type of hybrid self-propelled material, based on camphor and camphene, at the intersection between condensed and soft matter will be introduced along with preliminary characterizing experiments. The subjects for the soft-matter part in Part 3, are three different droplet systems. The first is a completely new type of self-propelled droplet system consisting of camphor and the dye Oil red O dissolved in paraffin oil. The second is a previously known self-propelled droplet system involving the interaction between ethyl salicylate and a surfactant solution. The third is a combination of two different oil-droplets (ethyl salicylate and 1-decanol) with the aim to study the interactions between different materials.

Reading recommendation:

I recommend reading the following three parts, while having the playlist of movies open which can be found here:

https://youtube.com/playlist?list=PLy9lT30tFAXYKPZ75hK4VbRQe6WvuhR2R

,

via this QR-code that can be scanned using your tablet or smartphone:

and

As a list in Chapter VII. Also, if this thesis is viewed digitally, the Movies can be accessed by clicking on the word.

II **Part 1: Camphor boats**

II. 1 Introduction

When a crystalline piece of camphor is placed on a clean water surface it will start to rapidly move across the surface in a seemingly random fashion. The object will decrease in size and mass during this motion and keep going until it has completely disappeared. These self-propelling properties of Camphor as a pure substance were known already during the Edo period in Japan where it was used in toy dolls which are self-propelled on a water surface (See Figure II.1). Camphor swimmers were first scientifically reported on in the late 19th century by Charles Tomlinson and Lord Rayleigh[20,21] and have in recent times been revisited and studied extensively by researchers who are interested in understanding the complex nature of this motion and describe it mathematically[9,23,24,87,88].

Figure II.1: Illustration from Japanese Edo period, depicting self-propelled floating toy dolls.

The motion is based on a unique combination of physical and chemical properties of camphor:

i. Camphor has a low enough density to float on a water surface and is practically insoluble in water[29].

ii. Camphor molecules can form a thin film on a clean water surface which will act as a weak surfactant and reduce the surface tension to below $50\ mN \cdot m^{-1}$ depending on the surface concentration of camphor [23–25].

iii. Camphor has a comparably high vapor pressure [89] at room temperature which means it will sublimate similarly to substances like naphthalene[90,91].

The mechanisms by which camphor particles deposit camphor molecules onto pure water surface include direct contact dissolution onto the surface and/or sublimation followed by vapor deposition onto the water surface in the immediate surroundings. The camphor layer

will diffuse away from the source and decrease in concentration as a function of distance as camphor evaporates from the surface.

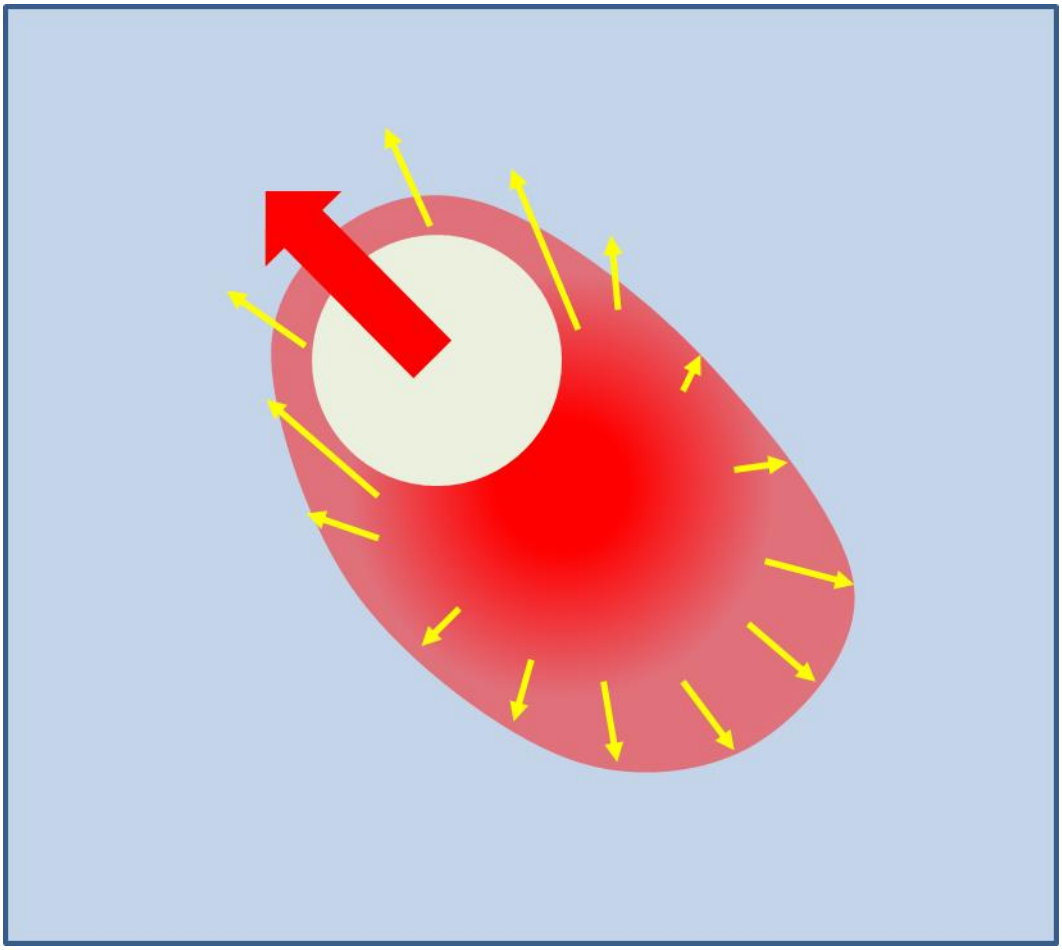

Figure II.2: Motion of a round camphor particle. The concentration of deposited camphor to the surface is represented by the red gradient behind the moving particle. Yellow arrows represent the surface Marangoni flow and the red arrow represents the force acting on the particle as a result of the flow.

This will result in a camphor surface-concentration gradient which due to the surfactant properties of camphor, corresponds to a gradient in surface tension. The gradient triggers a Marangoni flow[15,87] which effectively makes objects on the water surface move towards areas of higher surface tension. Hence, the camphor particle will start to move along the steepest gradient in surface tension. Simultaneously, these gradients are maintained over time via evaporation of camphor from the surface, sustaining the motion until all camphor has dissipated. In Figure II.2, a graphical representation of the camphor particle motion can be seen. The camphor concentration is represented by the red color gradient. The resulting surface flow is represented by the yellow arrows and the force acting on the camphor particle due to the surface flow is represented by the red arrow. In the most commonly used models to describe the camphor particle motion[9,27,32,42], the force $\boldsymbol{F}$ and torque N acting on the particle are expressed as follows:

$$\boldsymbol{F} = \iint_{\Omega(\mathbf{r}_c,\theta_c)} \nabla' \gamma\big(u(\boldsymbol{r}')\big) dA' \tag{1}$$

$$N = \iint_{\Omega(\mathbf{r}_c,\theta_c)} (\mathbf{r}' - \mathbf{r}_c) \times \nabla' \gamma\big(u(\boldsymbol{r}')\big) dA' \tag{2}$$

Where $\Omega(\mathbf{r}_c, \theta_c)$ geometrically describes the camphor particle ($\mathbf{r}_c$ is the center of the particle and θ_c the characteristic angle) and determines the region from which camphor is being released onto the surface, $\gamma\big(u(\boldsymbol{r}')\big)$ is an expression that describes the surface tension as a function of the camphor surface concentration u in that particular infinitesimal part of periphery $\boldsymbol{r}$, dA' is an area element of the particle region $\Omega(\mathbf{r}_c, \theta_c)$ and $\nabla'$is the vector differential operator with respect to $\boldsymbol{r}'$. This is described in further detail in reference [43]. The solid camphor pill could be thermodynamically described as a far-from-equilibrium system and the motion is driven by the dissipation of solid camphor into the atmosphere[82].

The seemingly complex motion of a camphor particle in a typical experiment heavily depends on the symmetry of the system. By controlling the symmetry, it should be possible to predict the behavior of the system[40–43,92]. Some main factors which influence the symmetry are: shape of the particle, shape of the vessel, initial conditions (where and how the particle is placed) and airflow. Imagine a perfectly symmetrical system, where a perfectly round particle is placed, precisely in the middle of a perfectly round dish, on a perfectly still water surface while the air around it is not moving. In such a case the particle should stay still in its initial position at least until the symmetry is broken somehow. Of course, creating such experimental conditions is next to impossible. A disk-shaped pill can be produced by using pressure; however, it will always have enough microscopic deformations such that the symmetry will be broken and methods to make a perfect geometrical shape from this solid crystalline material are not readily available therefore it will move in a seemingly random manner (see Movie 1). Even the crystal alignment in the particle could be enough to break the symmetry somewhat. Furthermore, controlling initial conditions repetitively is very difficult and even a very small perturbation will heavily influence the outcome. So, one has to come up with other ways to control the breaking of symmetry.

One way of doing so is to place a disk-shaped camphor particle underneath a rectangular "boat" which has two open and two closed sides (See Figure II.3).

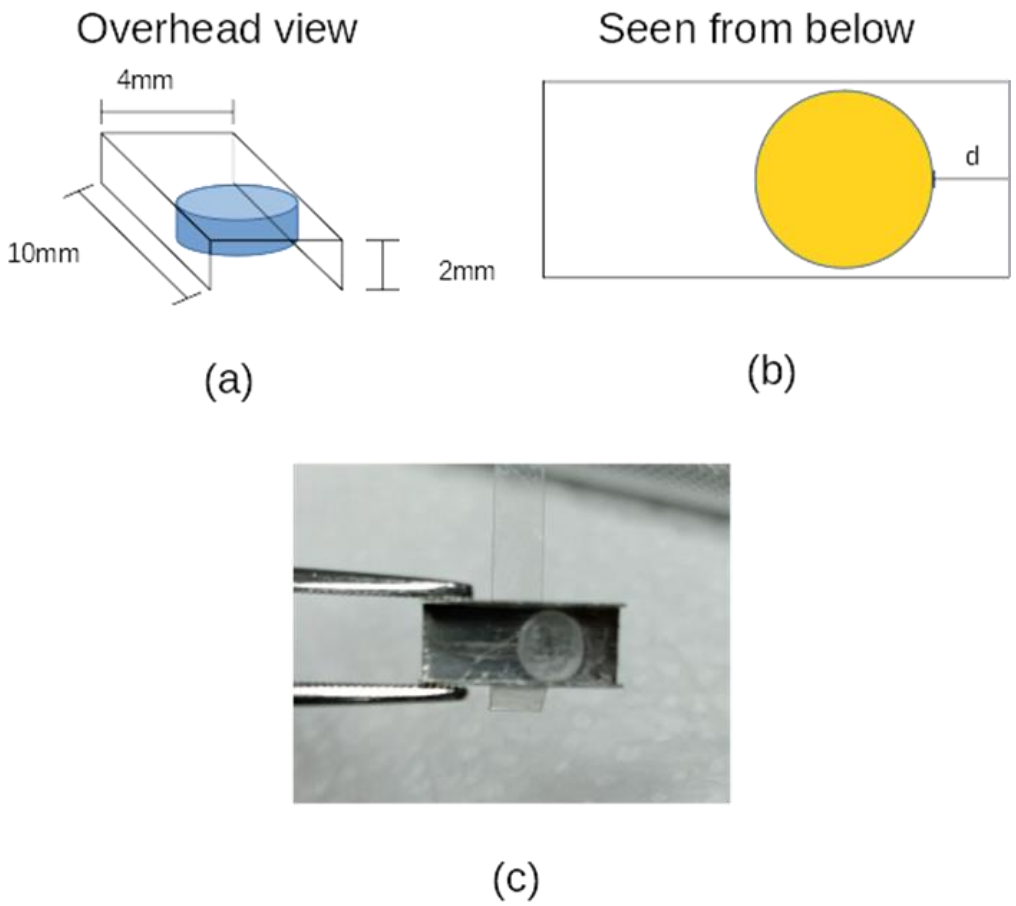

Figure II.3: (a) Overhead view of a typical camphor boat. (b) the camphor boat as seen from below with the pill at a distance, d, from the boat edge. (c) Photo of the actual 10mm boat used in experiments.

This restricts the diffusive flow of the camphor layer by slowing it down and making it bidirectional and simplifies the system. The symmetry can be changed by changing the distance between the pill and one of the open edges of the boat. Initial studies of such systems observed a mode-switching behavior where the mode of motion switched between a continuous motion when the pill was close the edge to an intermittent motion when the pill was further away from the edge [36] (See Movie 2 showing example of how the edge is interfering with motion). My initial work on this project was to reproduce these results and to come up with an improved experimental setup where the behavior of a camphor boat can be observed over much longer times, thus yielding more information.

II. 2 Development of new experimental setup

For early experiments we reproduced the experimental setup from Suematsu et al.[36]. A Petri dish with a diameter of between 9 and 12 cm is filled with 50 ml of MilliQ water. The boat is made of a 10x6 mm sheet of clear plastic which is folded over by 2 mm on two sides. Using a pill press, the camphor discs were produced by pressing commercially available (1R)-

Camphor (98% purity, Sigma-Aldrich) to obtain pills that are 3 or 4mm in diameter and 1mm in height. Such a pill was glued underneath the boat using LOCTITE 454 glue. A camphor disk with a diameter of 3 or 4 mm, depending on experiment, was glued underneath at a varying distance, d, between the edge of the disk and the edge of the boat (Figure II.3). We were able to phenomenologically reproduce the results from the paper. However, in this system the boat was moving freely on the dish such that it was colliding with the dish edge after a short time of motion which ended whatever mode of motion it was in at that moment. Our goal was to design a setup in which we could observe the evolution of motion types continuously over a long time depending on the position of the pill under the boat.

To this end, the first step was to exchange the material to something more durable, such that the same boat can be reused thus improving the repeatability of the experiments. We opted for a 0.2mm thick sheet of aluminium, which, when shaped to a boat, still can float on the meniscus of a water surface. An additional advantage of aluminium is that it can be washed with stronger solvents such as acetone, which makes it easier to remove the glue used to attach the pill underneath the boat.

In order avoid effects of dish edge, it was necessary to keep the boat on a circular trajectory. Our first attempt was to create a boat which is essentially constructed just like the conventional plastic boat but has an angled flap on one of the sides, which should maintain a circular trajectory when propelled. The obtained movement was not always as perfectly circular as can be seen in Movie 3.

The final design was to put the boat on a rod attached to a rotational axis in the middle of a Petri dish. This was done by attaching an arm made of plastic film to the top of the boat. The arm had a hole in the other end through which it could be placed on a fixed axis in the middle of the dish. A more precise schematic of the setup can be seen in Figure II.4. The boats all were 2mm tall and 4mm wide on the inside. Boat length (L) was either 10 or 15 mm. The best results were obtained using an arm-length of 70mm on a Petri dish with a diameter of 20cm filled with MilliQ water to obtain a 4mm water layer.

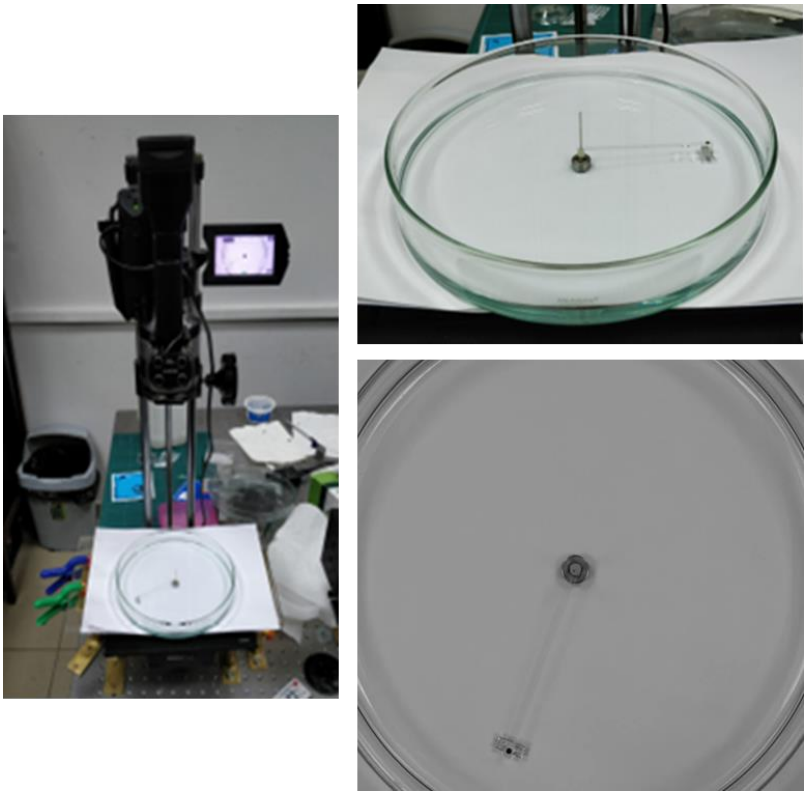

Figure II.4: Photos of the final experimental setup for a long-term continuous observation of camphor boat motion depending on the position of a camphor pill underneath the boat.

For any given experiment, the disk was glued at different distances, d, from the edge of the boat (As seen in Figure II.3). The distance was always measured from one side such that d could range from 0 to a maximum of 7 mm for the 10 mm boat and 0 to a maximum of 12 mm for the longer 15 mm boat (considering that the pill has a diameter of ca. 3 mm). This means that the effective diffusion distance, p, was maximum 3.5 mm for the short boat, at which point the pill would be positioned in the middle of the boat. For the 15mm boat the effective maximum diffusion distance, p, was 6 mm.

Working with superglue made it very difficult to glue the pill at very precise distances. Therefore, the pill usually was placed at an approximate of the desired distance by eye and the actual distance was then determined by taking a picture of the bottom side of the boat and measuring the distances compared to the known length of the boat. In order to track the movement of the boat, a black dot was glued on top of it. The experiments were recorded from above using a mounted digital camera (NEX VG20EH, SONY) and then digitalized using the ffmpeg and ImageJ software to extract the positional data. Data processing was performed using Mathematica. Angular velocity was obtained by averaging the angular change of positions two frames apart. By plotting the angular velocity as a function of time we get graphs for each experiment which give an overview over the behavior.

II. 3 Complex evolution of rotating camphor boat motion type for long observation times

Observing a camphor boat system at longer timescales revealed that the outcome, when working at this level of precision, is largely unpredictable unless the diffusion distance is very short i.e., the system is far away from symmetry. At longer effective diffusion distances we observe a range of mixed behaviors within most individual experiments. All observed behaviors can broadly be categorized into: continuous, intermittent, vibratory, inversive and reverse (See example of continuous motion in Movie 4). Those behaviors are recognizable from the angular velocity over time plots, examples of which will be presented.

II. 3.1 Continuous motion

The most predictable behavior was continuous motion where the boat would start moving in either direction, depending on which side of the boat the pill pas placed at, and keep going without stopping until the experiment was stopped. As already stated, this was only predictable for very short diffusion distances. For the longer 15mm boat we observed mostly continuous movement up to an effective diffusion distance of p=3 mm while at higher distances the behavior would be much less predictable as the probability of other behaviors occurring increases.

For example, at p=1mm we observe continuous motion with average rads/sec between 0.31 and 0.38 (between 2.2 and 2.7 cm/s) over two experiments in clockwise direction (d=1mm). Counter clockwise motion (d=11mm) was also continuous at average angular velocities of 0.35 and 0.38 rads/sec over two experiments. In Figure II.5 a) and b) we can see the angular velocity in rads/s as a function of time in s and the corresponding histogram of the angular velocity probability distribution ($P(v)$) for d=1mm, using the long boat (15mm) respectively. In Figure II.5 c) and d), the angular velocity and the corresponding speed histogram for d=11mm is depicted. It can be seen that the motion is continuous for times of up to 1h. Distribution of angular velocities is similar regardless of direction of motion.

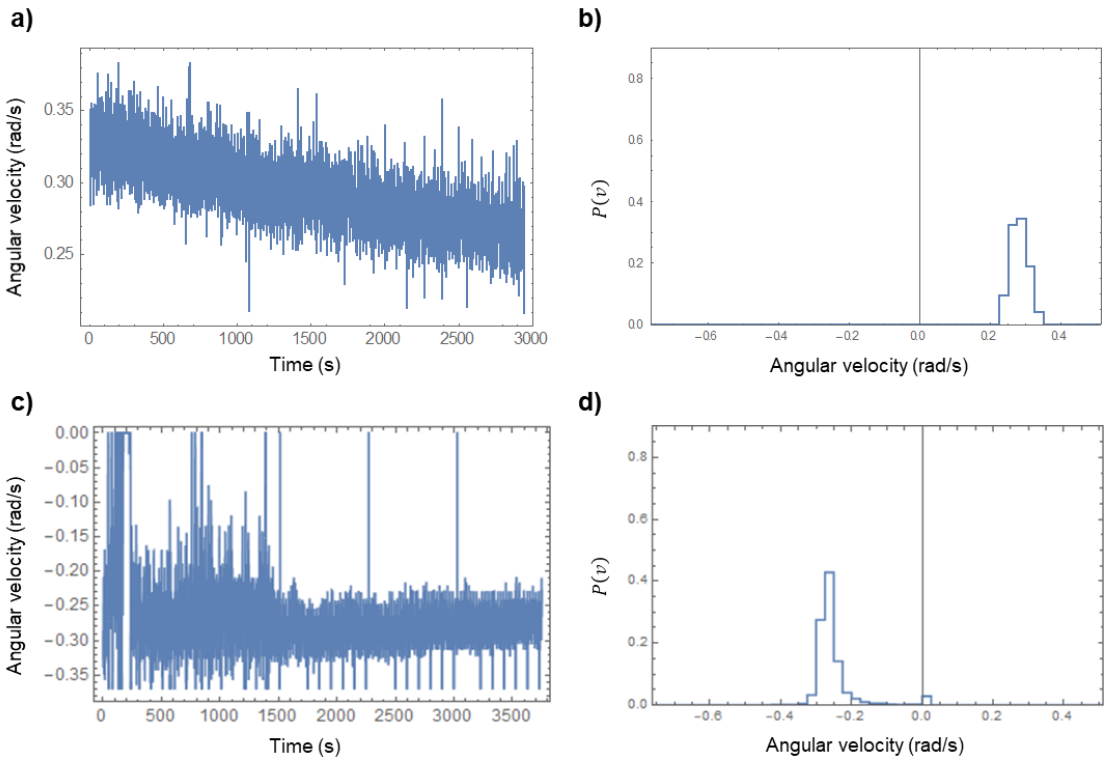

Figure II.5: Angular velocity traces and angular velocity histograms for p=1mm of a 15mm camphor boat. Clockwise (d=1mm) in a) and b), counterclockwise (d=11mm in c) and d). Regular outliers in c) are a result of postprocessing of video footage.

The large outliers of data that can be seen, especially in Figure II.5 c), are a result of changes in lighting such that in later treatment of the footage, the marker could not always get properly recognized by the software. Another contributing factor may be missing or added frames during the concatenation of individual raw footage files and later video editing to obtain workable file sizes (the raw footage is divided by the camera into chunks of 00:12:37 segments taking up 2GB of space). In both cases the angular velocity decreases over time. This is presumably due to the water phase slowly getting saturated with camphor. This provides a source of camphor molecules from the bulk which results in a small permanent surface concentration of camphor, lowering the surface tension slightly and resulting in a smaller gradient.

At p=3mm, one experiment was performed for each expected direction of motion (d=3 or 9mm respectively). In both cases continuous motion can still be observed over the whole duration of the experiment. In the case of clockwise rotation, the angular velocity was ca. 0.35 rads/sec (2.5 cm/s) and continuous motion was observed, slightly decreasing over time, for over 2 hours (See Figure II.6 a) and b)). In the counter clockwise direction the average angular velocity was higher at ca 0.4 rads/sec (2.8cm/s) (See Figure II.6 c) and d)).

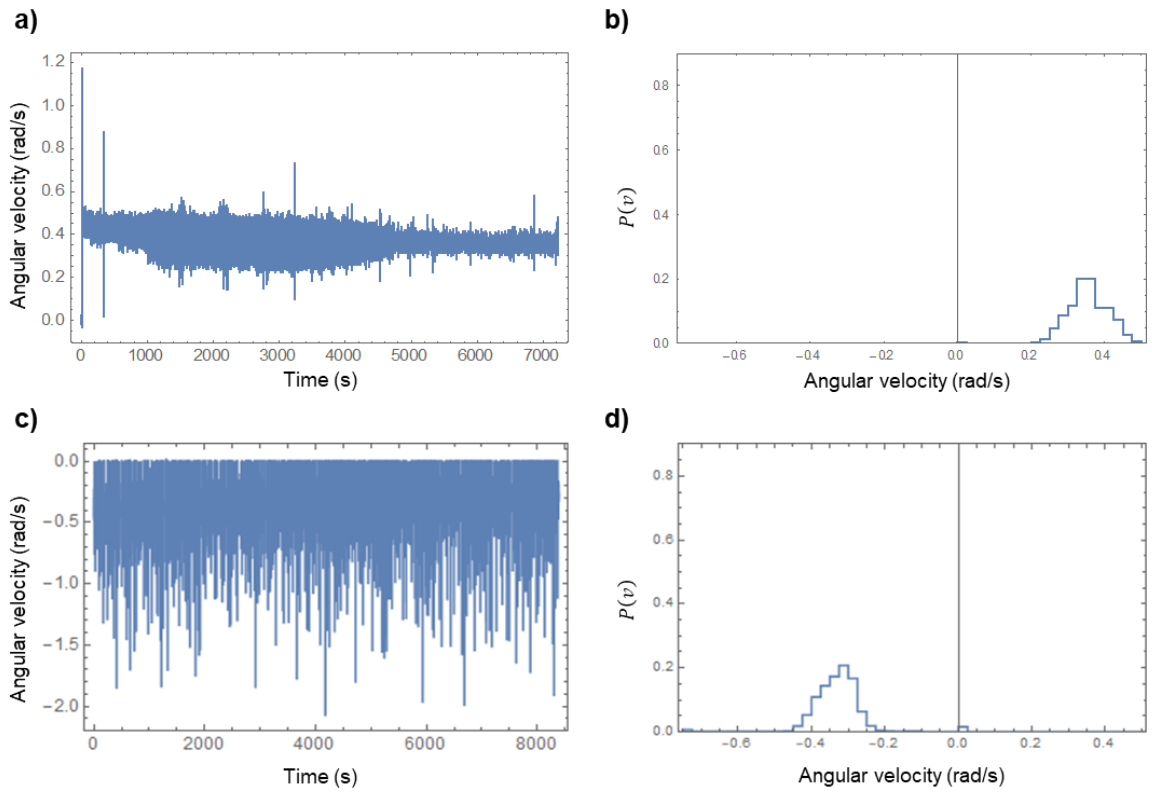

Figure II.6: Angular velocity traces and angular velocity histograms for p=3mm of a 15mm camphor boat. Clockwise (d=3mm) in a) and b), counterclockwise (d=9mm in c) and d). The fluctuations in c) are due artifacts picked up in post as the footage shows no such fluctuations in speed. They seem not to have a large influence on the histogram however.

At higher values of p, the occurrence of exclusively continuous motion becomes less likely with other types of behaviors occurring. Continuous motion can still be observed but usually at shorter time intervals. However, in few instances as for example at d=5,5mm (pill center only 0.5mm from the boat center), exclusive continuous motion was observed for the full length of the experiment of up to almost two hours.

In the case of the short 10mm boat, exclusively continuous motion could be observed at effective diffusion distances of up to ca. 1.5mm. In Figure II.7, the angular velocity plots and histograms can be seen for two individual experiments (d=1 and 1.5mm) are depicted.

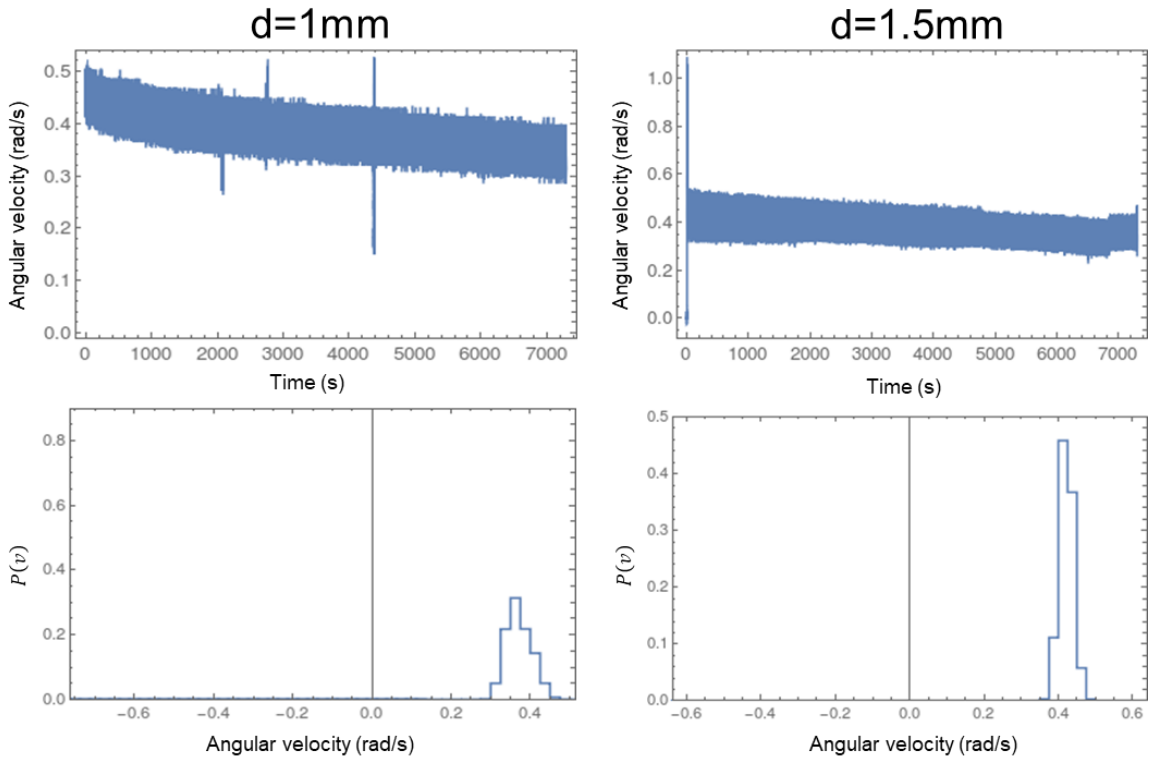

Figure II.7 : Two examples of continuous motion for the 10mm boat at d=1 and d=1.5mm. Continuous motion is maintained for over 2 hours with average velocity lying around 0.4 rads/s (2.8cm/s).

Also, for the short boat, pure continuous motion was observed above a distance of d=1.5mm. In one experiment with d=3.35mm (again very close to symmetric case) continuous motion was observed for longer than 2.5 hours (Figure II.8), albeit at a reduced average angular velocity. Again, this appears to be a random occurrence, as other behaviors were observed for other experiments at similar d.

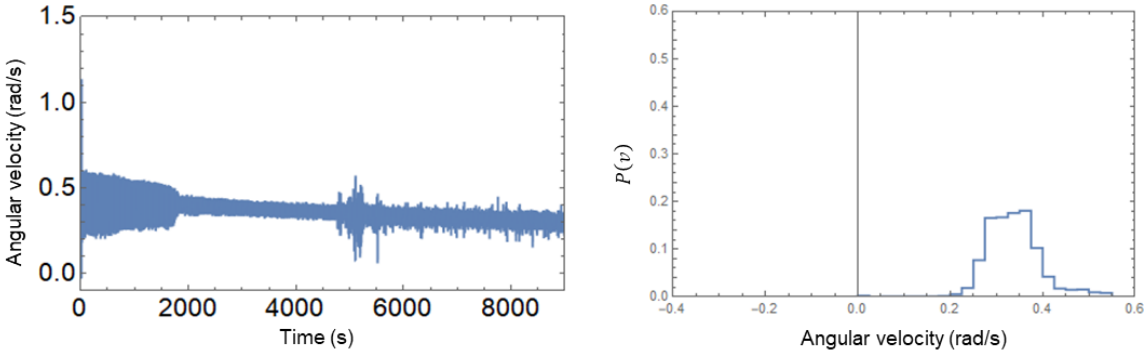

Figure II.8: Example of pure continuous movement (Left: angular velocity as a function of time. Right: histogram of angular velocities) observed for a pill position close to the symmetry point of the 10mm boat (p=3.35). Motion is continuous for up to 2.5 hours with lower overall speeds and a higher spread compared to the examples in Figure II.8, which is to be expected when the pill is positioned closer to the boat center.

II. 3.2 Intermittent motion

Intermittent motion is characterized by periodic bursts of motion with longer periods of

standstill. It usually occurs as one of several behaviors during any long-term experiment at diffusion distances above the highly broken symmetry case with the pill very close to the edge. Only in one experiment (L=15mm, d=5mm) was it the exclusive behavior with very regular bursts of motion with an increasing halt-period.

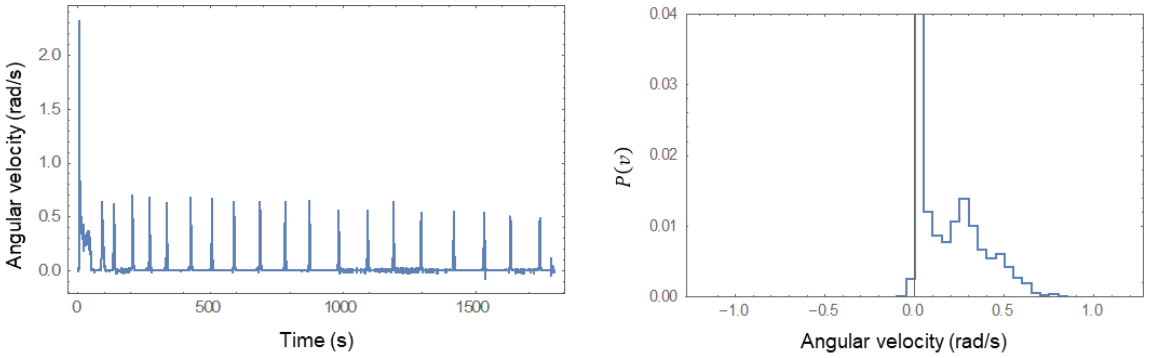

Figure II.9: Example of intermittent boat motion for a 15mm boat with pill position p=5mm. The angular velocity trace on the left illustrates periodic bursts of fast motion of more than 0.5 rads/s (3.5 cm/s). The Angular velocity probability distribution on the right shows that the boat is at standstill for most of the time (the peak for the lowest interval is cut off below its actual magnitude).

As can be seen in Figure II.9, the boat is motionless for most of the experiment with sudden bursts of motion which have more or less the same period in between (although it is increasing with time). This type of behavior can also be seen in Movie 5 where multiple bursts of motion are recorded. This experiment was not run for an exceptionally long amount of time, so it may very well be that it would have eventually changed its mode of motion. This is the for the example of L=10mm and d= 1.7mm. The angular velocity plot in Figure II.10 shows that both intermittent motion and continuous motion are present with continuous motion starting after ca. 2 hours of intermittent motion.

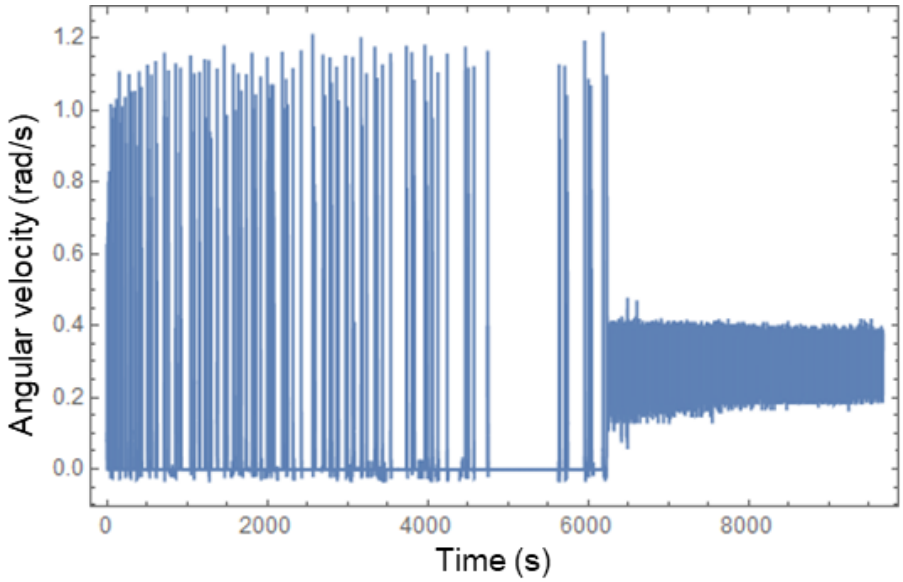

Figure II.10: Example of intermittent motion for the 10mm boat ad p=1.7mm. It is the prevalent mode of motion for the first 1.75h with sharp peaks of angular velocities above 1 rad/s (7cm/s). After that the motion changes to a continuous mode up to the point of experiment termination.

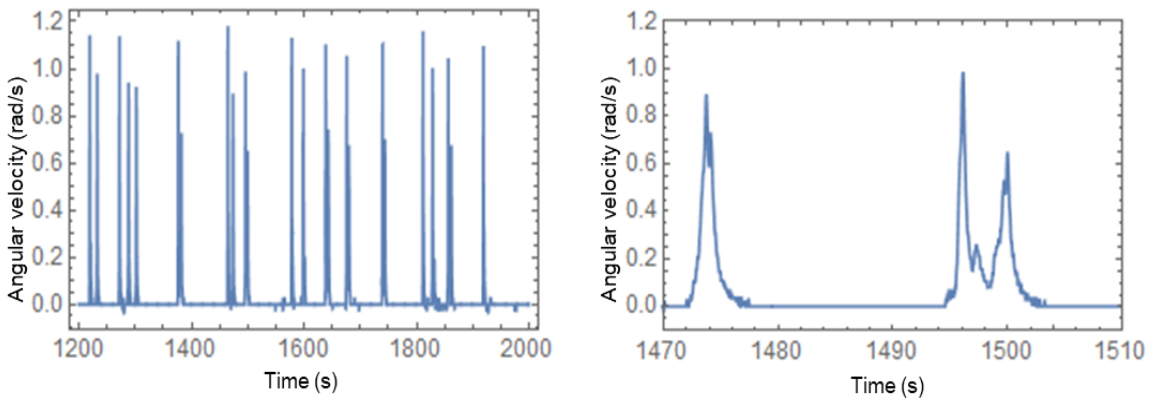

Figure II.11: Angular velocity from Figure II.10 at smaller time intervals to resolve the shape of peaks for bursts of motion. On the left it can be seen that it is not as periodic as in the example for the 15mm boat shown in Figure II.9. And even closer inspection reveals that the burst is split in two peaks for some cases.

Looking closer at smaller intervals (1200-2000s and 1470-1510s) in Figure II.11, we can resolve the individual bursts of motion, showing that the bursts of motion do not follow any particular periodicity. However, it is interesting to see that some bursts look like double peaks while others do not. If all peaks in this interval are superimposed (Figure II.12), one can recognize the two types of peak where the initial peak seems to have a universal shape (this has been confirmed for almost all experiments in which bursts of motion can be observed).

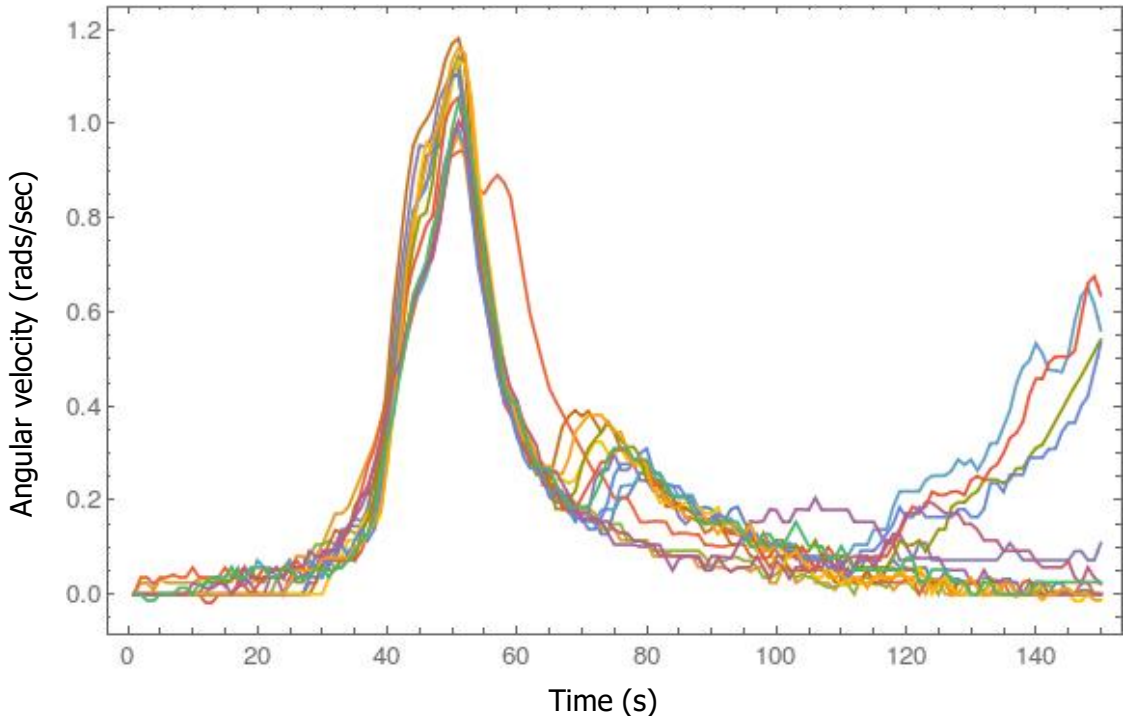

Figure II.12: Peaks from Figure II.11 (1200s-2000s, L=10, p=1.7). superimposed. Two types of peaks (single and double) can be seen while the initial peak appears to have a universal shape.

II. 3.3 Vibratory motion

During vibratory motion the boat appears to be standing still, while at closer inspection, it actually moves slightly back and forth. This type of motion can be seen basically at any diffusion distance that does not ensure continuous motion. However, the overall results show that intervals of standstill are more prevalent at pill positions close to the boat middle. For instance, at p=6mm (exact middle for the 15mm boat), it is visible in the interval of 130 to 1130s that the angular velocity switches between low positive and negative values (Figure II.13). This can also be seen in Movie 6, where the time is sped up to see the vibratory movement.

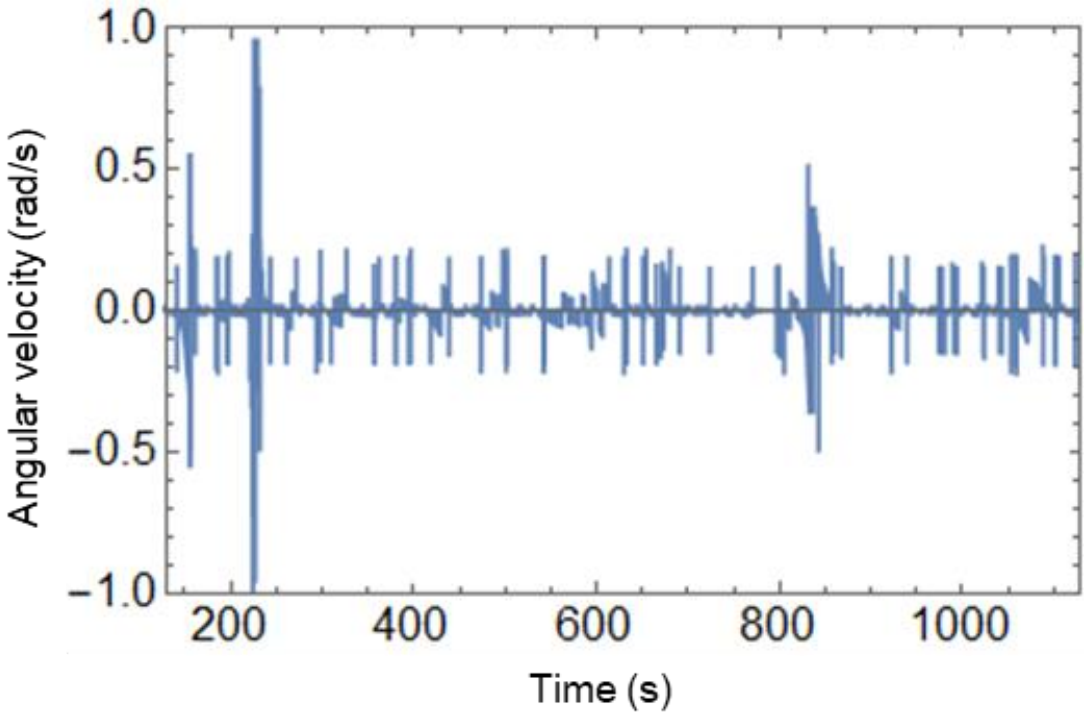

Figure II.13: Example of vibratory motion (L=15mm, p=6.0mm). It is expressed as low velocity bursts of motion in both clockwise and counter=clockwise direction. Often occurs in between bursts of motion for intermittent motion.

As for the long boat, vibratory motion is most prevalent for the 10mm at diffusion distance that correspond to the pill being close to the middle of the boat. The reason for this type of motion is assumed to be that the camphor under the boat is unable to produce a surface tension gradient in one direction large enough to overcome the static friction and/or meniscus. Another explanation would be that the gradient occurs in two directions and neither is large enough to overcome the other. This is probably the explanation for the behavior of configurations with longer diffusion distances (or rather diffusion distances in both directions are closer to equal). Vibratory motion was most often observed as the state in between bursts of motion but could also prevail for longer times up to several hours.

II. 3.4 Inversive motion

This type of motion is characterized by consecutive bursts of motion in two different directions (See Movie 7). Essentially it is similar to the vibratory motion but with a higher angular velocity and much larger distance travelled in each burst of motion (quarter to half rotation). Two examples of this are depicted for the short and the long boat in Figure II.14 where in a) multiple occurrences of inversive motion can be seen with standstill/vibratory mode in between, whereas for the longer boat in Figure II.14b), the inversive mode is prevalent for a shorter interval from 500 to 2000s.

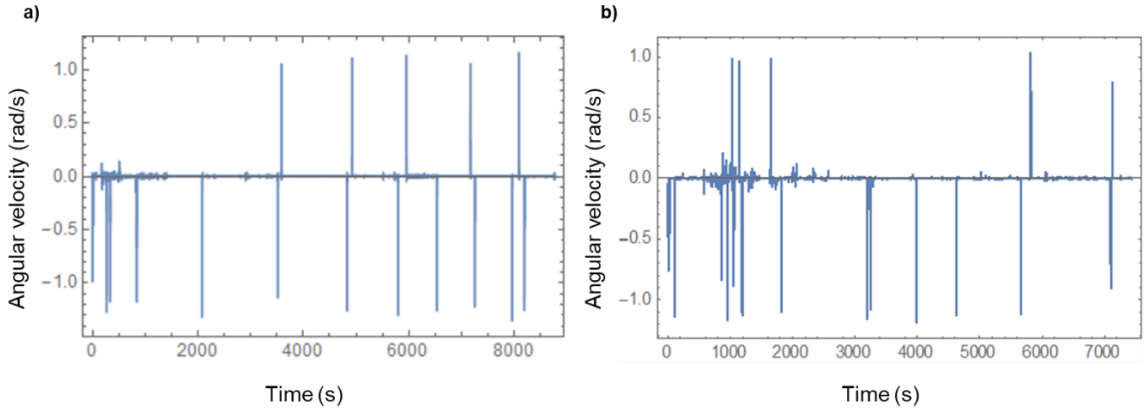

Figure II.14: Inversive motion examples for a) 10mm p=3 and b) 15mm p=5. In this motion a high velocity burst in one direction is followed by another I the opposite direction at intervals of standstill up to 100s in between. For a) it can be seen in the interval between 3000 and 8250s. For b) it occurs in a short interval between 500s and 2000s.

Resolving a set inversive bursts from Figure II.14 a), shows that there is a ca. 60s delay in between the bursts for the shorter boat (see Figure II.15 a)). This amount of delay was repeated in other experiments with similar behavior. For the longer boat the delays between inversive bursts were slightly shorter at ca 50s (See Figure II.15b)). When the inversive bursts were more isolated cases as is the case near the 6000s mark, the delay between bursts was usually around 120s, which also appears to be universally true from looking at other occurrences.

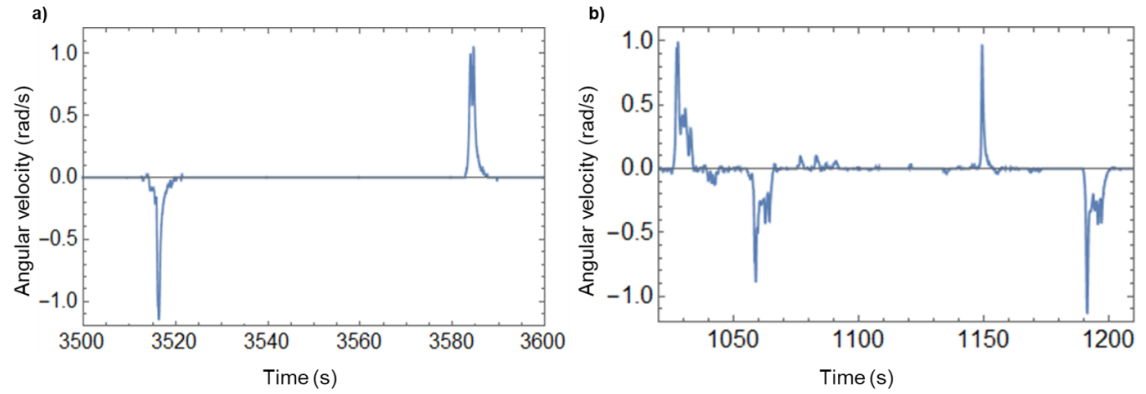

Figure II.15: Closer look at inversive peaks from Figure II.14 a) and b). It shows that there is a wait time of up to 100 seconds in between the bursts of motion.

II. 3.5 Overview of results

To once again emphasize, how unpredictable results could be at long time scales when working at this preliminary low degree of experiment preparation precision, the angular velocity plot of a 10mm boat with the pill placed at d=3.8mm (p=3.2mm) is shown in Figure II.16. In this experiment, the boat motion was observed for almost three hours. During this time, it can be seen from the plot that all of the previously introduced modes of motion occur at some point. Continuous motion in clockwise direction in the interval in the interval 3400s-5200s, continuous motion in counter clockwise direction at several short intervals ([1270,1390], [5470,5560], [6015,6090], [6570,6670], [7860,7940], [8320,8420] and [9300,9380]) and one long interval from 9750 to 10500 seconds. During the first 3000 seconds, vibratory and inversive motion occur, while the aforementioned short intervals of continuous motions occur as results of intermittent bursts.

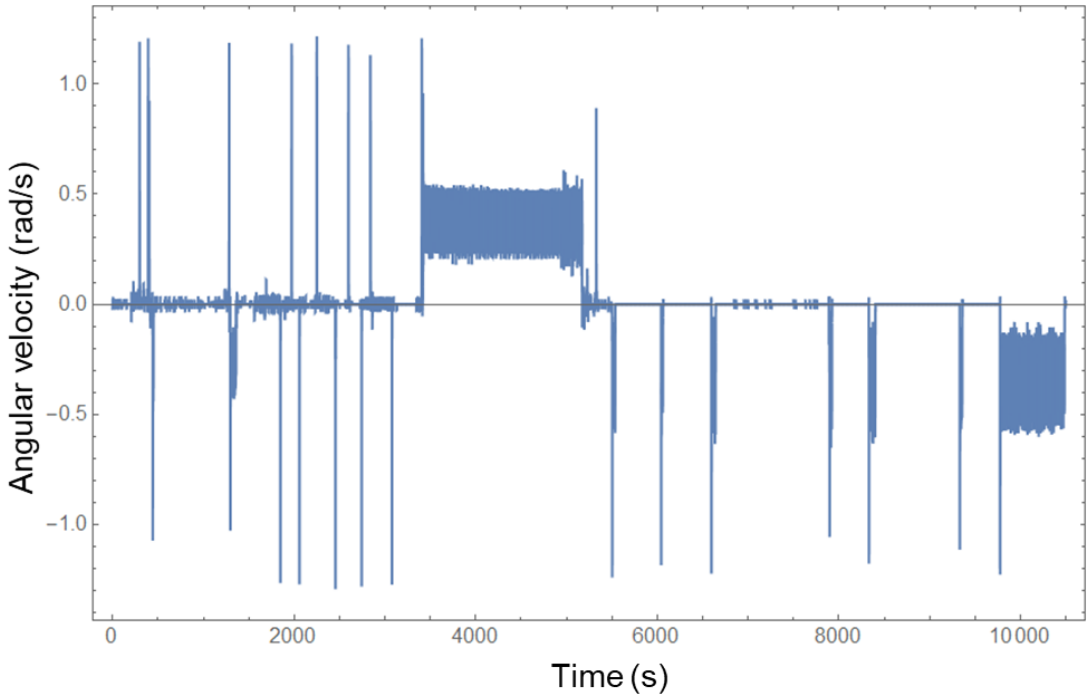

Figure II.16: Experiment using 10mm boat with the pill at d=3.8mm (corresponds to p=3.2mm). Over almost 3 hours of observation the boat exhibits all mentioned modes of motion. It shows how unpredictable the system is at long timescales.

To get a rough overview over the behavior, the angular velocity plots for all performed experiments at different pill distances, d, were observed to see which modes of motion occurred. In Table II.1 and Table II.2 this overview is depicted. If the mode of motion was observed for any experiment of a given pill distance, it is marked with a "+" and with a "-", if not. Any further statistical analysis was impossible with data we were able to achieve because it was not easy to precisely control the pill position. This means that for some distances in the

tables, there is only one experiment whereas for others there are up to three.

Table II.1: Overview of types of motion observed at different pill to boat edge distances for the 10mm boat.

L=10mm

Pill dist. d in mm (diff dist p in mm)	Continuous	intermittent	vibratory	inversive
1 (1)	+	-	-	-
1.5 (1.5)	+	-	-	-
1.7 (1.7)	+	+	-	-
3.4 (3.4)	+	-	-	-
3.5 (3.5 both)	+	+	+	+
3.8 (3.2)	+	+	+	+
4.0 (3)	-	+	+	+
4.3 (2.7)	+	-	-	+
4.5 (2.5)	+	+	+	+
5.0 (2)	+	-	-	-

Table II.2: Overview of types of motion observed at different pill to boat edge distances for the 15mm boat.

L=15mm

Pill dist. d in mm (diff dist p in mm)	Continuous	intermittent	vibratory	inversive
1.0 (1)	+	-	-	-
2.0 (2)	+	-	-	-
2.5 (2.5)	+	-	-	-
3.0 (3)	+	-	-	-
3.5 (3.5)	+	-	-	-
4.0 (4)	+	-	+	-
5.0 (5)	+	+	-	-
5.5 (5.5)	+	-	-	-
6.0 (6 both)	-	+	+	+
6.5 (5.5)	-	+	+	+
7.0 (5)	+	+	+	+
7.5 (4.5)	-	+	+	+
8.0 (4)	+	+	+	-
9.0 (3)	+	-	-	-
9.5 (2.5)	+	-	-	-
11.0 (1)	+	-	-	-

From looking at the two tables there is some correlation between complexity and the degree at which symmetry is broken. It would seem that there is a certain probability, which should

depend on the diffusion distance) for the boat to progress through the stages of motion. At standstill/vibratory, there is a certain probability to start movement once a gradient has gotten large enough to overcome the static friction and/or opposite gradient. Then the next threshold is whether it can maintain the motion or not. Thus, it goes through multiple forks: start moving or stay stationary. If movement starts, clockwise or counterclockwise. Next gate/fork: maintain motion or stop. If continuous state is reached it can stop again at any time and the string starts over. This implies a possible complex output to a very simple input (position of the pill).

II. 4 Conclusions

The overall results give an overview over what modes of motion can be expected during a long-term experiment depending on the diffusion distance. At intermediate to long diffusion distance (i.e., approaching the symmetry point), we observe the most diverse behavior, as at such ranges multiple or all modes of motion could occur within a single experiment. Despite the apparent high diversity in possible modes of motion for the experiments done on the symmetry point, the overall activity is decreased. That means that the overall traveled distances on average are shorter, the closer the pill is to the middle of the boat.

From looking at the results in Tables 0.1 and 0.2, it appears that the area of diverse behavior is skewed towards pill distances slightly beyond the symmetry point. The behavior at this tipping point/critical distance most likely is determined by asymmetries in our setup and external influences such as air flow. It would be very interesting to obtain better statistics of outcomes and have multiple equivalent experiments. However, this would require an updated, much more precisely fabricated and more controlled setup. With a precisely machined boat (possibly 3D-printed) and better way to attach the pill (we are working on a square pill setup in which the pill can be press fitted without using any glue) we could improve repeatability and increase the precision of pill positioning.

Even though the positioning of the pills was imprecise and results seem to be somewhat diffuse one can draw some general conclusions from these experiments. As expected, the behavior is more complex when symmetry is only slightly broken and becomes more predictive, the stronger symmetry is broken. The results over longer timescales resolve a complex evolution of behaviors which is not evident at shorter time scales[36]. This emphasizes the usefulness of the 1-dimensional/circular setup we designed.

III **Part 2: Hybrid material**

III. 1 Introduction

For the next step down the ladder of descending degree of hardness I present a new semi-soft-matter camphor-based material that was discovered by me during the course of my PhD-program. Since camphor by itself is a commonly applied in the field of self-propelled material and complex systems in general. It's motion on water surfaces has been widely studied extensively[9,12] and the field involving camphor swimmers/boats is rather saturated. Furthermore, camphor as a pure material exhibits a number of limitations for the study of certain aspects of self-propelled motion such as the easy production of self-propelled shapes that have already been investigated in theoretical experiments[42,44] for the real world verification of such results. Thus, in order to advance the field, it is necessary to develop modified materials that present different/new behaviors and mechanical properties. The main findings presented in this part were published in two separate papers[45,93] and some of the following sections contain direct excerpts from these papers. In this part, I present and discuss the properties of two similar materials as well as a side product with real world application potential.

III. 2 Discovery of camphor-camphene wax

In the search for a more versatile self-propelled material, the main limitation of camphor we aimed to improve is the shapability/malleability. When designing experiments with camphor it usually is formed into a small range of primitive geometrical shapes by pressing it into pills as described in the previous part or by making amorphous scrapings[23,32,87]. This is because camphor consists of white, translucent crystals at room temperature, delivered by chemical suppliers as small granules often times in bigger clumps.

In the search for alternatives to camphor, we purchased a number of materials which have a similar chemical structure to camphor such as camphoric acid or camphene. Camphoric acid is a white powder similar to kitchen salt granules. It does self-propel but motion is limited in time by the saturation of it in water, as it does not evaporate/sublimate from the surface like camphor does[26,48]. Furthermore, camphoric acid is more difficult to form into shapes than camphor. Camphene on the other hand, is very similar to camphor in structure (See Figure III.1) and another member of the terpene group of compounds.

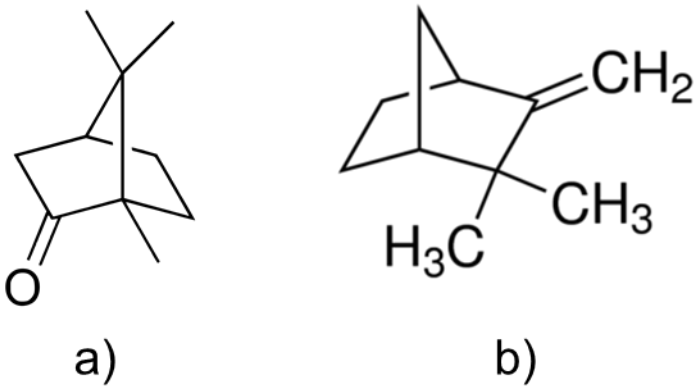

Figure III.1: a) Structure of camphor. b) Structure of camphene. Illustrations taken from suppliers website[94,95].

It is also a volatile compound although differently than camphor it does not seem to sublimate but rather melt on the surface at room temperature before that liquid on the surface evaporates[47]. There is one reference in the literature describing self-propelling nature of camphene[47] but initially we were unable to reproduce those results and did not pursue further experiments with pure camphene. When we started pursuing the goal of attaining a material which would have mechanical properties making it easy to manipulate the shape, we still wanted to keep camphor as the source of self-propulsion. We applied our findings from an earlier project[55] which is described in Part 3. During thar project it was discovered that camphor is readily soluble in liquid paraffin. Following that reasoning camphor was dissolved in several waxy hydrocarbons such as solid paraffin or beeswax. Camphor is easily soluble in such waxes when mixed at a temperature over their melting points. However, the resulting camphor-wax mixtures did not have the mechanical and physicochemical properties we were looking for. The first problem is that some of these hydrocarbons (for example fatty acids present in beeswax[96]) are actually amphiphilic and can themselves form a monolayer on the water surface which lowers the surface tension substantially[97] and will inhibit the propulsion by chemical gradient of the very weakly amphiphilic camphor (lowers surface tension to ca 50mN/m[23,24]). Furthermore, the resulting waxes were indeed softer than camphor by itself but often still crumbly and/or smeary which made it impossible to manipulate the shape by hand. Thus, simple mixtures of camphor with waxy hydrocarbons did not turn out to be feasible in this regard. The remaining option, camphene, has exactly the kind of mechanical properties we were looking for. At room temperature it is a very sticky malleable waxy material almost like the thick sap from some trees. Since camphor and camphene are structurally similar chemicals, we successfully were able to mix them. Camphene has a low melting point and camphor will readily dissolve/mix in the liquid camphene. At higher temperatures this process was faster so we settled on mixing the two components at minimum

140°C. Upon cooling down, we gain a waxy material. The thusly prepared material presents a number of advantageous mechanical properties. Firstly, it is malleable in a way that one can from it into any shape using your hands, which was the main desired property. It should be mentioned here that the material is very sensitive to any fatty substances which will make it crumbly and fall apart. This is most likely due to one or both of the components being more soluble in oils than they are miscible with each other so that the oil will quickly penetrate the substance (similar to gallium in aluminium[98]). Therefore, it is best to handle the material using gloves and on clean surfaces. Additionally, the material can be rather sticky (stickier with higher camphene content). It strongly adheres to most common surfaces such as glass, metal, hard plastics and even Teflon. It does not stick to the nitrile or latex, which makes it easy to handle, using such. Another advantage of the simple preparation method is that while the substance is in a liquid form, other soluble or non-soluble components can be added to it. Lastly, it is possible to cast the hot, liquid material into a mold (making sure it is of a material which the camphor-camphene wax releases easily from). This, along with the fact that it still can be pressed into pill form using the same method as for pure camphor, means that it is possible to produce more exact and repetitive shapes for repeat experiments. Possibly there are multiple ways to handle and manipulate the material which we have not yet thought of. Most importantly we expect that this material opens up a range of new kinds of experiments on active matter. As a demonstration of the material, we made a movie of several non-trivial shapes with different dyes added, moving on a water surface. A series of snapshots, 0.4 seconds apart, from said movie can be seen in Figure III.2. The live version of those shapes can be seen in Movie 8.

Because the speed and trajectory on a water surface as well as the qualitative mechanical properties of the material depend on the ratio between the two components, we introduce a variable, *w*, that defines the camphor mass ratio of the mixture:

$$w = \frac{mass\ of\ camphor}{total\ mass\ of\ mixture} * 100\% \quad (1)$$

The material stickiness decreased with an increase in w. We mainly worked with the following mixtures: w= 0% (pure camphene), 16,7%, 33%, 37%, 50% and 100% (pure camphor).
The effect of composition on the trajectory and speed will be explored in Section III. 2.1.3.

Figure III.2: Series of snapshots from Movie 8, 0.4s apart. It serves to demonstrate the self-motion of non-trivial, stained shapes on a water surface.

III. 2.1 : Description and discussion of experiments performed using the new material

III. 2.1.1 Preliminary phenomenological description

In order to show the versatility of the new material, a large spectrum of simple experiments was performed. For shapes, that previously have been studied using pure camphor, we go into more detailed follow-up experiments in a later section. One of the most obvious aspects to study, using a malleable material, was to produce crude handmade shapes for phenomenological investigation of the relationship between shape and trajectory of a self-propelled object. As explained before, it is very simple to make different shapes of the material using gloved hands. Therefore, the preliminary experiments we performed, were to create different simple shapes and observe their behavior on a water surface. We used a simple mixture of camphor and camphene ($w = 50\%$) which was manipulated into the following random, increasingly non-trivial shapes using gloved hands: marble, rod, spoon, pointed ellipse, crescent and rotator as seen in Figure III.3a-f respectively.

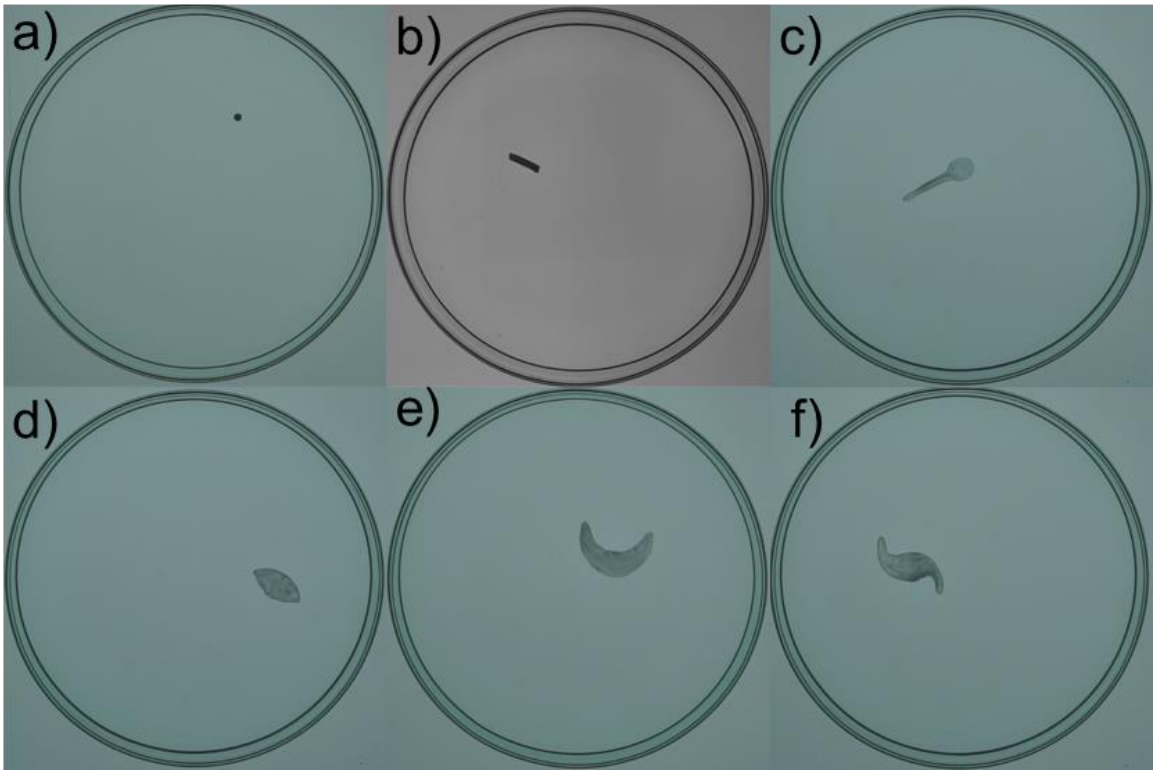

Figure III.3: From a) to f): Marble, rod, spoon, pointed ellipse, crescent and rotator made from camphor-camphene wax by hand. Dish diameter is 12 cm for scale.

The objects were then placed in a Petri dish with a 12 cm diameter filled with 50ml Millipore ELIX5 purified water. The dish was placed on an illuminated surface and filmed using a video camera (NEX VG20EH, SONY) to capture the different behaviors.

Performing the initial experiments using the crudely shaped non-trivial shapes gave us interesting examples of how the shape can determine the trajectory and also how this trajectory can change over time.

The marble behaves similarly to a round camphor disc[87], which is to be expected as it also is round and can deposit surface active camphor and camphene to the water surface at more or less the same rate into any direction. Small mixture and shape inhomogeneities in the material or simply the initial position result in random fluctuations of the resulting surface tension gradient field around the object. Thus, we obtain the random complex trajectories (See Movie 9).

The rod (i.e., an object where the length is several times larger than the width) has either a trajectory perpendicular to the length of the object and results in a larger distance traveled or it rotates on the spot. This does make sense as more surface-active material will be deposited from the long edges, creating a larger chemical and surface tension gradient in these directions. The rod then either moves into the direction perpendicular to one of the long edges (depending on small asymmetries or initial conditions) or it gets stuck in a semi-stable mode

of rotation (i.e., both sides contribute equally to motion) This can be seen in Movie 10.
The spoon shape behaved similar to the rod but was surprisingly less likely to be caught in a rotational state as it quickly would turn into a trajectory along the length before slowing down and reverting to the oscillating (due to boundary) trajectory perpendicular to the length (see Movie 11).
The pointed ellipse shape was chosen because droplets, moving at sufficient speed, oftentimes deform into such a shape during a phase of motion presumably due to drag between the water and the oil. The trajectory of it turned out to be pointing in the direction perpendicular to the longer axis of the object similarly to the rod as well as the moving droplet it is supposed to represent. The round boundary of the Petri dish resulted in the object bouncing off the wall, making a half rotation and moving towards the wall further down/up the barrier, thus going around the whole circle (See Figure III.4a). Later in such experiments the object settled in a circular trajectory along the edge (See Figure III.4b) Both of those behaviors can also be seen in Movie 12.

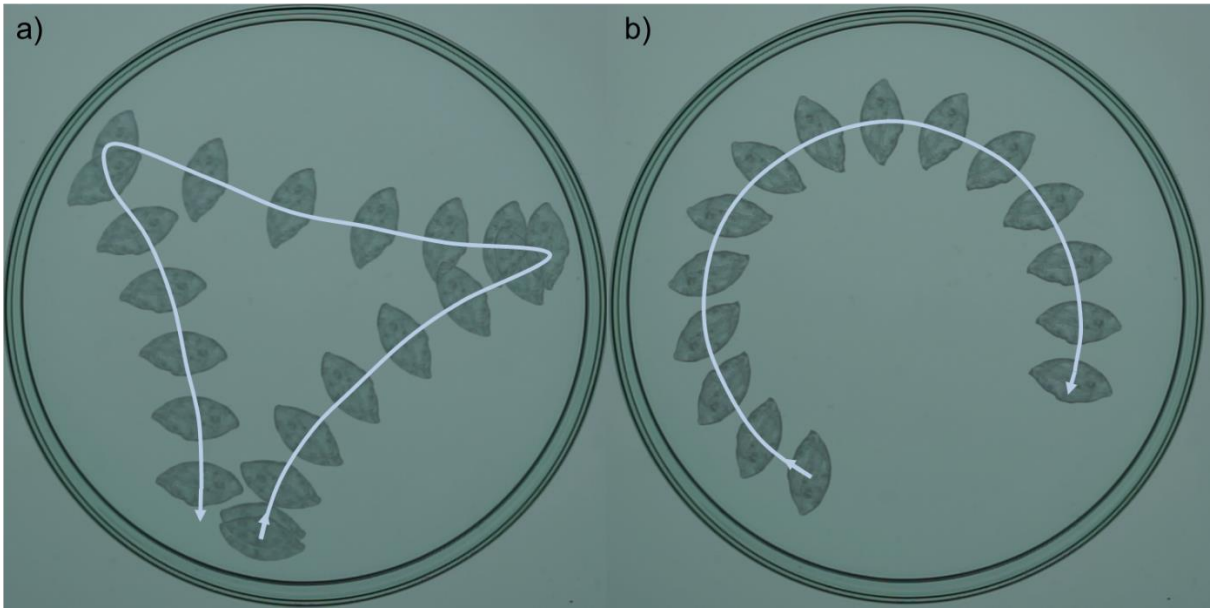

Figure III.4: Snapshots superimposed for two 5-second clips of a self-propelled pointed ellipse. During the first few minutes of the experiment the ellipse bounces off the dish edges to form a triangular pattern (a). At a later stage the movement changes into a circular motion with slightly decreased speed (b).

When the speed of certain self-propelled droplets is even higher, they deform into a crescent shape, dragging the tails behind it. Therefore, we made such a shape from our solid material to observe the trajectory. The expected trajectory thusly would be a continuous motion in the direction the convex side of the crescent is pointing (Figure III.5 left side).

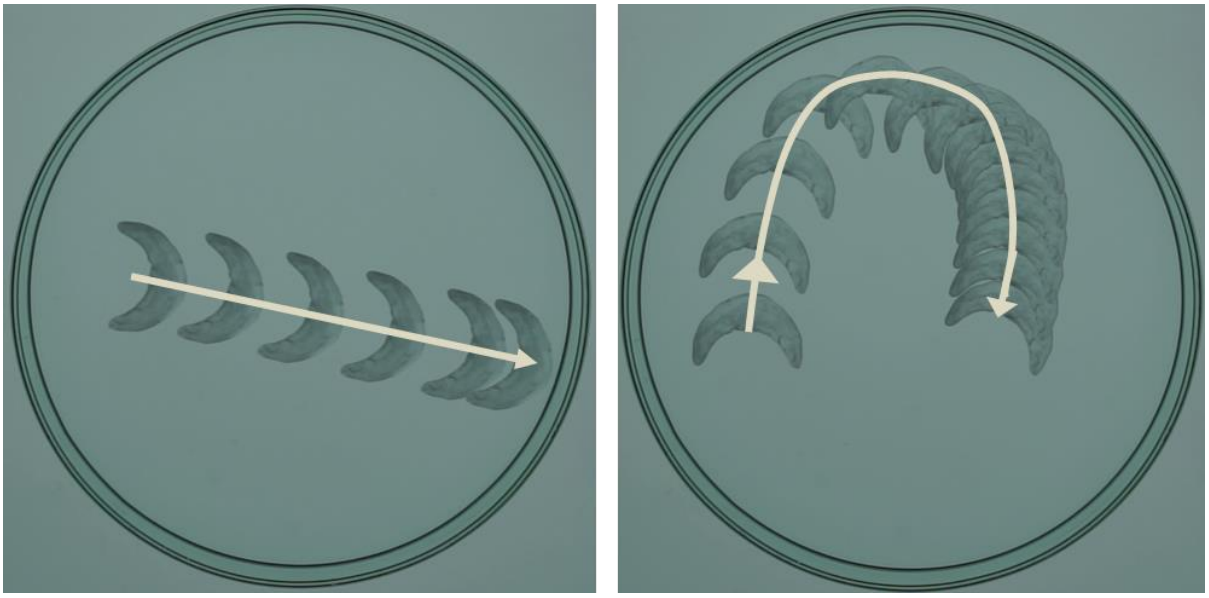

Figure III.5: Left: expected one-directional trajectory. Several snapshots of a 1 second crescent movement equal number of frames apart. Right: Switch from convex direction to concave direction. Superimposed snapshots from 4 second clip equal time between frames. It indicates that speed is lover in concave direction.

The actual behavior however, included also the opposite trajectory, towards the concave side which seemed to be at least as prevalent as the predicted one albeit slower (Figure III.5 right side). The reason for a decrease in velocity in the concave direction is most likely that the hydrodynamic drag is greater in that direction with a turbulent flow occurring within the concavity. Even just from an intuitive observation, the motion in convex direction appears more hydrodynamic. For this reason, this shape will be further explored in a later section with a more precisely fabricated shape.

The rotator shape was derived from Nakata et. al. 1997 [23]. From that source it is known that a yin or yan shaped (circle split by S-shape) scraping rotates in a circular trajectory. By mirroring that shape perpendicular to its length we obtain a shape (See Figure III.3f) that rotates in place (See Movie 13). This was done to show the ease of creating such a shape and to confirm that it would behave in the expected way. This can be useful for the fast experimental verification of theoretical results [41,44].

III. 2.1.2 Quantification of different shapes trajectories

Precise shapes were made from the material for repeatable quantitative study of shape-trajectory relationship for shapes such as an oval or crescent shape. A piece of the material (w = 50%) was rolled out into a flat sheet with a thickness of ca 2mm. For this, a small sheet of nitrile was laid out onto a metal bench. This sheet was held in place by magnets two thin bars of metal which would also ensure an even height of the camphor-camphene wax sheet. The material was rolled out between those two bars of metal using a rolling-pin with a

diameter of ca. 1.5 cm made of Teflon (the material does adhere to it but is easily separated). Shapes such as a crescent, an oval, a triangle or a rhomboid could then be cut out using a stencil. Motion of the different shapes on water was captured on film using the method described for the preliminary experiments. All shapes were filmed on a 12 cm Petri dish filled with 50ml Millipore ELIX5 purified water. Up to four black markers were placed onto the shapes (two on the oval, three on crescent and triangle, four on the rhomboid) in order to track the trajectory and orientation of the shapes. The positions of those markers were recorded from the individual frames of the obtained movies, using the ImageJ software. The resulting data was processed using Mathematica.

Qualitative observation of the rhomboid and the triangle revealed no obvious patterns of behavior as the objects move from wall to wall in seemingly arbitrary directions while a lot of the movement is self-rotation. The tracking of the markers from individual frames of the captured rhomboid and triangle movement is very difficult because the markers were placed too close to each other and the tracking software is unable to distinguish between positions occasionally (especially when the object rotates). Therefore, the rotational movement of the object was not resolvable from the data. It was however possible to use the averaged positions of all markers to obtain the trajectory of the object as a whole. The triangle trajectory had two modes: a circular trajectory along the edge (See Figure III.6a) or a random motion that occurred as a periodic interruption of the circular movement (See Figure III.6b). Over time the period of interruptions decreases. Also, from looking at the video footage (Movie 14) it can be seen that the triangle has more self-rotation during the random movement.

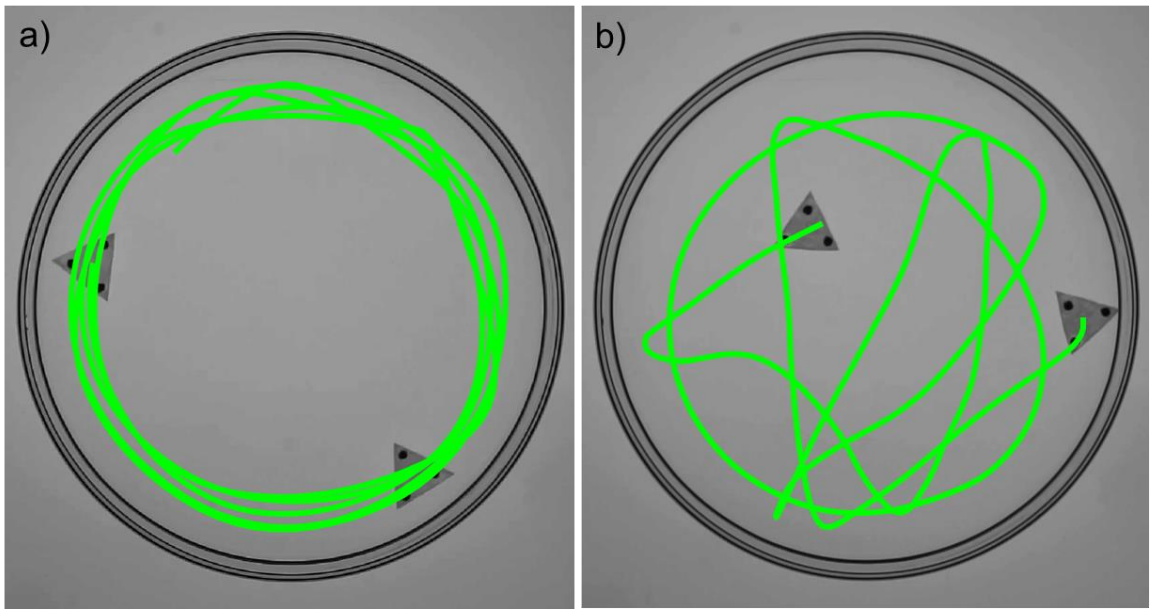

Figure III.6: a) Sustained circular trajectory of a triangle shape (longest period during the first 5 minutes of the experiment. b) At later stages the trajectory periodically interrupts the circle motion to become more complex.

Figure III.7 represents two snapshots of the rhomboid movement overlayed with the trajectories of the markers placed. A star-pattern can be recognized (see also Movie 15 where additionally the frequent self-rotation of the object is visible). The total time of movement for the given trajectory is 8 seconds.

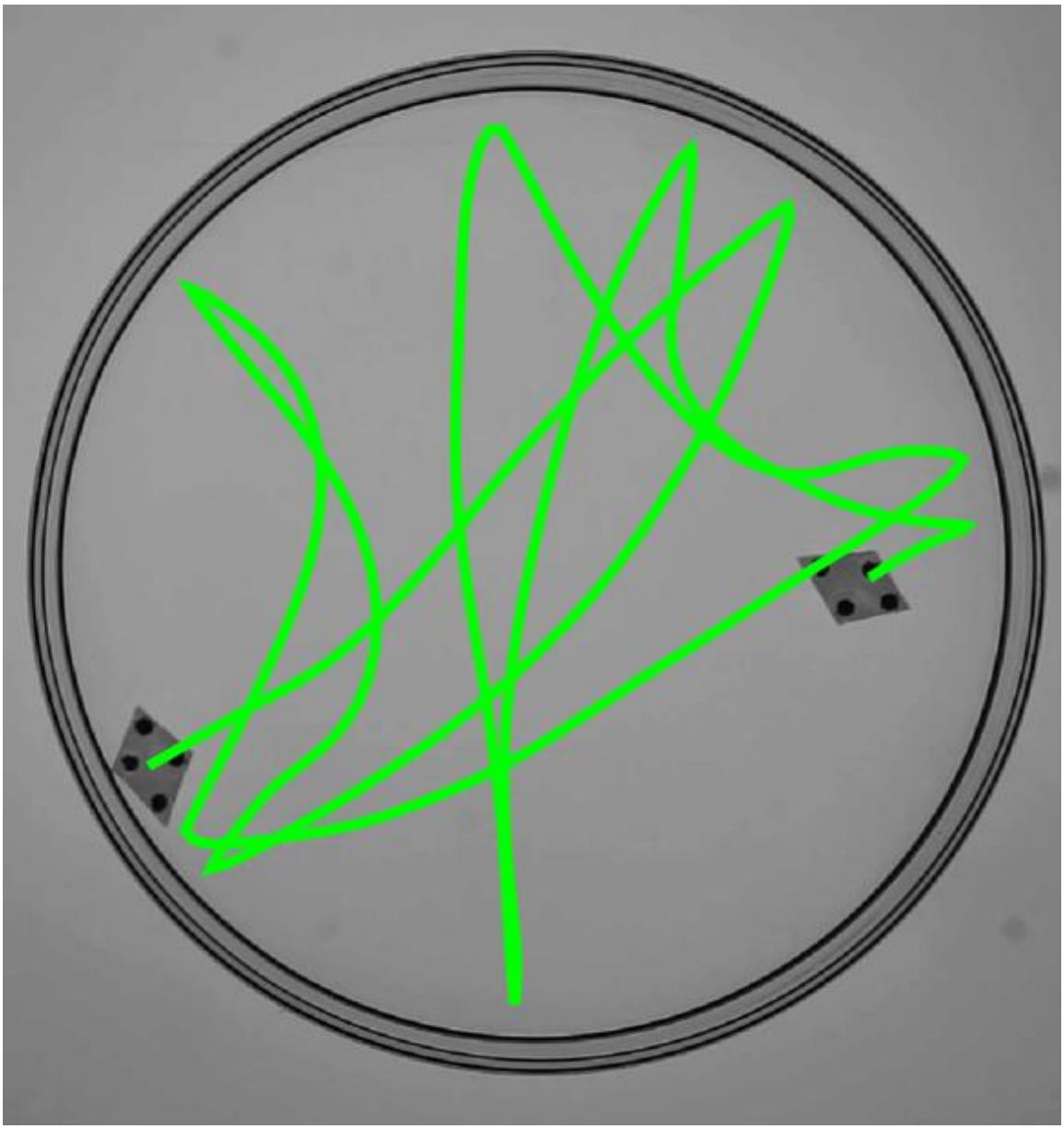

Figure III.7: Rhomboid motion included bouncing off the edges to form a star-like pattern similar to the triangular pattern for the pointed ellipse in Figure III.4a. During this motion the rhomboid self-rotates frequently.

The motion of a crescent (2x1.5cm size), observed for 40 minutes, was complex and, just as other shapes, combined translation with rotation (See Movie 16). However, metastable modes with recognizable patterns of motion can be observed during parts of the time-evolution of crescent movement. Two very clear examples are the rotational motion along the edge and a reciprocating inverting trajectory between dish edges without any rotation of the object. We

first analyzed the speed of the marker located at the crescent center. In order to represent the orientation of the object during motion we analyzed the angle between the direction of velocity and the bisector of that angle defined by connecting the other two markers. Figure III.8 was made to present and distinguish the two semi-stable modes of a crescent motion.

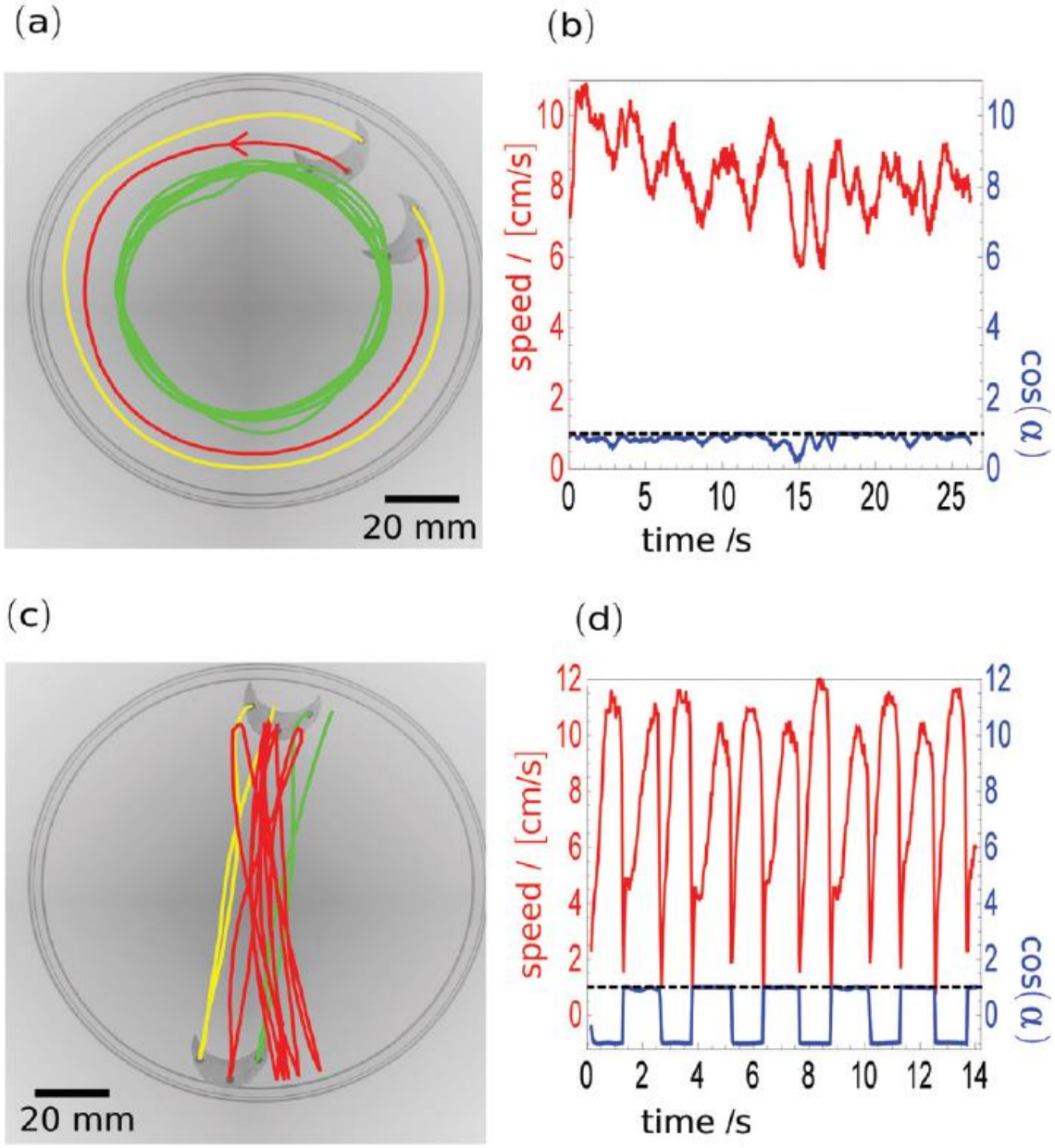

Figure III.8: Two examples of metastable modes observed during self-motion of a crescent-shaped object made of the hybrid material characterized by w = 50%. (a) The rotation along the dish: 25-second-long trajectory of the marker close to the dish center is drawn using the green line, the trajectories of the other markers are shown for 2.6 seconds only. The direction of motion is indicated by the arrow on the red line. (c) The oscillating motion: 2 snapshots separated by 1.2 seconds are superimposed and the 23-second-long trajectory of the central marker is illustrated using the red line. The trajectories of side markers (green and yellow) are indicated for one period only. Subfigures (b and d) show the speed of the central marker in $cm\ s^{-1}$ (the red curve) and the cosine of the angle a between the velocity and the bisector of the angle defined by the markers (the blue curve). The line representing $f\ (x)\ =\ 1$ is shown using a dashed line.

In Figure III.8a, we overlayed two superimposed snapshots of the movie 2.5 seconds apart

with the plots of the marker trajectories for certain timeframes. The green line trajectory of the marker on the side of the crescent being closest to the dish center for 25s, indicating the stability of the rotational mode. The other two trajectories (red for the central marker and yellow for the marker closest to the dish edge) were plotted for 2.5s only, confirming the constant orientation of the crescent towards the dish edge. A full circular motion took just over that amount of time (ca. 2.6s) and the direction of motion is indicated by an arrow on the red trajectory. The red curve in Figure III.8b depicts the speed of the central marker plotted as a function of time. It can be seen that the speed fluctuated around 8 cm/s without any significant changes. The cosine of the angle between velocity and the bisector of the angle formed by all three markers is plotted in the same figure as the blue curve. When this value is close to 1 it indicates that the crescent is moving in the direction of its concave side. Oppositely, a value of -1 indicates motion towards the convex side. As can be seen on the curve, the cosine of the angle was close to 1 for most of the considered time interval. This underlines the existence of a metastable mode of crescent motion with a circular trajectory along the dish edge in the direction of its concave side.

An additional metastable mode of motion is depicted in Figure III.8c where the crescent can be seen moving back and forth between opposite edges of the dish without rotation. On this figure we overlayed two superimposed snapshots of the film, 1.2s apart, with a 17 second trajectory of the middle marker (red) and single cycle trajectories of the side markers (yellow and green). The blue and red curved in Figure III.8d describe the same quantities as in Figure III.8b. Both curves are characteristic for the proposed mode of motion as the speed peaks during the traverse of the dish and dips near the edge while the cosine of the angle between the velocity and the bisector of the angle, defined by the three markers switches between 1 and -1, indicating an inversion of the direction of motion. This inversion also coincides with the minima of speed. The speed during crescent motion in the direction of its convex side ($cos(\alpha) = -1$) tends to be slightly higher than in the opposite case. This seems to align with the intuitive assessment of the crescent shape hydrodynamics. Comparing it to the preliminary result presented in Figure III.5 it appears that the difference in speeds for the convex/concave directions of motion is smaller for the more precisely fabricated crescent shape which may be due to the difference in curvature of the semicircles creating different amounts of drag.

Even though the hydrodynamics seem to favor motion in the direction of the convex side, during 40 minutes of motion we only ever observed the stable rotation along the edge with the opposite direction. That this direction of motion is at least as favorable as the one in the direction of convex shape may be due to the longer perimeter of the shape on the convex side. On that side it can deposit more surface-active material to the water surface on a larger

area. This wide, cone-shaped, area of surface tension gradient may result in a larger net force/Marangoni flow) than the one created by the higher concentration of camphor and camphene in a smaller area on the concave side. This effect also may be significant for behavior of camphor-paraffine droplets presented in Part 3. The question is whether a, presumably smaller, concentration gradient of surface-active substances on a larger area creates a larger Marangoni flow than the opposite flow created by a stronger gradient distributed on a smaller area? Based on the results presented here, this can be the case. Likely it depends on how much the surface-active material can lower the surface tension. During this project we only had time to do experiments with that one particular geometry of the crescent. Also, the shape and size of the boundary may influence the overall behavior. Further studies should be performed, using different sized and shaped containers (larger container may enable longer periods of motion in convex direction, different compositions of material (does the degree of surface tension change affect the direction of motion?) as well as performing a series of experiments, changing the ratio between radii of convex and concave side.

III. 2.1.3 Effect of composition ratio on trajectories

Preliminary results indicated that the ratio of components in the material have an influence on the speed and trajectory of objects. Despite their structural similarity, camphor and camphene interact differently with a water surface. A layer of camphor lowers the surface tension more than a layer of pure camphene does [23,47]. To study the effect of the composition on the speed and trajectory of self-propelled objects, a series of disks (diam: 4mm height: 1mm) were fabricated using a pill press. The disks composition ranged from pure camphene to pure camphor. Compositions with higher amounts of camphene ($w < 30\%$) were too soft at room temperature so it was necessary to place the material and the die in the freezer at -18°C before making the disk. Once made, a disk was immediately placed on the water surface inside of a 12cm Petri dish, illuminated from below and filled with 50ml Millipore ELIX5 purified water. An experiment lasted for at least 30 minutes and was and filmed at 25 frames per second using a mounted, downward facing camera (NEX VG20EH, SONY). The films of the disks were then split into individual frames, digitized using ImageJ and processed using Mathematica. To qualitatively characterize the motion of a disk, two quantities were chosen: the probability distribution of observed speeds and the time distribution of disk locations on the Petri dish.

Let us assume that the movie is a sequence of M frames and the time difference between consecutive frames is Δt. Therefore, the m-th frame corresponds to the time $t_m = m * \Delta t$ $(0 \leq$

$m < M$). The basic information extracted from the movie are the positions of the marker center(x_m, y_m). This information allows us to investigate the object's trajectory and velocity. The presented results allow comparing the properties of self-propelled motion of disks made from different compositions. We investigate the shape of trajectory, the distribution of pill locations on the Petri dish, and both the pill speed as a function of time and the distribution of speed values.

The system is characterized by the circular symmetry. Therefore, the statistics of pill positions on the water surface can be characterized by the distribution function of pill centers $g(r)$ that measures the difference between the observed distributions of pill locations with respect to the dish center and the uniform distribution. Let the dish radius be R and the pill diameter d. In the case of uniformly distributed pill positions the number of frames in which the pill center is observed within the fragment S of the water surface $n_0(S)$ is:

$$n_0(S) = M \cdot \frac{||S||}{\pi(R-d/2)^2} \tag{2}$$

where $||S||$ is the area of the fragment S. For example, if we consider a ring around the dish center $U[r, r+\Delta r]$ with the inner radius r and the outer radius $r+\Delta r$ then the number of frames at which the pill center is located between the two radii is described by:

$$n_0(U[r, r+\Delta r]) \sim \frac{2Mr\Delta r}{(R-d/2)^2} \tag{3}$$

However, the real distribution of pill locations can be different from the uniform one. Let $n(U[r, r+\Delta r])$ denotes the number of frames of the movie in which the pill center is located within the ring. The function $g(r)$ is defined as:

$$g(r) \cong \frac{n(U[r,r+\Delta r])}{n_0(U[r,r+\Delta r])} \tag{4}$$

where Δr is reasonably small.

Having the positions of the pill center at successive frames of the movie (x_m, y_m) we can calculate is speed at the time t_m as:

$$v(t_m) = \frac{\sqrt{\left(x_{(m+1)}-x_{(m-1)}\right)^2+\left(y_{(m+1)}-y_{(m-1)}\right)^2}}{2\Delta t} \tag{5}$$

In our analysis, we study the pill speed as the function of time and the probability distribution of speed values $P(v)$.

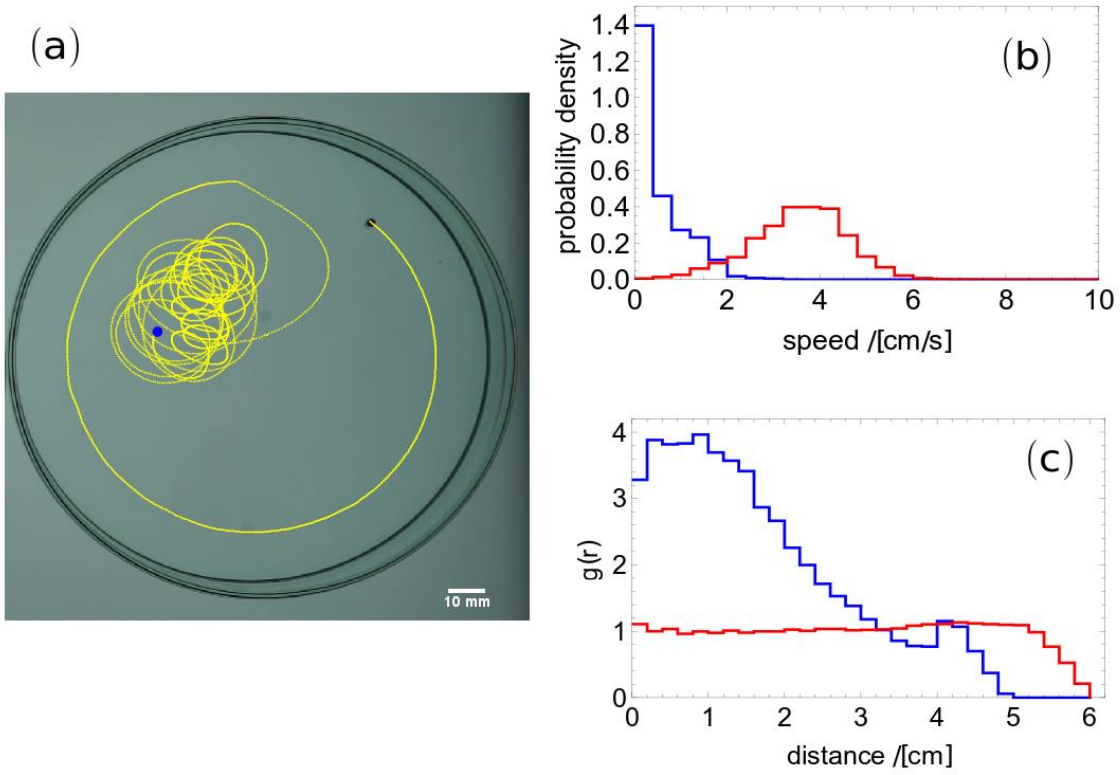

Figure III.9: Typical motion of camphor and camphene pills. (a) A fragment of a typical trajectory of self-propelled pill (0.4 cm diameter, 0.1 cm high) on the water surface in a Petri dish (12 cm diameter). The grey dot with a black marker shows the initial position of a camphor pill. The illustrated fragment terminates at the blue dot. (b) The probability distribution of observed speeds ($cm\ s^{-1}$). (c) The radial distribution function of pill positions at a given distance (in cm) from the dish center. The blue and red curves show results for camphene and for camphor respectively.

The results for pure camphor and for pure camphene are shown in Figure III.9. Both $g(r)$ and the probability density of speed summarize results of a few independent experiments. Figure III.9a, shows the typical short-term trajectory of a camphor or camphene pill for about one minute. The results for camphor, i.e., $w = 100\%$ were averaged over three experiments. In each experiment the observation time was longer than 1 hour (90 000 frames) and the total number of analyzed frames was 310 000. The speed distribution and radial distribution for pure camphor are represented as the red curves seen in Figure III.9b and c respectively. For pure camphene i.e., $w = 0\%$, the presented result covers five experiments and the total number of frames was almost 600 000.

The speed distribution and radial distribution for pure camphor are represented as the blue curves seen Figure III.9b and c respectively. Although in both camphor and camphene pills are self-propelled, the quantitative character of motion is different. For camphor, the pill distribution on the water surface is uniform. On the other hand, the camphene pill hardly penetrates the area 1 cm away from the dish edge. For a camphor pill, the probability

distribution of observed speeds is Gaussian with a maximum at 4 cm/s and the mean is equal to 3.6 cm/s. For a camphene pill the probability distribution of speeds has a Poissonian character and the average speed is 0.6 cm/s. A similar characteristic of camphor disk motion (Poissonian character of velocity, avoiding close proximity to the edge of Petri dish) were reported in[47]. Quantitative differences between both results can be attributed to larger Petri dish diameter in our setup. The results characterizing typical motion of pills made of camphor–camphene mixtures at different compositions are presented in Figure III.10. Here each presented result was obtained from averaging over 2 independent experiments that were more than 1 hour long (over 200 000 frames). We observed a good agreement between results of individual experiments (Figure III.10e and f). As expected from the results shown in Figure III.9c, the values of $g(r)$ for distances close to the disk radius (6 cm) increase with w, which means that more of the dish surface becomes available to the pill. The dependence of the probability distribution of observed speeds is more interesting: the Poissonian character of speeds is observed for $w = 16.7\%$, however the mean speed is much higher ($1.4 cm \cdot s^{-1}$) than for pure camphene. For moderate concentrations of camphor ($w = 33\% \; and \; 37\%$) the distribution becomes bimodal and contains a low-speed maximum at 2 $cm \cdot s^{-1}$ and a high-speed maximum at 12 $cm \cdot s^{-1}$. This result seems surprising because on the basis of Figure III.9b one could expect a bimodal distribution of speeds, but with the second maximum about 4 $cm \cdot s^{-1}$. We observe that camphor and camphene synergistically interact and pills made of the hybrid material can move much faster than those prepared using pure components. For yet larger concentrations of camphor ($w = 50\%$) there is only a single maximum of speed distribution, but it is located around 10 $cm\, s^{-1}$, that is almost 3 times more than the maximum of the speed distribution for pure camphor. This increase in speed could be explained as follows. For pure substances the propulsion results from fluctuations in concentrations of active molecules on different sides of a self-propelled object. In the case of a mixture these fluctuations can be increased by fluctuations in the composition of active molecules and the overall effect increases. As supported in Figure III.10, we claim that the properties of the hybrid material can be tailored on demand by the camphor–camphene ratio. We believe that the obtained material is homogeneous. Molecules of camphor and camphene are similar and thus we do not expect that the system decomposes into camphor- and camphene-rich phases. When in liquid form, the mixtures are thoroughly stirred before solidification and the liquid looks homogeneous. If significant inhomogeneities appear during solidification then results of different experiments should differ. The results of individual experiments contributing to Figure III.10 show good reproducibility (Figure III.10e and f). This implies that the microscopic variations if existent have a minor influence on the time evolution of studied objects.

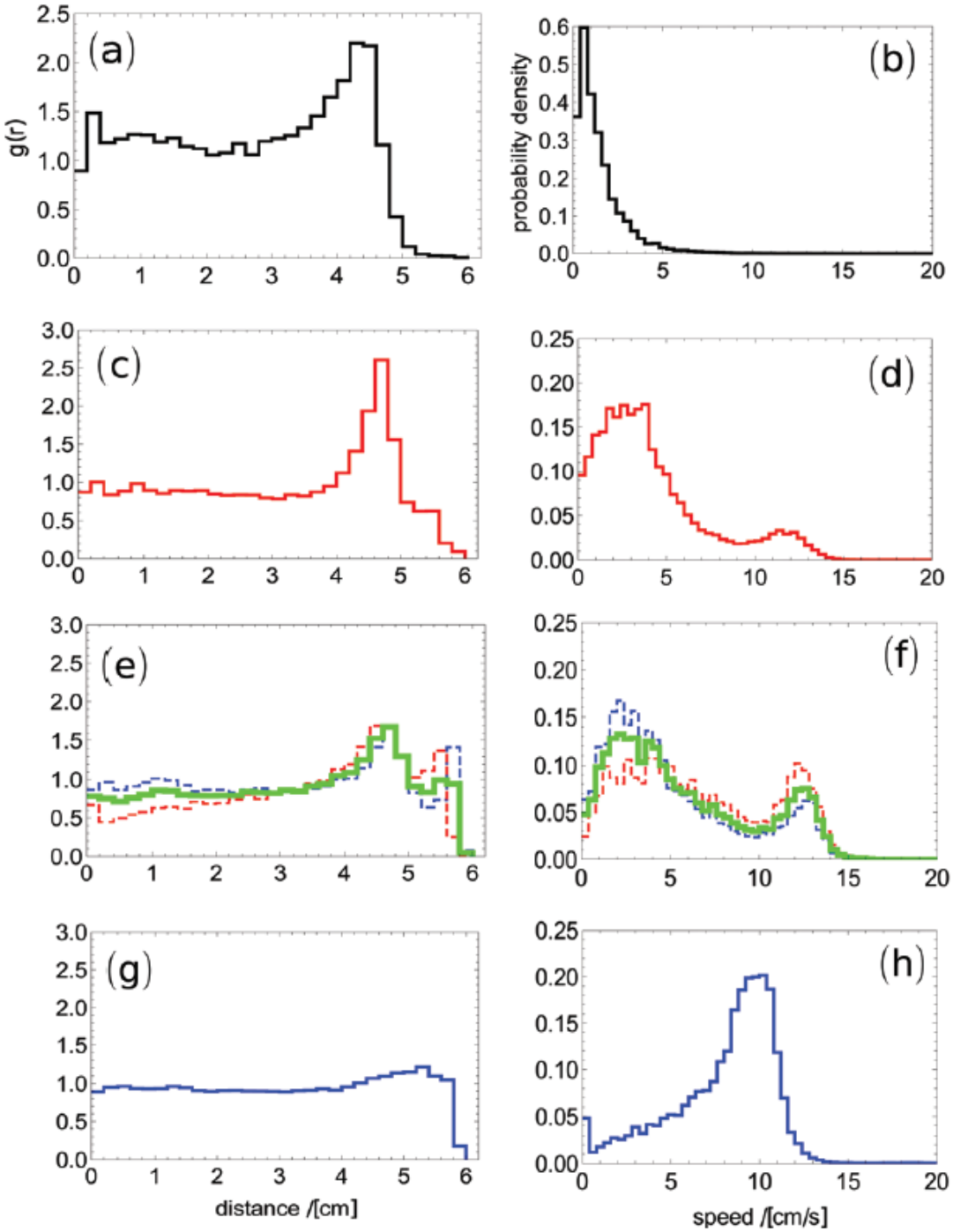

Figure III.10: Analysis of motion of pills made from camphor and camphene mixtures with varying w. The radial distribution of pill positions as a function of distance from the dish center (a, c, e and g) and the probability distribution of observed speeds (b, d, f and h) for a few selected weight ratios: (a and b) w = 16.7%, (c and d) w = 33%, (e and f) w = 37%, (g and h) w = 50%. The red and blue dashed lines in (e and f) represent results of two individual experiments that contributed to the average shown by the green curve.

III. 2.1.4 Extrusion of material for mass production of equal shapes

The malleability of the material enables us to easily produce larger quantities of different shapes. Those can then be used to observe the collective motion of different shapes on water.

One way to do this is to extrude a solid tube of material and cut it into sections of equal lengths. A simple method to perform this extrusion is to suck the material into a syringe while it is still hot and molten, then push the plunger at the right time to produce a long cylinder of material (for these early experiments with the material, a 50% camphor and camphene mixture by weight was chosen). With a hydraulic press or similar it might even be possible to extrude the material cold. Extrusion dyes could then be used to extrude even more complex shapes. For preliminary experiments with the material, we cut such a long cylinder into sections of 10mm or smaller 2mm sections. The longer pieces were used as is while the short sections were rounded off using a gloved finger on a non-stick surface to produce marbles with diameters of ca 2mm. Finished objects could be stored in a camphor saturated atmosphere or in the freezer. For experiments differing numbers of the shapes were placed on differing sizes of bottom-lit Petri dishes and filmed from above.

In both cases we observed individual behavior to start with, followed by more collective behavior. The individual rods moved just as seen in preliminary experiments: rotation around itself or movement perpendicular to their primary axis. When a multitude of these objects are observed on a larger dish, the individual rods, will switch between the described modes of motion. Occasionally the rods will run into each other. During a collision there is a chance that the two objects will stick to each other depending on their respective orientations towards the other. A collision of two long edges towards each other will almost never result in an attachment. However, when the thin edges touch an attachment is very likely to occur. A possible explanation for this is the surface tension gradient field around the objects: More surface-active material can be emitted onto a larger surface from the long edges of a rod than from the very short perimeter on the thin edge. Thus, the capillary attraction combined with the stickiness of the material on the short edge is larger than the repulsion due to surface tension gradients.

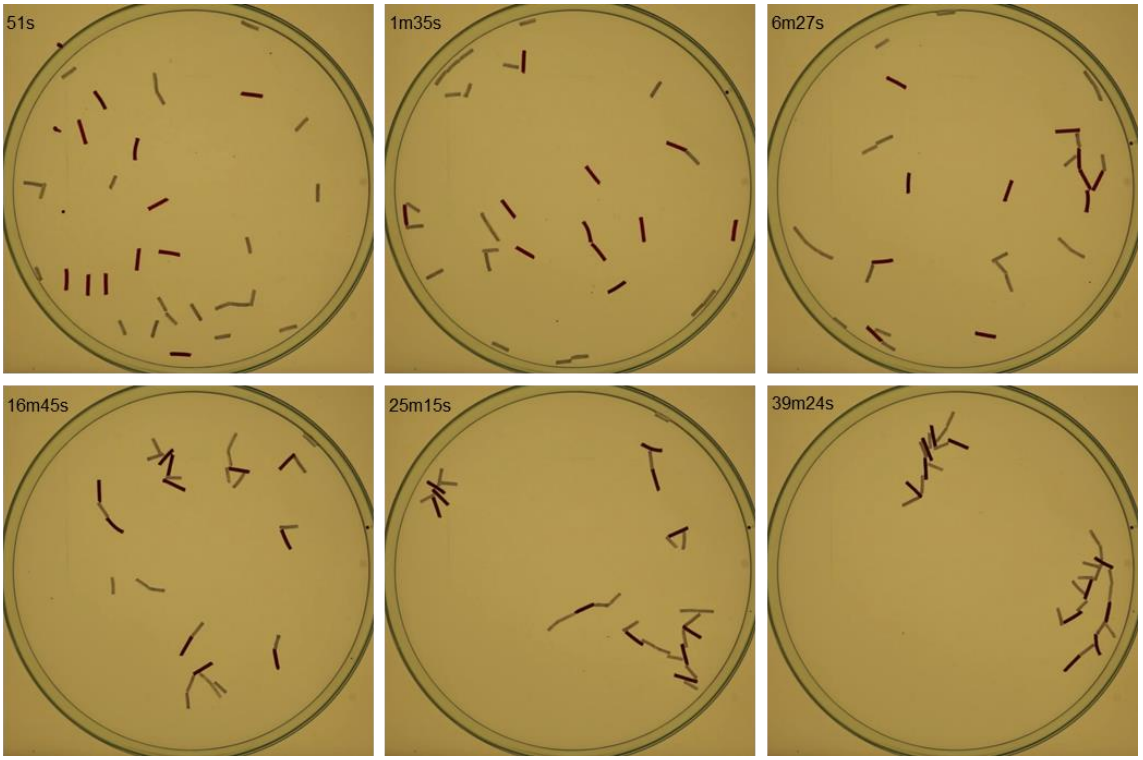

Figure III.11: The time evolution of camphor camphene wax rods on the water surface. The surface-active materials deposited to the water surface result in repulsion of the rods from each other. In a crowded environment, collisions do occur. The stickiness of the material enables aggregation with contact point tending to be on the tips of the rods. In the beginning (at 51s) most rods are moving independently of each other. As time progresses more and more dimers and trimers emerge and start to aggregate into ever larger clusters that divide and rearrange (1m35s to 25m15s). At even later stages only very few large clusters are left moving slowly on the water surface while occasionally rearranging or colliding (39m24s).

In Figure III.11, chronologically arranged snapshots from Movie 17 of 32 rods (12 red and 20 white. The coloring was merely to show that coloring is possible) on a 20 cm Petri dish are depicted showing the different types of clusters which form and grow over time. In the early stages, dimers and trimers of rods will form that occasionally split or gather additional links. As time progresses, the clusters will coalesce into larger clusters eventually finding a "steady state" as on large colony of rods. In this state we observe rearrangement of the cluster for some time. This type of motion will be revisited in the latter part of this part. The behavior of the marbles is similar except for the completely random trajectories of individuals. Just as described for the rods, in Figure III.12 we can see in snapshots of Movie 18 how the marbles form small clusters of less than five individuals.

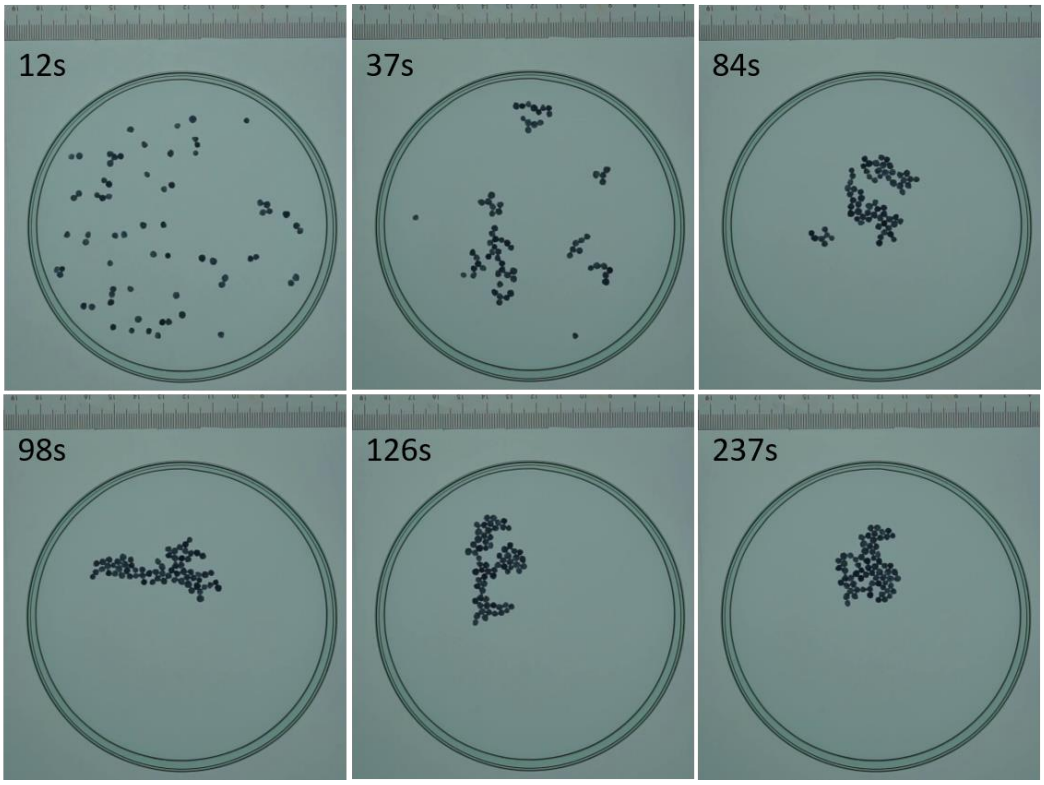

Figure III.12: The time evolution of camphor camphene wax spheroids on the water surface. As the spheroids contain camphor, a continuous gradient of surface tension is formed around each of the objects. This repels them from each other. In a crowded environment, collisions do occur. The stickiness of the material enables aggregation. In the beginning (at 12s) most spheroids are moving independently of each other. As time progresses more and more dimers and trimers emerge and start to aggregate (37 to 84s) which eventually organize into a single large cluster that changes conformation over time (98 and 126s) before settling into a fixed shape (237s).

These tend to break up or fuse with other clusters until few large clusters remain and eventually form one large cluster who's only activity is to rearrange. One possible real-world analogue for these systems may be colonies of bacteria which tend to have similar shapes and also form clusters that are similar to what we see in our macroscopic system[7,8,51,99]. But it remains to be seen how this analogue may prove useful in any way. In the very least what we have is another form of active matter which, embodies some aspects of actual living systems. Further, it may be interesting to observe systems of mixed shapes. Both the simple and mixed systems could be representations of energy minimization and it would be an interesting exercise to replicate the behavior in a computer simulation.

III. 3 Discovery of polymer-enhanced camphor-camphene plastic

We discovered that we could obtain a truly "plastic" material, with significantly different properties, from the camphor-camphene wax mixture by combining it with a thermoplastic polymer, creating an alloy of the three combined components. The discovery of the materials ability to dissolve certain thermoplastic polymers (Specifically polyolefins. In our case we have used polypropylene) goes back to the point when we made the rods from long extruded

cylinders. The production of such cylinders was as follows: A 15ml falcon centrifuge tube (made of polypropylene and initially what we stored the material inside) containing the new material (w=50% and stained with the dye Oil red O) was placed into a hot water bath to liquify the contents. The contents were then sucked up into a 1ml polypropylene single use syringe and the plunger pressed once the material inside the syringe has solidified but was still hot and soft, thus producing a long cylinder with a diameter equivalent to the syringes opening. These cylinders were then cut into pieces with a length of 1cm, with which we performed some preliminary experiments as they are described in the previous section. After finishing the filming of such experiments, we would store the rods in a covered Petri dish under a camphor rich atmosphere to prevent the full evaporation of the rods. If left uncovered however, rods did not completely evaporate but left behind a red, very fragile and light foam/sponge, still mostly in the shape of the rod. An example of these early "accidental" foam samples can be seen in Figure III.13 where the material had been shaped into a boat-shape before being left exposed to the open atmosphere. On the right side of the figure the approximate shape of the boat can still be recognized.

Figure III.13: Remnants of objects made from camphor-camphene wax that was stored and reheated inside polypropylene falcon tubes and left exposed to an open atmosphere.

One possible explanation for this light foam was that there may have been some chemical reaction with the added dye creating a non-evaporative species, however similar structures were left behind from samples containing no dye. Upon review of literature describing both camphor and camphene as well-known plasticizers[100–102], it was clear that the camphor-camphene wax is miscible with certain polymers. This meant that the foam is made of polypropylene which was dissolved from the falcon tube when repeatedly reheating the

material. This was confirmed by cutting a falcon tube into small pieces and adding them to the liquid camphor-camphene mixture in a conical flask and keep stirring at high temperatures (up to 250°C) until they had dissolved completely. The resulting material has similar mechanical properties as the original camphor-camphene mixture and appears homogeneous. Particles of this polymer-enhanced material are still self-propelled on a water surface. Just as expected, we are left with a light foam of the polymer after evaporation of the volatile components. Using this simple method of production, we were able to dissolve up to 10% of polypropylene (CAS:9003-07-0, Sigma Aldrich, product number 427861) by weight in our camphor-camphene wax at previously investigated ratios of w=0%, 16%, 33%, and 50%). At higher concentrations of added camphor, the polymer did not dissolve easily, indicating that the dissolution of polymer is mainly facilitated by the camphene in the mixture.

III. 3.1 Properties of the plastic and qualitative comparison with the wax

In order to compare the two new materials, we made a series of camphor-camphene-polypropylene plastic by adding either 5 or 10% polypropylene by weight to most of the camphor-camphene wax ratios from the previous section (w= 0% (pure camphene), 16,7%, 33% and 50%). This way the ratio between camphor and camphene remains the same regardless of amount of polypropylene added.

The new mixtures will be defined by three new mass ratios w_{CN}, w_{CR} and w_{PP} which are the mass ratios of camphene, camphor and polypropylene respectively:

$$w_{CN} = \frac{m_{CN}}{m_{CN}+m_{CR}+m_{PP}} * 100\% \quad (4)$$

and

$$w_{CR} = \frac{m_{CR}}{m_{CR}+m_{CN}+m_{PP}} 100\% \quad (5)$$

Here m_{CN} is the mass of camphene, m_{CR} is the mass of camphor and m_{PP} is the mass of polypropylene. The mass ratio of polypropylene will then always be $w_{PP} = 100\% - (w_{CN} + w_{CR})$. So, for example if a mixture of original $w = 16.7\%$ is used and 5% of polypropylene by weight is added we get a $w_{CN} = 79.3\%$, $w_{CR} = 15.9\%$ and $w_{PP} = 4.8\%$. In this section the different compositions of the camphor-camphene-polypropylene plastic will be given as a combination of the camphor and polypropylene mass ratio (example above would be $[w_{CR}, w_{PP}] = [15.9\%, 4.8\%]$).

As mentioned earlier, the polymer-enhanced materials, have the same homogenous appearance as the simple camphor-camphene mixtures. The polymer-containing material is

less sticky but just as malleable, although stickiness and rigidity depend on the polymer content. This makes it easier to handle the material at absent or low camphor contents for example when using the pill press to create small discs of the material. At higher camphor contents, a lot more force is needed to manipulate the shape by hand. Additionally, there are two aspects in which the polymer-enhanced material differs significantly from the wax. The first of them is that upon evaporation of the volatile material, a porous lattice of the non-volatile polymer is left behind, retaining the shape of the object. This remnant material has interesting properties and will be discussed in a later section. The other important aspect is how a particle of the material behaves on a water surface. On initial observation, movement of camphor-camphene-polypropylene plastic particles on water is complex and resembles what we have observed using particles without added polymer. However, the addition of the polymer changes two things: 1. The movement of a particle lasts for much longer than it would previously, 2. The difference in camphor-camphene ratio has a significantly diminished effect on the speed and trajectory of a simple disk-shaped particle as will be presented in the following section. As for the improved timescale of self-propelled motion, it is reasonable to assume that the polymer limits the emission/evaporation of the volatile components from the mixture. In fact, we see that the surface of this material turns into the white polymer foam described earlier as evaporation occurs. This surface layer could act as a passivating layer that modulates the emission of camphor and camphene. Simultaneously the object loses the majority of its mass (in our mixtures makes out 5 or 10% of the total mass) over time while maintaining the shape. Thus, the speed of the object can remain constant for long times.

III. 3.2 Effect of composition on the behavior of camphor-camphene-polypropylene plastic discs

In order to quantitatively compare the self-propelled motion of the polymer enhanced material, we made a series of disks (diam: 4mm height: 1mm), using a pill press, from the different mixtures:

$[w_{CR}, w_{PP}]$ = [0%, 4.8%], [0%, 9.1%], [15.9%, 4.8%], [15.2%, 9.1%], [31.4%, 4.8%], [30%, 9.1%], [47.6%, 4.8%] and [45.45%, 9.1%] with the rest being camphene.

We recorded three trajectories of individual disks made of each mixture on a 12cm Petri dish, illuminated from below and filled with 50ml Millipore ELIX5 purified water. The following sections are excerpts from[93]. In our study on camphene-camphor wax we demonstrated that the radial position distribution of a moving disk, $g(r)$, depends on camphene-camphor

weight ratio. For the pure camphene $g(r) = 0$ if $|R - r| < 10\,mm$ meaning that the pill never got closer to the dish edge than 10mm. The probability of finding a pill close to the dish edge increased with the amount of camphor in the mixture. For equal weights of camphene and camphor, the pill positions were uniformly distributed on the whole surface. Here we also use the function $g(r)$ for quantitative characterization of the character of motion of a pill made of camphene-camphor-polypropylene plastic for different weight ratios of the compounds. For the previous material without polymer, we also observed a qualitative difference between the speed probability distribution, $P(v)$, for a pill made of pure camphene and $P(v)$ for a pill made of a camphor-camphene wax. In the first case, the distribution was Poissonian; in the second, it was bimodal. The magnitude of the peak corresponding to a high velocity was growing with the weight ratio of camphor.

III. 3.2.1 Quantification of the time evolution of a single 4 mm pill moving on the water surface

In this section, we describe the time evolution of a 4 mm pill made of camphene-camphor-polypropylene plastic on the water surface. Experiments demonstrating properties of the plastic were performed at 23°C$\pm$1° in a Petri dish with a diameter of 12 cm for material with the 10% weight ratio of polypropylene, containing 50ml water purified using a Millipore ELIX5 system. Therefore, the water level was 0.44 cm. For the material with the 5% weight ratio of polypropylene, a Petri dish with 11 cm diameter was used. In this case, the water level was 0.53 cm. The Petri dish was illuminated from below while recording from above using a mounted digital camera (NEX VG20EH, SONY (25 fps), or Logitech C920 Webcam (30 fps)). The studied self-propelled objects were marked with black stickers that help to trace their trajectory. The movies were digitalized, edited, and analyzed using the ffmpeg, ImageJ, and Mathematica software. The quantification was performed in the same way as described in Section III. 2.1.3.

III. 3.2.2 Time evolution of pills made of camphene-polypropylene plastics

First, we tested pills made of camphene-polypropylene plastics. We can expect, based the pure camphene results, presented in the first half of this part, that the self-propelled motion of such pills qualitatively differs from that observed for camphene-camphor-polypropylene plastic. We observed that a pill, just after placement onto the water surface, moves at high speeds and slows down to approach a stable speed. Such effect is illustrated in Figures III.14a

and b for a 4mm pill made of 90.9% by weight camphene and 9.1% by weight polypropylene moving inside a Petri dish with a 12 cm diameter. The trajectory in Figure III.14a shows the first 60 seconds of motion after the pill was placed on the water surface. The yellow disk marks the initial position of the pill. The corresponding pill speed as a function of time is presented in Figure III.14b. It reaches a stable value around $t = 40$ seconds. Figure III.14c shows a typical trajectory of a camphene-polypropylene pill observed at long times. Here, the yellow disk marks the pill position at $t = 66$ minutes after the pill was placed on the water surface. The green line illustrates the trajectory observed in the time interval [66 minutes, 70 minutes], while the red line corresponds to the time interval [70 minutes, 79 minutes]. The length of the green line, representing 4 minutes of motion, is much longer than the red one covering 9 minutes. It indicates that the speed of a pill made of camphene-polypropylene plastic can significantly decrease after 1 hour of activity. For the following analysis of camphene-polypropylene pill motion, we restricted motion analysis to the time interval [1 minute, 61 minutes].

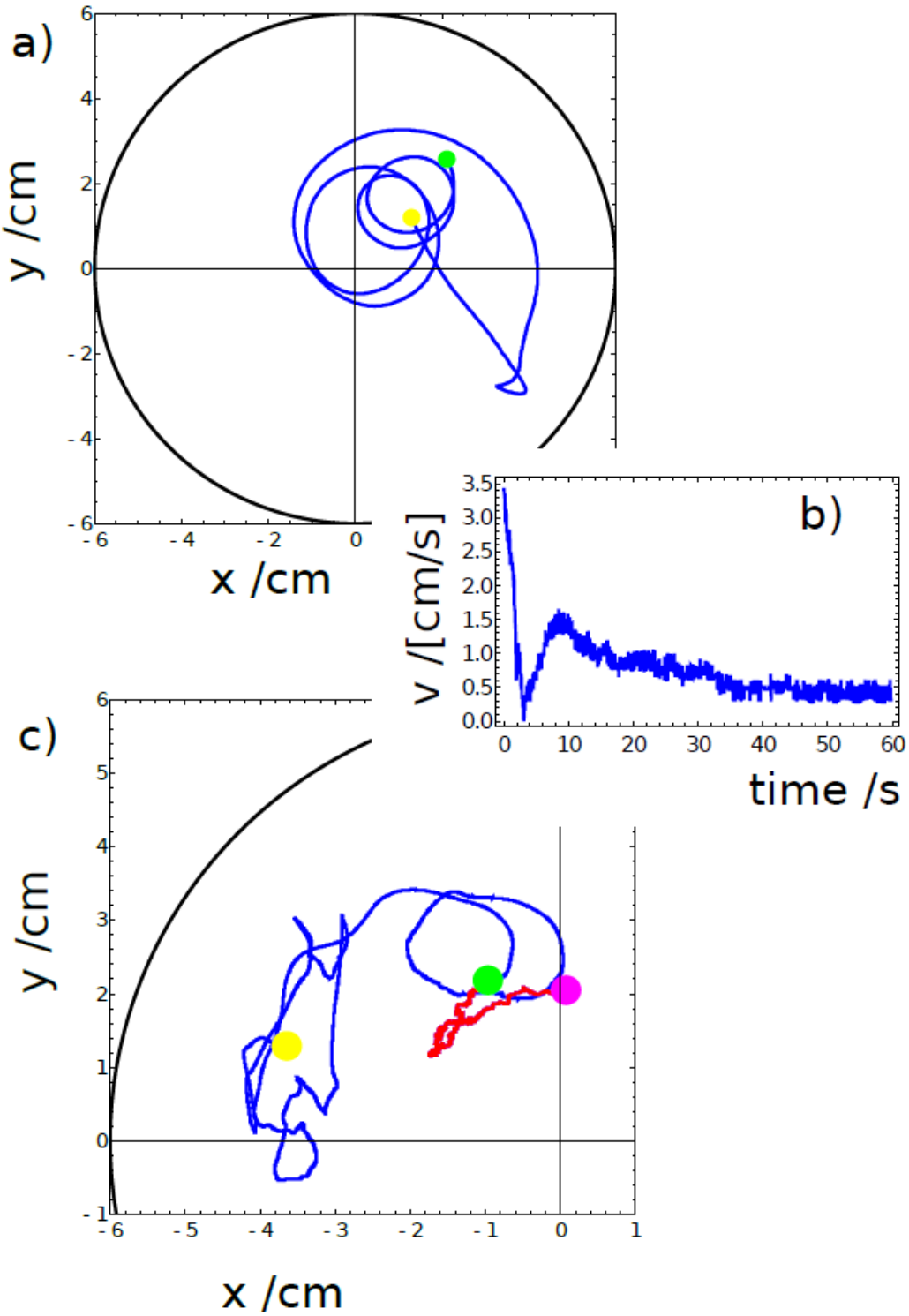

Figure III.14: The motion of a 4mm pill made of 90.9 % weight camphene and 9.1 % weight polypropylene observed at short and long times. (a) The trajectory of the first 60 seconds of motion after the pill was located on the water surface. The yellow disk marks the initial position of the pill and the green one shows its location after 60 s. (b) The pill speed measured for the trajectory shown in (a). (c) The blue and red lines show the trajectory observed in the time intervals [66 minutes, 70 minutes] and [70 minutes, 79 minutes] after the pill was placed on the water surface, respectively. The yellow, green and magenta disks mark the pill positions at t = 66, 70 and 79 minutes.

In Figure III.15-III.18 we summarize three independent experiments in which the motion of a 4mm pill made of 95.2 % weight camphene and 4.8 % weight polypropylene was observed. The dish diameter was 11 cm. The trajectories and the distances between the pill center and

the dish center are shown in Figure III.15.

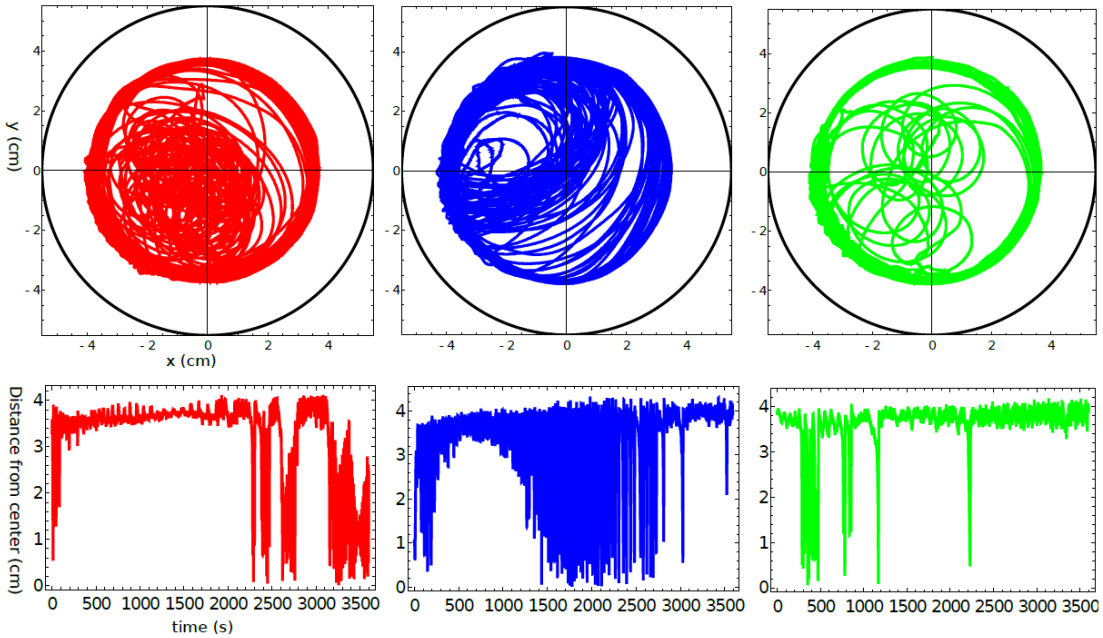

Figure III.15: The upper three figures show the trajectories of a 4mm pill made of 95.2 % camphene and 4.8 % polypropylene in a Petri dish with an 11 cm diameter. The black circle indicates the location of the dish wall. The distance between the pill center and the dish center as a function of time is plotted in figures located below the corresponding trajectories.

The results were obtained by analysis of individual frames recorded at a rate of 30 fps. In each experiment, we observed transitions between the rotational motion along the edge of the dish and the random motion inside the dish. Neither of these types of motion seem to dominate the evolution. In one case (the red trajectory), the random motion covering the dish interior appeared after almost 40 minutes long stable rotation. In another case (the blue trajectory), stable, elliptic-shaped motion crossing the dish center switched into the rotation after almost 50 minutes of evolution. In the third case (the green trajectory), the motion was strongly dominated by rotations. The dominating character of rotation can be seen in Figure III.16 as a strong peak of the radial distribution function $g(r)$ around 3.7 cm from the dish center. A similar radius of stable rotation was observed in all experiments. As reported in [45], a pill self-propelled by camphene only does not come closer to the dish edge than 1.3 cm. Such character of motion was also observed in experiments with camphene pieces[26]. The stable motion along the edge can be explained as follows: We can assume that the surface-active molecules are symmetrically dissipated around the disk. Those that move towards the dish center are dispersed over a larger area than those that move towards the dish edge because the edge restricts their motion. As a result, one can expect a higher concentration of surface-active molecules in the region between the pill and the dish edge than in the central part of the dish. The gradient of concentration translates into the gradient surface tension that repels a pill away from the edge.

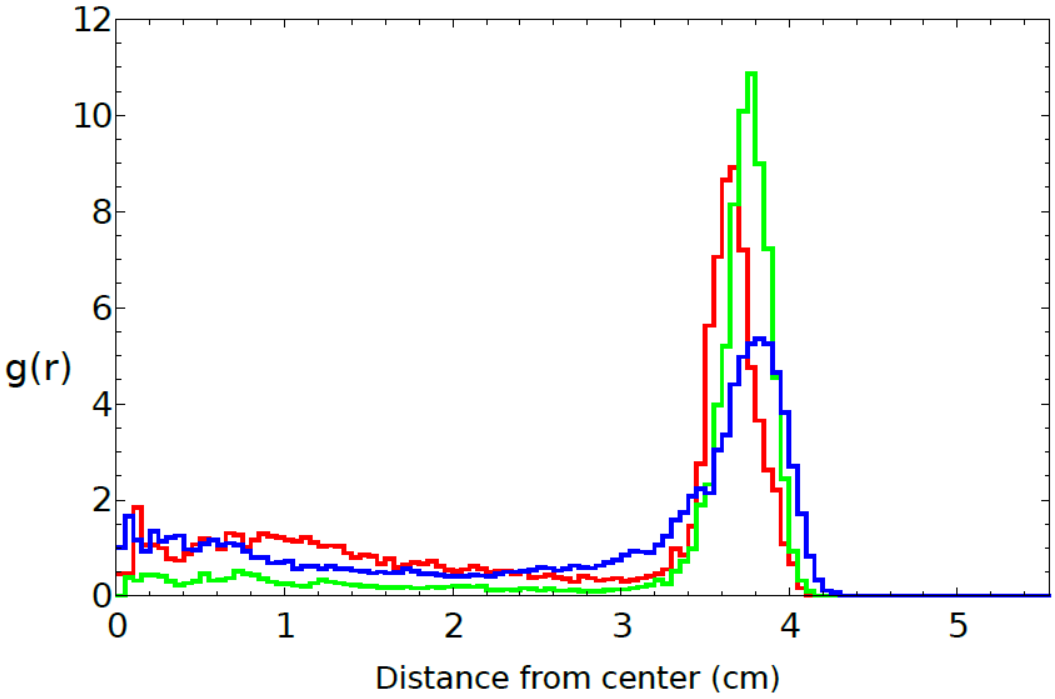

Figure III.16: The radial distribution function $g(r)$ of the positions of pill centers calculated from the distances illustrated in Figure III.15. The same color is used to draw the radial distribution function and the trajectory.

Figure III.17 presents the speed of a pill as a function of time for the trajectories illustrated in Figure III.15. The majority of measured speed values are below 1.5 cm/s, but there are occasional high-speed bursts approaching 3 cm/s. Such increases in speed do not strongly correlate with the character of motion. Even so, the speed of characterizing the stable rotation was, on average, a bit lower than that corresponding to the random motion.

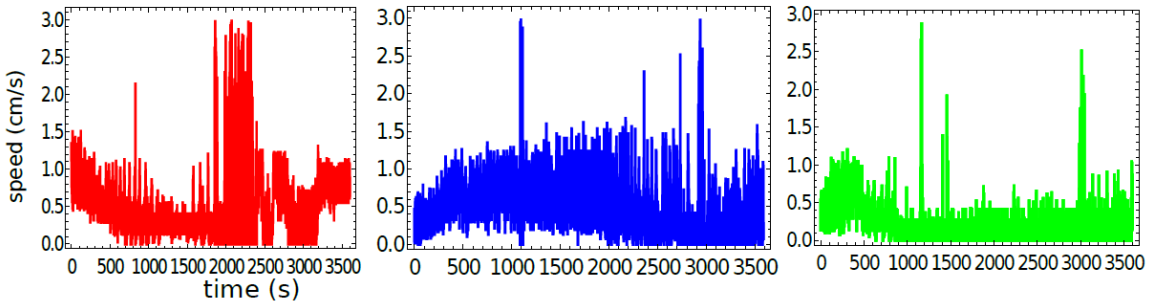

Figure III.17: The speed of a pill made of 95.2 % camphene and 4.8 % polypropylene as a function of time, as observed in three independent experiments.

The speeds averaged over the observation time were 0.46 cm/s, 0.47 cm/s and 0.21 cm/s for the "red", "blue" and "green" experiments respectively. These numbers are slightly lower than the average speed measured in experiments with a pill made of pure camphene (0.6 cm/s in Section III. 2.1.3[45]).

Figure III.18 shows the probability distribution of speeds for a pill made of 95.2 % camphene and 4.8 % polypropylene. The main figure shows the results of individual experiments. The distribution of speed values observed in all experiments collectively is shown in the insert. It

has a Poissonian character which confirms observations for self-propelled objects made of pure camphene[45,47].

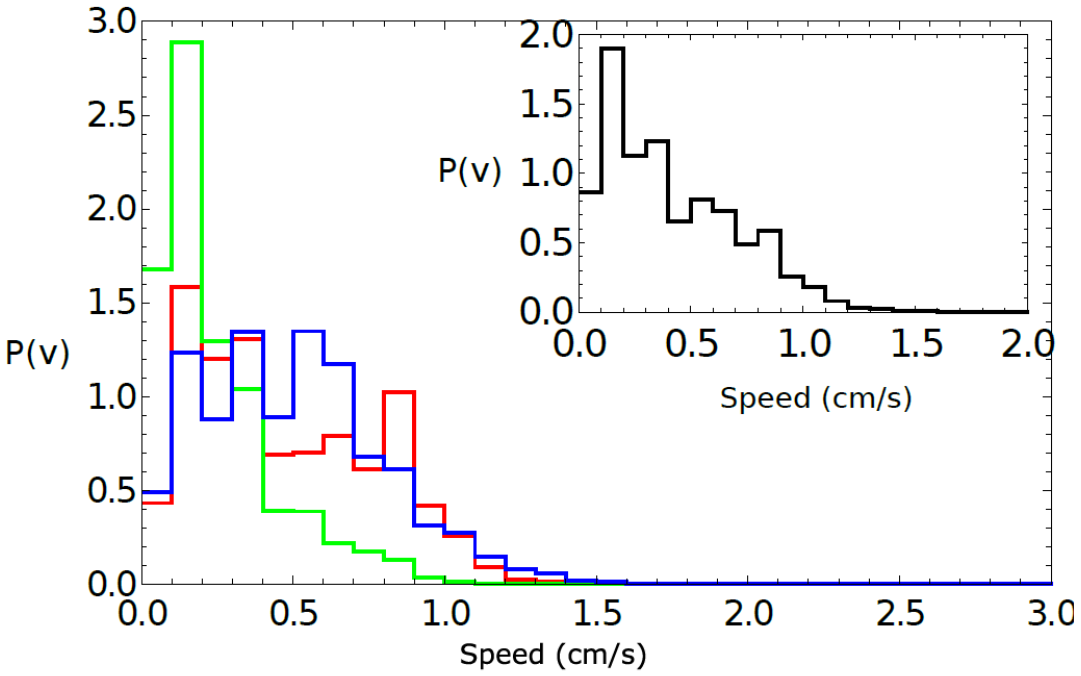

Figure III.18: The probability distribution of speeds for a pill made of 95.2 % camphene and 4.8 % polypropylene. The large figure shows results of individual experiments. The distribution of speed values observed in all experiments is shown in the insert.

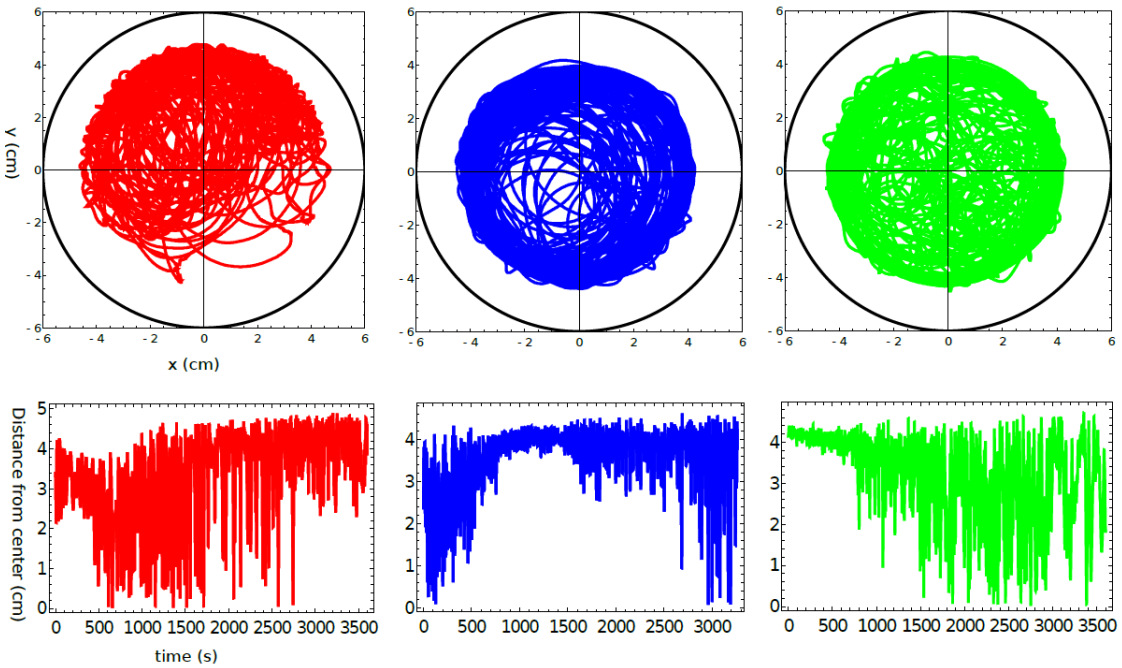

Figure III.19: The upper three figures show the trajectories of a 4mm pill made of 9.1 % polypropylene and 90.9 % camphene in a Petri dish with a 12 cm diameter. The black circle indicates the location of the dish wall. The distances between the pill center and the dish center as functions of time are plotted in figures located below the corresponding trajectories

To study the influence of the polypropylene content on the self-motion of a camphene pill, we

performed three independent experiments with a 4mm pill made of plastic composed of 90.9 % weight camphene and 9.1 % weight polypropylene. The dish diameter was 12 cm. The trajectories and the distances between the pill center and the dish center are shown in Figure III.19. The results were obtained by analysis of individual frames recorded at a rate of 25 fps. The character of motion is similar to that observed for a pill made of 95.2 % camphene and 4.8 % polypropylene. In each experiment, we observed random motion inside the dish. Moreover, in two of three experiments, we also observed a stable rotation along the dish edge. The dominating character of rotation can be seen in Figure III.20 as a strong peak of the radial distribution function $g(r)$ at the 4.0 cm distance from the dish center. The increase in peak position if compared with $g(r)$ shown in Figure III.16 can be attributed to a larger diameter of the dish.

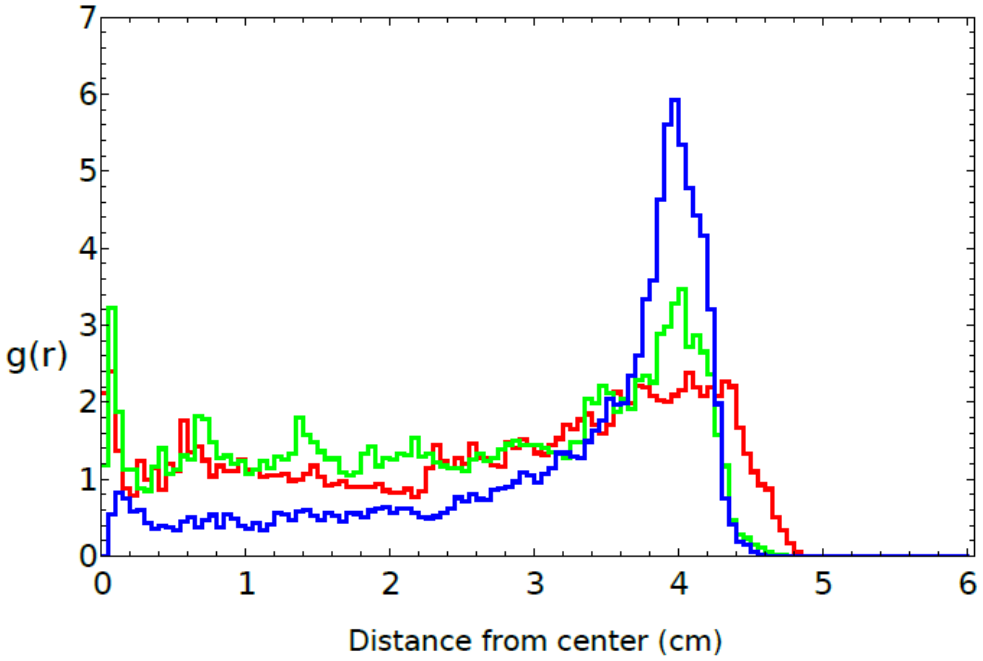

Figure III.20: The radial distribution function of the positions of pill centers calculated from the distances illustrated in Figure III.19. The same color is used to draw the radial distribution function and the trajectory.

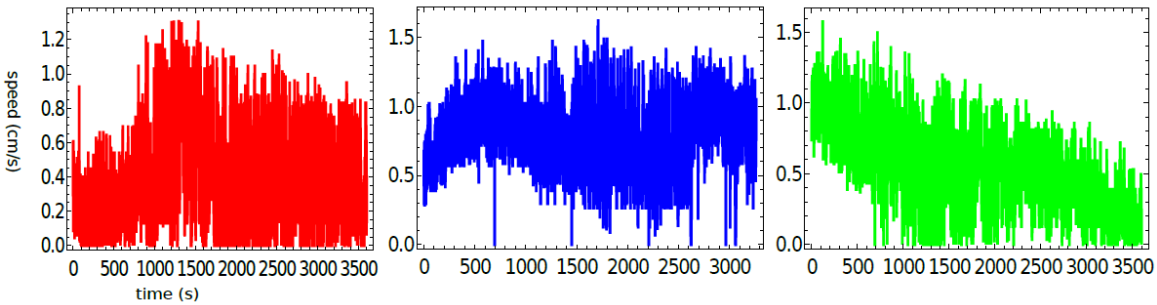

Figure III.21: The speed of a pill made of 9.1 % polypropylene and 90.9 % camphene. as a function of time, as observed in three independent experiments.

Figure III.21 presents the speed of a pill as a function of time for the trajectories illustrated

in Figure III.19. Here, all of the measured speed values are below 1.5 cm/s, and we do not observe any spikes. The speeds averaged over the observation time were 0.38 cm/s, 0.79 cm/s and 0.54 cm/s for the "red", "blue" and "green" experiments respectively. These numbers are in good agreement with the average speed measured in experiments with a pill made of pure camphene (0.6 cm/s in Section III. 2.1.3[45]).

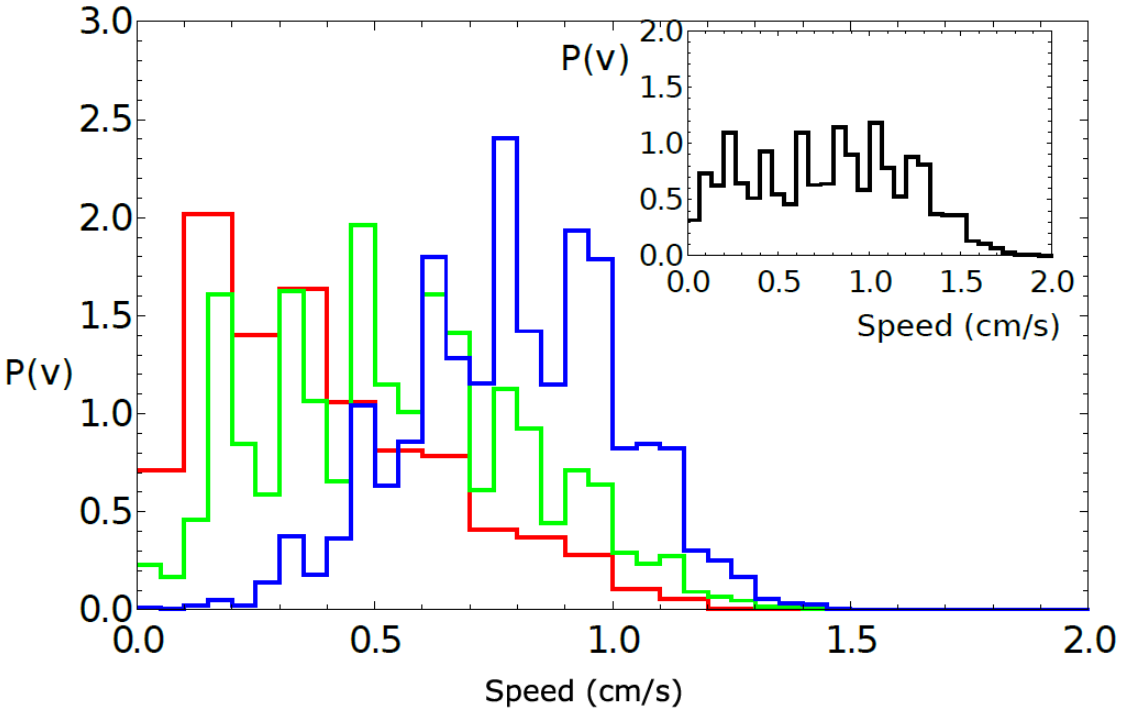

Figure III.22: The probability distribution of speeds of pill made of 9.1 % polypropylene and 90.9 % camphene. The large figure shows results of individual experiments. The distribution of speed values observed in all experiments is shown in the insert.

Figure III.22 shows the probability distribution of speeds for a pill made of 90.9 % camphene and 9.1 % polypropylene. The large figure shows the results of individual experiments and, in the insert, the distribution of all speed values observed in three experiments. The probability distributions of speed observed in the "red" and "green" experiments have a Poissonian form. The third distribution is Gaussian, with a maximum of around 0.8 cm/s. As a result, the distribution of all values of speed is almost flat for speeds $< 1\,cm/s$.

III. 3.2.3 Self-motion of a pill made of camphene-camphor-polypropylene plastic depending on material ratio

The results presented above suggest that the self-motion properties do not depend on the amount of polypropylene in the pill. Next, we consider if and how the weight ratio between camphene and camphor modifies the character of motion. For the camphene-polypropylene plastic system, we observed an initial decrease in the pill speed that stabilized after 30 s (See

Figure III.14b). In the case of camphene-camphor-polypropylene plastic, the speed stabilization is much slower, and it can be observed after 300 s as illustrated in Figure III.23. The results shown below illustrate the approach towards the stable speed for 9.1 % polypropylene, 75.7 % camphene, and 15.2 % camphor mixture. Three independent experiments were done. The observed speeds as functions of time are plotted in Figure III.23 with different colors. The results for other compositions of the material showed a similar time of speed stabilization. Therefore, we neglected the initial 300 s of the pill motion for the results presented in the following subsections.

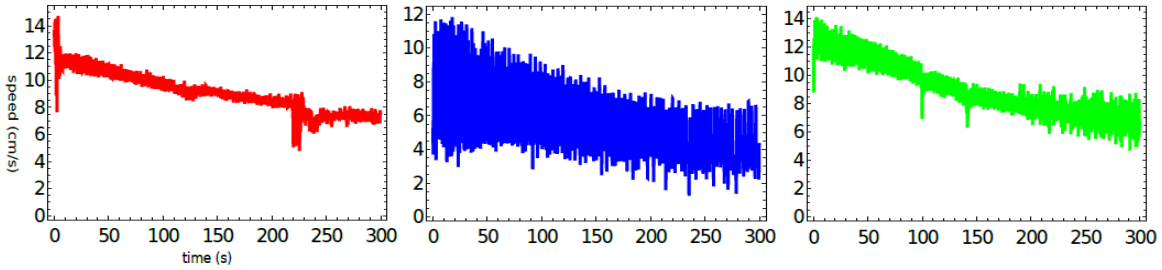

Figure III.23: The speed of a 4mm pill made of 9.1 % polypropylene, 75.7 % camphene and 15.2 % camphor mixture as a function of time for the initial stage of the pill motion. The motion was observed in a Petri dish with 12 cm diameter and for 0.44 cm water level.

III. 3.2.3.1 A pill made of 4.8 % polypropylene, 79.3 % camphene and 15.9 % camphor

We present the results of three independent experiments in which the pill motion was observed. The dish diameter was 11 cm. The trajectories and the distances between the pill center and the dish center are shown in Figure III.24. These results were obtained by analysis of individual frames recorded at a rate of 30 fps. In each experiment, we observed a different character of motion. The red trajectory covers the central part of the dish. In the second experiment (the blue curve), we observed the rotational motion of the pill along the dish edge. The third experiment also showed such rotational motion, but it was separated by time intervals in which a complex motion at a distance from the dish center was observed. Let us notice that in all cases, the pill never comes into contact with the dish edge. The largest recorded distance between the pill center and the dish center were 4.56, 4.46 and 4.91 cm; thus, the distance between the pill edge and the dish wall was always larger than 5 mm.

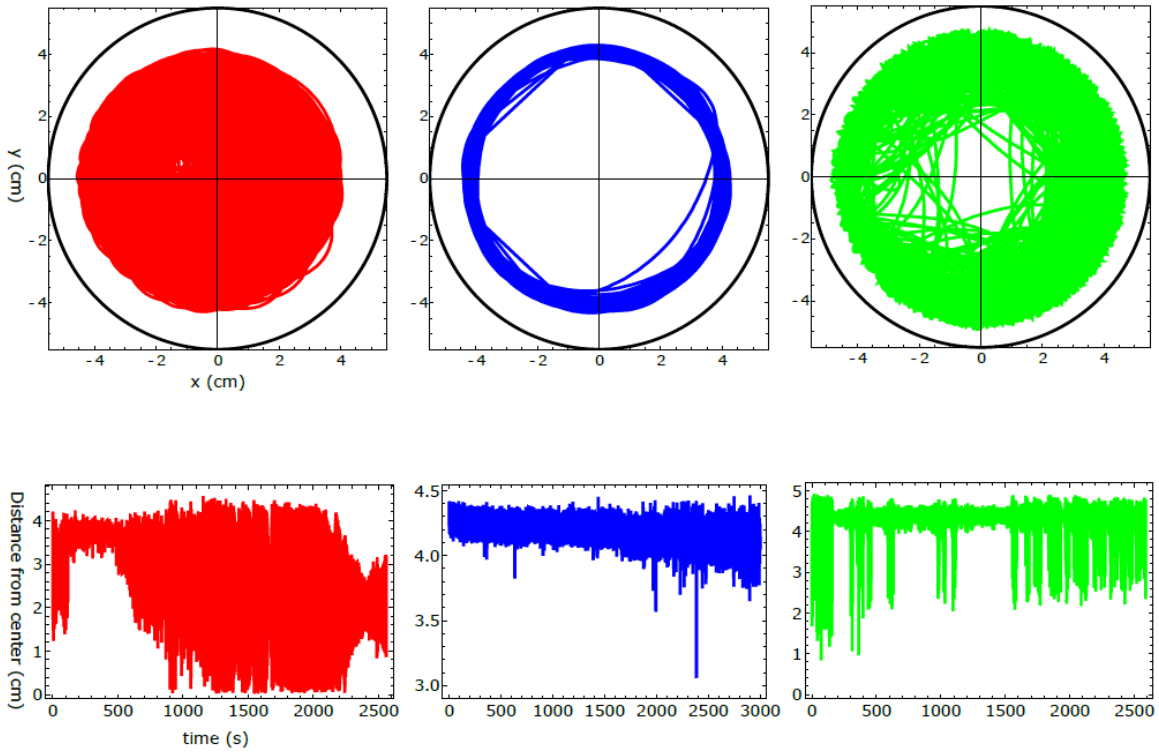

Figure III.24: The upper three Figures show the trajectories of a 4mm pill made of 4.8 % polypropylene, 79.3 % camphene and 15.9 % camphor in a Petri dish with a 11 cm diameter. The black circle indicates the location of the dish wall. The distance between the pill center and the dish center as a function of time is plotted in the figures located below the corresponding trajectories.

Figure III.25 shows the radial distribution function $g(r)$ calculated from the distances seen of all frames of the recorded movie. Three curves illustrate functions $g(r)$ measured in separate experiments.

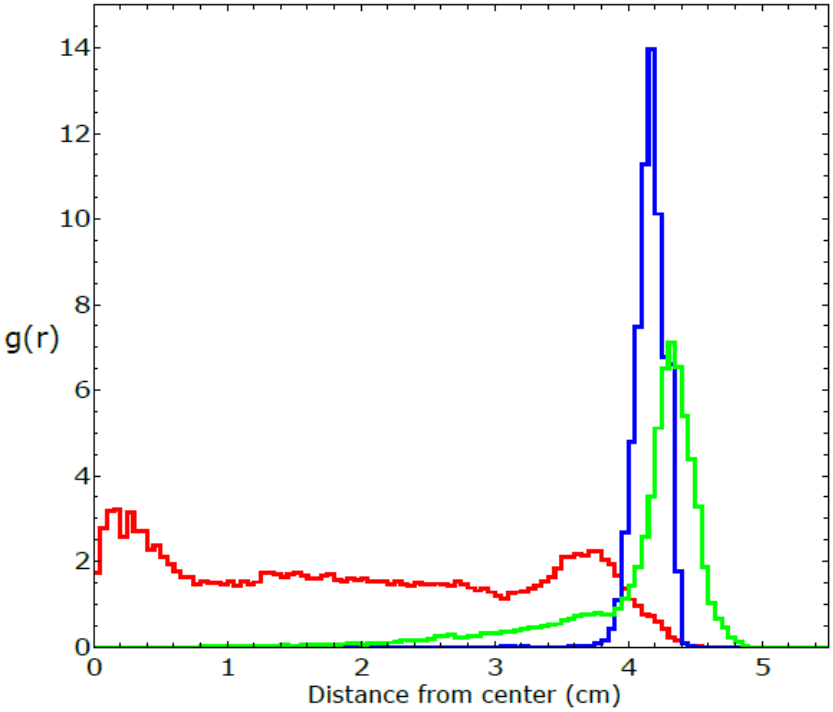

Figure III.25: The radial distribution function of the positions of pill centers calculated from the distances illustrated in Figure III.24. The same color is used to draw the radial distribution function and the trajectory.

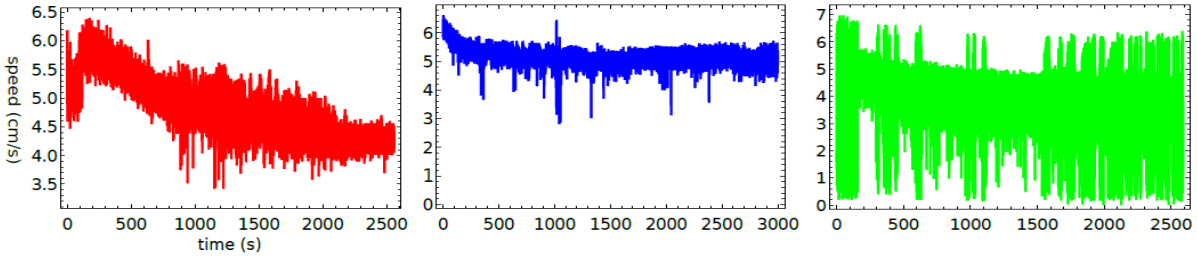

Figure III.26: The speed of a pill made of 4.8 % polypropylene, 79.3 % camphene and 15.9 % camphor as a function of time, as observed in three independent experiments.

Figure III.26 presents the speed of a pill as a function of time. In all experiments, we observed an initial decrease of speed, but it does not exceed 25 % of the stationary value. As expected, the most stable speed is observed for the most regular trajectory (rotation along the dish wall). Figure III.27 shows the probability distribution of speeds. The large figure shows the results of individual experiments. The distribution of speed values observed in all experiments is shown in the insert. The average values of speed observed for a pill made of 4.8 % polypropylene, 79.3 % camphene and 15.9 % camphor were 4.81, 5.21 and 3.82 cm/s.

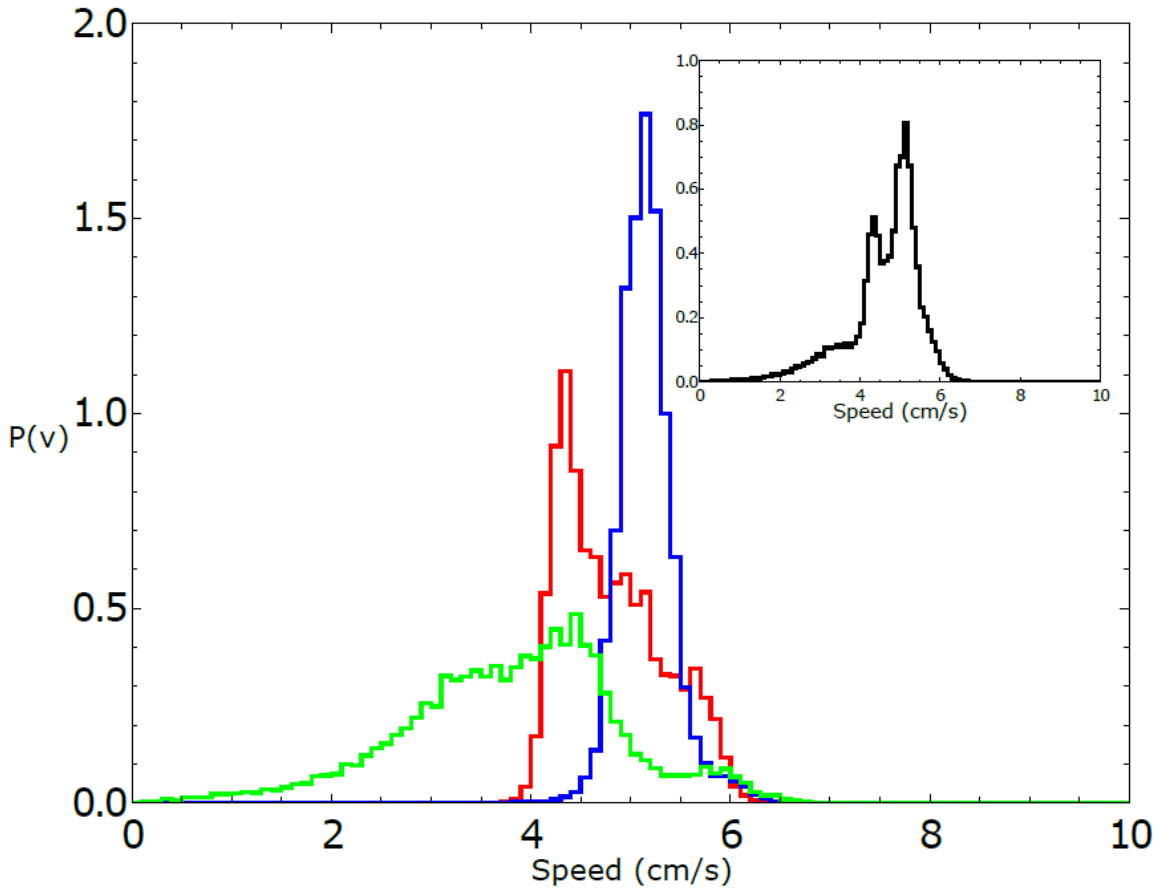

Figure III.27: The probability distribution of speeds for a pill made of 4.8 % polypropylene, 79.3 % camphene and 15.9 % camphor. The large figure shows results of individual experiments. The distribution of speed values observed in all experiments is shown in the insert.

III. 3.2.3.2 A pill made of 9.1 % polypropylene, 75.7 % camphene and 15.2 % camphor

The dish diameter was 12 cm. The trajectories and the distances between the pill center and the dish center are shown in Figure III.28. These results were obtained by analysis of individual frames recorded at a rate of 25 fps. The red trajectory covers the central part of the dish. In the second and the third experiments (blue and green curves), we observed the rotational motion of the pill along the dish edge. The pill does not come into contact with the dish edge in any of the experiments. The largest recorded distances between the pill center and the dish center were 5.19, 5.25, and 5.13 cm, respectively; thus, the distance between the pill edge and the dish wall was always larger than 5 mm.

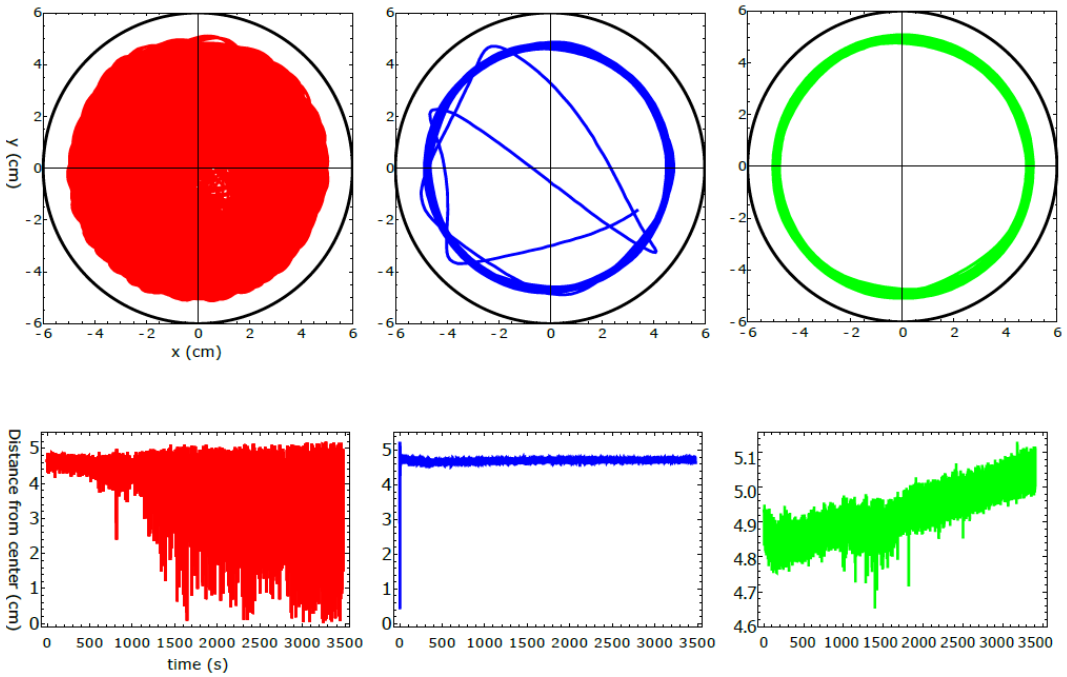

Figure III.28: The upper three figures show the trajectories of a 4mm pill made of 9.1 % polypropylene, 75.7 % camphene and 15.2 % camphor in a Petri dish with a 12 cm diameter. The black circle indicates the location of the dish wall. The distances between the pill center and the dish center observed in individual experiments as functions of time are plotted in figures located below the corresponding trajectories.

Figure III.29 shows the radial distribution function $g(r)$ calculated from the distances seen of all frames of the recorded movie. The curves present $g(r)$ measured in separated experiments.

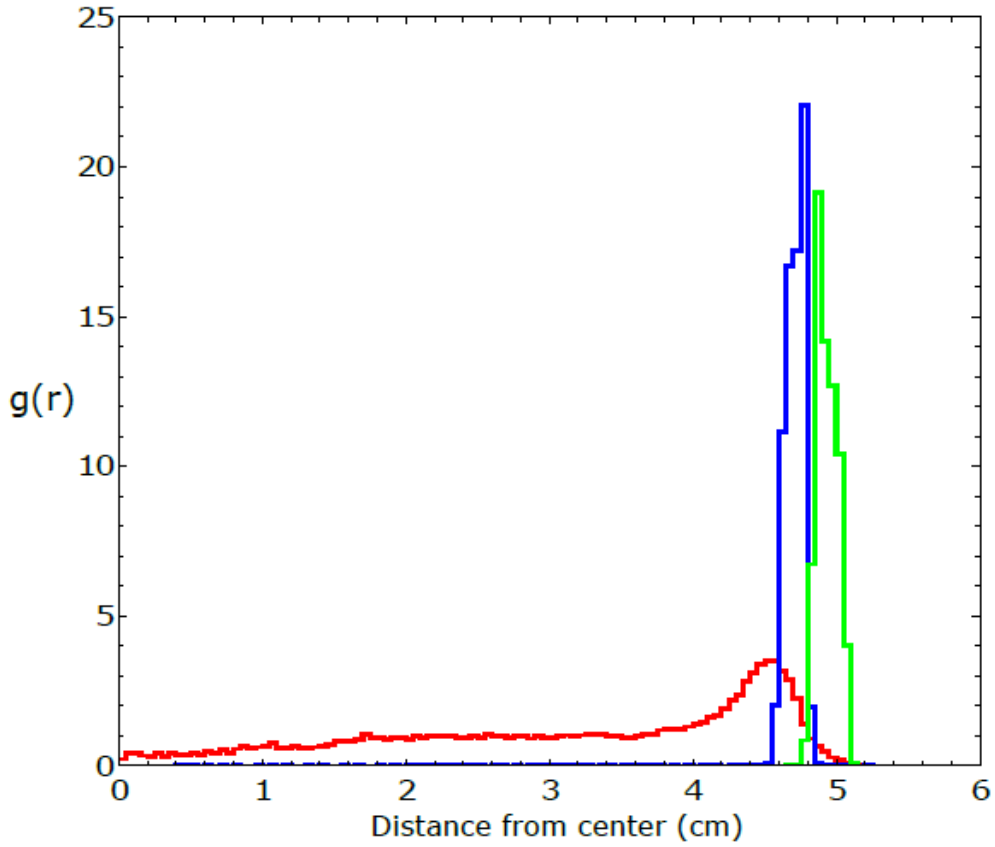

Figure III.29: The radial distribution function of the positions of pill centers calculated from the distances illustrated in Figure III.28. The same color is used to draw the radial distribution function and the trajectory.

Figure III.30 presents the speed of a pill as a function of time. In all experiments we observed an initial decrease of speed but it does not exceed 25 % of the stationary value. As expected, the speed is most stable for the most regular trajectory (rotation along the dish wall).

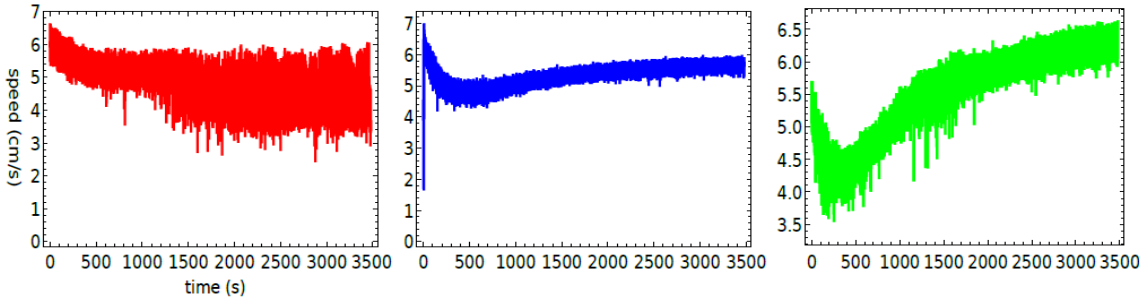

Figure III.30: The speed of a pill made of 9.1 % polypropylene, 75.7 % camphene and 15.2 % camphor as a function of time, as observed in three independent experiments.

Figure III.31 shows the probability distribution of speeds. The large figure shows results of individual experiments. The distribution of speed values observed in all experiments is shown in the insert. The average values of speed observed for a pill made of 9.1 % polypropylene, 75.7 % camphene and 15.2 % camphor were 4.73, 5.32 and 5.53 cm/s.

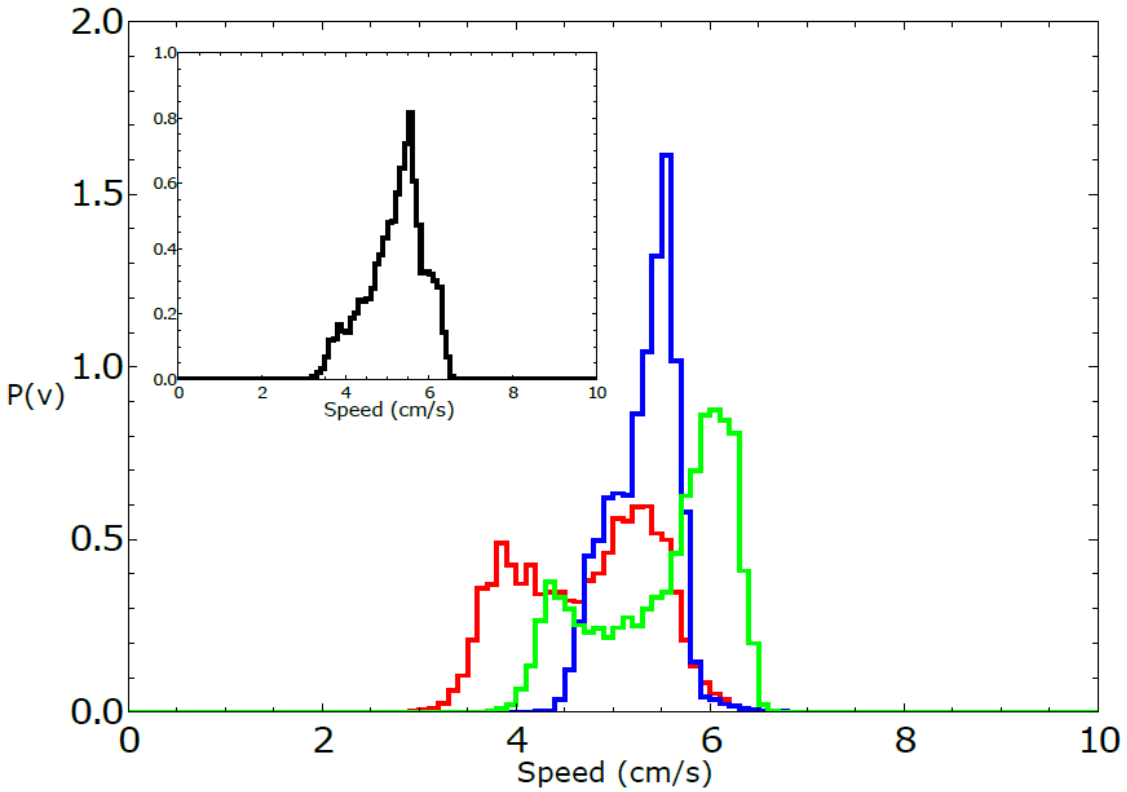

Figure III.31: The probability distribution of speeds of pill made of 9.1 % polypropylene, 75.7 % camphene and 15.2 % camphor. The large figure shows results of individual experiments. The distribution of speed values observed in all experiments is shown in the insert.

III. 3.2.3.3 A pill made of 4.8 % polypropylene, 63.8 % camphene and 31.4 % camphor

The dish diameter was 11 cm. The trajectories and the distances between the pill center and the dish center are shown in Figure III.32. These results were obtained by analysis of individual frames recorded at a rate of 30 fps. In the first and second experiments (the red and blue curves), we observed the rotational motion of the pill along the dish edge. The third experiment also showed rotational motion, but the trajectory covered a large part of the dish area. Let us notice that there is no contact between pill and dish edge in any of the experiments. The largest recorded distances between the pill center and the dish center were 4.44, 4.53 and 4.71 cm respectively; thus, the distance between the pill edge and the dish wall was always larger than 8 mm.

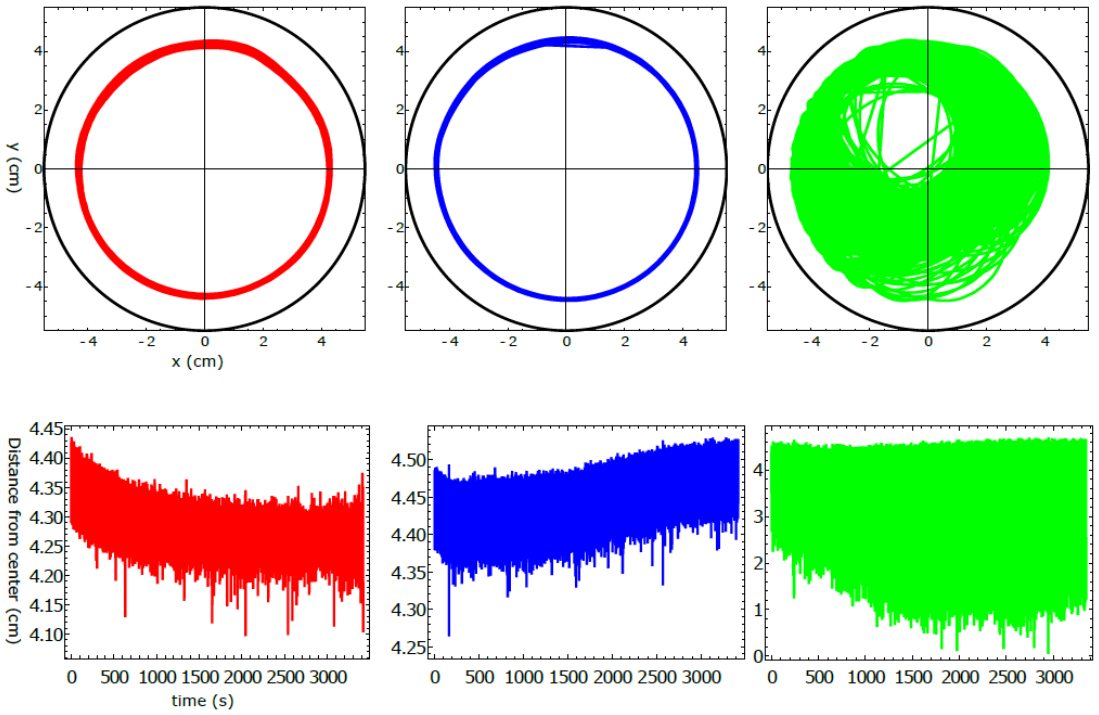

Figure III.32: The upper three figures show the trajectories of a 4mm pill made 4.8 % polypropylene, 63.8 % camphene and 31.4 % camphor in a Petri dish with an 11 cm diameter. The black circle indicates the location of the dish wall. The distances between the pill center and the dish center observed in individual experiments as functions of time are plotted in figures located below the corresponding trajectories.

Figure III.33 shows the radial distribution function $g(r)$ calculated from the distances seen of all frames of the recorded movie. The curves illustrate $g(r)$ measured in separated experiments.

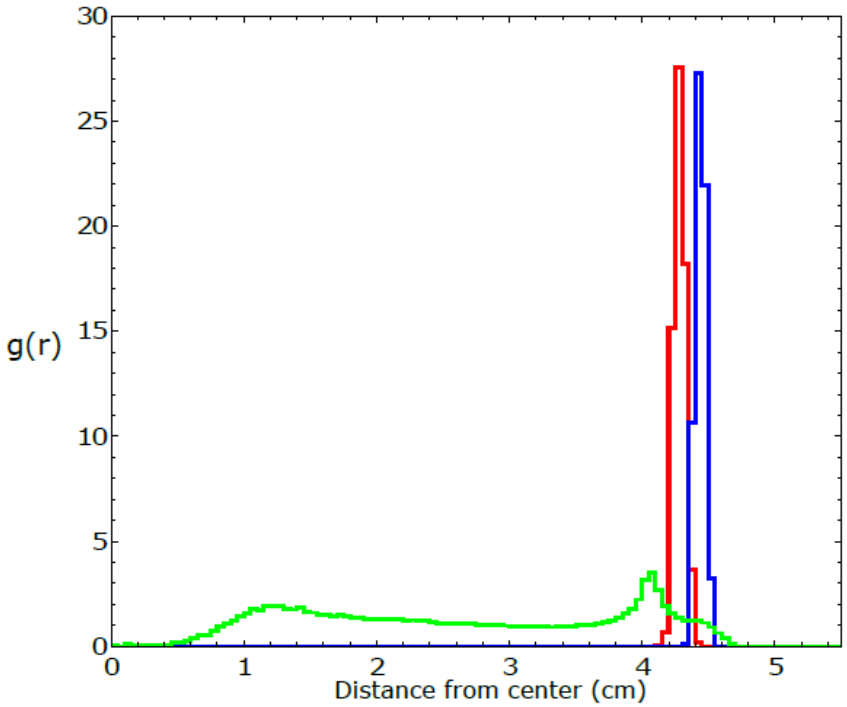

Figure III.33: The radial distribution function of the positions of pill centers calculated from the distances illustrated in Figure III.32. The same color is used to draw the radial distribution function and the trajectory.

Figure III.34 presents the speed of a pill as a function of time. In all experiments we observed an initial decrease of speed but it does not exceed 30 % of the stationary value. As expected, speed is the most stable for the most regular trajectory (rotation along the dish wall).

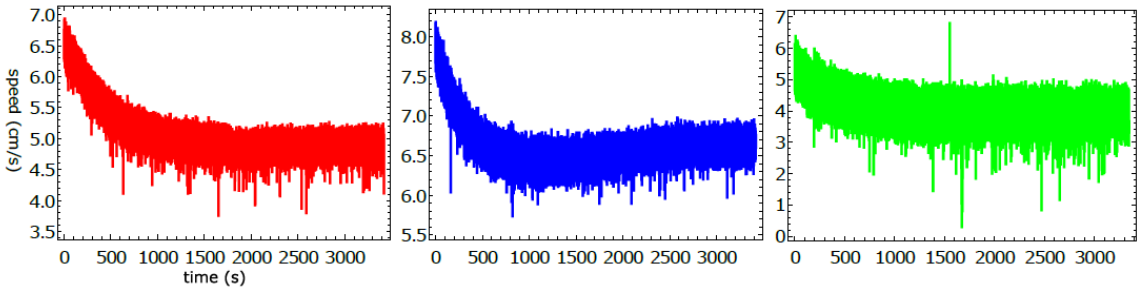

Figure III.34: The speed of a pill made of 4.8 % polypropylene, 63.8 % camphene and 31.4 % camphor as a function of time, as observed in three independent experiments.

Figure III.35 shows the probability distribution of speeds. The large figure shows results of individual experiments. The distribution of speed values observed in all experiments is shown in the insert. The average value of speed observed for a pill made of 4.8 % polypropylene, 63.8 % camphene and 31.4 % camphor were 5.09, 6.60 and 3.93 cm/s.

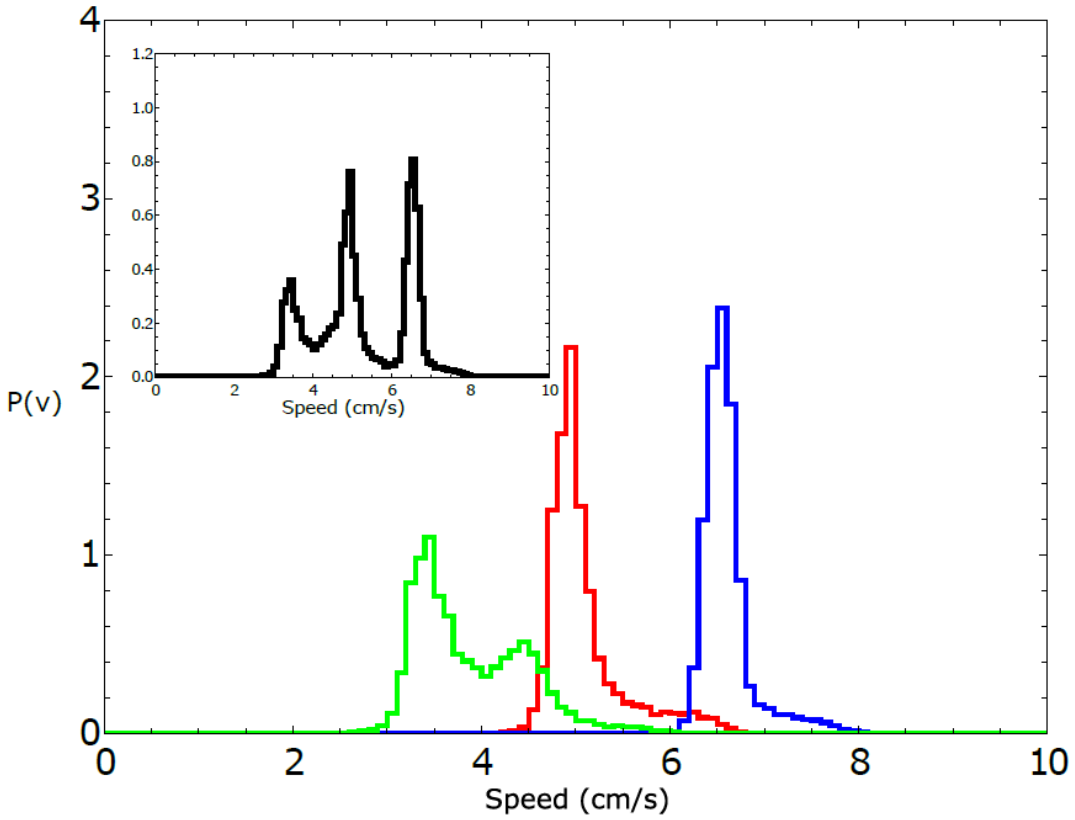

Figure III.35: The probability distribution of speeds. The large figure shows results of individual experiments. The distribution of speed values observed in all experiments is shown in the insert.

III. 3.2.3.4 A pill made of 9.1 % polypropylene, 60.9 % camphene and 30 % camphor

The dish diameter was 12 cm. The trajectories and the distances between the pill center and

the dish center are shown in Figure III.36 These results were obtained by analysis of individual frames recorded at a rate of 25 fps. In each experiment, we observed a different character of motion. In the first and second experiments (the red and blue curves), we observed a complex motion covering the whole surface of the dish. In the second experiment (the blue curve), this complex motion switches into the rotational motion along the dish edge after 30 minutes. In the third experiment (the green curve), we also observed the rotational motion of the pill along the dish edge. The dispersion of the radii decreased with time. Notice that there is no contact between pill and dish edge in any of the experiments. The largest recorded distances between the pill center and the dish center were 5.41, 5.15 and 5.10 cm respectively; thus, the distance between the pill center and the dish center was always larger than 4 mm.

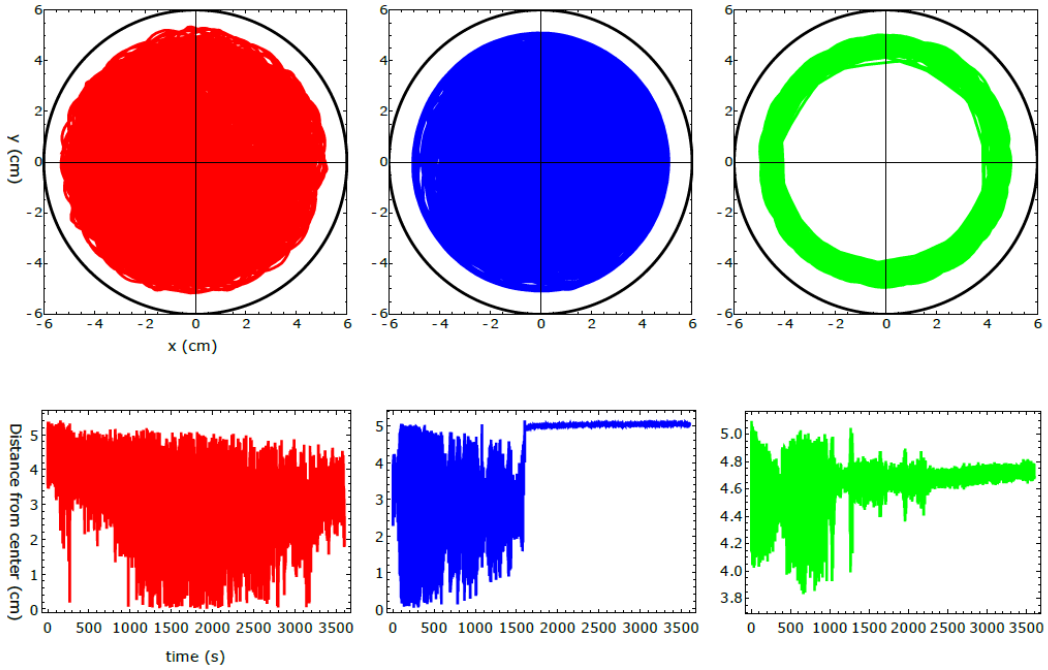

Figure III.36: The upper three figures show the trajectories of a 4mm pill in a Petri dish with a 12 cm diameter. The black circle indicates the location of the dish wall. The distances between the pill center and the dish center observed in individual experiments as functions of time are plotted in figures located below the corresponding trajectories.

Figure III.37 shows the radial distribution function $g(r)$ calculated from the distances seen of all frames of the recorded movie. The curves show $g(r)$ measured in separate experiments.

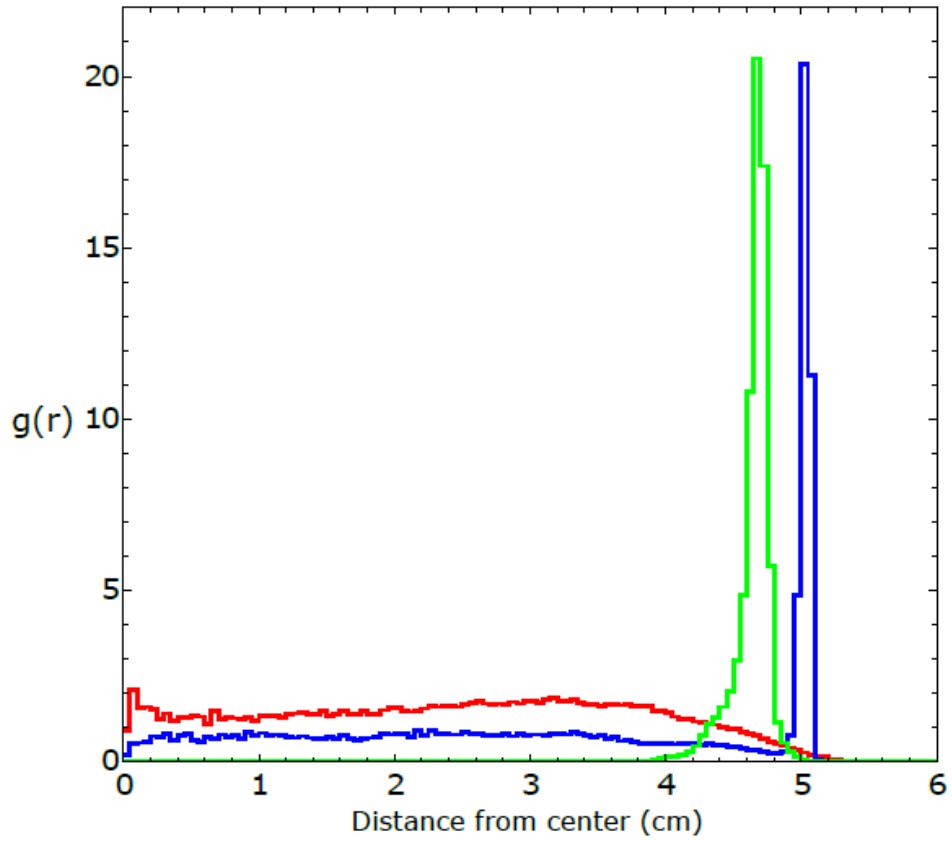

Figure III.37: The radial distribution function of the positions of pill centers calculated from the distances illustrated in Figure III.36. The same color is used to draw the radial distribution function and the trajectory.

Figure III.38 presents the speed of a pill as a function of time. In all experiments, we observed an initial decrease of speed, but it does not exceed 25 % of the stationary value. As expected, speed is most stable for the most regular trajectory (rotation along the dish wall).

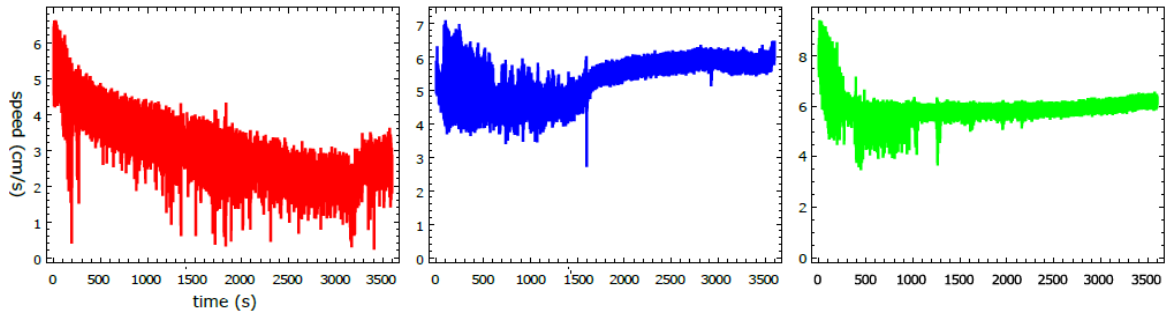

Figure III.38: The speed of a pill made of 9.1 % polypropylene, 60.9 % camphene and 30 % camphor as a function of time, as observed in three independent experiments.

Figure III.39 shows the probability distribution of speeds. The large figure shows the results of individual experiments. The distribution of speed values observed in all experiments is shown in the insert. The average values of speed observed for a pill made of 9.1 % polypropylene, 60.9 % camphene and 30 % camphor were 3.01, 5.30 and 5.90 cm/s in separate experiments.

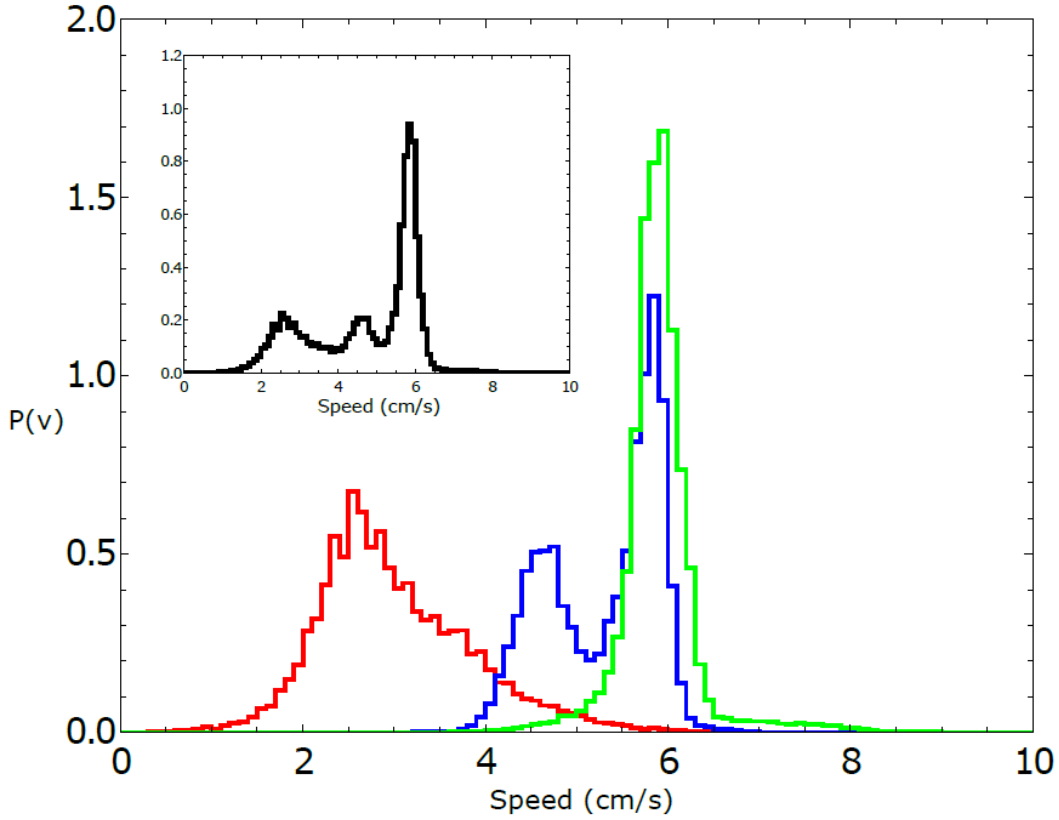

Figure III.39: The probability distribution of speeds. The large figure shows results of individual experiments. The distribution of speed values observed in all experiments is shown in the insert.

III. 3.2.3.5 A pill made of 4.8 % polypropylene, 47.6 % camphene and 47.6 % camphor.

The dish diameter was 11 cm. The trajectories and the distances between the pill center and the dish center are shown in Figure III.40. These results were obtained by analysis of individual frames recorded at a rate of 30 fps. In each experiment, we observed a different character of motion. The red trajectory shows the motion around the dish center with a large dispersion of radii that, after 2200 seconds, stabilizes to rotation characterized by a constant radius. In the second experiment (the blue curve), we observed the rotational motion of the pill along the dish edge with a fixed radius. The third experiment also showed complex motion that mainly occurs at a 1 cm distance from the dish center. In none of the cases, the pill comes into contact with the dish edge. The largest recorded distance between the pill center and the dish center were 4.78, 4.32 and 4.66 cm, respectively; thus, the distance between the pill center and the dish center was always larger than 5 mm.

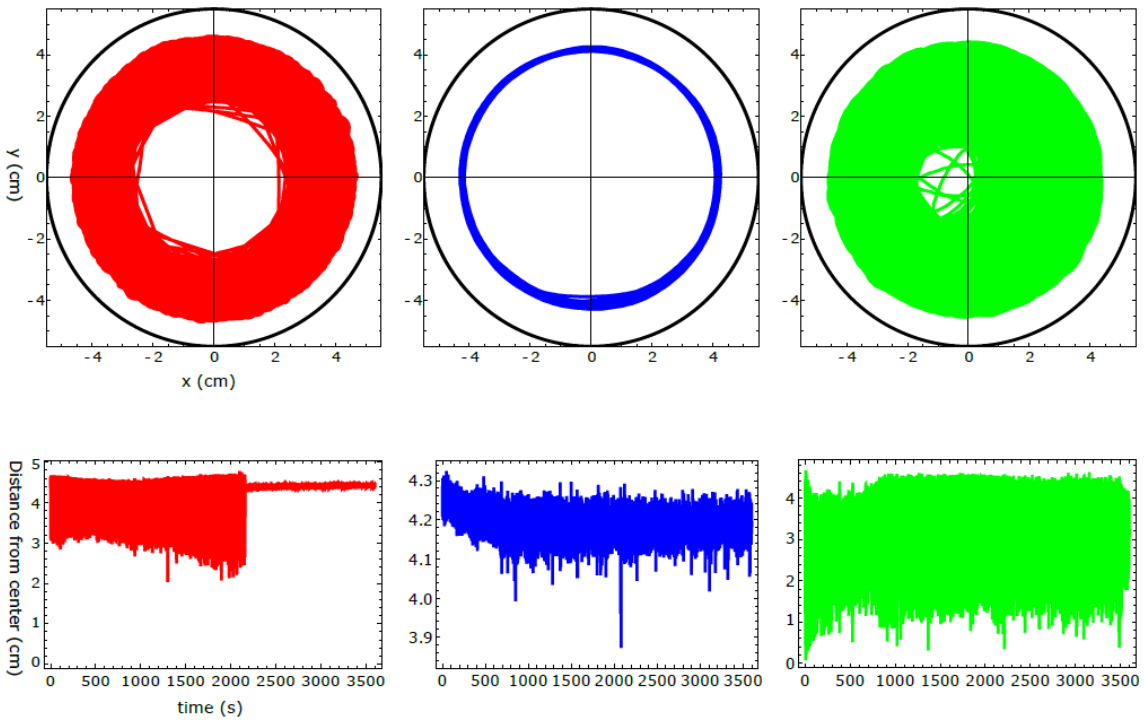

Figure III.40: The upper three figures show the trajectories of a 4mm pill made of 4.8 % polypropylene, 47.6 % camphene and 47.6 % camphor in a Petri dish with the 11 cm diameter. The black circle indicates the location of the dish wall. The distances between the pill center and the dish center observed in individual experiments as functions of time are plotted in figures located below the corresponding trajectories.

Figure III.41 shows the radial distribution function $g(r)$ calculated from the distances seen of all frames of the recorded movie. The separated curves show $g(r)$ measured in separated experiments.

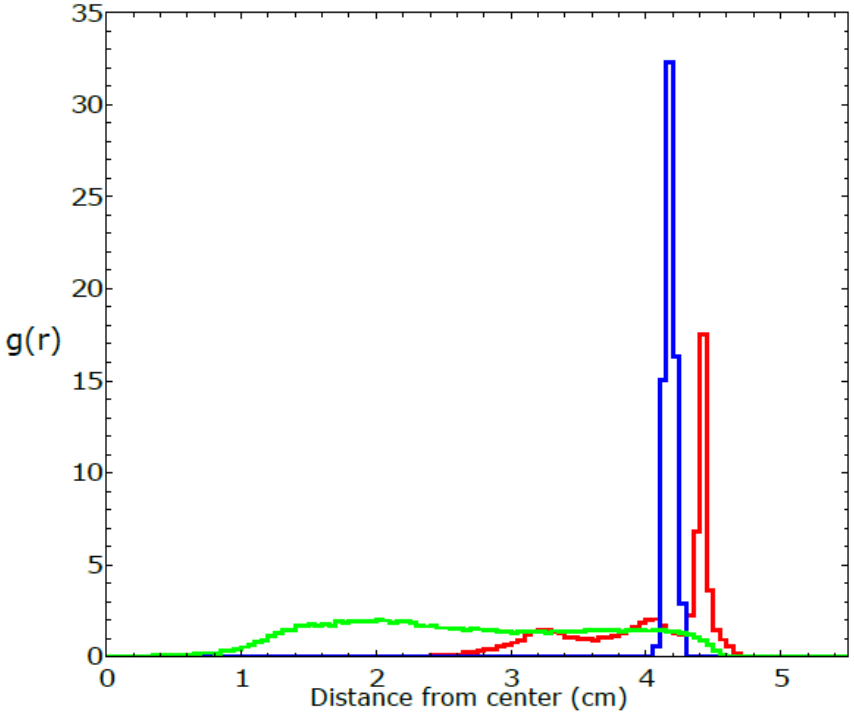

Figure III.41: The radial distribution function of the positions of pill centers calculated from the distances illustrated in Figure III.40. The same color is used to draw the radial distribution function and the trajectory.

Figure III.42 presents the speed of the pill as a function of time. In all experiments, we observed an initial decrease of speed, but it does not exceed 25 % of the stationary value. As expected, the speed is most stable for the most regular trajectory (rotation along the dish wall).

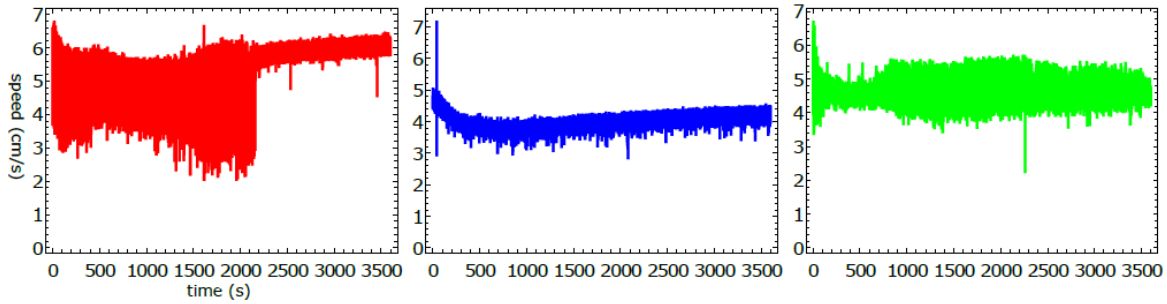

Figure III.42: The speed of a pill made of 4.8 % polypropylene, 47.6 % camphene and 47.6 % camphor as a function of time, as observed in three independent experiments.

Figure III.43 shows the probability distribution of speeds. The large figure presents the results of individual experiments. The distribution of speed values observed in all experiments is shown in the insert. The average value of speed observed for a pill made of 4.8 % polypropylene, 47.6 % camphene and 47.6 % camphor were 5.23, 3.99 and 4.57 cm/s.

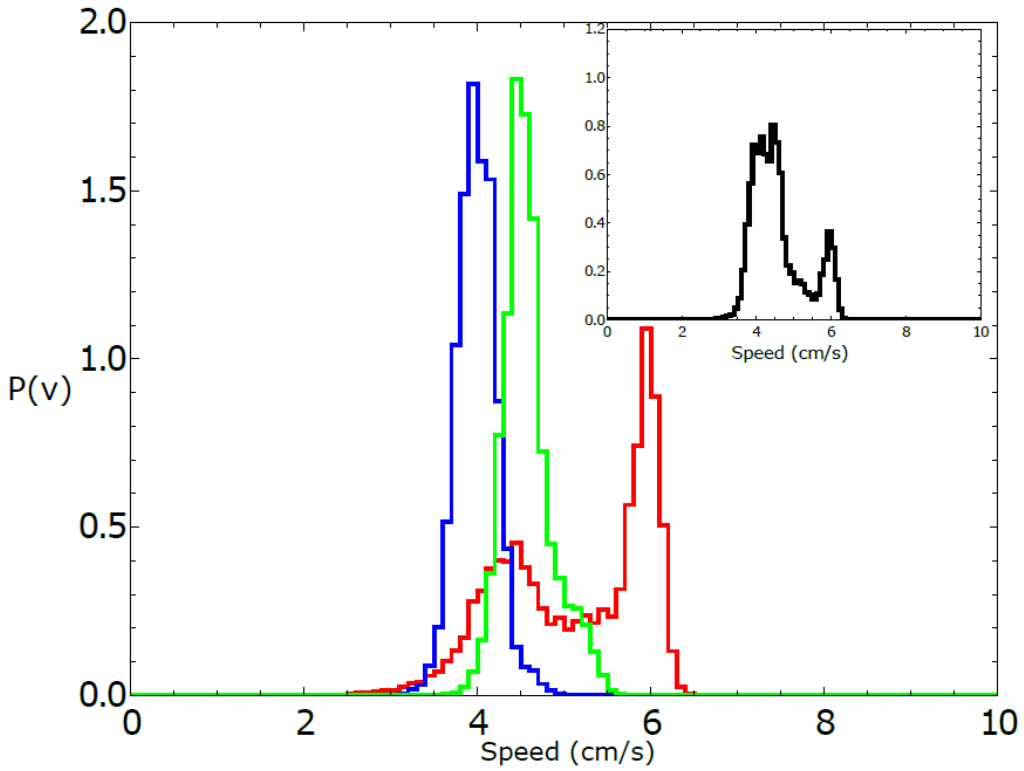

Figure III.43: The probability distribution of speeds. The large figure shows results of individual experiments. The distribution of speed values observed in all experiments is shown in the insert.

III. 3.2.3.6 A pill made of 9.1 % polypropylene, 45.45 % camphene and 45.45% camphor

We show results for 9.1 % polypropylene, 45.45 % camphene and 45.45% camphor weight

ratios (Figure III.44-0). In the experiment, the dish diameter was 12 cm, and the trajectory was recorded at the rate of 25 fps. The trajectories and the distances between the pill center and the dish center obtained in three independent experiments are shown in Figure III.44.

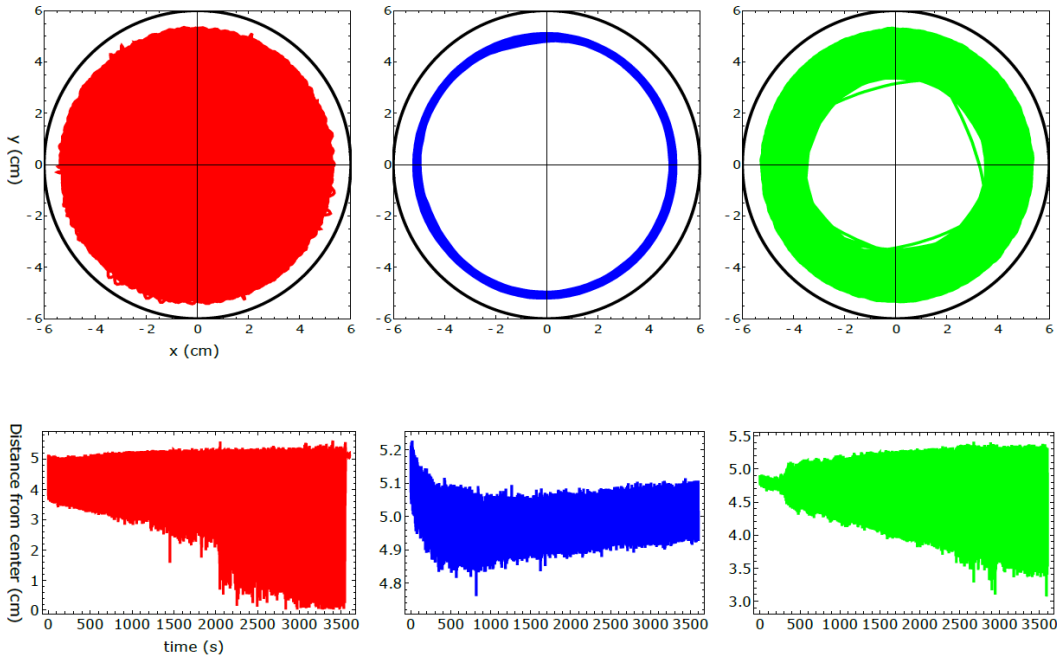

Figure III.44: The upper three figures show the trajectories of a 4mm pill made of 9.1 % polypropylene, 45.45 % camphene and 45.45% camphor in a Petri dish with a 12 cm diameter. The black circle indicates the location of the dish wall. The distances between the pill center and the dish center as functions of time are plotted in figures located below the corresponding trajectories.

The red trajectory covers the whole dish. The time evolution of the distance between the pill center and the dish center indicates that in the beginning, the pill rotated along the dish edge with the dispersion of radii exceeding 1 cm (also observed in the "green" experiment). Next, the dispersion of distance increased, and after 2000 s, the pill started to move irregularly on the whole surface. In the second and the third experiments (blue and green curves), we observed the rotational motion of the pill along the dish edge. In the "blue" experiment, the radius of the motion was in a narrow range (between [4.9 cm and 5.1 cm]) and remained stable. In the "green" experiment, the initial (circa 2 minutes long) stable rotation with a narrow dispersion of radii changes into a complex rotation characterized by large dispersion of radii that increases over time. Results in Figure III.44 show that the pill came much closer to the wall than in experiments with camphene-polypropylene plastic. Nevertheless, we observed no contact between the pill and the wall. The largest recorded distances between the pill center and the dish center were 5.62, 5.23, and 5.41 cm, respectively; thus, the distance between the pill edge and the dish wall was always larger than 2 mm. Figure III.45 shows the radial distribution function $g(r)$ calculated from the distances measured in separated experiments. The results of individual experiments are strongly dominated by the

type of observed motion.

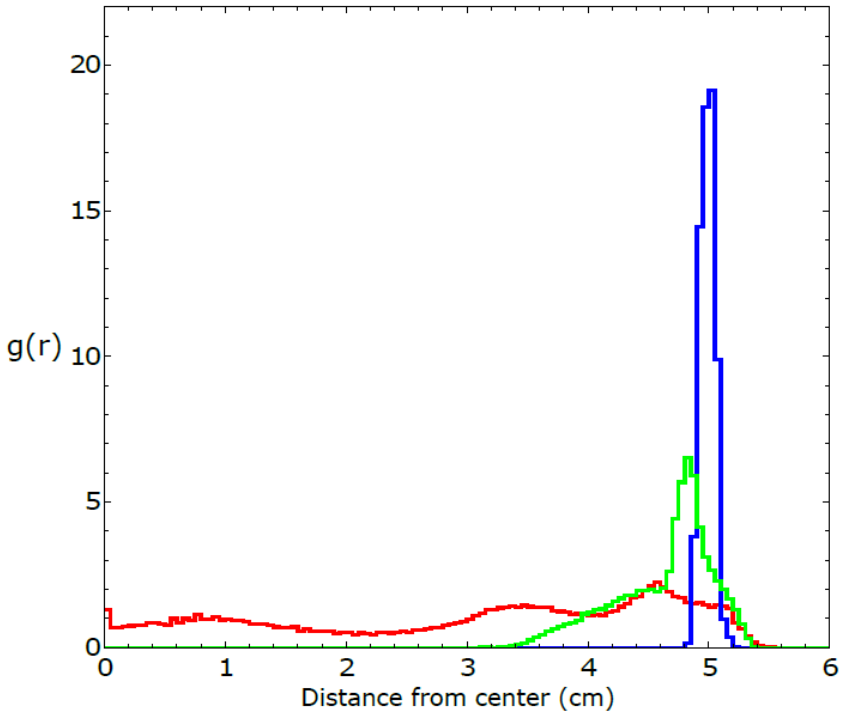

Figure III.45: The radial distribution function of the positions of pill centers calculated from the distances illustrated in Figure III.44. The same color is used to draw the radial distribution function and the trajectory.

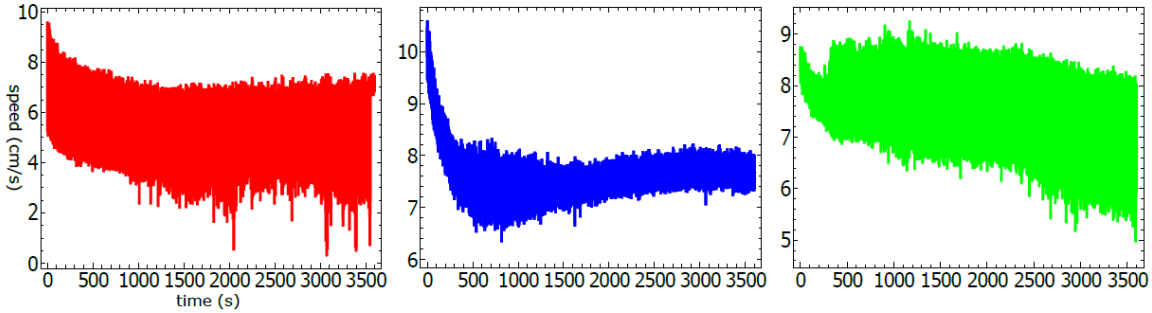

Figure III.46: The speed of a pill made of 9.1 % polypropylene, 45.45 % camphene and 45.45% camphor plastic as functions of time observed in three independent experiments (See Figure III.44).

Figure III.46 presents the speed of a pill made of 10 % polypropylene, 45 % camphene, and 45 % camphor as a function of time. The average value of speed observed for a pill made of 10 % polypropylene, 45 % camphene and 45 % camphor were $5.28, 7.63$ and $7.57\ cm/s$ for the red, blue and green function respectively. In all experiments, we observed an initial decrease of speed, but it does not exceed 25 % of the stationary value. As expected, speed is the most stable for the most uniform trajectory (rotation along the dish wall). Figure III.47 shows the probability distribution of speeds. The large figure shows the results of individual experiments. The distribution of speed values observed in all experiments is shown in the insert.

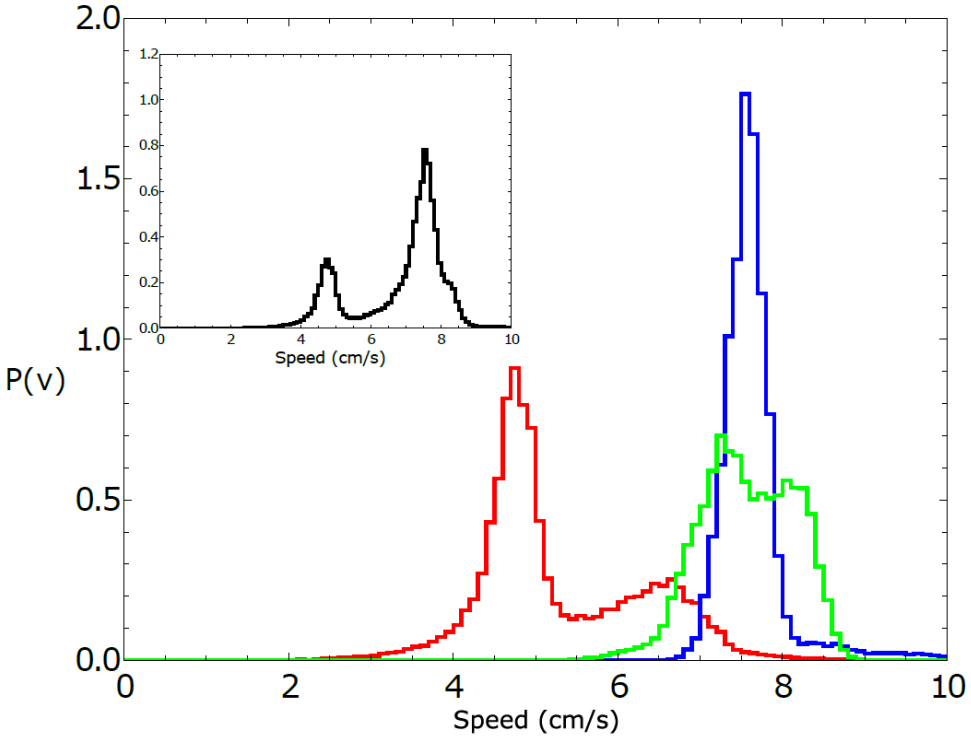

Figure III.47: The probability distribution of speeds. The large figure shows results of individual experiments. The distribution of speed values observed in all experiments is shown in the insert.

III. 3.2.4 Discussion of results for self-propelled motion of a 4mm camphene-camphor-polypropylene disk

A strong influence of the proportions between amounts of camphor and camphene on the speed of pills made of camphene-camphor wax was observed in section III. 2.1.3[45]. We did not observe such an effect for camphene-camphor-polypropylene plastics. The properties of pill self-motion do not depend on camphene/camphor weight ratio in the range from 5/1 to 1/1.

In all cases, we observed a circular motion along the dish wall with a narrow dispersion of radii $\sigma_r < 0.5$ cm, a complex rotation mode with a large rotation of radii $\sigma_r \sim 3$ cm, and a complex motion on the whole dish surface as metastable modes of pill motion. Contrasted with results of camphene-camphor waxes, there is no indication that a pill made of camphene-camphor-polypropylene plastics comes closer to the wall when camphor concentration increases. In all experiments except a single one (the red trajectory in Figure III.44), the pill center was more than 6 mm away from the dish edge. No systematic decrease in the minimum approach distance with increasing camphor concentration was observed.

The probability distributions of speed observed in a single experiment (cf. Figs III.22, III.27, III.31, III.35, III.39, III.43 and III.47) were Gaussian in the majority of cases. There were also

experiments in which we recorded a bimodal speed distribution (cf. Figs. III.31, III.35, III.39, III.43 and III.47). The bimodal distribution of speed was also observed for camphene-camphor waxes, and camphor weight ratio 33 % and 37 % in Section III. 2.1.3[45]. For the waxes, the low-speed and the high-speed maxima of the probability distribution appeared at $2\ cm/s$ and $12\ cm/s$, respectively. For camphene-camphor-polypropylene plastic, the difference between locations of maxima is much smaller and does not exceed $3\ cm/s$. In general, speeds observed for camphene-camphor-polypropylene plastics are smaller than for camphene-camphor waxes. For the waxes, speeds exceeding $10\ cm/s$ were observed with a high probability. On the other hand, the speed of pills made of camphene-camphor-polypropylene plastics hardly exceed $10\ cm/s$. The decrease in speed in comparison to camphene-camphor waxes can be explained by the dissipation of camphene and camphor from the pill surface within the neglected initial 300 s of experiment. For longer times the passivating polypropylene layer modulates the outflow of surface-active molecules. The results presented in Section III. 3.2.3.1 to III. 3.2.3.6 indicate that the self-propelled motion of pills made of camphene-camphor-polypropylene plastics is independent of the component weight ratio.

III. 3.2.5 Long term behavior of a pill made of 9.1 % polypropylene, 45.45 % camphene and 45.45% camphor

In this Section, we discuss the long-time motion of a 4 mm pill made of camphene-camphor-polypropylene plastic with a 9.1 % polypropylene, 45.45 % camphene and 45.45% camphor weight ratio on the water surface. The motion was observed in a Petri dish with 12 cm diameter and for 0.44 cm water level. Figure III.48 (a) presents the distance between the pill center and the dish center as a function of time for an experiment recorded for 5.5 hours.
The colors of the curve mark different types of motion illustrated in Figure III.48 (b), (c) and (d). In the red part (Figure III.48 (b), $t \in [3200\ s, 3700\ s]$), the pill was randomly rotating on the whole dish surface. Following that, the type of motion changed to a stable rotation along the dish edge with a ~ 7 s period. The transition from an irregular motion to a stable rotation was predicted in theoretical studies[92]. As seen in Fig. Figure III.48 (a) the radius of rotational motion slightly increases with time due to reduced outflow of surface-active molecules. The trajectories of pill motion in long time intervals $t \in [4400\ s, 6000\ s]$ (Fig. Figure III.48 (c)), and $t \in [16000\ s, 20200\ s]$ (Fig. Figure III.48 (d)) show that rotation is very stable. Figure III.48 (d) includes over 500 individual cycles, and we do not observe any significant dispersion of radii.

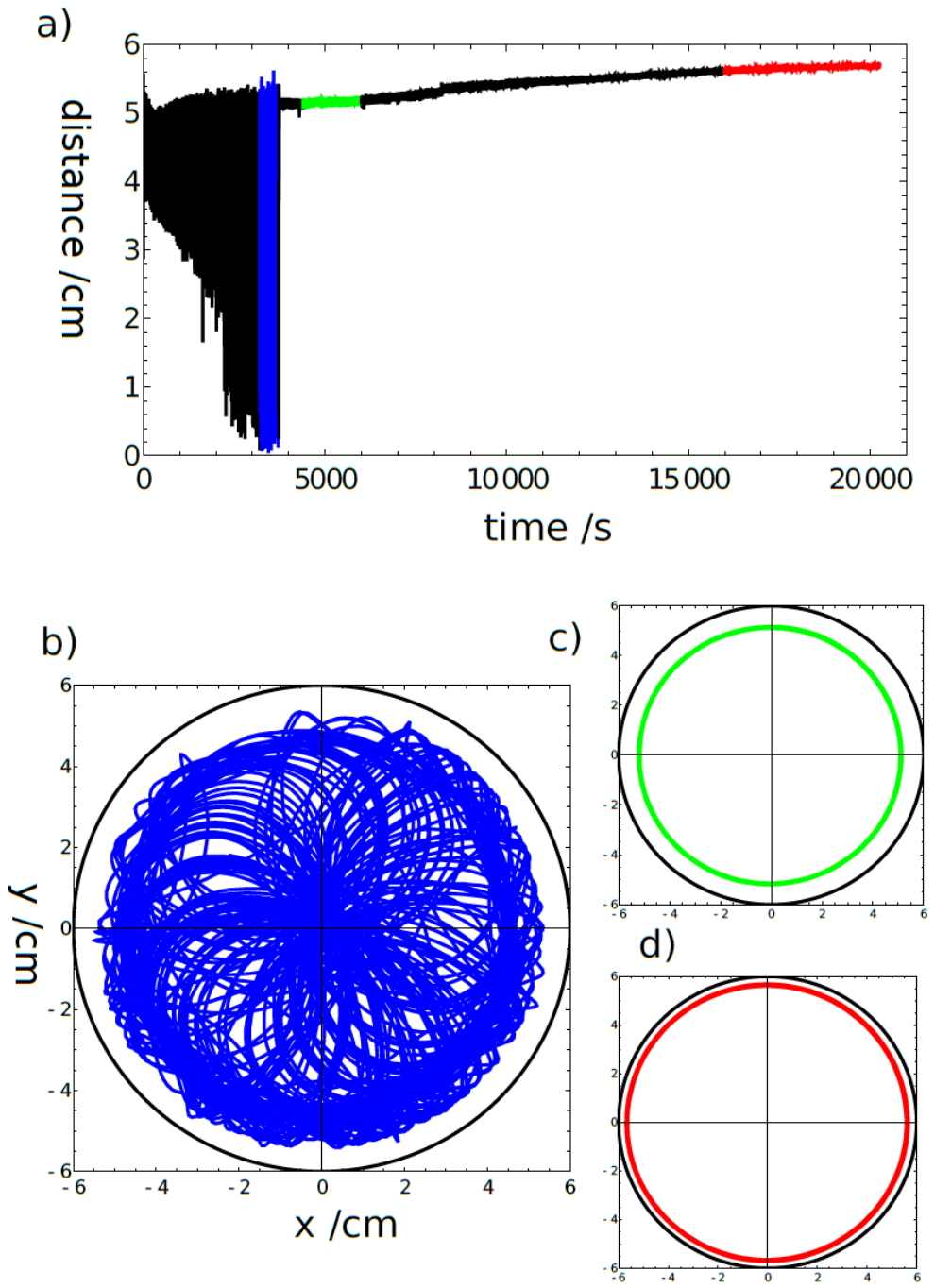

Figure III.48: Long time evolution of a 4 mm pill made of camphene-camphor-polypropylene plastic with 9.1 % polypropylene, 45.45 % camphene and 45.45% camphor weight ratio. (a) The distance between the pill center and the dish center as the function of time. The color fragments correspond to trajectories shown in figures located below. (b), (c) and (d) Trajectories observed in time intervals [3200s, 3700s], [4400s, 6000s], and [16000s, 20200s], respectively. The black circles in (b), (c) and (d) indicate the location of the dish wall.

The speed of a pill as the function of time is plotted in Figure III.49. The total distance traveled by the pill exceeds 1 km (!), which is probably a record in experiments with self-propelled objects. In the rotational mode, the speed decreases slowly (from 7 cm/s to 4 cm/s during a 4-hour period) as the result of reduced dissipation of camphor and camphene. However, we hardly notice any decrease during the first hour of the rotational motion. We believe that such high stability of motion makes camphene-camphor-polypropylene plastic an ideal candidate

for experiments with self-propelled objects.

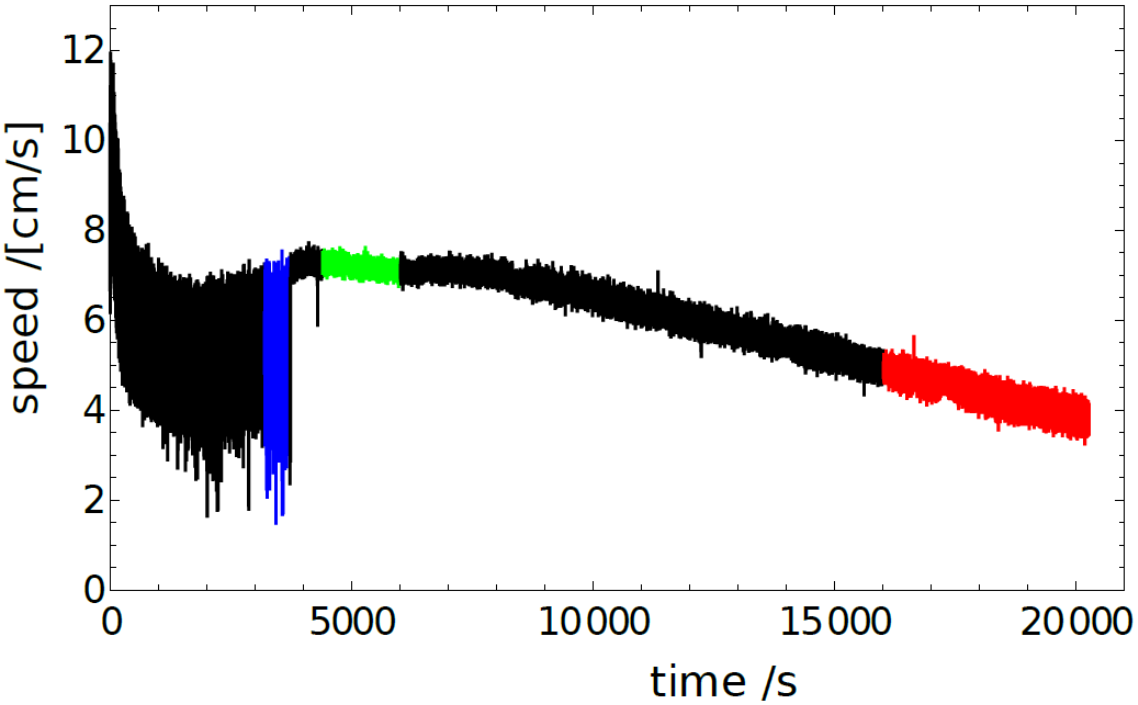

Figure III.49: The speed of a 9.1 % polypropylene, 45.45 % camphene and 45.45% camphor weight mixture as a function of time obtained from the trajectory illustrated in Figure III.48a. The colored parts of the plot correspond to modes of motion illustrated in Figs. III.48b - III.48d.

III. 3.3 Motion of self-propelled rods

In the previous Section, we discussed the self-propelled motion of pills made of camphene-camphor-polypropylene plastic. However, pill-shaped objects can be made of camphene or camphor in a pill maker. The advantage of new materials like camphene-camphor wax or camphene-camphor-polypropylene plastic lies in the fact that they can be formed into non-trivial shapes. Here we show results for self-propelled motion of rods made of plastic composed of 9.1 % polypropylene, 45.45 % camphene and 45.45% camphor weight ratio. Figure III.50 shows types of motion observed in a single experiment with a rod (10 mm long and 2 mm diameter) moving on the water surface in a Petri dish with 5 cm diameter.

Figure III.50(a-d) illustrate how the type of motion changes with time (see also Movie 19). Each subfigure illustrates positions of rod center (the red curve) and the rod orientation (color lines) during a 17-second-long evolution. For each subfigure, the time is indicated as the line color. The color coding is defined on the bar below the figures.

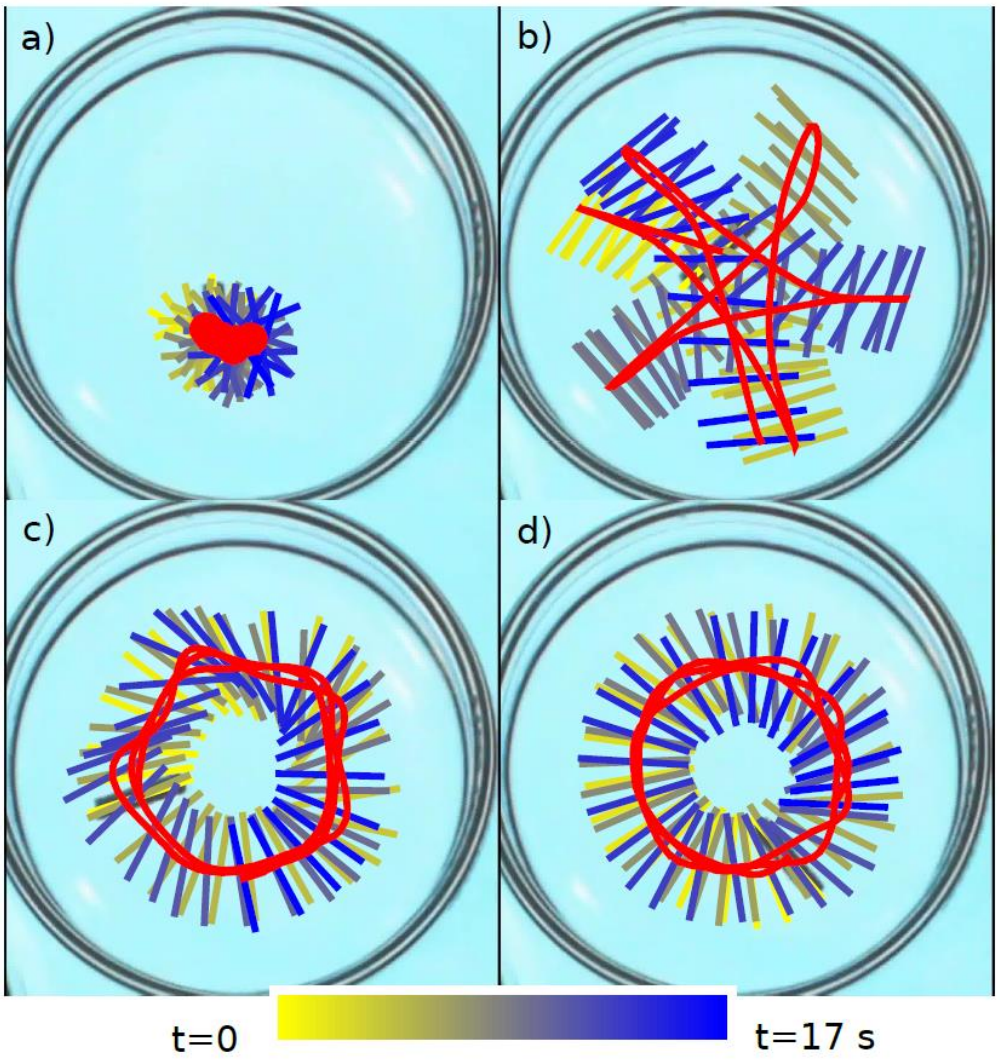

Figure III.50: A few modes of motion of 1 cm long rod in made of 10 % polypropylene, 45 % camphene and 45 % camphor in a Petri dish with the diameter of 5 cm. The red curve marks 17 s long evolution of the rod center. The lines indicate rod orientation. Time is indicated by the line color as defined by the bar below the figure. The time evolutions shown in subfigures a), b), c), and d) start 72 s, 240 s, 920 s, and 1200 s after the rod was placed on the water surface. For video see Movie 19.

After the rod is placed on the water surface, the fast rotation dominates. In this mode, the center of the rod hardly moves (cf. Figure III.50 (a), recorded $72\ s$ after the rod was placed on the surface). A few minutes later, the character of motion changes. The rod shows irregular motion in the whole dish (Figure III.50 (b), $240\ s$ after the experiment initiation). Such mode is stable for a few minutes and transforms into the rotation along the dish edge. In this mode, the angle between the rod orientation and the vector linking the dish center with the rode center does not change significantly, so the rode rotation is synchronized with rotation along the edge. Initially, the trajectory of the rod center has a polygonal shape (Figure III.50 (c), $920\ s$ after the experiment initiation), for longer times, it becomes circular (Figure III.50 (c), $1200\ s$ after the experiment initiation). The explanation of such a sequence of modes is an interesting challenge for theoretical studies.

The fact that rods can be easily made with camphene-camphor-polypropylene plastic encouraged us to study the time evolution of systems containing multiple rods. A few snapshots illustrating the evolution of 20 rods that were 1 cm long on the water surface in a Petri dish with the diameter of 12 cm are shown in Figure III.51. The rods are made of 10 % polypropylene, 45 % camphene, and 45 % camphor. The movie showing the first 4 minutes of the time evolution is included in Movie 20. In the beginning, the rods were moving individually on the surface, followed by the formation of clusters, increasing in size as time progresses.

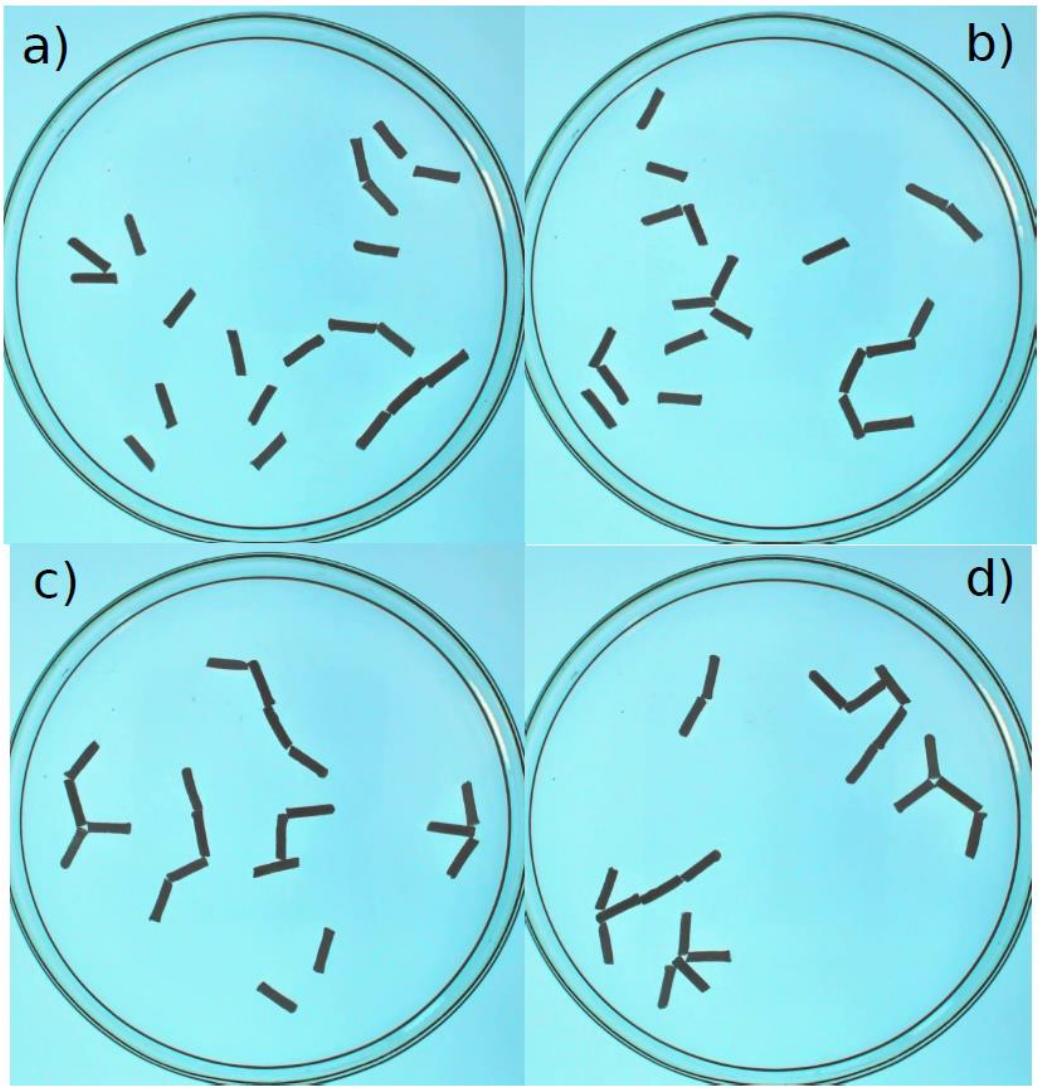

Figure III.51: The time evolution of 20 rods that were 1 cm long on the water surface in a Petri dish with the diameter of 19 cm. The rods are made of 10 % polypropylene, 45 % camphene, and 45 % camphor. The snapshots a), b), c), and d) correspond to times - 5 s, 30 s, 100 s, and 200 s after all rods were placed on the surface. The movie showing the time evolution is included in Movie 20.

It can be seen that the dominant form of rod attraction is the one between the rod ends. We also observed attraction between the end of one rod and the center of the long edge of another (Figure III.51 (c-d)). This type of attraction seems weaker than the end-to-end one

because the pairs of rods attached end-to-center are less frequently seen than those sticking at the ends. The geometry of interaction makes sense if one considers that the deposition of surface-active material from the rods is asymmetrical such that more material is deposited at the long edges than at the ends. Thus, the repulsion between rods is larger at the long edge. The clusters are dynamically changing in time. They can merge or separate into fragments. Figure III.52 illustrates the number of rods grouped in clusters of given sizes. It can be noticed that the numbers of separated rods and small clusters decrease with time, and most rods are trapped in a small number of large clusters.

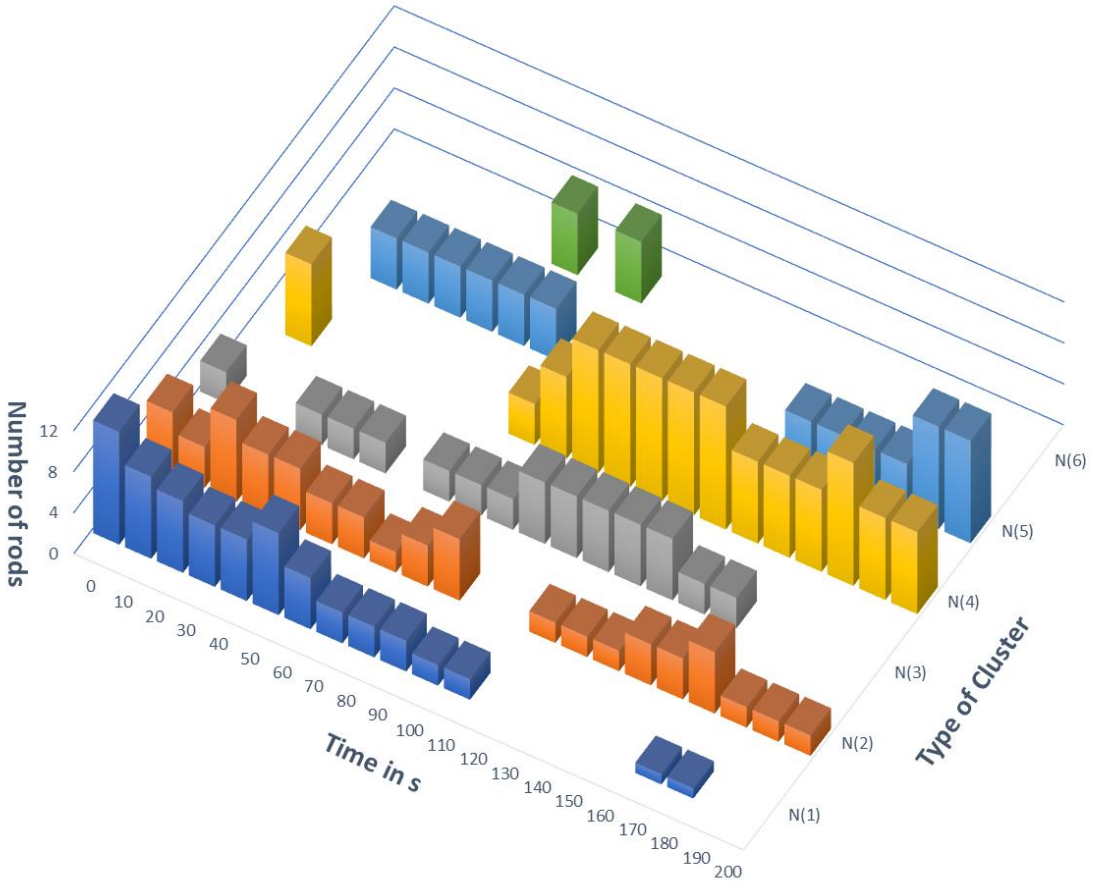

Figure III.52: The number of rods that are linked together in clusters of s given size for times in [0s, 200s] range. The results were obtained from the analysis of the Movie 20 and match Figure III.51.

III. 3.4 Polymer foam as byproduct

As described in the previous sections, the alloy described here has an unforeseen permanent state which it attains once all of the volatile components have evaporated. This soft foam-like material is made of a porous lattice of polypropylene. The density of the foam appears to

increase with an increasing polypropylene content of the homogenous precursor material. This foam has interesting properties such as a very hydrophobic surface as can be seen in Figure III.53 where a 50 µl water droplet is placed onto a cross sectional surface of the material. The contact angle appears to be large enough for it to be considered superhydrophobic[103] .

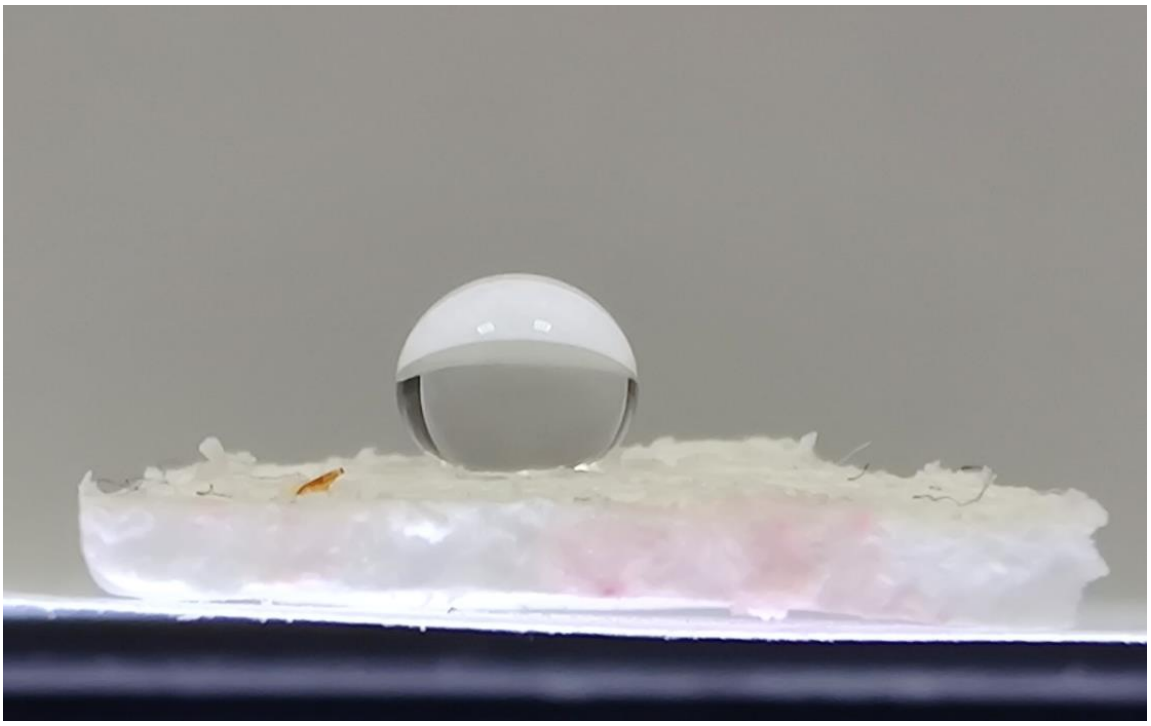

Figure III.53: 50 µl water droplet on foam sample. Large contact angle indicates that the surface is highly hydrophobic

This hydrophobicity stems from the native hydrophobicity of polypropylene[104] and the apparent roughness of the surface, which produces a sort of lotus effect[105]. This roughness/porosity is a result of polypropylene forming a scaffold within the alloy (either immediately when solidifying after mixing everything at 250° C or when the camphor and camphene evaporates). The removal of the evaporating components can be sped up by immersing the material in ethanol or acetone which will dissolve all of the camphor and camphene but not the polypropylene[104]. The foam produced this way retains an organized microscopic porous structure. Furthermore, is seems that that the pore size depends on the polypropylene concentration in the mixture as the foam becomes denser with increasing polypropylene content. We observe that, when the polypropylene concentration is increased from 5% to 10%, the size of pores is about halved as can be seen in Figure III.54.

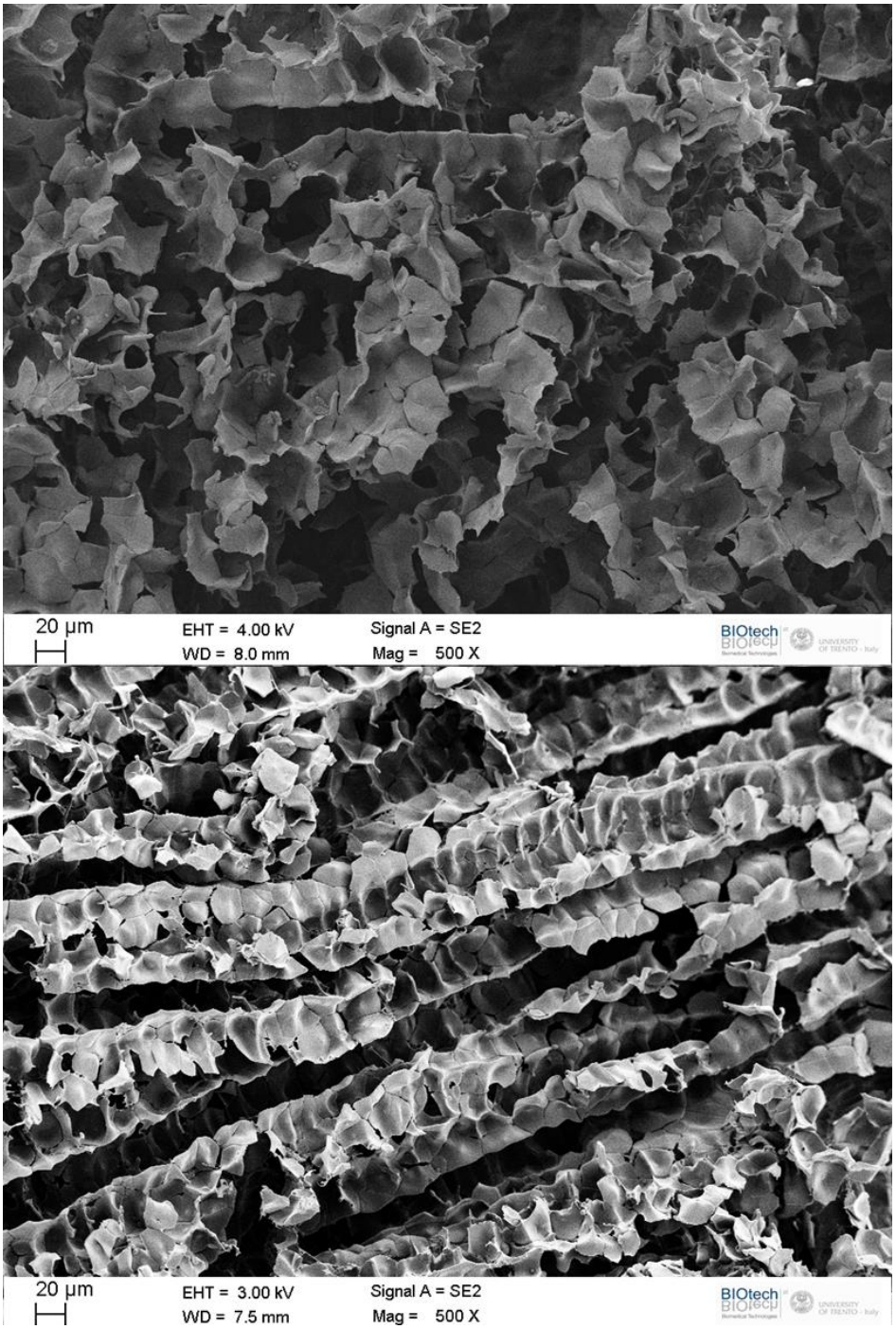

Figure III.54: Upper: Electron micrograph of a foam piece produced as described in the text. The composition was 70:30 CN:CR with 5 wt% of PP added. Magnification 500x; we observe that the porous structure is made of small platelets (size range 20-50 mm). Lower: The composition was 70:30 CN:CR with 10 wt% of PP added. Magnification: 500xWe observe unidirectional spinodal channels and the organized porous structure is made of small platelets (size range 15-40 mm).

The images reveal microscopic ordered structures resulting from spinodal decomposition[106] and composed of small polymer platelets, loosely connected to each other. The spinodal channels seem to be formed as evaporation/dissolution pathways. It appears that the micro-structure of the 10% mixture is slightly denser and more ordered at higher magnifications. We believe that this method of foam production provides an alternative to the formation of

foams using supercritical CO_2, which appears to be a more complicated and expensive method[107]. The requirement of only simple ingredients: camphor, camphene and a non-polar polymer which melts at up to 250°C could make their own polymer foams using the simple method described here. It should be mentioned that, in literature, there is a very similar method to what is described here, called thermally induced phase separation. (TIPS)[108–111], which is used to produce thin porous membranes using a slightly different methodology and with much higher polypropylene contents. Additionally, as far as we can tell, no one has combined camphor and camphene for it until now and the phase separation in our case occurs at room temperature or may be chemically assisted using solvents.

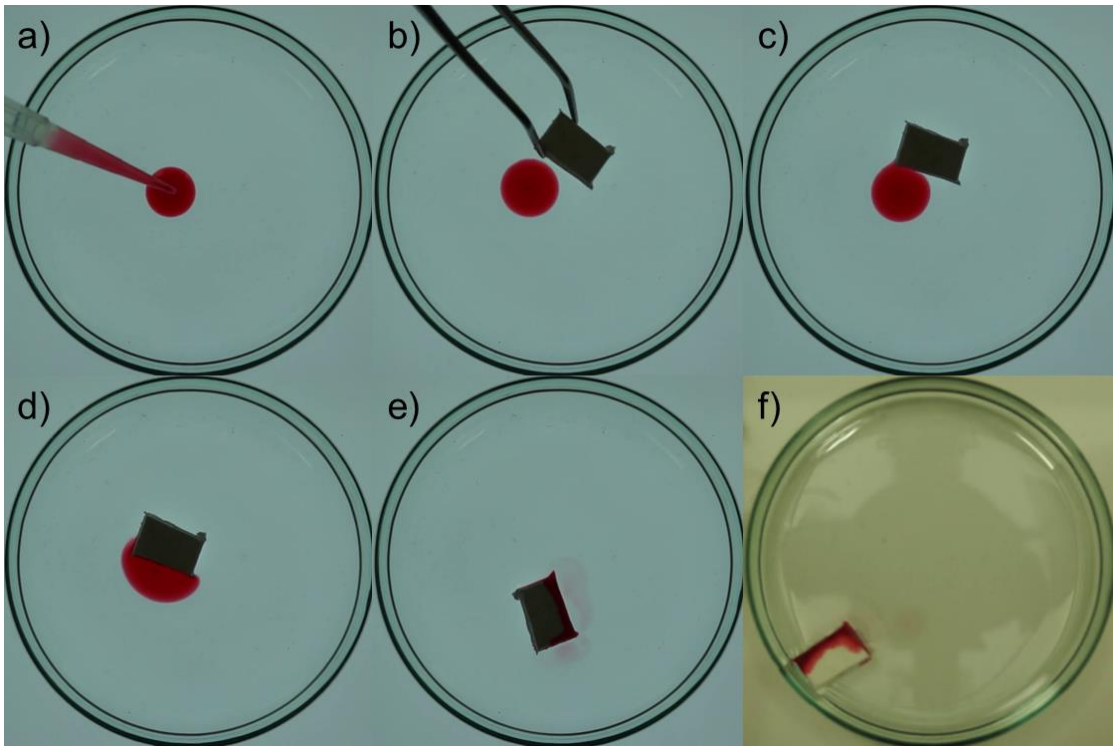

Figure III.55: Snapshots taken from Movie 21. a) A 200 microliter drop of paraffin oil, containing a red dye (Oil red O) is added to a clean water surface in a Petri dish. b) and c) A foam sample with the dimensions 0.5x1x1.5cm is placed on the surface as well. d) and e) Within less than 4 minutes, the foam sample absorbs most of the oil on the surface. In the last frame (f) the backlight is turned off so it can be seen that the foam sample is stained red due to the dye in the oil.

Due to its structure and chemical composition, the foam we made is able to very effectively absorb non-polar liquids. This is especially useful for the removal of oils from water surfaces, as is demonstrated in Figure III.55 and Movie 21. In this movie a 200µl droplet of paraffin oil stained with the dye Oil red O was added to a water surface inside a Petri dish. A foam sample made from 45% camphor, 45% camphene and 10% polypropylene mixture (the camphor and camphene have been removed) with the dimensions 0.5x1x1.5cm is placed on the surface as well. Within four minutes the foam sample is able to almost completely absorb all of the oil

from the surface and can be removed along with it. It is even possible to recover some of the oil by squeezing it out of the foam sample (will destroy the foam) or by finding an appropriate solvent to extract it. This has obvious possible applications in any industry that is interested in the separation of liquids with different polarities or other filtering processes. Additionally, the foam could be used in research: For example, during surface tension measurements where you need clean the surface of all surfactants before starting your measurement. Usually, a Teflon vacuum is used for this purpose. Exploiting the foam's affinity for non-polar liquids it could also be used as a platform for surface active non-polar liquids, similarly to filter papers [31,112]. In this case one could use the same object made of the polypropylene foam with different substances as it can be cleaned in between experiments, using most strong solvents without attacking the polypropylene foam[104].

The polypropylene foam can be mechanically manipulated without breaking easily but does get plasticly deformed i.e., is not very elastic. Another interesting point is that, before removing the evaporating components it is essentially a wax, so it can be formed into different shapes prior to washing out the camphor and camphene. We have observed that the material maintains the shape. We have had limited success turning the polymer alloy into 3D-Printer filament using a heated filament extruder but the temperature control is very tricky since the material only has a small temperature window in which it extrudes nicely. Using a very high-pressure extruder may yield more consistent results and adjustment of the component ratios may improve the temperature window of extrusion. If usable filament can be obtained, it would provide a method to print parts made of polypropylene foam. Considering that the material can be shaped by hand, this may be unnecessary though.

III. 4 Conclusions and further application

We were able to produce two different iterations of malleable self-propelled material and demonstrate the possibility of easily producing non-trivial shapes. Furthermore, it is possible to create larger quantities of shapes for the study of collective behavior of self-propelled objects. Experimentally the wax (only camphor and camphene) and the plastic (camphor, camphene and polypropylene) complement each other such that the self-propelled behavior of the latter appears to be independent of its composition, while the behavior of the wax can be controlled by changing the composition.

Considering the simple production method for both, they provide the perfect properties for experiments with self-propelled objects. The camphor-camphene-polypropylene material that can be used to make new experimental setups that can be used to obtain fast verification of

theoretical results. The stickiness of the wax makes it slightly more complicated to work with but we were able to solve this drawback though the addition of polypropylene, which, due to evaporation of camphor and camphene, leaves a passivating layer of non-sticky polypropylene on the surface. The reason why the plastic does not change its behavior with a change of composition is the formation of a microporous polypropylene scaffold spanning the whole object. This scaffold mediates the release of the surface-active components which is the reason for the unprecedented long-term activity.

The polypropylene foam left after camphor and camphene molecules have dissipated fully, has an interesting microscopic structure and can find many applications. Although for the amount of polypropylene concentration in the investigated range (5 - 10 %), we observed changes in the foam structure, they have not influenced the self-motion. However, it can be expected that for dense foams, the migration of camphor and camphene from the interior to the surface of a particle is significantly reduced thus, the self-motion speed is lower. We plan to investigate this problem and experiment with plastics characterized by higher concentrations of polypropylene. We believe the method of obtaining plastic structures through the dissipation of easily evaporating components can be applied to other polymers. The foam, which was discovered as a side product provides a possibly highly useful real-world application as is can be used for the removal of non-polar liquids from water surfaces or as superhydrophobic surfaces.

Finally, the discovered wax, plastic and foam materials represent novel functional materials that can find application in fields beyond self-propelled complex systems. For example, the plastic material could potentially be used in combination with other functional materials or substances to form hybrid objects that can fulfil certain tasks similarly to Braitenberg vehicles[80,81,113], thus providing an addition to the field of soft robotics[13,76,77].

IV Part 3: Self-propelled droplets

IV. 1 Introduction

Working on the self-propelled camphor particles and boats during the beginning of my PhD-studies provided a first glimpse into the world of active matter. Getting an overview over some of the literature dealing with self-propelled objects sparked an interest in the field of artificial life and soft active matter.

Camphor and the hybrid camphor materials described in the previous two parts are very interesting in their simplicity and therefore very suited for the study of complex behavior. Soft active matter in the form of droplets that move on a water surface[51,59,114,115] , floating in the bulk of a liquid or on the bottom of a dish[13,53,56,70,116,117] or even in the absence of water[63,118] retain similar propulsion mechanisms based in physicochemical principles such as Marangoni flow and convection[15,16,56,97,119,120]. Apart from the aspect of movement, many droplet systems also include the aspect of responsiveness to the surroundings because their propulsion relies on the interaction between the droplet and its surrounding area, inducing surface tension gradients along the droplet-water interface which in then triggers an internal convection, propelling the droplet[54,68]. Therefore, systems based on processes occurring at the liquid-liquid interface appear more lifelike than our condensed and hybrid matter systems, that merely deposit surface-active material to a liquid. Of course, this is because life as we know it is soft matter and for good reason, as there can occur many more chemical and physical interactions at a liquid-liquid boundary (life as we know it occurs based on liquid-liquid interfaces that create a partition and an exchange of all kinds of solvents). While this makes soft active matter very interesting, it is also much more complicated because of the abundance of possible systems as well as completely unforeseen physicochemical interactions can influence the system. In this part I present my contribution to the world of soft active matter which includes the development of a new self-propelled droplet system and a further exploration of a known system from literature which led to the discovery a system in which two droplets have a direct influence on each other.

IV. 2 The surprising effect of a dye on droplet behavior

IV. 2.1 Design of a new droplet system based on camphor, paraffin and Oil red O

Part of the work described in this section was published as a peer-reviewed article in the conference proceedings of the 2018 Conference on Artificial Life, ALIFE 2018 (Tokyo)[55]. The inspiration to come up with another droplet system came from visiting the European Conference for Artificial Life in Lyon 2017 and learning about the work being done on soft-matter self-propelled systems. The work presented here shows how unforeseen interactions can lead to interesting results and ultimately new collaborations with researchers who are affected by these new results.

While working on the camphor-propelled boat system, I tried to come up with a system that is a soft-matter version of the self-propelled camphor particle. The goal was to see if such a camphor-droplet would: 1. be self-propelled and 2. be in any way responsive to the other chemicals in the system. The resulting droplet system is very straight forward. Camphor was kept as the surface-active substance, so we would either need to come up with a way to liquify camphor at room temperature or to find an inert solvent. Camphor itself is a non-polar molecule and not very soluble in water (up to 1.2 g/l[29]) so any non-polar solvent should be sufficient to dissolve camphor. Due to immediate availability and good suitability, paraffin oil was chosen. It is a slightly viscous liquid composed of a mixture of long-chained saturated hydrocarbons. It has a density of 0.827-0.890 g/ml at 20°C, is not volatile and does not mix or interact with water [121]. Camphor turns out to be very soluble in paraffin oil at up to 150mg/ml. Using this simple mixture droplets are obtained which are not driven by internal convection but, just like camphor particles, create a surface flow triggered by a surface tension gradient[23]. The behavior of such droplets is complex and evolves depending on time, droplet composition and initial conditions. The types of behaviors we observe include translation, morphing (shape change), rapid explosive splitting and coalescence. The latter, was especially observed at high concentrations of camphor over 15mg/mL where camphor is being deposited at rates and in such quantities that it disturbs the droplet to a point where it splits, creating a larger interfacial area, which further speeds up the deposition. This leads to a fast-paced cascade of these events repeating, which lasts until enough camphor has dissipated to lessen this chain reaction. This whole process only takes a few seconds after which the smaller droplets start coalescing into larger morphing droplets. At lower concentrations we observe simple movement with complex trajectories just as observed for camphor particles. We do not

observe much deformation of the droplets except for the extreme case of explosive splitting at high camphor concentrations. All this could be nicely illustrated in an attached movie or a figure, if it was not for the fact that the droplets are just as transparent as the water they swim on and are therefore hardly distinguishable on a photo or film. For that reason, we added a dye to our new droplet system, which would create a contrast between the droplet and the aqueous phase. The dye we chose, due to availability in the lab, was Oil red O (OrO, See Figure IV.1).

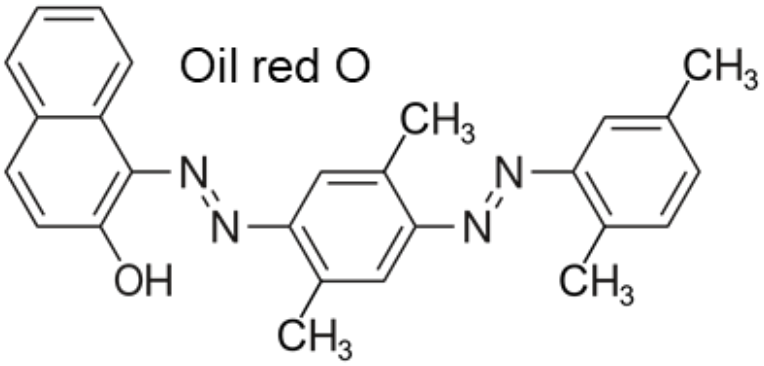

Figure IV.1: Structure of Oil red O dye. Illustration from Wikipedia [122].

It is a dye that is used to stain fatty tissue in medical research but also is used as a visual aid to color droplets for the purpose of tracking and quantifying the behavior[10,79] using image analysis software. As it is insoluble in water, it is assumed to be completely inert in such circumstances.

During initial experiments with paraffin droplets containing camphor as well as the dye, an abundance of the dye was added to the solution. Not controlling the dye concentration led to very inconsistent behavior of different droplets with equivalent concentrations of camphor. This led to the suspicion that the concentration of the dye has a significant effect on the initial behavior and the time evolution of the droplet. For instance, a 50 ul droplet of paraffin oil containing 7.5mg/ml camphor, exhibits stable steady movement on a water surface without any change in the droplets size or shape. When repeating such an experiment using a droplet with the same amount of camphor but added dye in excess the behavior became much more complex: Initially the droplet area expanded significantly before forming long tendrils that elongated until spread over a large area in a distribution that resembled a Turing-pattern[82,123]. As elongation progressed, the tendrils split into smaller droplets that slowly started coalescing before reaching a state without much further activity. The timescale of this whole process was less than a minute. In Figure IV.2 this process in illustrated using timestamped snapshots of the described behavior (See Movie 22).

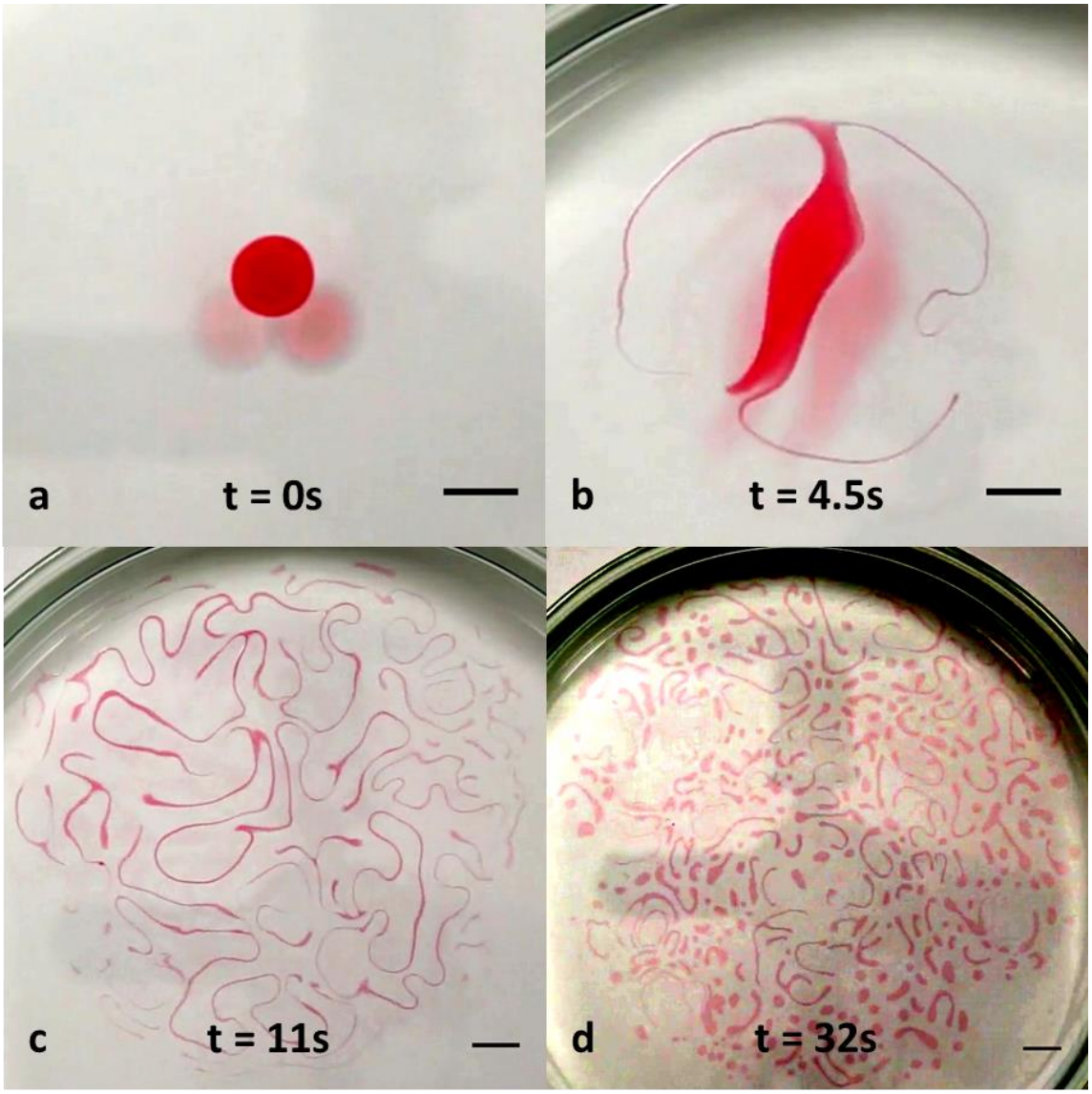

Figure IV.2: Droplet containing 7,5 mg/ml camphor and surplus of Oil red O dye in paraffin placed on a water surface inside a 19 cm diameter glass Petri dish. Snapshots are taken at different times: 0s, 4.5s, 11s and 32s as shown in a, b, c and d respectively. The different snapshots show the very complex evolution of the droplets at different stages. Scale bars = 1cm. For video see Movie 22.

This clearly confirmed the suspicion that the dye has an influence on the interaction of the droplet with the water surface and since this unexpected behavior was quite fascinating, we decided to start a series of experiments observing and categorizing the droplet behavior at different concentrations of camphor and Oil red O.

IV. 2.1.1 Phenomenological description of camphor-paraffin-droplets behavior influenced by camphor and Oil red O content

We produced the following stock solutions: **1.** 150 mg/ml commercially available (1R)-(+)-Camphor (98% purity, Sigma-Aldrich) in paraffin oil (puriss., CAS-Number: 8012-95-1, Sigma-

Aldrich), **2.** 1.5 mg/ml Oil red O (BioReagent, Sigma-Aldrich) paraffin oil and **3.** 150mg/ml camphor and 1.5mg/ml Oil red O in paraffin oil. Stock solutions were prepared in bulk on a hotplate at 50◦C with a magnetic stirrer. From these three stock solutions as well as pure paraffin oil we could make samples at any combination of concentrations. Samples were prepared in 1.5 ml Eppendorf microtubes and mixed on a vortex. All experiments were performed at 22±2 ◦C in a 19cm diameter glass Petri Dish containing 150 ml water purified using a Millipore ELIX5 system. Amounts of oil mixture added as singe droplet were either 50 or 200 µl. The time evolution of the system was recorded for a minimum of 20 minutes from above using a mounted digital camera (NEX VG20EH, SONY) and then digitalized, edited and analyzed using on a computer using the ffmpeg and ImageJ software. The entire system, including experiment and camera, was enclosed to eliminate confounding effects from air flow in the laboratory.

In order to assess the acquired footage, a set of distinct behaviors was chosen by which the behavior of differently composed droplets could be categorized over time. We assigned symbols $0, A, B, C, D, E, F$ and G to increasingly complex stages of droplet evolution.

The behavior we assigned the symbol, 0, is no behavior at all and is only expected to occur when using a droplet of pure paraffin or at very low concentrations of camphor and Oil red O. With the symbol A, we denote pure expansion of a droplet. This type of behavior can be attributed mostly to the presence of the dye in the droplet. In Figure IV.3 (two snapshots from Movie 23) we depict this behavior by comparing two a pure paraffin droplet with a paraffin droplet containing only Oil red O at a high concentration (1.5mg/ml). Both droplets have a volume of 50 ul and in Figure IV.3a it can be seen that already at the time when the red droplet has been deposited it has a slightly bigger area than the clear droplet. The red droplet keeps expanding until it forms a circular film on the water surface within ca. 35 second as is depicted in Figure IV.3b**.**

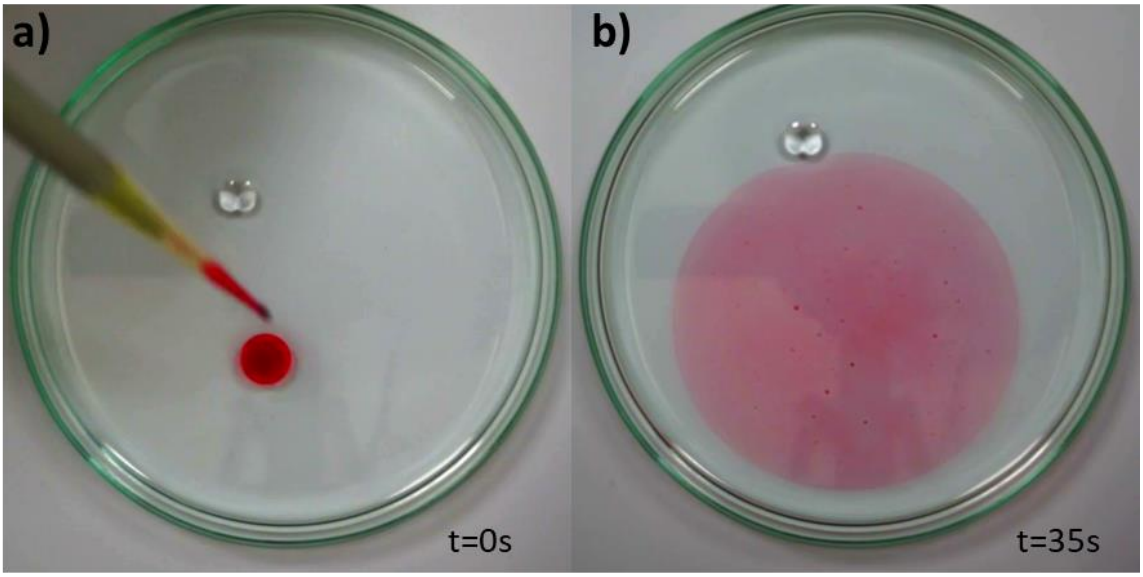

Figure IV.3: Example of behavior 0 and A. The transparent droplet does not expand and is displaced only due to the expansion of the other. Change from a) to b) shows expansion of the red droplet into a thin layer on the water surface without displacement of the center of mass within 35seconds.

Purely translatory behavior is assigned to the symbol B. In such a case a droplet moves while maintaining its size and shape. In this case we distinguish between two types of B: simple (B) describes continuous movement where a droplet moves for several second without stopping, while (B_i) describes intermittent motion where a droplet moves, but slows down to a halt periodically. A graphical representation of these behaviors is depicted in Figure IV.4 where we have extracted single frames from a movie. Frames, one second apart, are then superimposed in one image to show the displacement of the droplet at even time steps. Continuous motion (B) is depicted in Figure IV.4a (Movie 24) where a 20 second clip of a droplet moving along the dish edge is depicted in the way described above. It can be clearly seen that the distances between the positions, one second apart, are even, which suggests a constant speed. In Figure IV.4b (Movie 25) the same has been done with a 50 second clip of intermittent motion (B_i). It can be seen that the distances between the time-resolved positions periodically become very small, which indicates a slowing of the droplet.

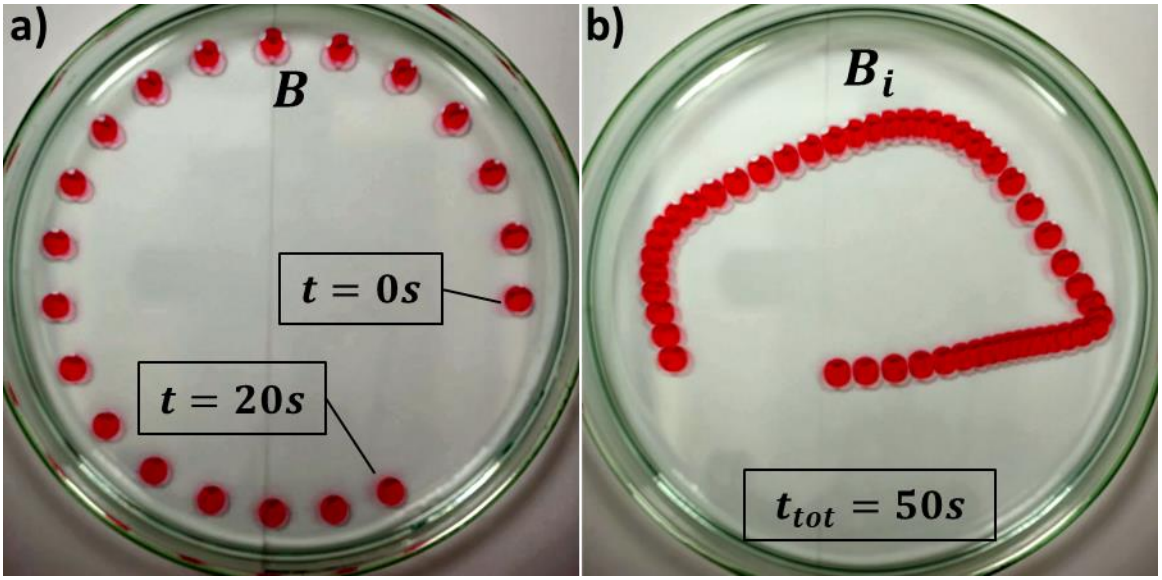

Figure IV.4: Graphical representation of movement type B (a) and B_i (b). Single frames, one second apart, are superimposed to represent continuous movement along the dish edge in (a) and intermittent motion in (b). The intermittent part is visible through the distances between the droplet frames changing. Small distance means slow movement, larger distances mean faster movement. It can also be seen that in neither case does the droplet deform significantly during movement.

The next step in complexity, C, combines motion with deformation. This symbol is assigned when we observe droplet deformation, in the form of elongation perpendicular to the velocity, during motion. Again, we distinguish between two sub-categories. C_c describes the constant elongation of a droplet during continuous movement and is depicted in Figure IV.5a (Movie 26). We observe a constant speed but also that the elongation remains perpendicular to the velocity. The other subcategory, C_o, is oscillatory elongation that occurs during intermittent motion of some droplets and is not constant as the droplet returns to a circular shape at standstill (See Figure IV.5b (Movie 27)). The oscillatory motion is quite interesting in regards to its shape, trajectory and speed. As can be seen in Figure IV.5b, the droplet forms a crescent shape during the point in motion with the highest velocity. In fact, this is why we looked at a crescent shape motion with the plastic-material in Part 2 Section III. 2.1.2. There we observe that the surface tension gradient induced on the convex side may be larger than the one on the concave side. This may explain why the droplet in this case starts to slow down and stop just after the point of highest speed and crescent elongation.

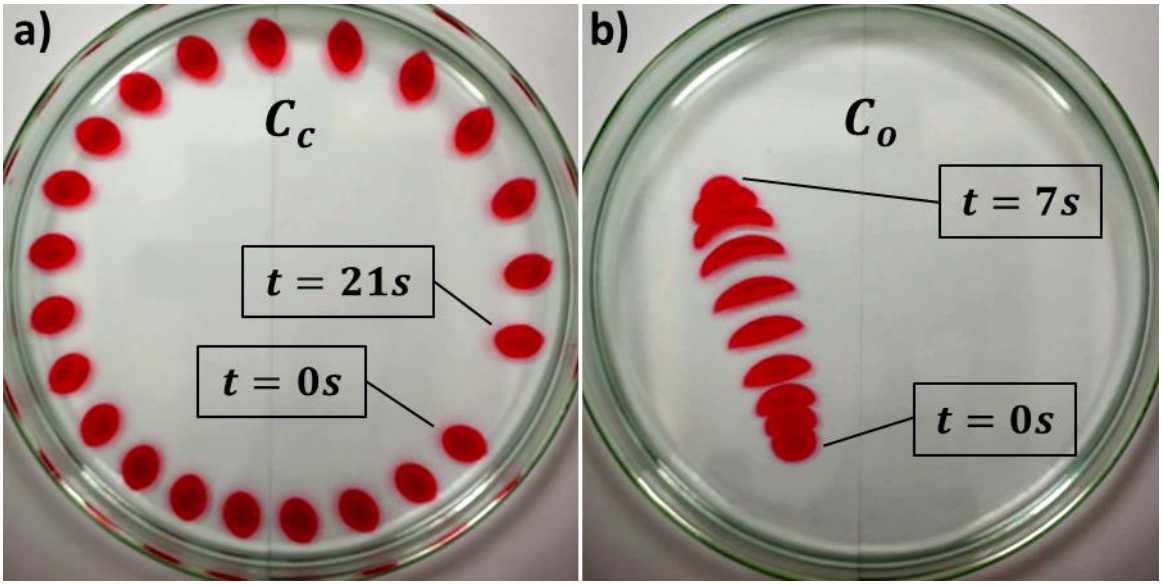

Figure IV.5: Droplet elongates on the axis perpendicular to its velocity. The change can reach a continuous steady state, C_c, in (a) or oscillate (C_o) in an intermittent motion combined with an oscillating elongation in (b).

In category D, we have behaviors that combine motion, deformation and expansion. Here we observe significant elongation triggered by periodic movement (or rather surface flow triggered by deposited camphor) while the droplet loses any symmetry due to that anisotropic expansion. This category is assigned as soon as we observe an elongation of the droplet where its arms extend by an order of magnitude larger than the original droplet diameter. An example of this is depicted in Figure IV.6 (Movie 28) where two snapshots, 15 seconds apart, are superimposed and display how the droplet forms a very long arm. This type of behavior could best be described as a sort of 2-dimensional lava lamp.

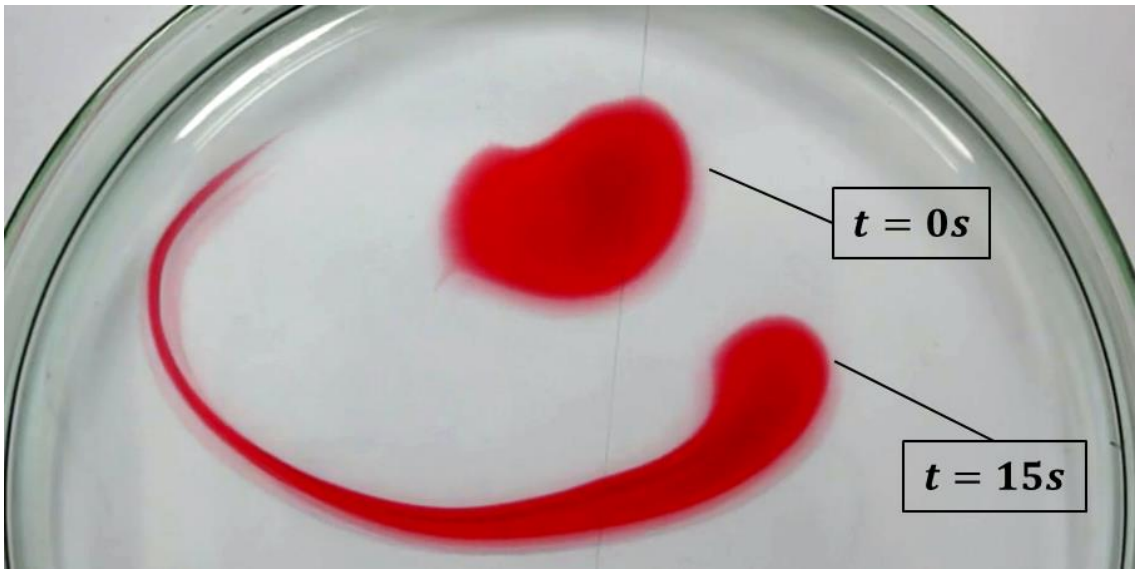

Figure IV.6: Graphical representation of movement type D. The droplet periodically elongates, its arms extending by an order of magnitude larger than the original droplet diameter. No droplets separate from the extension.

When the elongation of arms, described in the previous category, gets to a certain magnitude, we observe smaller droplets splitting off from the original droplet. This type of behavior is

represented by the symbol E. In Figure IV.7 (Movie 29) several snapshots of a movie containing such behavior are superimposed. It can be seen how the droplet forms a long arm during movement within one second. By the following second, part of the arm close to the tip has started to thin out. The last snapshot, four seconds later, shows that a small droplet has split off from the original one. Behavior E can be subcategorized into splitting of droplets occurring during an oscillatory type motion (E) or during continuous motion (E_C).

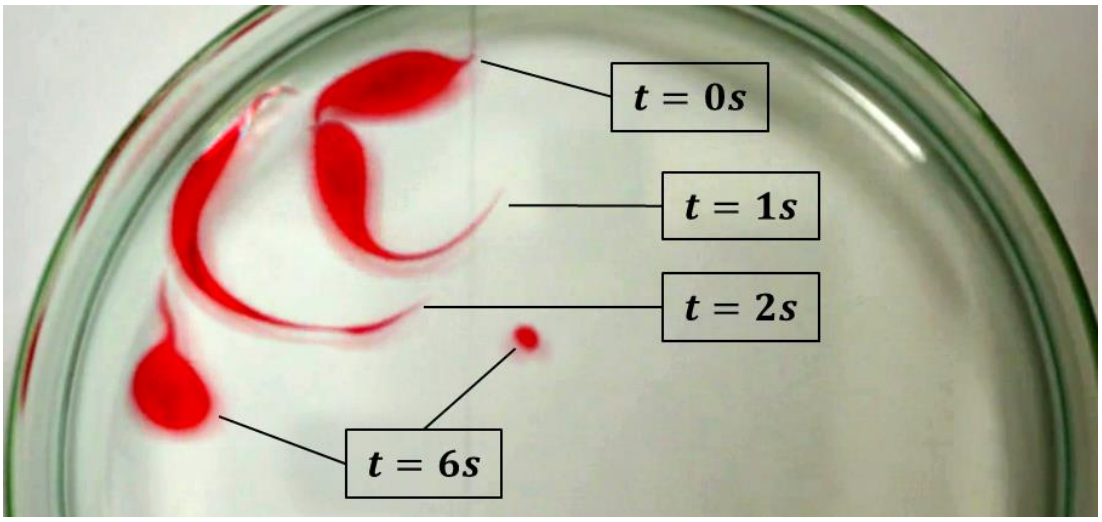

Figure IV.7: Graphical representation of movement type E. The Droplet develops long arms from which smaller droplets occasionally separate. This occurs while the droplet is either moving in an oscillatory manner (E) or in a steady state (E_c).

Category F denotes the behavior described earlier, where the droplet rapidly forms multiple very long arms that arrange themselves in a maze-like structure just before splitting into many small droplets. Another example of this is depicted in Figure IV.8 (Movie 30). This type of behavior could be considered the most complex one at humanly visible timescales.

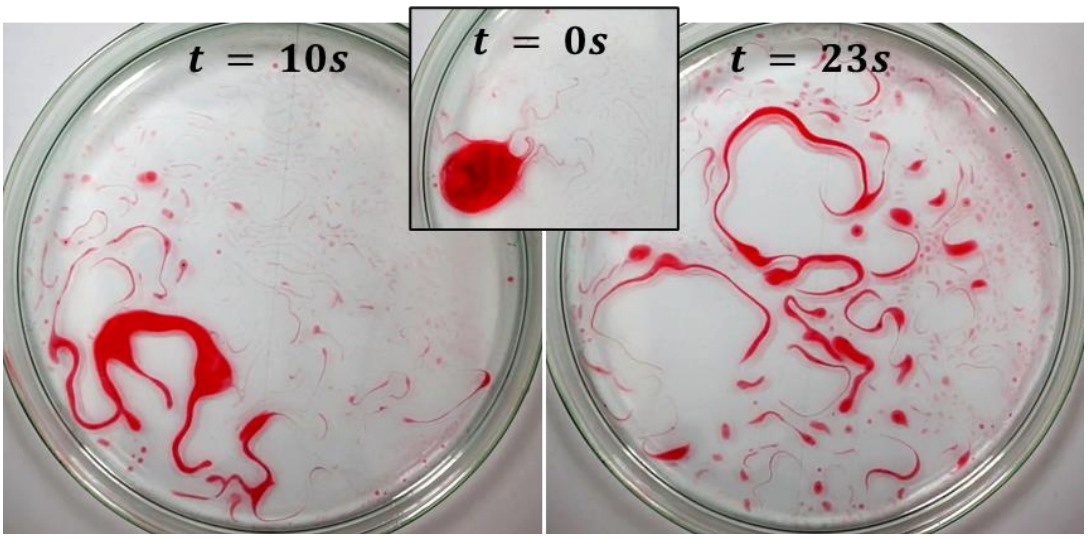

Figure IV.8: Graphical representation of behavior F. The droplet develops multiple very long arms, which arrange themselves in a maze-like structure before splitting into many smaller droplets.

Finally, the last category, G, is also assigned to previously described behavior. Namely, the

rapid and violent spread into a thin layer which quickly coalesces into many small droplets. See Figure IV.9 (Movie 31) for a graphical representation of such behavior.

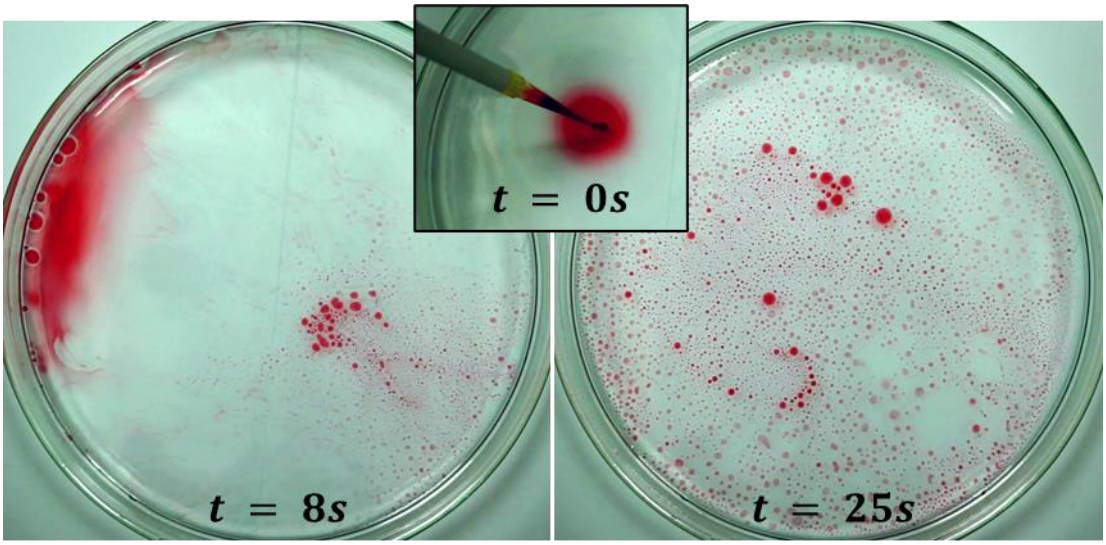

Figure IV.9: Graphical representation of behavior G. Upon contact with the water surface, the droplet spreads out violently in a thin layer. At the edge of the layer small droplets coalesce from it and spread over the entire area.

IV. 2.1.2 Logical description of camphor-OrO-paraffin droplets over time

Using the categories that were introduced in the previous section, we can quantify the behavior of paraffin droplets at different volumes and concentrations of camphor and Oil red O over time. We restrict our analysis to the time evolution of the single initial droplet added to the water surface with a timescale of up to 20 minutes. During the analysis, we use the symbol C^t to indicate that the evolution matching category, X, was maintained for t seconds for very rapid processes, we use the symbol $X^{<t}$ to describe that the X category was maintained for less than t seconds. If no time is given, the state lasted until the end of the experiment at $t = 20min$. Furthermore, if the primary droplet becomes indistinguishable from any secondary offspring before the end of the experiment, we assign the symbol T. Thus, we gain a string of letters and numbers that describe the time evolution of a given droplet. A string with higher symbols (G being the highest and 0 the lowest) would be considered more complex than one with lower symbols. Additionally, considering time evolution, a longer string would also constitute higher complexity. This is because a droplet with an evolution that only contains one but complex behavior could be considered less complex than one that goes through several increasingly complex behaviors over the course of the observed 20-minute timeframe. The strings resulting from droplet volumes of 50 and 200 µl are presented in Tables 0.1 and 0.2.

Table IV.1: The categories of motion observed during time evolution of 50µl droplets at different ratios of camphor to dye. Symbols 1 and 2 indicate results of separate experiments. Longer strings with "higher" letters indicate more complex behavior.

Dye conc. (mg/ml) \ Camphor conc. (mg/ml)	150	7.5	1.8	0
1.5	$G^{<10}T$	1:$B^{20}C_o^{80}D^{40}E^{60}D^{50}E^{360}T$ 2: $C^4D^5F^{15}T$	A	A
0.75	-	1: $B^{355}C_c^{120}C_o^{120}D^{480}E$ 2: $B^{260}C_c^{150}E_c$	-	A
0.35	$G^{<10}T$	1:$B^{1140}B_i$ 2:$B^{1055}B_i^{50}C_o$	0	0
0.19	-	$B^{685}B_i$	-	0
0.1	$G^{<10}T$	B_i	0	0
0	$G^{<10}T$	B_i	0	0

Table IV.2: The categories of motion observed during time evolution of 200µl droplets at different ratios of camphor to dye. Longer strings with "higher" letters indicate more complex behavior.

Dye conc. (mg/ml) \ Camphor conc. (mg/ml)	150	7.5	1.8	0
1.5	$G^{<10}T$	$A^4G^2F^{21}E^{20}T$	$A^3B_i^{200}C_o^{360}D^{480}E$	A
0.35	$G^{<10}T$	B	B_i	A
0.1	$G^{<10}T$	B	B_i	0
0	$G^{<10}T$	B	B	0

Seeing as the category G behavior persists regardless of dye concentration, we show that at very high concentrations of camphor, the effect of camphor dominates over the influence that Oil red O has on the droplet behavior. In this case a large amount of camphor was released from the oil in a very short time, saturating the water surface with camphor and thereby approaching a steady state at which the camphor supply rate was close to the evaporation rate. The resulting lowered surface tension and overabundance of the camphor stabilizes the oil phase in form of small droplets. The supply rate of camphor rapidly drops off as multiple small droplets with a larger surface to volume ratio can dissipate more of the available

dissolved camphor. At this point we observe coalescence of the droplets. A camphor concentration of 7.5mg/ml seems to be near the optimal point for self-propelled motion as we observe the most motile behaviors at this concentration. At the same time the column best shows the effect of the dye since the behavior becomes drastically more complex with higher concentrations of Oil red O. At lower concentrations of camphor, we show that the volume of the droplet also has a significant influence on the droplet evolution. For 50ul in Table IV.1 at 1.8mg/ml of camphor we see no droplet activity except expansion at high dye concentrations whereas for 200ul in Table IV.2 we observe B-behavior for low dye concentrations and more complex behavior at 1.5mg/ml of Oil red O.

At a later stage we performed repeated and additional experiments to fill out some of the gaps for the 50ul behavior and to confirm reproducibility. The diagram depicted in Figure IV.10 shows an overview for the most complex observed behaviors observed for each of the tested concentration pair. With this diagram it is easy to reproduce any of the behaviors, taking into account possible systematic errors that may shift the landscape slightly. In the cases where it shows X/Y, we were not certain if it was one or the other behavior but are leaning towards the aforementioned. These follow-up experiments also show that there is no considerable change of behavior above 15 mg/ml of camphor as we already here see the same behavior as for 150mg/ml.

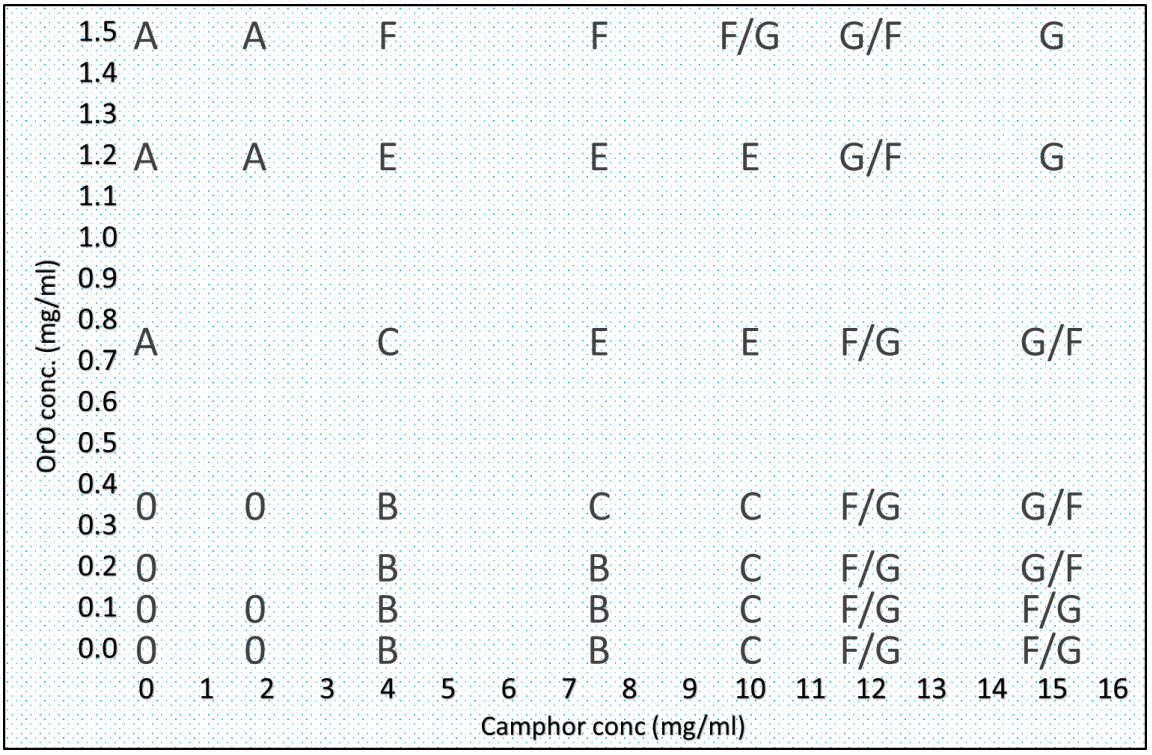

Figure IV.10: Diagram of droplet behaviors depending on the droplet composition. In the cases where it shows X/Y it means we were not certain if it was one or the other behavior but are leaning towards the aforementioned.

IV. 2.2 Experimental analysis of interfacial dynamics for the camphor-OrO-paraffin droplets

We have established that a paraffin droplet containing camphor and/or Oil red O, depending on concentrations of the two added components and also the volume, can have very complex but predictable behaviors. To explain these behaviors, we have to look at how the components interact with the droplet and the environment. The mechanism of movement due to deposition of camphor onto the water surface is well known[124] and has also been described in Part 1. We have shown that paraffin oil can act as a vessel for camphor, similarly to mixing it with camphene to make it malleable as described in the previous part. One advantage of having camphor completely dissolved in a medium that does not interact with the water surface, is that there is no direct contact of solid camphor with the water surface such that one can modulate the camphor deposition rate by concentration and droplet size, thus controlling the behavior. The effect of Oil red O was unforeseen because, as stated earlier, it was chosen partly because it is not a polar or amphiphilic molecule and should therefore have no interaction with the water phase or the surface of the oil phase. The intention was that it would merely act as a pigment in the oil, creating a contrast between the droplet and the water. We saw significant changes in behavior only at very high concentrations of the dye, close to the saturation point, but even at lower concentrations it could induce subtle differences in droplet behavior. Furthermore, other droplet experiments occasionally use concentrations of Oil red O at similar magnitudes.

From the observations made during the behavioral study it seems that the main effect of the dye on the droplets is that it lets them expand and deform. This indicates that the presence of Oil red O lowers the tension at one or several interfaces. Another explanation could be that the dye forms a precursor layer on the water with lowered surface tension on which the oil could spread. To investigate this, we measured the interfacial and surface tensions involved in this system.

The first round of experiments was performed using a pendant droplet tensiometer (See Section VI. 1.3.2 in the Experimental part). A dilution series of paraffin oil containing Oil red O was prepared. For the measurement of interfacial tension between the lower density oil phase and the water we had to use the inverted pendant droplet method, where a hooked syringe is lowered into a water filled cuvette such that the syringe opening points upwards and the droplet can "hang" upwards. Two measurements were performed for each sample at concentrations of $0, 0.1, 0.25, 0.5, 0.75, 1.0$ and $1.5\ mg/ml$ of Oil red O in paraffin oil. The

average initial interfacial tension for each sample is plotted as a function of Oil red O concentration in Figure IV.11. The plot clearly shows that an increase in Oil red O concentration lowers the interfacial tension.

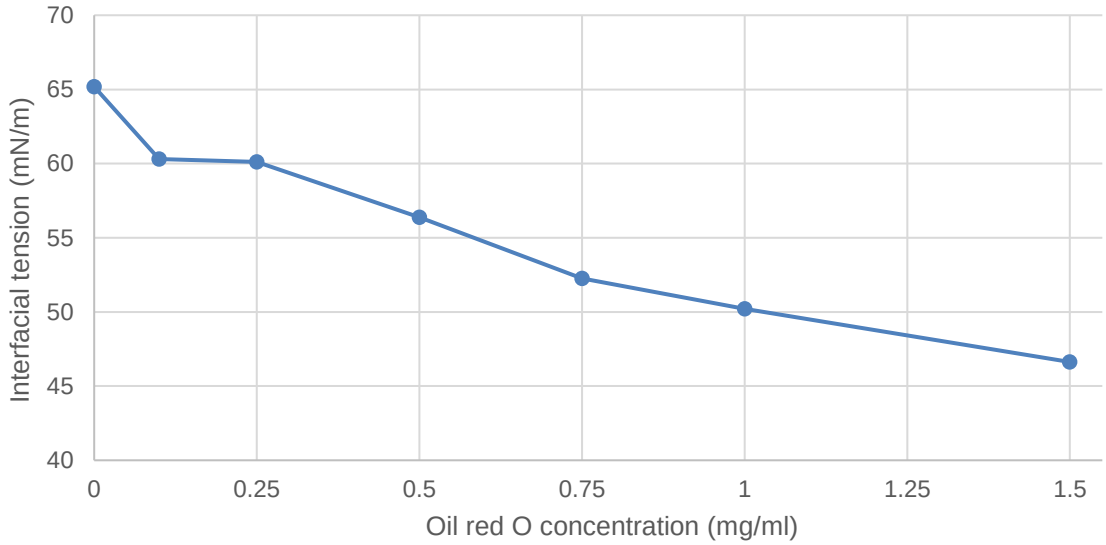

Figure IV.11: Plot of averages interfacial tensions between water and paraffin oil as a function of the concentration of Oil red O in the paraffin.

Another thing which was noticeable from these experiments was that the interfacial tension lowered over time as the droplet was left in the water. This was even the case for the pure paraffin oil sample (could be instrument error or impurities in the system). However, with increasing dye concentration this decrease becomes more pronounced as can be seen in Figure IV.12 where the time curve of individual measurements at different concentrations of Oil red O are compared. It can be seen that even though there is some decrease in the pure sample, it only changes by ca. 1 mN/m over 1000 seconds. At 0.75mg/ml we see that the interfacial tension decreases by ca. 3 mN/m in less than 600 seconds. Finally, at 1.5 mg/ml we measured it for a longer time and see that the interfacial tension decreased by ca. 5 mN/m in 1500 seconds. The last curve shows us that the decrease seems to be exponential and comparing it with other results over 0.25 mg/ml of Oil red O, the decay factor seems to be very similar (at least according to the limited data), while the initial value is lower with increasing concentration. If this is not due to the instrument or user (at lower concentrations the decay factor seems different) then it could indicate that some process is occurring at the interface. It could be an aggregation of dye at the interface.

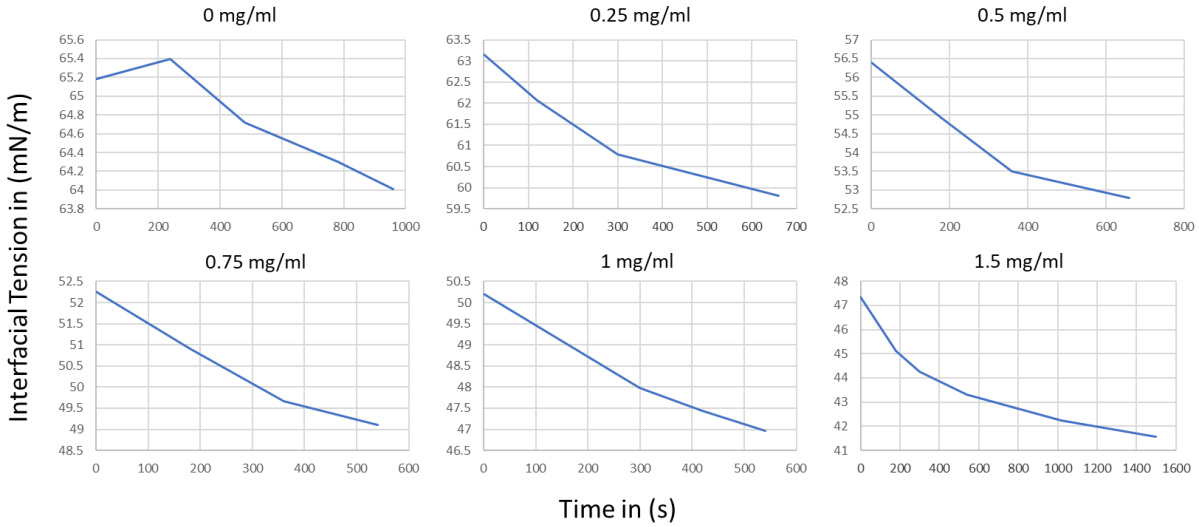

Figure IV.12: Individual time resolved measurements of oil/water interfacial tensions at different concentrations of Oil red O. The measurements show that there is an initial instant decreased value of interfacial tension which then decreases even further over time. This effect increases as well with an increase in the concentration of Oil red O.

The surface tension of paraffin oil with and without dye was measured as a reference using the standard pendant droplet method and as can be seen in Figure IV.13, there is no difference between a sample containing no dye and one saturated with dye. Furthermore, the oil-air interface does not change over time as it did with the water immersed droplet. Since the dye is not soluble in water, we did not measure the surface tension of water at this time and with that method.

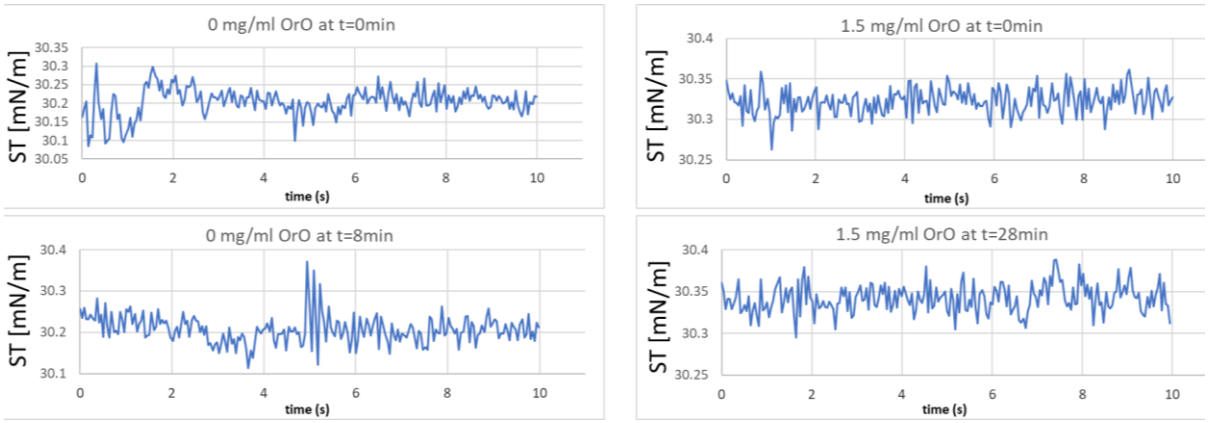

Figure IV.13: The surface tension of the paraffin droplet in air was measured at two different concentrations of Oil red O (0 and 1.5 mg/ml). As can be seen from the plots, it is unchanged by addition of high concentrations of Oil red O.

In order to confirm the results obtained with the pendant droplet method we also tested surface and interfacial tensions of this system using the Wilhelmy-plate method (See Section VI. 1.3.1 in the Experimental part). This was done using the balance of a Langmuir-Blodgett trough as well as on a dedicated surface tensiometer. For the LB-trough, two types of probes were available: Filter paper cut into a small rectangle or a homemade Platinum plate. Samples of pure water, water saturated with paraffin oil, water saturated with camphor and water saturated with Oil red O were prepared for this purpose. The saturated samples were created

by adding excess of the chosen substance to a 15ml Polypropylene Falcon centrifuge tube filled with MilliQ water. The tubes were left for several days and thoroughly stirred using a vortexer as well as a sonication bath regularly. Samples were then extracted from the bulk using a pipette. As expected, paraffin had no effect on the water surface tension while camphor saturated water had a reduced surface tension of 60±1mN/m. The dye-saturated water also did not show any change in several measurements except in two measurements performed using the platinum probe where the initial surface tension value was 52mN/m and increased to ca 66mN/m after cleaning the surface with suction. These results could not be reproduced afterwards, so it may have been due to other contaminations. The surface tension measurements of paraffin oil made using the pendant droplet method could also be confirmed. We measured 30±3 mN/m (using several instruments and probes) regardless of Oil red O concentration. Using the Langmuir-Blodgett trough we measured a surface pressure isotherm of Oil red O on water. The same was done for dyes that have a similar chemical structure to Oil red O but do not have the same effect on a paraffin droplet on water at equivalent concentrations. Sudan IV for example (See comparison in Figure IV.14).

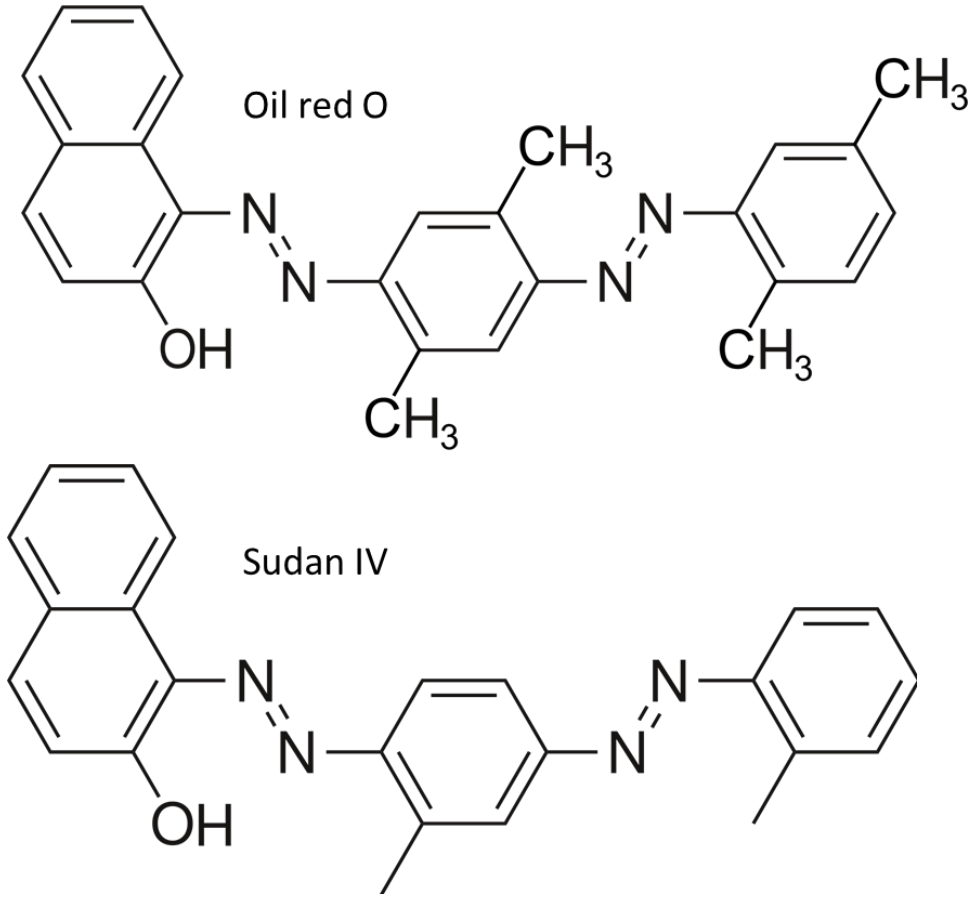

Figure IV.14: Comparison of Oil red O (top) and Sudan IV (bottom). The structure formula is very similar as Sudan IV is merely missing two methyl groups compared to Oil red O.

The Isotherms of Oil red O and Sudan IV were performed by adding the dyes to a water

surface as a drop dissolved in chloroform such that the number of molecules added to the surface is known. Once the dyes have been allowed to spread while the chloroform evaporates, a barrier is reducing the surface area of the trough while the surface pressure is measured using a Wilhelmy-plate. The two Isotherms are depicted in Figure IV.15. These results, to a certain extent, indicate that Oil red O interacts with a water surface in a different way than Sudan IV as the surface pressure has an initial early increase followed by a plateau with slow increase which could mean that there is ordering taking place on the surface whereas for Sudan IV it looks much more like sheets of crystalline dye floating on the surface and increasing pressure when colliding (first peak) and eventually interdigitating (following plateau). But the Isotherm of Oil red O does not clearly exclude such a mechanism either even though the surface activity is supported by the fact that the surface pressure curve for Oil red O looked the same in several experiments. From other tensiometric results however it seems that Oil red O does not interact with the water surface and only gets into clear contact with it when there is a non-polar solvent acting as intermediary (which of course is the case for the droplets).

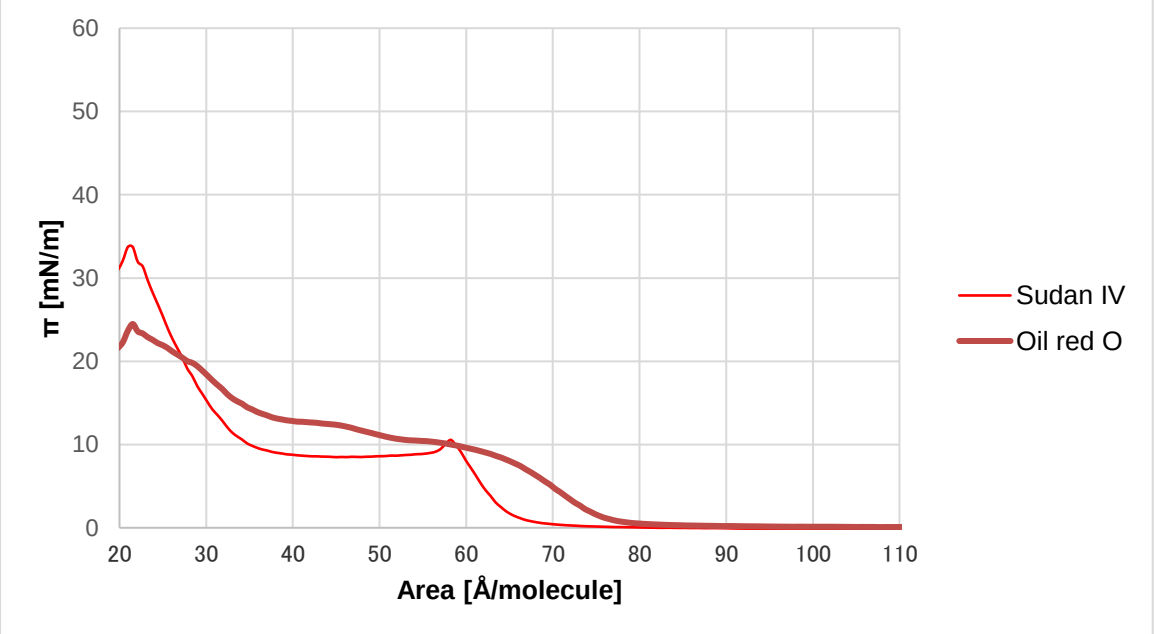

Figure IV.15: Surface pressure measurement as a function of decreasing area. The curve for Oil red O (green) indicates that there is a possible shift in orientation going on (especially as several experiments yield the same curve). Sudan IV (red curve) is shown as a comparison and behaves more like a crystalline sheet the gets compressed and eventually overlaps.

The question remains: What exactly occurs at the oil/water interface in the presence of Oil red O? At this point it cannot be said for sure. Oil red O has a single hydroxy group that could potentially interact with an aqueous phase via hydrogen bonds and we have clearly shown that the oil-water interfacial tension is lowered by the dye so the best explanation would be an aggregation of Oil red O at the interface that somehow minimizes the interfacial energy.

These aggregates may be stabilized by π-π stacking of the aromatic rings of the dye. Here it may be important to point out once again that similar dyes to Oil red O do not have the same effect. The only difference between Oil red O and Sudan IV are two additional methyl groups in Oil red O (See comparison in Figure IV.14). A likely explanation therefore is that these two methyl groups change the steric orientation of the molecule in such a way that it either is better at stacking; the hydroxy group is less shielded or a combination of both. From these conclusions, Oil red O as expected is not a surfactant but it does seem to be a liquid-phase interfactant. For further study it may be useful to study the structure of Oil red O using methods such as density functional theory and combine it with molecular dynamic simulations to investigate what occurs at the paraffin water interface. Furthermore, it may be possible to determine whether Oil red O after all is a weak surfactant using Brewster-Angle microscopy on a water surface on which the dye has been deposited using the same method as for the surface pressure Isotherm. In any case it is an unexpected interaction that would warrant further investigation.

IV. 3 Ethyl salicylate droplets on Surfactant solution

IV. 3.1 Description of ethyl salicylate-surfactant system

After publishing the discovery of the effect of Oil red O on the behavior of paraffin droplets[55], a collaboration was started with Dr. Shinpei Tanaka from Hiroshima University. Tanaka et. al. had published a series of papers on a different droplet system in which droplets made of alkyl salicylates (butyl salicylate, BS, and ethyl salicylate, ES, in particular) and paraffin display complex individual and collective on a surfactant solution surface[10,14,52,54,79]. In these experiments Oil red O was used as a colorant to create a contrast. In fact, the dye, which was used for initial experiments on the camphor-paraffin droplets had been provided to us by Prof. Tanaka for other preliminary experiments on a different system. Upon reading our paper he performed some preliminary experiments with his droplets[125] using a different dye, Sudan black B (Figure IV.16), that indicated a slight change in behavior. This result is quite interesting because the concentrations of dye used in typical ES-droplet experiments are very low (0.0025-0.005 % by weight). In the resulting collaboration I was tasked to further explore the effect of these two dyes on the ES-droplet system.

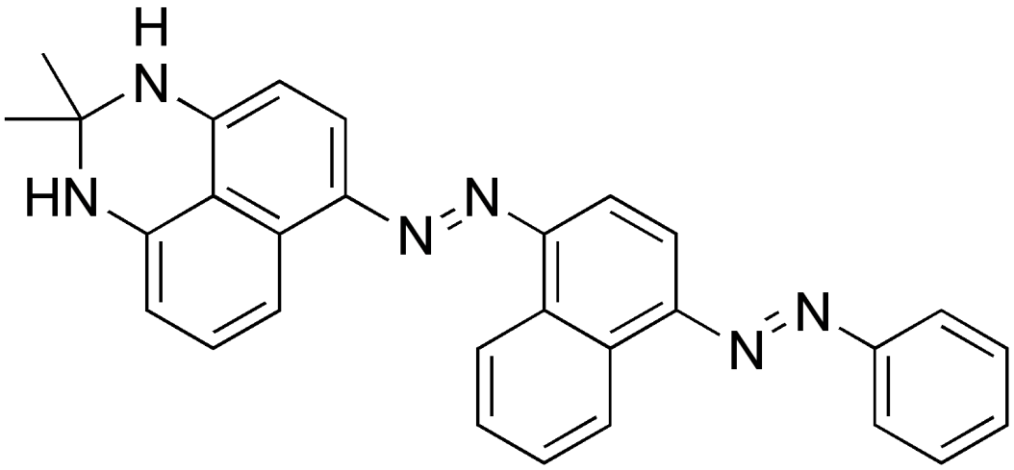

Figure IV.16: Structure formula of Sudan black B.

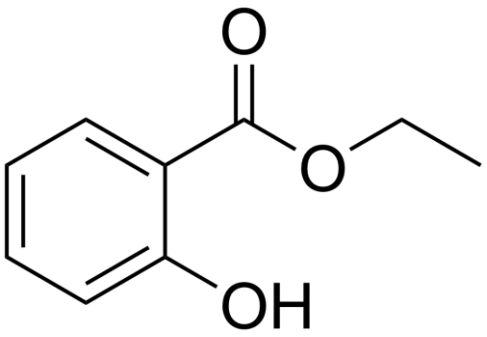

Figure IV.17: Structure of ethyl salicylate

An ES-droplet experiment is set up in the following way: The droplet solution is produced by mixing ethyl salicylate (Sigma Aldrich (CAS: 118-61-6), See Figure IV.17) with between 10 and 20 percent paraffin oil (same as used for camphor-droplets) by weight and 0.0025 to 0.005% dye (Oil red O: OrO or Sudan black B: SbB) by weight. The paraffin oil is added in order to lower the density of the mixture as ethyl salicylate has a higher density than water (1.13 g/cm^3[29]). A surfactant solution, usually 10g/l sodium dodecyl sulfate (SDS, Sigma Aldrich, CAS: 151-21-3) is added to a Petri dish and droplets are placed onto the surface of this solution. The dish is covered non-hermetically with a glass cover and filmed for very long timespans of up to 24 hours. Here I will describe a typical time evolution of 50 or 60, 20ul droplets (20wt% paraffin oil and 0.0025 to 0.005 wt% Oil red O added to ES) placed in a 90mm Petri dish containing 50ml of SDS solution. The overall behavior was split into several stages similarly to the original paper describing this system[10]. The time intervals of each stage vary depending on the system composition and initial conditions. The following figures describing the different stages of the system can be seen in Movie 32.

Stage I: The droplets move around at high speeds while oscillating between each other (Figure IV.18). Only lasts a few minutes.

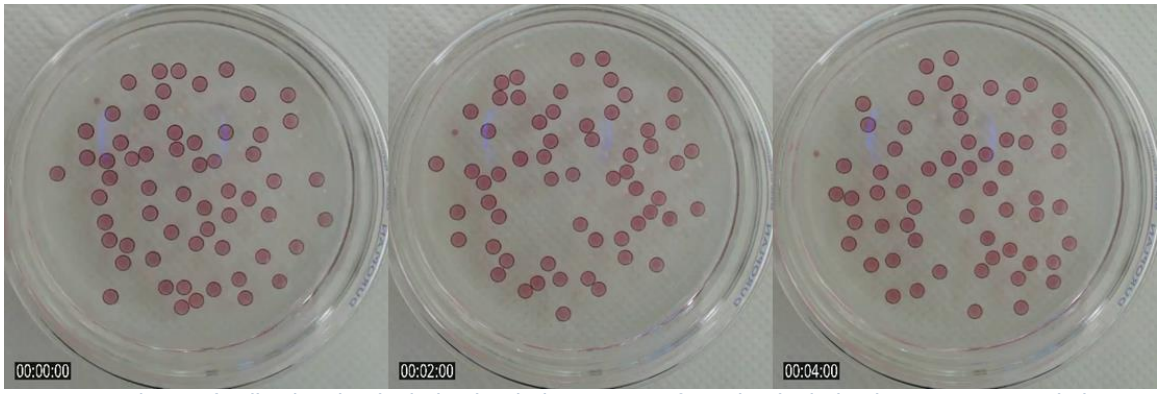

Figure IV.18: Figure of collective droplet behavior during Stage I of ES-droplet behavior on an SDS-solution. It can be seen that there is movement but no order. Snapshots taken at times 0m, 2m and 4m as seen from left to right. Full time interval is 4 minutes.

Stage II: Droplets slow down and decrease in size (seen from above). At this stage the droplets also start to collide more often and the middle of the dish starts to open up occasionally. As time progresses, droplet-droplet contact times increase. Eventually the droplets begin to form a loose order with the droplets starting to form loosely connected, shuffling (rearranging through elongation and collapse) clusters in which droplets are oscillating between each other (Figure IV.19).

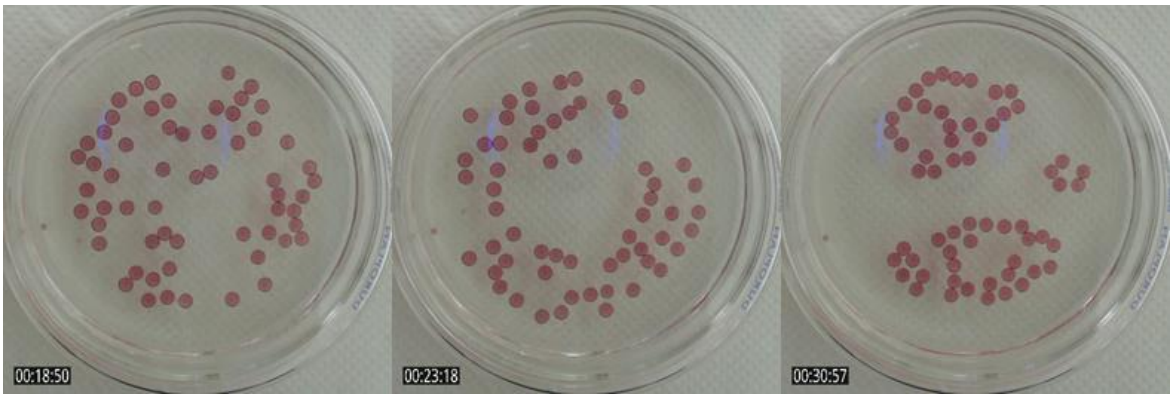

Figure IV.19: Behavior during Stage II. The droplets are beginning to loosely associate in clusters. Snapshots taken at times 18m50s, 23m18s and 30m57s as seen from left to right. Full time interval is 11minutes.

Stage III: Coexistence of fully connected short chains and loose clusters of oscillating droplets during the transition (Figure IV.20 (1-3)). Once longer chains are the dominant state, they exist as smaller connected shuffling clusters with the occasional small ring formation (Figure IV.20 (3-6)).

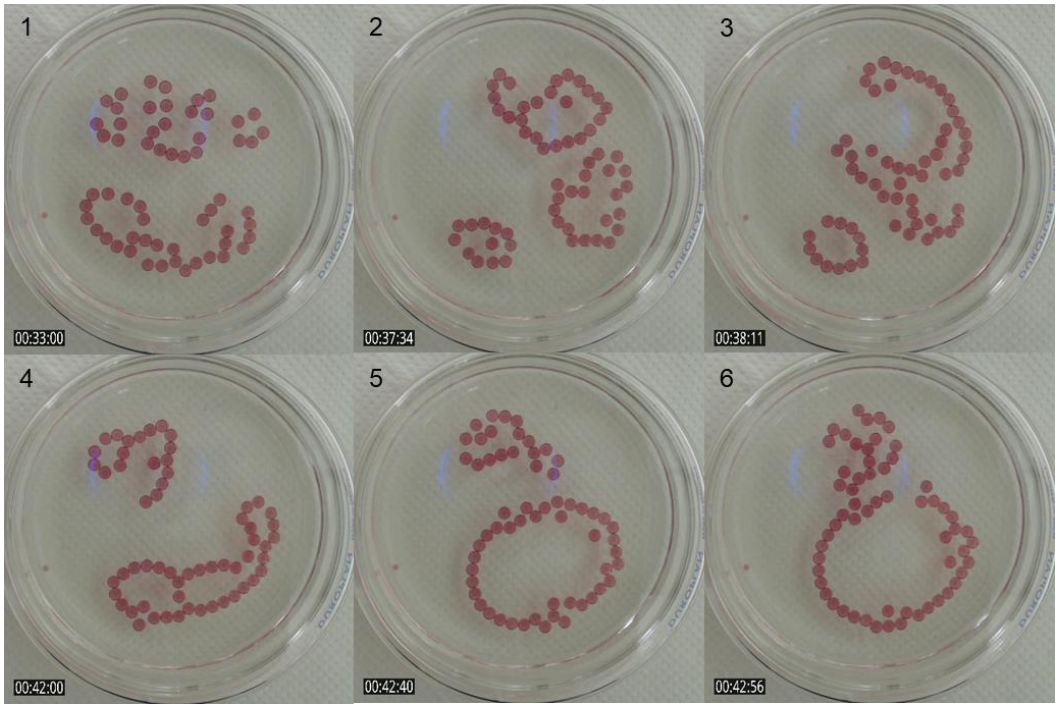

Figure IV.20: During Stage III the droplets start to form clusters made of droplet chains that rearrange constantly (1-3). Occasionally smaller rings form and collapse (4-6). Snapshots taken at times (1)33m, (2)37m34s, (3)38m11s, (4)42m, (5)42m40s and (6)42m56s. Full time interval is 10 minutes.

Stage IV: Smaller cluster forming chains combine into one large cluster that can form large rings. These large rings sometimes can either be stable for very long times (Figure IV.21) or periodically collapse and reform (Figure IV.22).

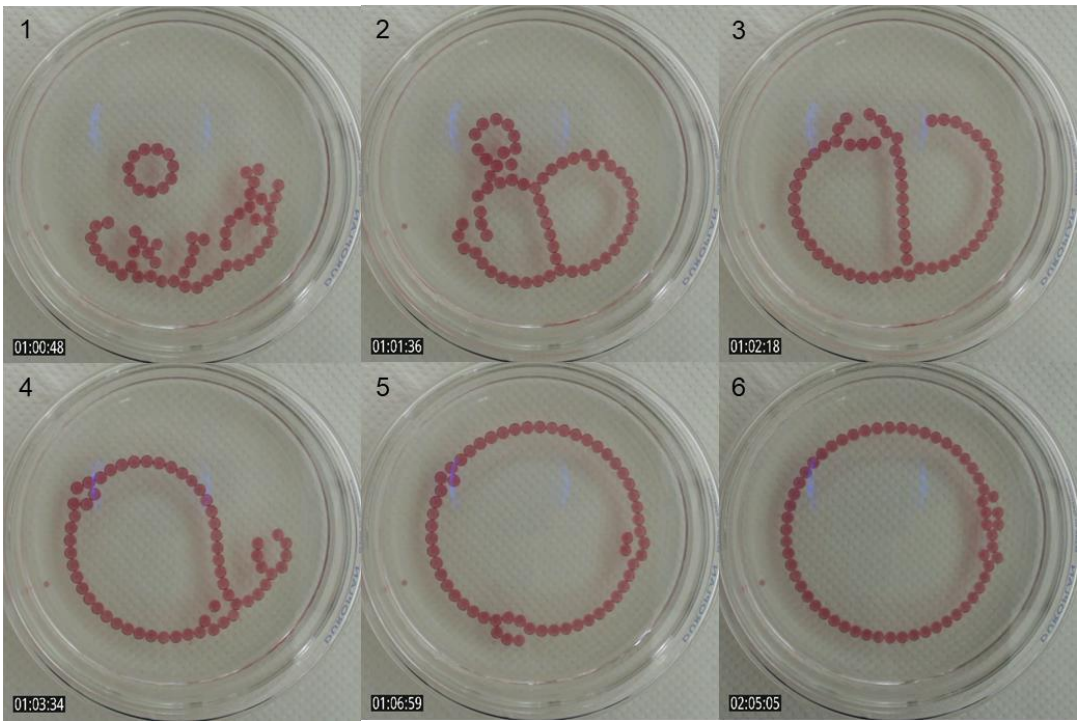

Figure IV.21: During Stage IV the smaller clusters come together to form one long chain which opens up to form one large ring. The formation can be seen from 1-5. In this case, the ring is very stable and is still connected one hour later (5-6). Snapshots taken at times (1)1h00m48s, (2)1h01m36s, (3)1h02m18s, (4)1h03m34s, (5)1h06m59s and (6)2h05m05s. Full time interval is 1 hour and 5 minutes.

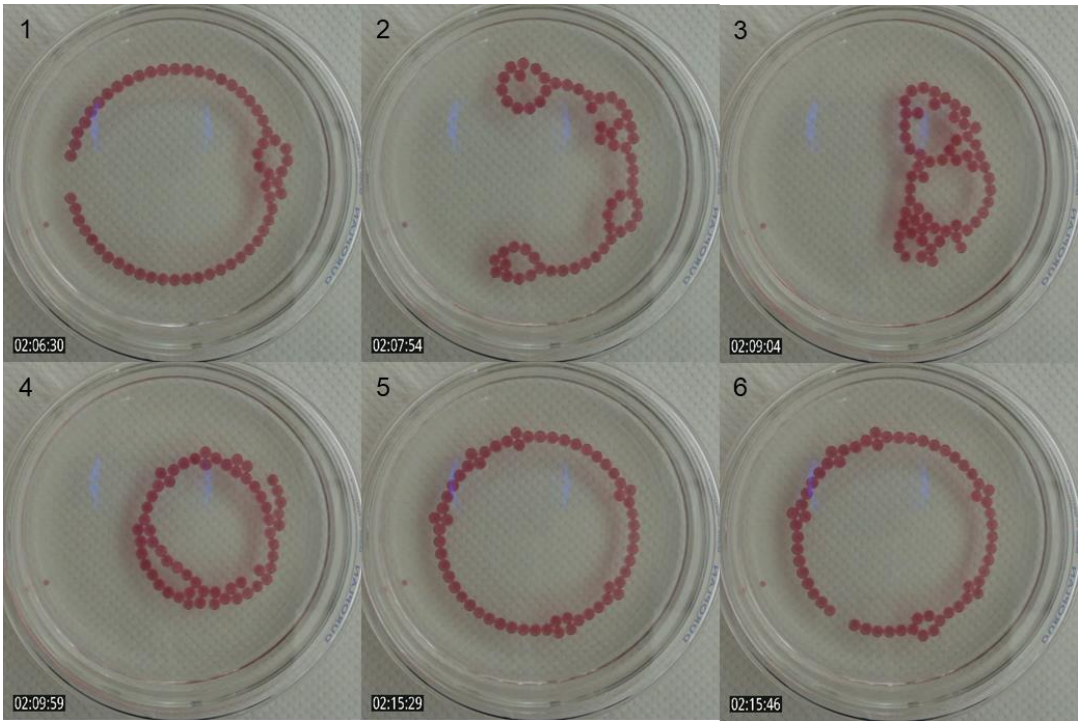

Figure IV.22: During Stage IV the large rings can also be short lived as we from 1-6 see a ring collapsing (1-3), reforming (4-5) and opening up again for the next collapse (6). This all happens within less than 10 minutes. Snapshots taken at times (1)2h06m30s, (2)2h07m54s, (3)2h09m04s, (4)2h09m59s, (5)2h15m29s and (6)2h15m46s. Full time interval is 9 minutes.

Stage V: As time progresses even further, the probability of droplets being linked with more than one droplet increases. Ring formation is still happening at decreasing periods but without full extension before collapse occurs (Figure IV.23).

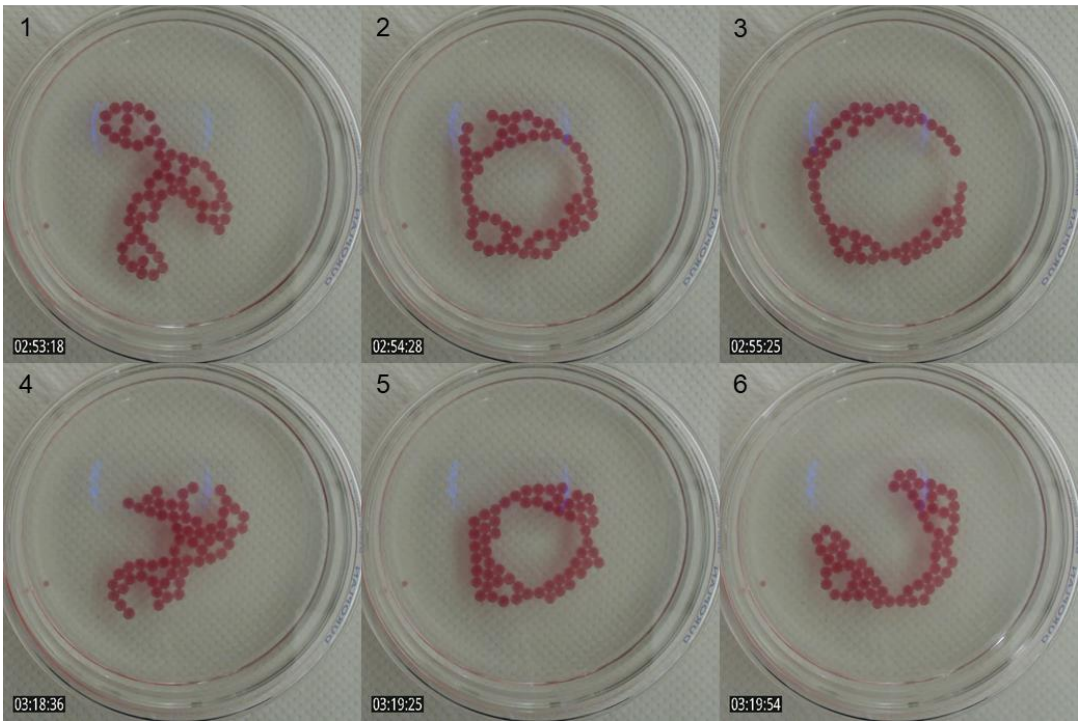

Figure IV.23: During Stage V, ring formation and collapse can still be observed, but the droplets are not connected as single chains, such that some are connected to more than two other droplets. Snapshots taken at times (1)2h53m18s, (2)2h54m28s, (3)2h55m25s, (4)3h18m36s, (5)3h19m25s and (6)3h19m54s. Full time interval is 27 minutes.

Stage VI: Eventually the droplets cease most activity and form densely packed "crystalline" clusters. At this point the system is considered "dead" (Figure IV.24).

Figure IV.24: Stage VI is the "dead" stage in which the droplets "crystallize" into hexagonal patterns. The figure shows the final rearrangement the occurred in this experiment after which the structure ceased any activity until Stage VII. These patterns occasionally rearrange before remaining in a steady state. Snapshots taken at times 4h05m29s, 4h09m42s and 4h13m19s as seen from left to right. Full time interval is 8minutes.

Stage VII: The system can be reactivated to some degree by lifting the glass lid, which will make the droplets scatter. The activity of the droplets however, remains low (see Movie 33).

The going hypothesis for this section is that the general droplet evolution (formation of loosely locked droplets clusters followed by chain-formation with subsequent increase in number of droplet-droplet contacts up to six, that eventually lead to crystalline close packed clusters) is determined by the decreasing ES deposition rate due to an increasing saturation of ES in the bulk and closed atmosphere. This is balanced with the capillary attraction and a directional ES deposition geometry along with boundary conditions and geometry of the container. This will be discussed in Section IV. 3.3 after all of the experimental results have been presented.

IV. 3.2 Investigation of ES-droplet behavior

All experiments performed during this project were set up in the same way as described for the "standard" droplet experiment. The perimeters investigated for this thesis are the number of droplets (N), the diameter of the dish (D) and the type of dye (SbB=blue or OrO=red). In all experiments presented here, the volume of the droplets was 20 ul while the composition was 20wt% Paraffin and 0.0025 wt% (unless otherwise stated) dye added to ethyl salicylate. The aqueous phase consisted of a 10g/L SDS solution for all experiments. When using differently sized dishes, the volume of added SDS-solution was adjusted to maintain the same water level. We found that the population density and scale of the system results in different time evolutions of the droplet system including different types of clusters compared to the "normal" case. It was confirmed that droplets containing Sudan black B instead of Oil red O

have a slightly different behavior and mixing the two types of droplets at different population ratios resulted in interesting interactions.

IV. 3.2.1 Phenomenological observation: Effect of population density and scale of the system on the behavior.

At $D = 140mm$ and $N = 60$, the population density of droplets is decreased while at the same time the scale of the boundary in relation to the droplet size is increased compared to the standard experiment. In such a less constrained system we observe a very different time evolution of droplets that over long time-scales form increasingly large clusters that differ in their collective behavior. The overall tendency of droplets to form chained clusters and eventually to increase the number of droplet-droplet contacts which leads to the crystallized cluster structures remains in this case. But without the geometrical constraint clusters do not grow to sufficiently large sizes to form rings before the stage at which long chains are possible has passed. Instead, we observe several types of clusters with different behaviors at different stages of the time evolution. For the first 1.5 to 2 hours, the droplets in this setup exist as singlets moving at comparably high speeds. As they slow down towards the end of this period, they start to associate in several loose clusters with regular shapes depending on the number of droplets in them. Motion at this stage is vibratory with occasional fast bursts of motion by individual droplets. In Figure IV.25 the time evolution of two experiments is depicted as two montages of periodical snapshots taken every 20 minutes on the left and right side respectively. The figure shows that repeated experiments have similar time evolutions which shows some reproducibility of the behavior. See Movie 34 for whole behavior of left side.

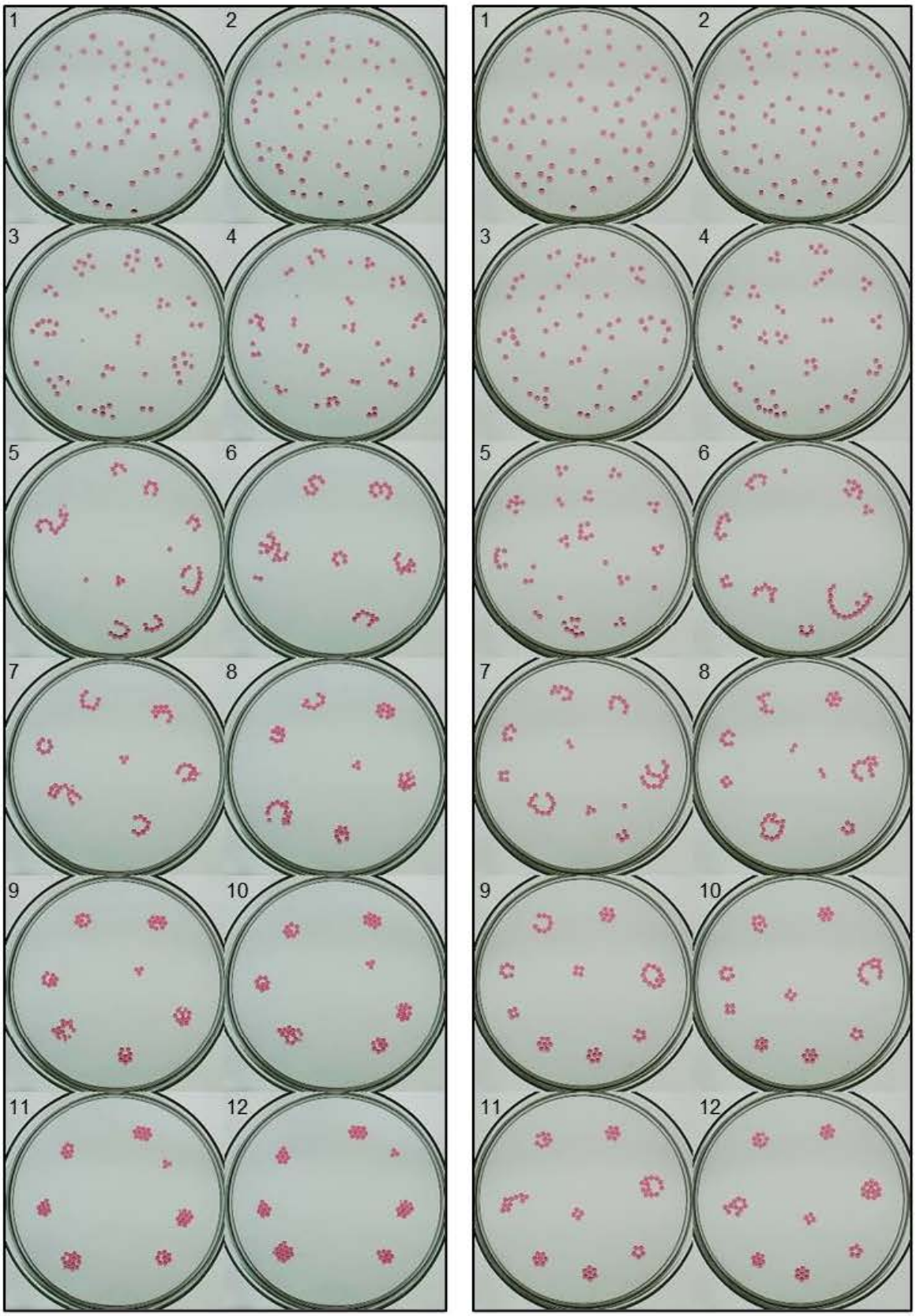

Figure IV.25: Snapshots 20 minutes apart (for 1: t=0, 2: t=20m, 3: t=40m etc.) taken from two independent experiments (left and right side) with 60 droplets swimming on a 5mm layer of SDS-solution in a Petri dish with a diameter of 140mm. It can be seen that the time evolution of both experiments is similar.

From ca. t=1h the loose clusters start to have regular shapes depending on the number of

droplets in the vicinity. At this point we see the first few types of chain clusters: Dimers, dimer-singlets and trimers (see Figure IV.26 a), b) and c) respectively). Dimers and trimers are self-explanatory while dimer-singlets are a special case in which a third droplet is loosely locked to a dimer.

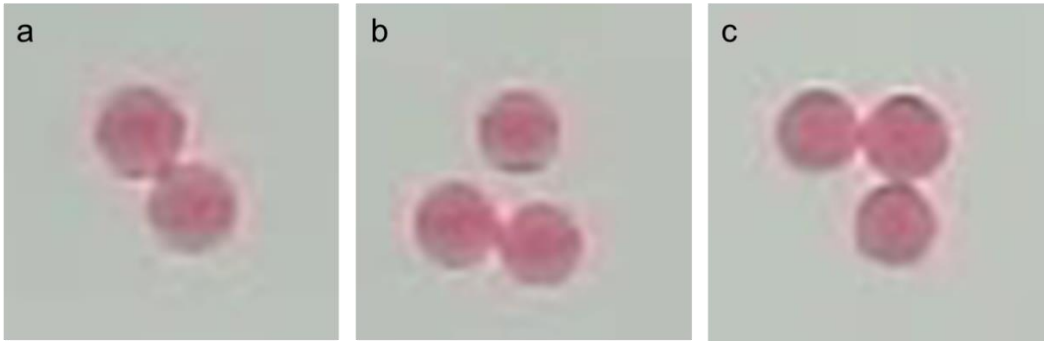

Figure IV.26: Smallest types of chain clusters: a) dimer, b) dimer-singlet where a singlet is "locked" to the dimer and c) a trimer which translates.

Trimer chains already tend to be slightly curved which induces a directional ST-gradient around them such that they are propelled in direction of their convex side acting similarly to crescent movement described in [45]. This translation induces mixing of the system and when clusters collide often an internal rearrangement takes place from which either one larger cluster or several smaller ones emerge. Advancing further in time to ca t=2h, we observe the first chain clusters with four or more droplets. Clusters of 4-5 droplets (See Figure IV.27 a) and b)) in a chain were also originally observed by Tanaka et. al in [10].

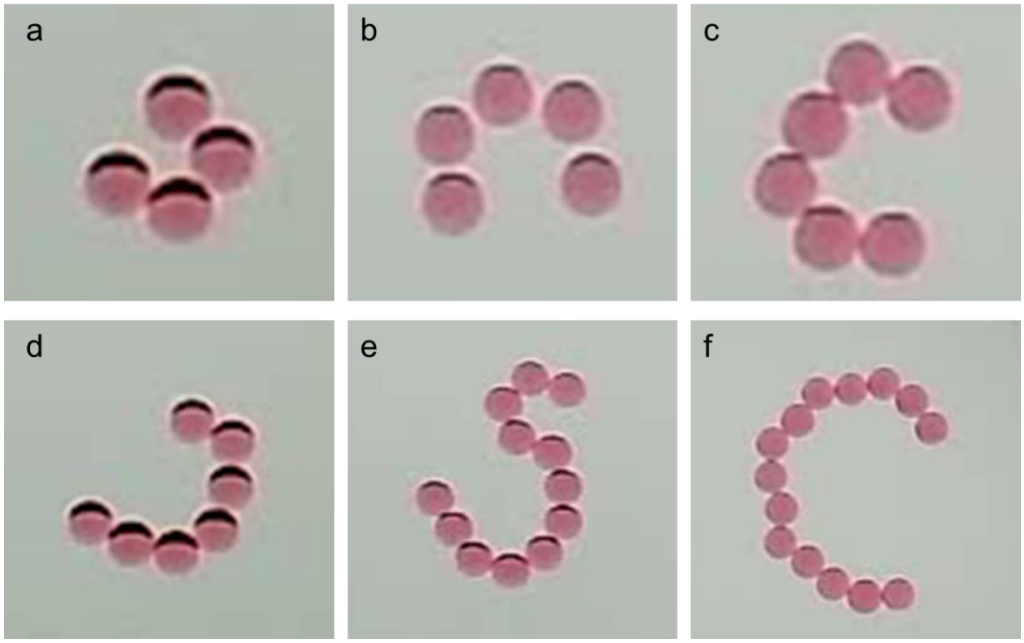

Figure IV.27: Higher order clusters with increasing chain-lengths.

Pentamers appear to be the most translative species. As time progresses the chains become increasingly longer and collapse followed by rearrangement can be observed. This

rearrangement can spew out single droplets. Some long chains even form rotating S-shaped clusters. Examples of these longer chained clusters can be seen in Figure IV.27 c)-f).
An interesting feature that can be observed in some of the clusters is the "locking" between droplets at a certain distance to each other, such as for the dimer-singlet, which may be a result of favorable structured emissions of ethyl salicylate from the droplets[52]. Furthermore, some of the translatory clusters are very reminiscent of so called "gliders" known from game of life simulations[86]. Overall, the behavior is strikingly evolutionary with recombination of cluster phenotypes to new phenotypes with different "abilities" as the changing environment (approaching equilibrium – saturation of bulk and atmosphere with ES) favors increasingly large phenotypes until eventually highly ordered structures emerge.

In the opposite case where the density of droplets along with a smaller size ratio between dish and droplets ($D = 90mm$, $N = 100$, see Movie 35). For this experiment we used droplets containing 0.0025wt% Sudan black B instead of Oil red O for reasons that will be mentioned later on in this section. The droplets immediately start to spatially arrange themselves while vibrating among each other. A loosely connected ring along the edge is formed at the same instant. Non-connected chains are formed within the first 5 minutes. In less than 10 minutes fully connected chains are formed. Since there are too many droplets to form one big ring along the dish edge, the remaining droplets form chains with in the ring, such that are on both ends attached to the outer ring. These bubbles occasionally burst and reform. Major rearrangement of the structure only occurs when two droplets fuse and fall to the bottom of the bulk (this fusion mechanism may partially be enabled due to the different dye as will be discussed in Sections IV. 3.2.2 and IV. 3.2.3). In such a case, new "optimal spatial arrangement" is formed until the next fusion event. These periodical fusion and rearrangement event continue for ca 1.5 hours until droplet activity has dropped to the point where multiple links between droplets are possible such that continuous rearrangement occurs until the structure "crystallizes" at ca $t = 3h$. The time evolution of this experiment is depicted in Figure IV.28 where periodic snapshots of a video are depicting the different stages and arrangements of the system. In this setup, the system is quite similar to the "normal" ring system. However, we do see higher order structures due to the spatial constriction while rearrangement (breaking and reforming of structures) is triggered by droplets fusing and sinking to the bottom instead. The sunken droplets can be seen in Figure IV.28 where they from frame number 21 start congregating at the dish edge.

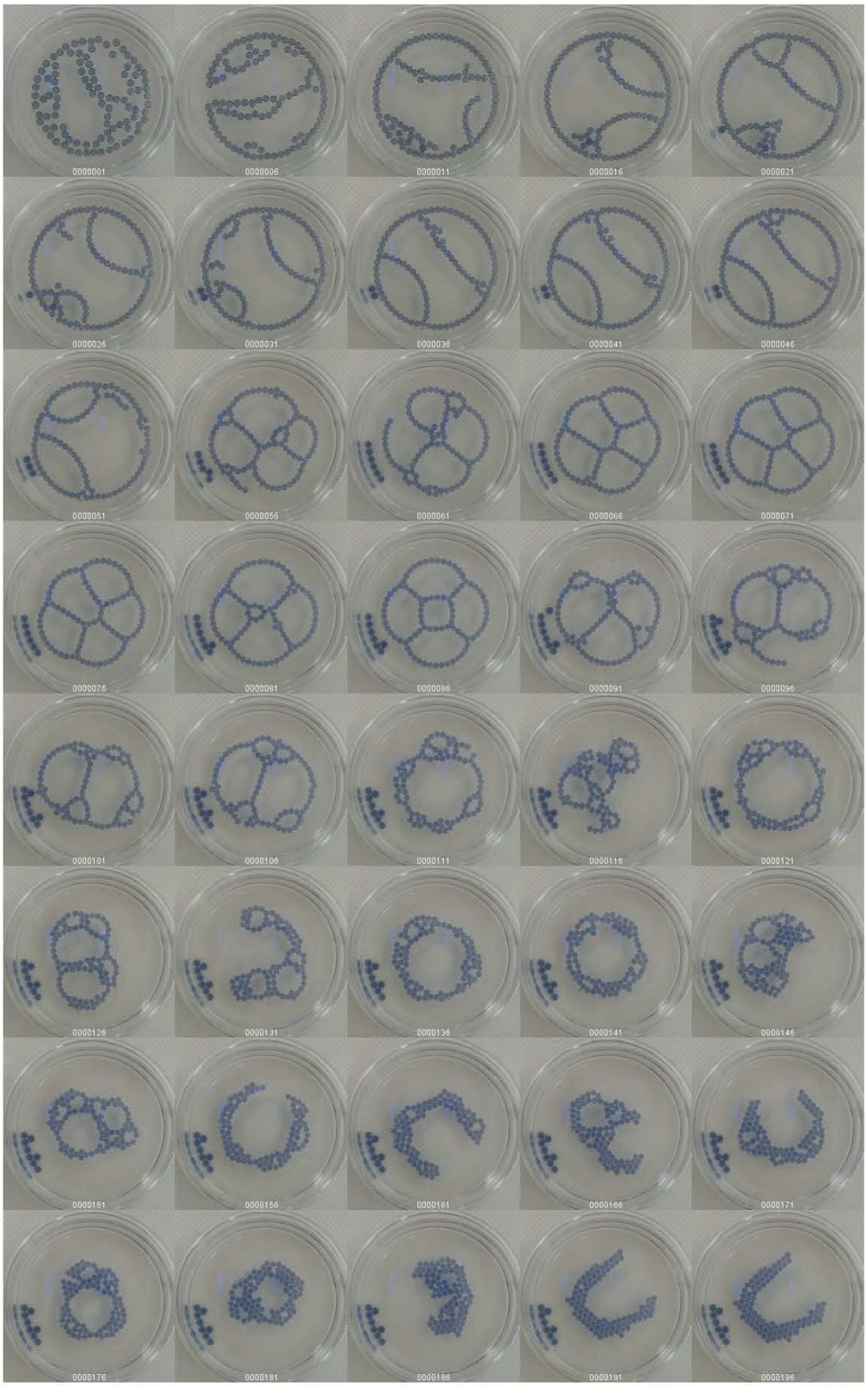

Figure IV.28: Series of snapshots from experiment in which 100 20ul droplets containing 0.0025 wt% of Sudan black B were placed on a 5mm layer of SDS solution in a 90mm Petri dish. Time between each frame is 5 minutes. The larger droplets which are congregating at the dish edge are a product of droplet fusion and subsequent sinking to the bottom of the dish.

It was not possible to reproduce this result with Oil red O droplets as they dissipate ES much

faster and are less likely to fuse. The faster dissipation has the effect that the system already was at a late stage by the time 100 red droplets had been deposited (deposition took ca. 5 seconds per droplet). This may be circumvented in the future by using a microfluidic device to deposit droplets more quickly than can be done by hand using a pipette.

IV. 3.2.2 Phenomenological observation: Influence of the dye on system behavior

IV. 3.2.2.1 Pure systems (only red or only blue droplets)

Experiments on the influence of the dye were done on the "standard" system setup ($D = 90mm$, $N = 50$ and $N = 60$) which should form the collapsing ring clusters. Experiments performed with unmixed systems both expressed this "typical behavior. However, the activity of droplets containing Sudan black B was consistently lower than the droplets containing Oil red O.

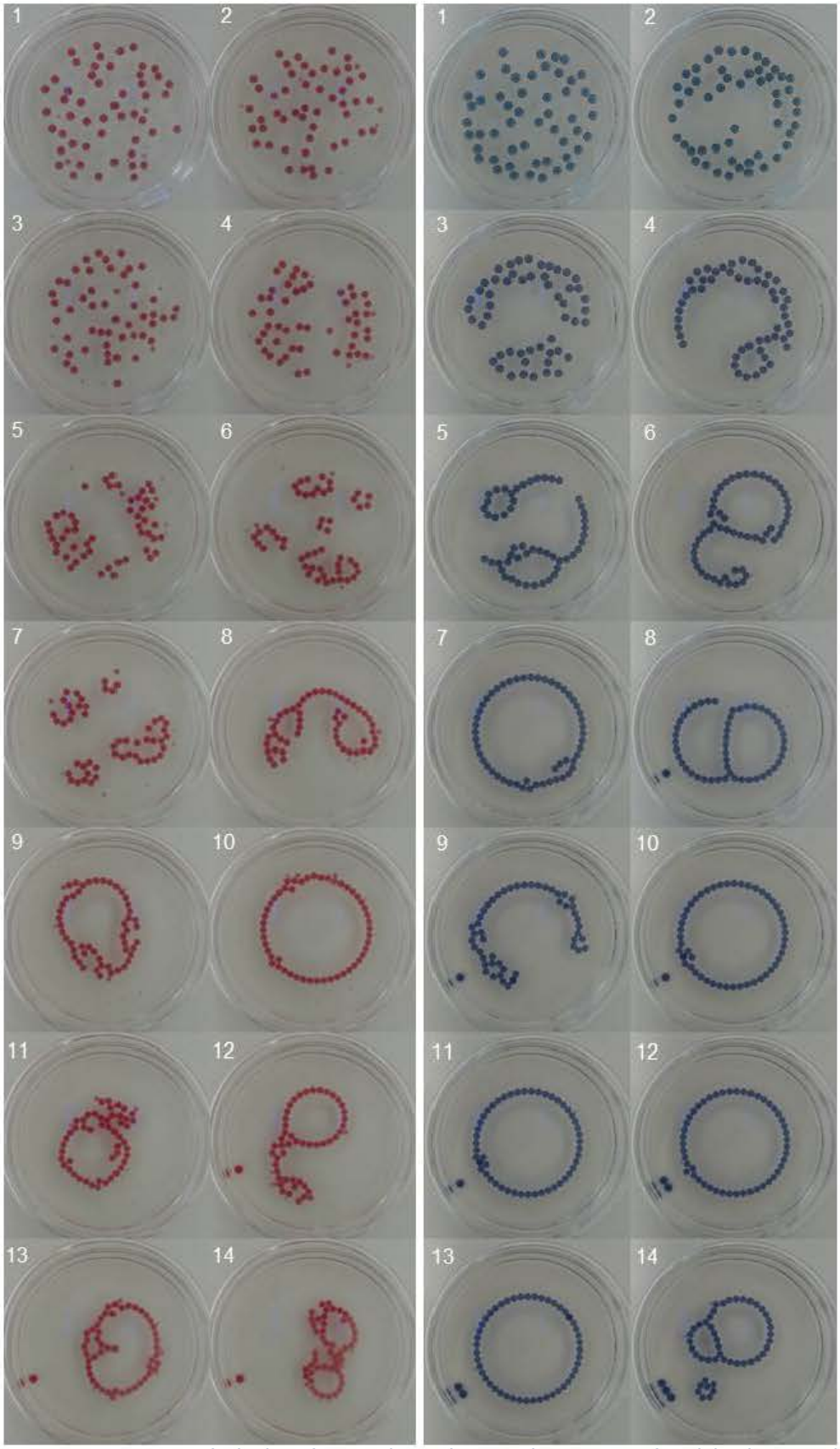

Figure IV.29: $D = 90mm$, $N = 50$ for both. Left: Snapshots taken 12 minutes apart of 20ul droplets containing 0.005 wt% Oil red O. Right: Snapshots taken 12 minutes apart of 20ul droplets containing 0.005 wt% Sudan black B. In both cases we observed ring formation however at different times with the blue system "maturing" faster. The larger droplets that can be seen on the edge of the dish in both experiments (more so for the blue droplets) are a result of droplet fusion and subsequent sinking to the bottom.

Blue droplets tend to stay in a smaller area, moving just slightly back and forth, while red droplets tend to have periodic bursts of motion (See comparison of activity in Movie 36). This would indicate that the dye has an effect on the deposition of ES onto the aqueous surface. The reduced activity has the effect that blue droplets enter the stage of loose vibrating clusters as well as chain formation earlier than red ones. In Figure IV.29 snapshots of two unmixed independent experiments are set up side by side with each frame 12 minutes apart. It can be seen that both systems go through a similar evolution despite the different activity of the two types of droplets. However, the stages are shifted in time with ring formation occurring earlier on the right side of the figure where the droplets contain Sudan black B. If we compare the time evolution of the red droplets with one where the number of red droplets is 60 it can be seen that the rings appear earlier and last longer (Compare frames 5-8 in Figure IV.29 left and both sides in Figure IV.30). If additionally, the concentration of Oil red O is lowered, this effect is reinforced slightly (See Figure IV.30 right side). If we compare blue droplets at different concentrations of dye, we observe a similar but opposite effect. In Figure IV.31 we are comparing the time evolution of equal N blue droplets with a high concentration of SbB and low concentration of SbB. It can be seen that the evolution progresses faster in the case of a higher concentration of dye. Another thing recognizable is that with a higher concentration of dye, fusion events become more likely (especially for Sudan black B) as can be seen in Figure IV.29 and Figure IV.31.

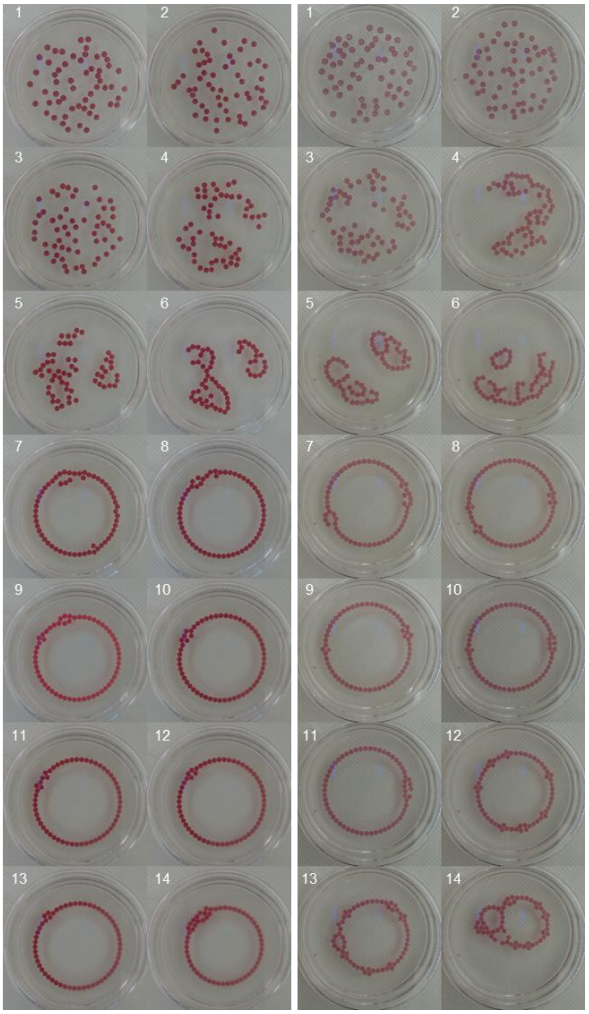

Figure IV.30: $D = 90mm$, $N = 60$ for both. Left: Snapshots taken 12 minutes apart of 20ul droplets containing 0.005 wt% Oil red O. Right: Snapshots taken 12 minutes apart of 20ul droplets containing 0.0025 wt% Sudan Oil red O.

Figure IV.31: $D = 90mm$, $N = 50$ for both. Left: Snapshots taken 12 minutes apart of 20ul droplets containing 0.005 wt% Sudan black B. Right: Snapshots taken 12 minutes apart of 20ul droplets containing 0.0025 wt% Sudan black B. The larger droplets that can be seen on the edge of the dish are a result of droplet fusion and subsequent sinking to the bottom.

All repeated experiments done on unmixed systems give similar outcomes and indicate that the time of chain and ring formation is influenced by two parameters (at constant dish size, paraffin content and droplet volume):

1. Number of droplets: regardless of dye rings are formed earlier and last longer before collapse in a N=60 system than in a N=50 system.
2. Dye: Blue droplets cluster earlier and form longer lasting rings at earlier points than red droplets. At higher concentrations of dye (0.005% by weight) this effect is reinforced further such that droplets form the first full ring earlier. For red droplets the

effect is the opposite with lower concentrations of Oil red O forming stable rings at an earlier stage than the higher concentration.

These results show that the two dyes are changing the behavior of droplets in two opposing ways due to the red dye increasing activity and the blue dye decreasing activity. The "more stable" behavior observed for higher N is important for my suggested mechanism of droplet behavior, discussed later on in this section.

IV. 3.2.2.2 Mixed systems (both blue and red droplets in one system at different ratios)

The altered behavior of droplets containing different dyes becomes even more evident in mixed setups where blue and red droplets are placed onto a surfactant solution at differing ratios. A good example is when the number of blue droplets is 49 ($N_b = 49$) and red droplets is one ($N_r = 1$). Such a system will go through the same evolution as a pure blue system, except that the single red droplet is much more active than the blue even during the early stage of the experiment (Movie 37). In Figure IV.32, four snapshots taken one minute apart during the stage when the blue droplets are gathered in loose clusters. It can be seen how the blue droplets stay closely associated to their local cluster while the red droplet with this time frame can be seen translating across the entire dish without interacting with the blue droplets. During later point of the time evolution the red droplet is occasionally able to disturb the formation of a ring until the point when its activity also decreases to the point that it will be part of a droplet chain. When rings are formed from this point on, the chain-breaking occurs, in most cases, at the location of the red droplet. The behavior persists in repeat experiments.

Flipping the system, ($N_b = 1$ and $N_r = 49$) is not very interesting as the evolution is dominated by the high activity of the red droplets. The passive blue droplet has little to no effect on the time evolution.

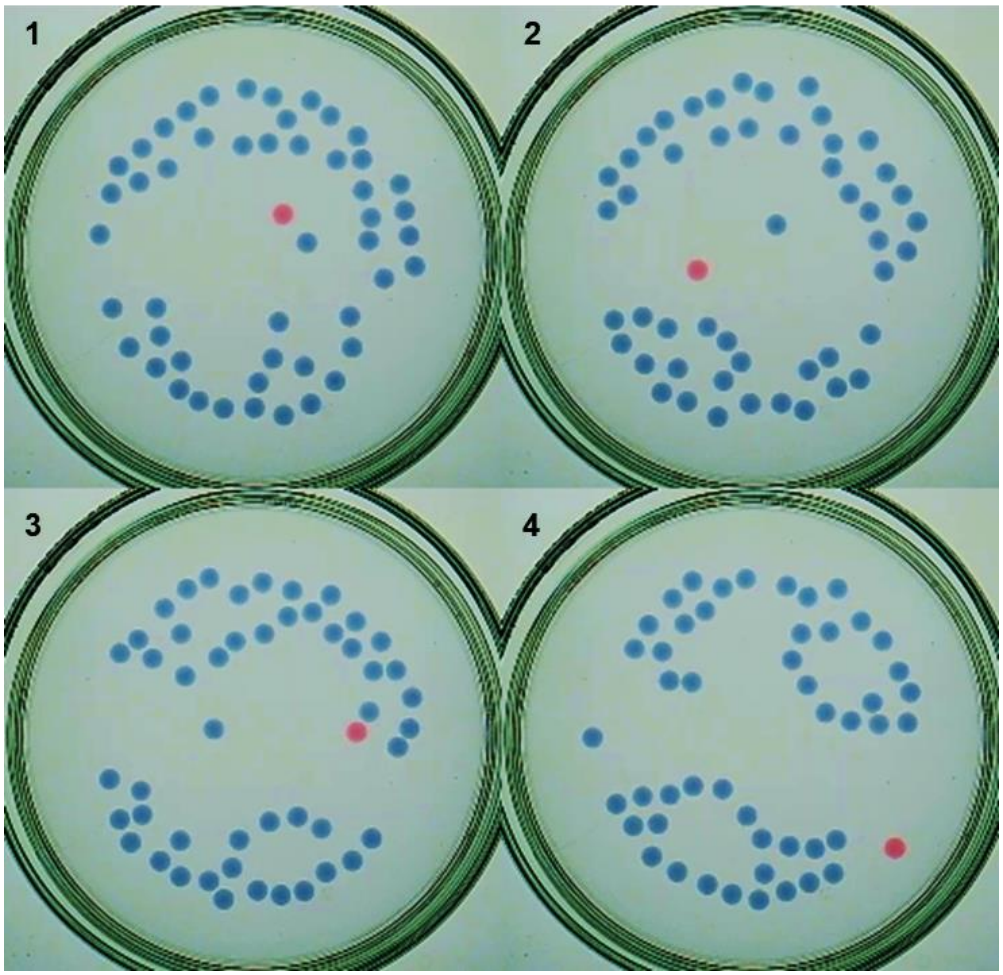

Figure IV.32: $D = 90mm$, $N_r = 1$ and $N_b = 49$. Consecutive snapshots taken from individual experiment 1 minute in between each. Contrast, brightness and saturation was adjusted in post. It can be seen that while the blue droplets are in a semi-ordered phase, the single red droplet is very active and translates across the dish without interacting with the other droplets.

Decreasing the ratio between blue and red droplets to 40:10 (for either combination see comparison in Figure IV.33 or Movies 38 and 39) revealed that with a red majority the formation of rings is inhibited as only one full ring formation was observed during two independent experiments. With a blue majority, full ring formation occurred at a similar rate as in equivalent unmixed systems (however at a later time).

Furthermore, we observed that due to their lowered activity, blue droplets tend to prefer associating with each other rather than red ones which leads to the red droplets being located around clusters of blue as can be seen in Figure IV.33 (Right: frames 4-7 and 13-15) where a minority of red droplets are located mostly in the outskirts of the dish during the stage before ring formation and during the end stage where the red droplets are located at the outer perimeter of the close packed structures. For the blue minority this "phase separation" also becomes visible during the crystalline state where the red droplets tend to encapsulate the blue droplets (See Figure IV.33, Right: frames 9-15).

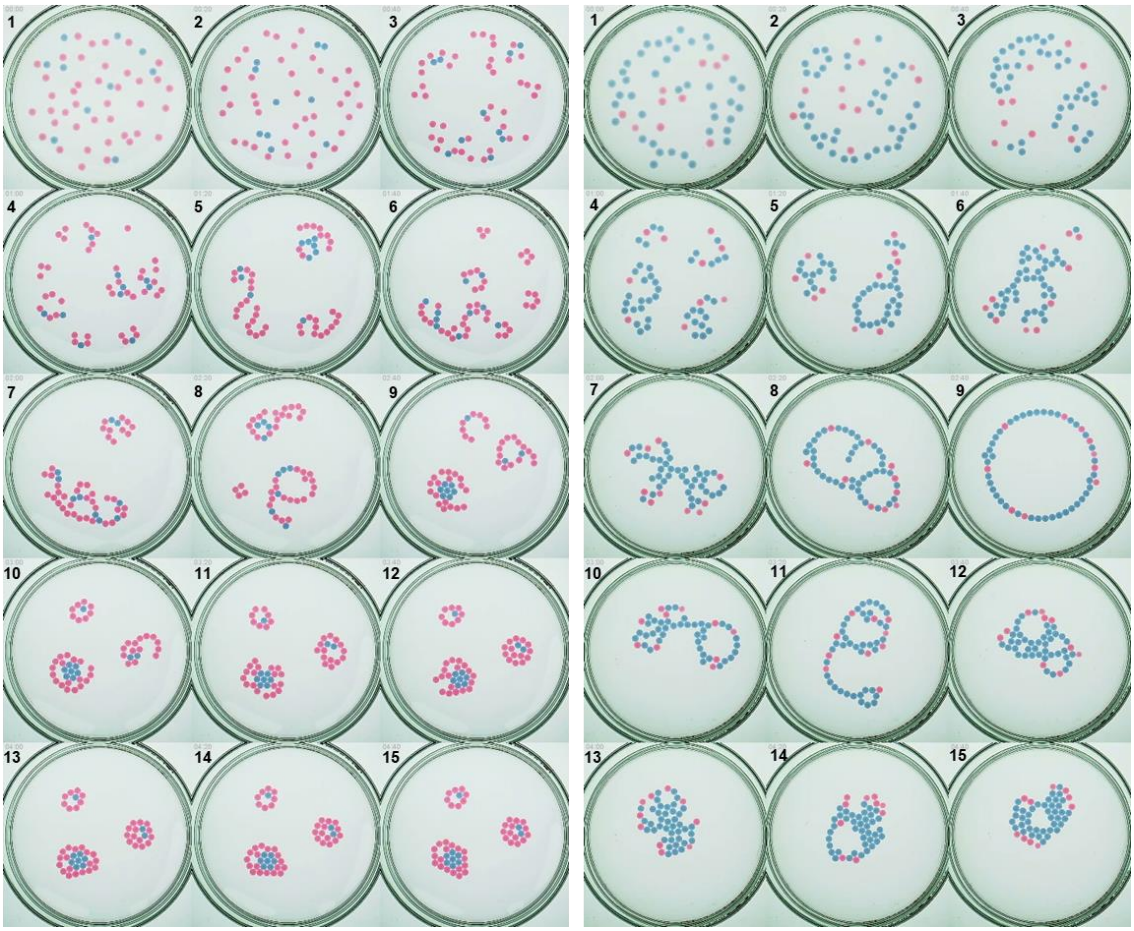

Figure IV.33: All: $D = 90mm$, 20ul droplets, snapshots 20 minutes apart. Left: ($N_b = 10$ and $N_r = 40$). Right: ($N_b = 40$ and $N_r = 10$). The long-term evolution of both systems is similar although ring formation for the red majority (Left) is much less likely or at least does not occur as a single large ring. Furthermore, it can be seen that there is some "phase-separation" between red and blue with the red droplets preferring to be on the outer perimeter of clusters

Mixing the two types of droplets evenly ($N_b = 25, N_r = 25$, see Movie 40), results in a system where no full rings are formed at any point. The two different behaviors disturb such formations. Some of the previously observed interaction can be seen here as well though. During early stages there is a soft phase separation as blue droplets start to form loose vibrating clusters with the red ones joining ca. 10 minutes later (see Figure IV.34 frames 2-5). Blue droplets are also the first ones to form fully connected chains and clusters involving both types of droplets can be seen at ca. t=1h. From this point we see two types of clusters: very active blue majority clusters in which the red droplets tend to occupy outside positions or smaller clusters with a red majority that are not very active but have interesting symmetrical geometries (Figure IV.34 frames 6-11). Eventually all droplets are collected in one very actively rearranging cluster (Figure IV.34 frames 12-14) in which blue droplets tend to occupy the middle. Blue droplets crystallize ca 45m to 1h before the red ones which will still be active around the blue close packed structure (Figure IV.34 frames 15 to 22). Eventually, the activity of red droplets ceases as well and they stay attached, encapsulating the blue droplets fully

(Figure IV.34 frames 23 and 24).

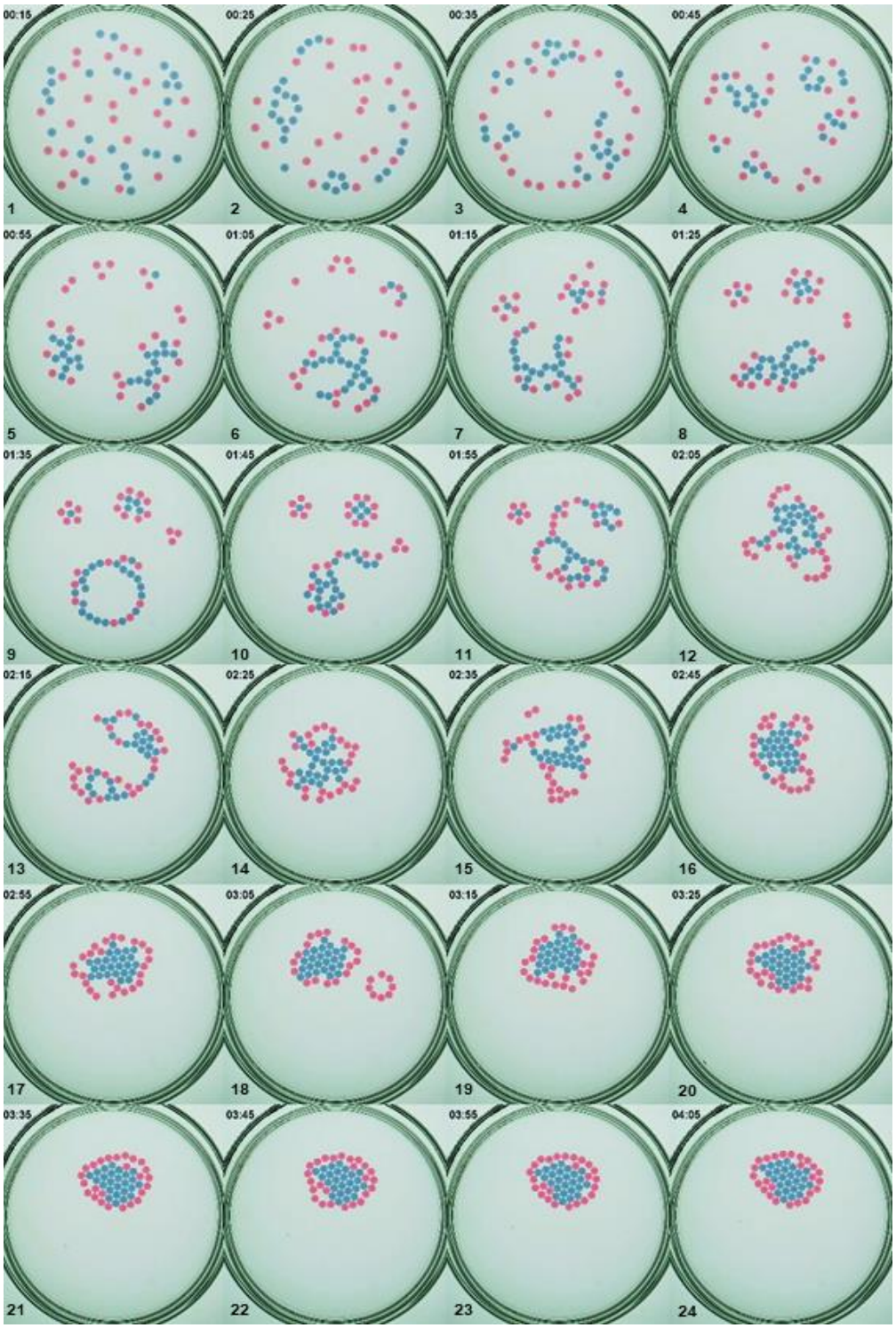

Figure IV.34: $D = 90mm$, 20ul droplets, snapshots 10 minutes apart. ($N_b = 25$ and $N_r = 25$). The first 15 minutes have been skipped.

IV. 3.2.3 Quantification of interfacial interactions of ethyl salicylate droplets

Measurements of tensions at the various interfaces involved in this system were performed to investigate the general mechanism of the ES-droplet propulsion as well as the influence of the dyes on the system. A pendant droplet tensiometer (Biolin Scientific Attension Theta Life, 0.01

mN/m accuracy) was used for this. The aqueous phases were MilliQ-water or 10g/l SDS solution. Oil phases were made of pure ES, ES+dye (0.005% Oil red O or Sudan black B), ES+paraffin (20% paraffin) and ES+paraffin+dye (20% paraffin, 0.005% Oil red O or Sudan black B). Table IV.3 gives an overview over the measured interfacial tensions. Since the pendant droplet tensiometer measures surface tensions as a function of time, the data was averaged for each independent measurement (at least three measurements per interface) and the mean value of those averages is recorded in the table below with the standard deviation derived from those averaged measurements as well (this eliminates the effect of outliers caused by vibrations). The interfaces found to change over time will be discussed in further detail.

Table IV.3: Collected results from measuring interfacial tensions (γ) of the several interfaces involved in the ethyl salicylate (ES)-Paraffin-Oil red O (OrO) or the ethyl salicylate (ES)-Paraffin-Sudan black B (SbB) droplet behavior on a sodium dodecyl sulfate (SDS)-solution.

interface	*γ (mN/m)*	*std. deviation of γ*
H_2O-ES	56.55	0.23
H_2O-ES+OrO	55.61	0.24
H_2O-ES+SbB	55.38	0.15
H_2O-ES+Paraffin	24.95	0.21
H_2O-ES+Paraffin+OrO	25.18	0.16
H_2O-ES+Paraffin+SbB	25.31	0.1
SDS-ES	7.75	0.04
SDS-ES+OrO	8.01	0.11
SDS-ES+SbB	~7.71 (decreasing)	-
SDS-ES+Paraffin	2.60	0.01
SDS-ES+Paraffin+OrO	~2.5 (decreasing)	-
SDS-ES+Paraffin+SbB	~2.36 (decreasing)	-
ES-air	41.30	0.03
ES+OrO-air	40.85	1.44
ES+SbB-air	39.36	0.11
ES+Paraffin-air	33.07	0.07
ES+Paraffin+OrO-air	33.55	0.03
ES+Paraffin+SbB-air	33.52	0.02
H_2O (saturated ES)-air	~69.01 increasing	-
SDS (saturated ES)-air	~33.23 increasing	-
SDS-air	37.86	0.13

From the results presented in Table IV.3 It can be concluded that neither Oil red O or Sudan black B change the interfacial tension between the oil and the pure water phase regardless of presence of paraffin. This is surprising as we have observed a change at this interface for the camphor-paraffin droplets stained with Oil red O. However, the previously observed effect was only noticeable at considerably higher concentrations of dye. Further, the oil-air interface appears to be unaffected by the presence of the dyes as well. There merely is a decrease in surface tension when paraffin is added to ethyl salicylate.

IV. 3.2.3.1 Interface without paraffin present

The most interesting interface regarding the dyes is the one with the aqueous surfactant - solution containing 10g/L SDS. The interfacial tension of pure ES and the surfactant solution was measured to be ca. 7.8 mN/m. Adding OrO to the ES does not significantly change the interfacial tension (it slightly increases if anything). When SbB was added to the ES, the interfacial tension was decreasing over time. Initial values in different experiments ranged from 7.4 to 8.1 mN/m. In the short term (Figure IV.35) the interfacial tension decreased almost linearly by ca 0.2 mN/m per 60s.

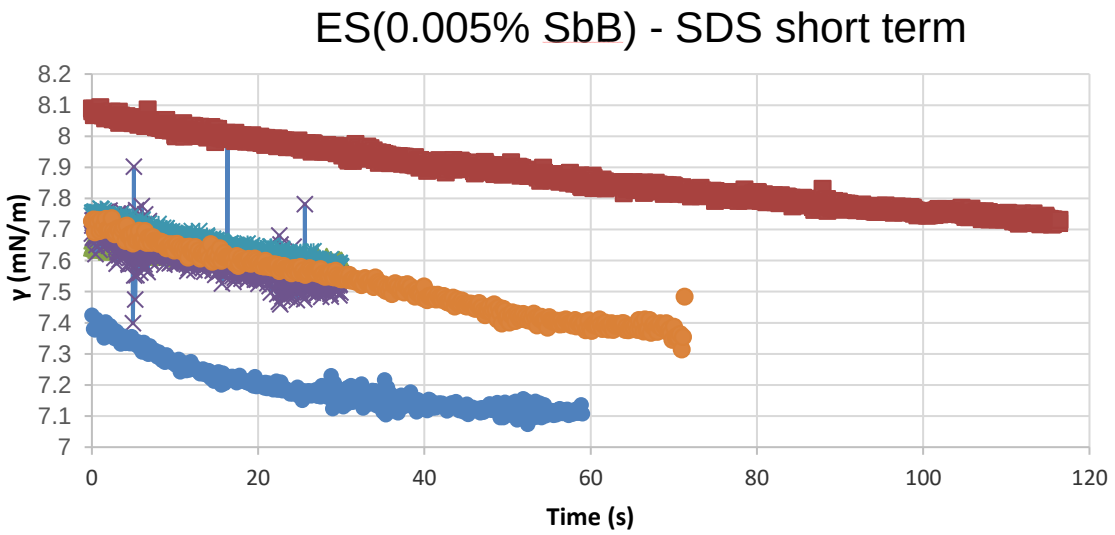

Figure IV.35: Change in oil-water interfacial tension over a short time interval for a drop of ethyl salicylate containing 0.005wt% Sudan black B in contact with a 10g/l SDS-solution. A decrease in interfacial tension of ca 0.2 mN/m per minute can be observed in multiple experiments.

Over the long term however, it keeps decreasing at a lower rate after about 250 seconds with the curve starting to flatten out (see Figure IV.36). For whatever reason, the decrease in some experiments was much faster and flattened out around 6.9 mN/m after about 3-500 seconds (see Figure IV.37).

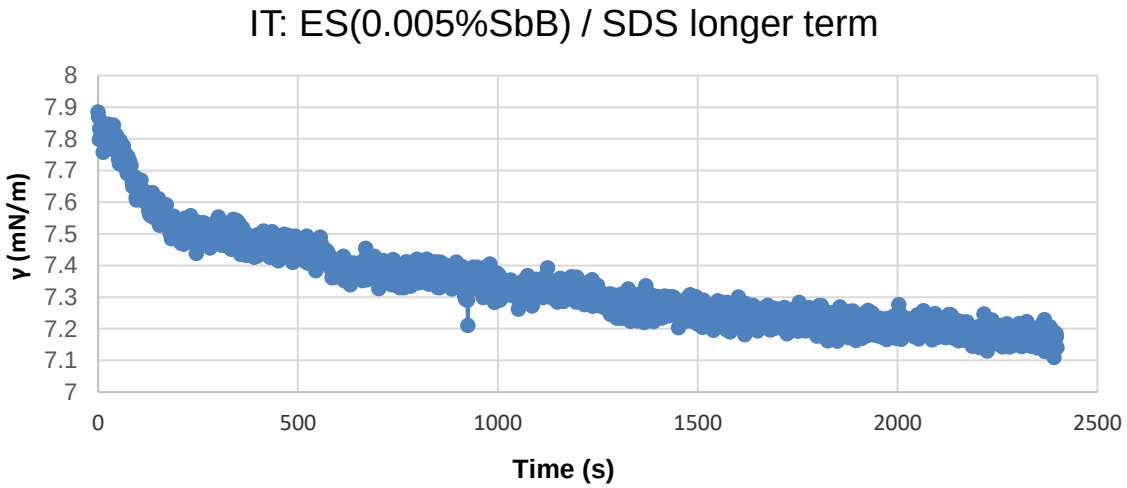

Figure IV.36: Change in oil-water interfacial tension over a long-time interval for a drop of ethyl salicylate containing 0.005wt% Sudan black B in contact with a 10g/l SDS-solution. An initial decrease of ca 0.2 mN/m per minute in interfacial tension flattens out after ca. 250 seconds but continues to decrease for a very long time period.

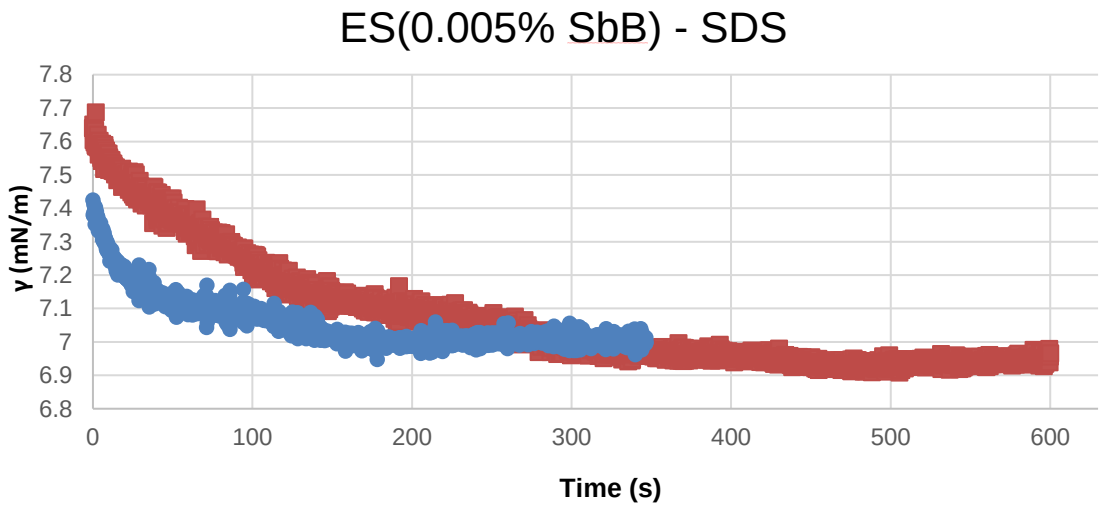

Figure IV.37: Change in oil-water interfacial tension over a long-time interval for a drop of ethyl salicylate containing 0.005wt% Sudan black B in contact with a 10g/l SDS-solution. This graph represents a much faster decrease in interfacial tension where it flattens out at ca. 6.9 mN/m after only 3-500 seconds.

In the case of the slow decrease in interfacial tension (Figure IV.36), the droplet was left hanging in the SDS solution, leaving the setup completely unchanged over night and the interfacial tension was measured the next day. Figure IV.38 shows that the interfacial tension also in this case reaches an equilibrium interfacial tension at ca 6.85 mN/m.

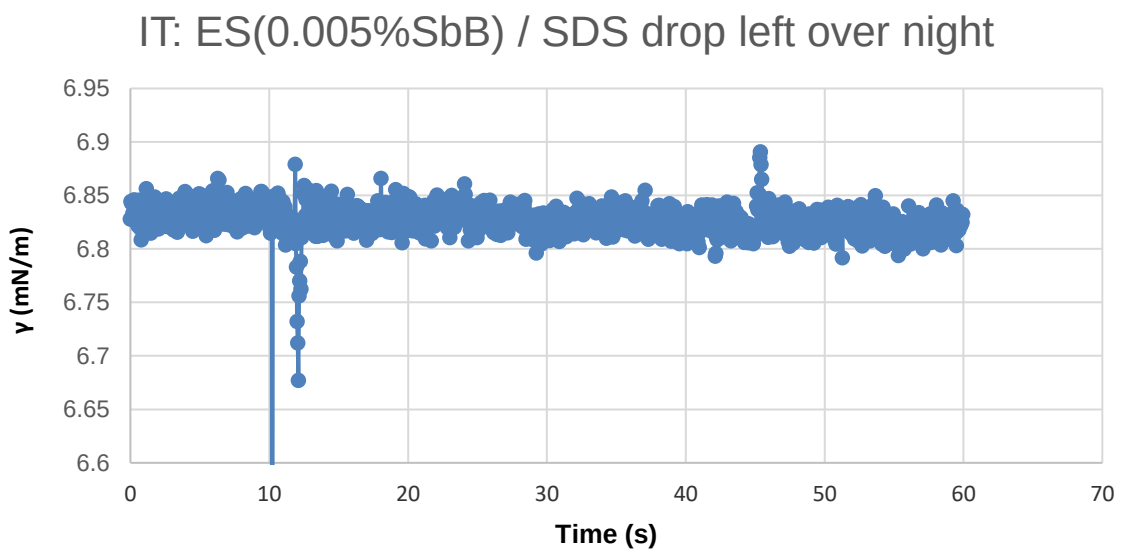

Figure IV.38: Interfacial tension measurement of the same droplet that was measured to obtain the graph in Figure IV.36. In this case the drop was left immersed in the SDS-solution overnight, maintaining the experimental setup, and measured the next morning. It indicates that the equilibrium interfacial tension between an ethyl salicylate and 10g/l SDS-solution is ca 6.85 mN/m.

These numbers would indicate that some process is happening towards some equilibrium at the interface when Sudan black B is present even at very small concentrations. To prove that this process occurs at the interface and not in either of the bulk liquids, the "equilibrated" droplet was expelled to the bottom of the cuvette containing the aqueous phase and a fresh droplet extruded from the needle in this unaltered setup. The interfacial tension of the fresh droplet was once again at ca 8 mN/m and slowly decreasing (See Figure IV.39). It indicates that the equilibration occurs only at the interface and no chemistry affecting interfacial tension occurs in the bulk of either phase.

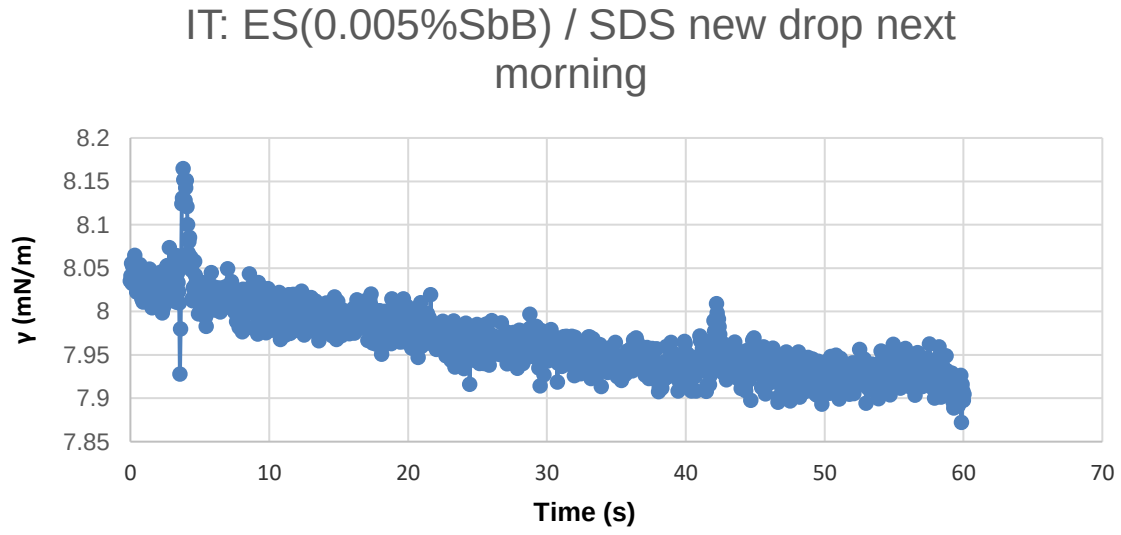

Figure IV.39: Measurement of fresh drop from the same reservoir after the drop from Figure IV.38 was expelled from the needle. As interfacial tension again is around the initial values seen in Figure IV.35 to 0. It shows that the equilibration occurs only at the interface and no chemistry affecting interfacial tension occurs in the bulk of either phase.

IV. 3.2.3.2 Interfaces with paraffin present

Adding Paraffin at 20 weight % to ES lowered the interfacial tension with the SDS solution to ca. 2.6 mN/m. In this case, the presence of Oil red O resulted in a further slow decrease over time. Figure IV.40shows that the interfacial tension in this case decreased from a value of ca 2.5 mN/m to ca 2.35 mN/m within 20 minutes.

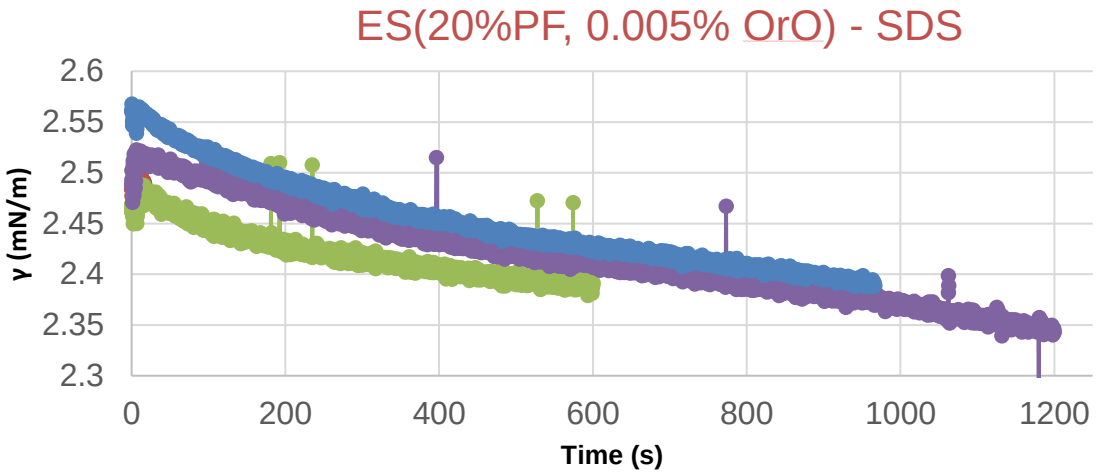

Figure IV.40: Change in oil-water interfacial tension over an up to 1200s-time interval for a drop of ethyl salicylate containing 20wt% paraffin oil and 0.005wt% Oil red O in contact with a 10g/l SDS-solution. Initial interfacial tension is very low but decreases further by ca. 0.2 mN/m over 1200 seconds. It shows that the Oil red O dye has an influence on the interface when paraffin oil is present.

Sudan black B on the other hand, had an even stronger effect on the interface, resulting in an initial value of ca 2.35 mN/m and a rapid decline that flattened out at ca 1.2 mN/m after 75 minutes (See Figure IV.41 and 0).

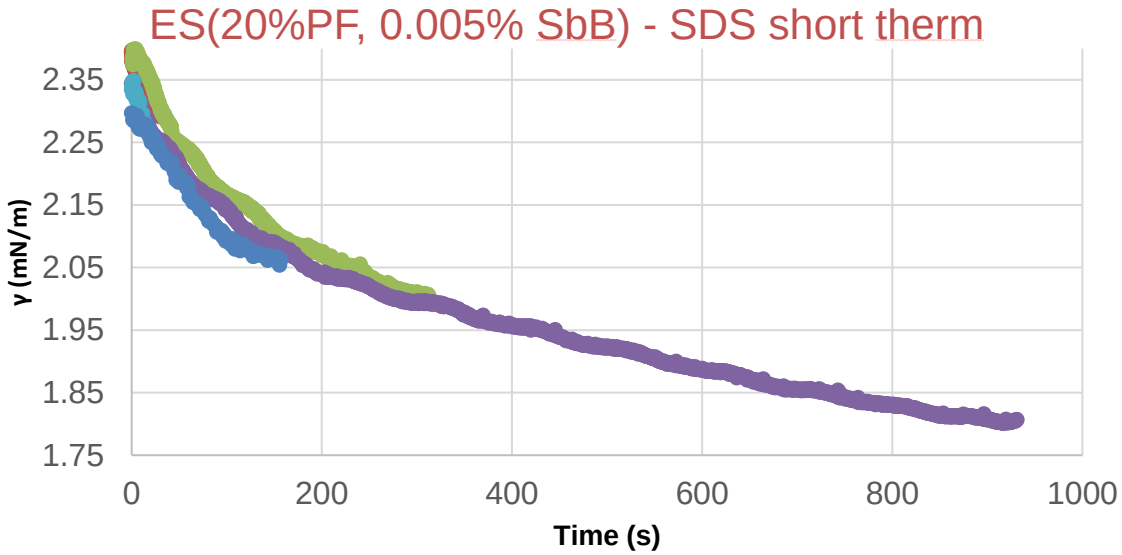

Figure IV.41: Change in oil-water interfacial tension over a ca. 900 second time interval for a drop of ethyl salicylate containing 20wt% paraffin oil and 0.005wt% Sudan black B in contact with a 10g/l SDS-solution. Initial interfacial tension is even lower than for Oil red O (Figure IV.40) and decreases further by ca. 0.55 mN/m over 900 seconds. It shows that the Sudan black B dye has about the same short-term influence on the interfacial tension as it does when no paraffin in present (See Figure IV.36).

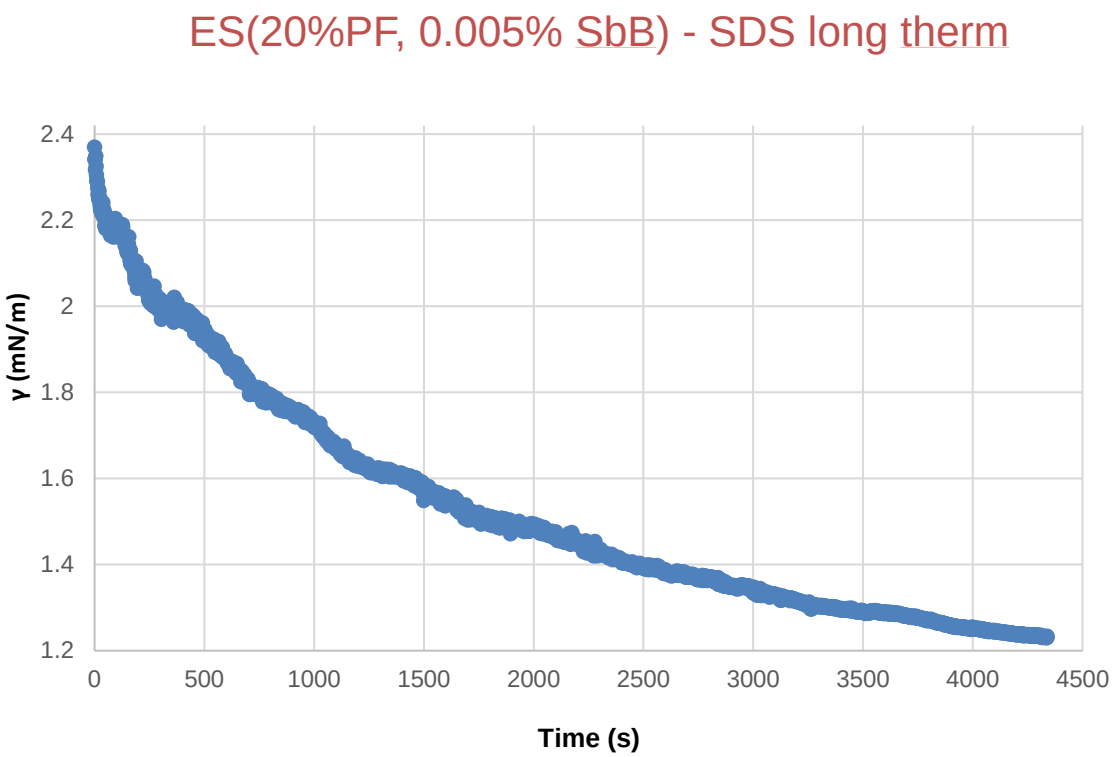

Figure IV.42: Change in oil-water interfacial tension over a 72-minute time interval for a drop of ethyl salicylate containing 20wt% paraffin oil and 0.005wt% Sudan black B in contact with a 10g/l SDS-solution. It can be seen that the interfacial tension decrease flattens out towards 1.2 mN/m which is a total decrease of 1.2mN/m. This long-term measurement shows that Sudan black B in the long term lowers the interfacial tension for such a droplet about the same or slightly more in comparison to when no paraffin is present (see Figure IV.36 to 0).

These results would indicate that Oil red O does not interact with a pure ES and surfactant solution interface but it does when Paraffin is present. Sudan black B on the other hand, clearly interacts with the ES and surfactant solution interface. When paraffin is present in the droplet as well, the effect of Sudan black B appears to be slightly increased (reduction of ca. 1.2 mN/m as opposed to ca. 1 mN/m) but this difference could be due to sample preparation inaccuracies.

IV. 3.2.3.3 Air-water interface

Another interesting interface to consider for this system, is the water-air interface. Two samples were measured: MilliQ water and a10g/L SDS-solution. Both were saturated with ethyl salicylate by adding excess ES to a falcon tube filled with either of the liquids, followed by vortexing and sonication. In the case of ES-saturated MilliQ water, the surface tension had been lowered to ca. 69 mN/m initially but quickly increased back to the reference value of ca. 73 mN/m within 2 minutes due to the evaporation of ES from the surface as can be seen in Figure IV.43.

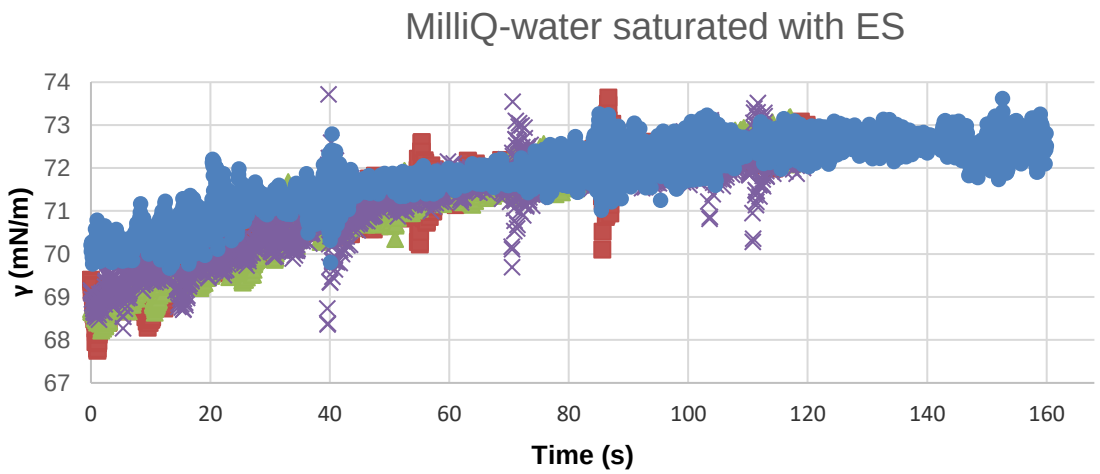

Figure IV.43: Surface tension measurement as a function of time for four individual drops of purified water, that was saturated with ethyl salicylate. It can be seen that the surface tension increases from ca 69mN/m back to the reference value of ca. 73 mN/m for water. This indicates that the ethyl salicylate evaporates from the water surface.

With the ES-saturated SDS-solution, a similar effect could be observed. Here, the initial surface tension was ca. 33.2 mN/m and it linearly increased to ca 35.2 within the measuring time of 10 minutes (see Figure IV.44).

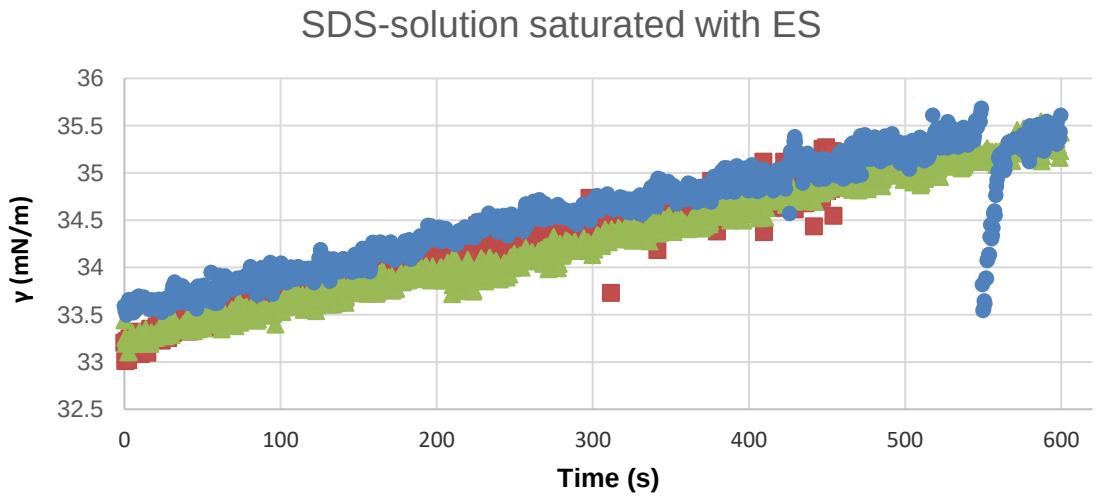

Figure IV.44: Surface tension measurement as a function of time for three individual drops of a 10g/l SDS-solution that was saturated with ethyl salicylate. It can be seen that the surface tension increases linearly from ca 33 mN/m back towards the reference value of ca. 37.8 mN/m for a 10 g/l SDS-solution over more than 600 seconds. This indicates that the ethyl salicylate evaporates from the surfactant solution surface at a much slower rate than for pure water as the surfactant increases ethyl salicylate surface solubility.

As this increase appears to be linear, the liquid would presumably approach the measured refence value of a pure SDS-solution surface of 37.9 mN/m within 15 minutes. These numbers indicate that, deposition of ES to the SDS-solution surface does decrease the surface tension slightly and increases again via evaporation. Presumably according to [REF], the surface tension after deposition of ES would increase above the 37.9mN/m due to removal of both ES and SDS from the surface in a dissolution reaction. However, with the hanging droplet setup we could not come up with a good way to measure that. If the bulk is already saturated with

ES, the experiments show that the removal of ES from the surface can only occur due to evaporation and is slower compared to pure water.

IV. 3.3 The mechanism for collective droplet behavior

The mechanism of the movement and the droplet interaction has not definitively been determined but several mechanisms have been proposed[14,52,54]. According to the literature, movement of droplets is driven due to the depositions of ethyl salicylate onto the surface which is covered with a layer of surfactant (SDS). The ES and SDS molecules can combine to form aggregates that go into solution in the bulk aqueous phase. This will remove SDS and ES from the water surface, momentarily increasing the surface tension more than just from removal of ES. This triggers a convective surface flow until the SDS is replenished from the bulk. As the bulk aqueous phase and atmosphere becomes saturated with ES over time and the rate of the dissolution reaction with SDS decreases. This will result in smaller surface tension gradients since less ES and SDS can be removed from the surface. Due to the lowered force created by the decreasing surface tension gradients combined with the assumption that there can be a stable, non-uniform, directional flow of ES as indicated by [52], droplets get locked towards each other in configurations stabilized by the ES flow and eventually caught in capillary attraction.

Here I propose the mechanism for the standard ring-forming setup, going through the different stages:

Stage I: active droplets

Bulk and atmosphere are far from saturation (i.e., a system far away from equilibrium). Movement is driven by ES deposition (ES+SDS on surface close to droplet lowers surface tension), simultaneously at some distance it has been proposed that the droplet SDS can form micelles/aggregates with ES on the surface and go into the bulk[14,54]. This dissolution reaction can ST significantly as both SDS and ES are removed from the surface. These two ST-changing interactions create a reaction-diffusion system of ST gradients[14]. The droplets are repelled from each other at short distances and attracted at longer distances when both ES and SDS are removed from the surface by micellization (working above critical micelle concentration of SDS) [54]. It would seem that the rate removal of ES through dissolution as well as evaporation at this stage is faster than the rate of deposition. A graphical representation of this can be seen in Figure IV.45.

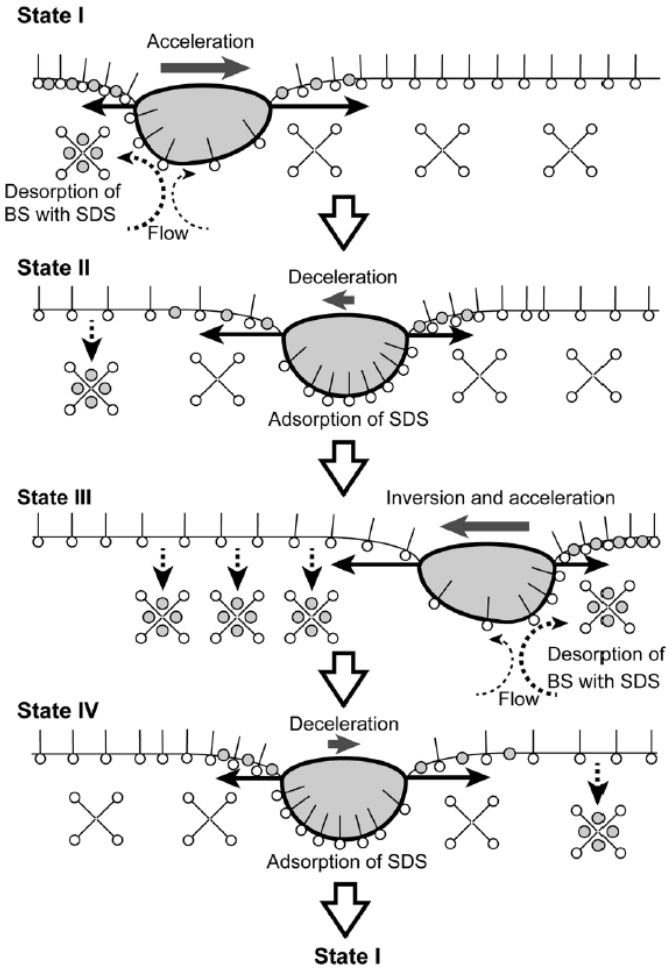

Figure IV.45: Graphical representation of the reciprocal motion mechanism of a butyl salicylate droplet on a surfactant solution. Figure from Satoh et. al. 2017[14].

Stage II: Droplets start to slow down and start to form vibrating clusters.

At this point removal of ES from the surface slows down as concentration of ES increases in the atmosphere and bulk. i.e., According to the Le Chatelier principle this should start to decrease the rate by which ES is removed from the surface by evaporation and dissolution. As a result, the rate of deposition and removal is close to equal, thus flattening the surface tension gradients. Therefore, the droplets can be seen in clusters, vibrating close to each other. Presumably at this point already areas of very high surface tension where ES and SDS have been removed from the surface completely, do not occur anymore. The rate of SDS supply from the bulk should be constant and SDS is replenished just as fast as it is removed together with ES. The vibration may be due to local increases in ES surface concentration close to the droplet i.e., deposition by droplets and removal by dissolution, evaporation and diffusion while SDS surface concentration stays constant. As immobilized ES-droplets have shown non-uniform deposition of ES onto the surface [52] it may be that we already start to see slightly ordered structures at this stage due to a non-uniform ES-deposition geometry.

Stage III: Formation of chains

As ES-concentration in the bulk and atmosphere keeps increasing, removal of ES from the surface continues to decrease. As the removal is the limiting factor of inducing ST gradients, these gradients become smaller which results in less repulsive force between individual droplets. With the decrease in activity of droplets, capillary attraction can overcome repulsion and lead to the slow formation of droplet chains in which the droplets are partially immobilized. It has been demonstrated that immobilized ES-droplets have an altered convective flow with directional ES deposition into two opposite directions[52] (See comparison of a single droplet to a short chain in Figure IV.46). It is plausible to assume that this stabilizes the formation of chains. A further possible stabilizing factor may be that, due to the higher average surface concentration of ES, the rate of deposition from droplets is limited such that a faster bidirectional convective flow around the droplet is favorable over a slow omnidirectional/circular convective flow. The collective deposition of ES by these chains will propel them. We also observe formation of shorter chains in an open system as well as a system which has a much higher ratio between bulk volume and droplet volume but in the original experiment of 50 droplets in a 90mm dish, chains elongate further. In the open case evaporation of ES from the surface is a factor that creates enough local minima of ES-concentration that droplets in shorter chains tend to distribute over the whole dish. In the case of a large dish with few droplets the available atmosphere (dissipation though non-hermetic lid may be enough to keep ES-concentration in air low enough) and bulk volume can absorb much more ES.

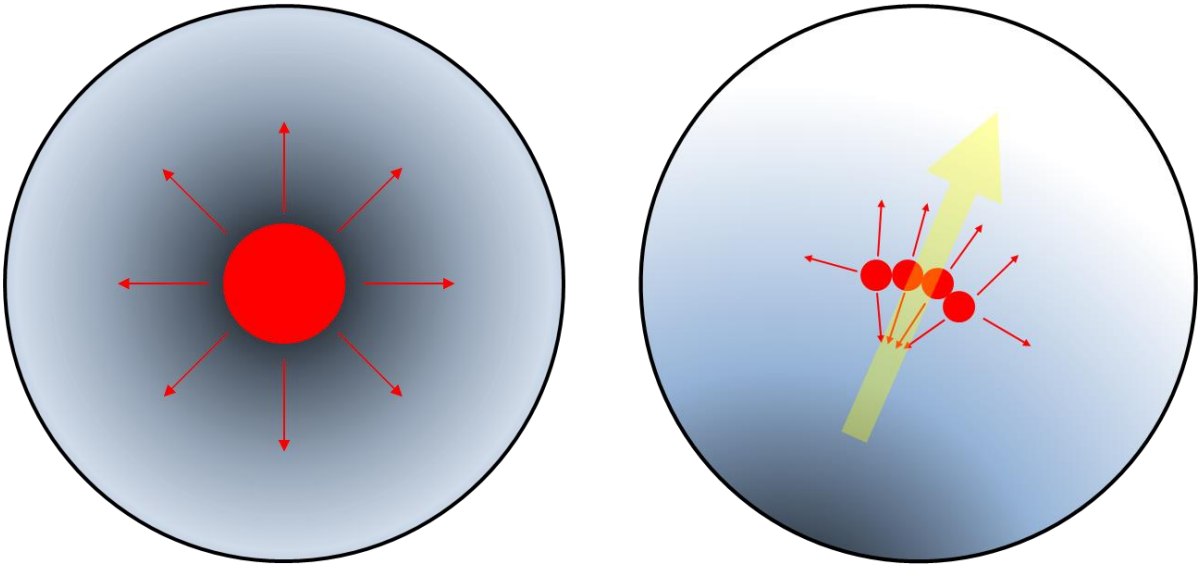

Figure IV.46: Left dissipation of ES from single droplet. Goes in all directions with minor stochastic fluctuations which finally will cause it to move into a random direction. Right: Short chain of droplets. Immobilized droplets in the middle only dissipate ES into two directions. Minor fluctuations or a barrier will cause a chemical gradient which will determine movement direction of the chain.

Stage IV: Ring formation. Rings periodically collapse and reform

Bulk partially saturates while atmosphere fully saturated. As the atmosphere becomes almost fully saturated with ES, the resulting low activity leads to very long chain clusters. These chains induce more ordered directional surface tension gradients creating only few local maxima towards which they will orientate and move. As a result, curvature of the chains increases which will eventually lead to the formation of rings. These rings then grow until they are composed of one long circular chain that eventually breaks by opening at one or two spots followed by a collapse and repetition of the process. In order to explain this behavior, we need to consider the following points:

i. The atmosphere is already more or less saturated with ES so that any ES on the surface has nowhere to go but to the bulk.

ii. ES may be removed from the atmosphere slightly near the edge as the container is not hermetically sealed.

iii. In experiments where we observe collapsing rings the area outside the fully extended ring of droplets is larger than the area inside.

When the droplets are in a ring formation the deposition of ES is ordered in such a way that it flows circularly away from the ring and towards the middle of the ring. Let us consider the surface tension at the following three areas:

1. At the center of the ring, γ_C, where ES is removed from surface by dissolution such that only SDS is present on the surface (maybe even lowered concentration if dissolution is faster than supply rate from bulk)
2. Outside the ring γ_O, where ES is removed from surface by dissolution such that only SDS is present on the surface (maybe even lowered concentration if dissolution is faster than supply rate from bulk)
3. Close to the ring (inside and outside), γ_R, where ES is supplied to the surface (ES+SDS on surface)

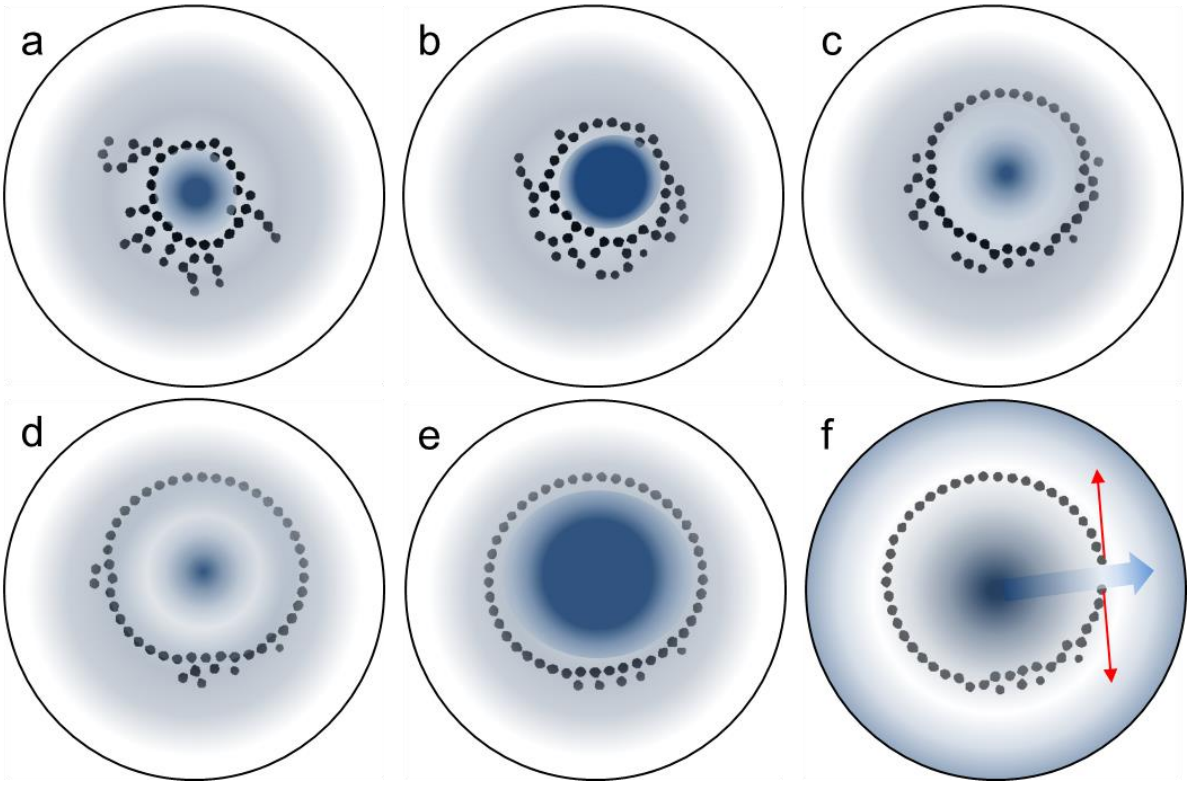

Figure IV.47: This figure illustrates the growth of a droplet ring up until it collapses. The blue shade is an attempt to visualize the surface tension gradient magnitude inside the ring. From (a) to (b), the concentration of ES on the inside of the small ring is increasing more than outside the ring as the area is much smaller than the outside area. This creates a surface tension gradient that will drive the ring to expand. It expands from (c) to (d) which constitutes a sort of relaxation of the system during growth as the increasing area decreases the surface tension gradient. This increase in area can only occur as long as there are droplets available to be incorporated into the ring. After this point, (e), the gradient inside the ring will start to increase again as the area inside is smaller than the area outside while ES is being deposited to both. Once the surface tension gradient between inside and outside the ring results in a force of flow larger than the capillary attraction between droplets, the ring opens and releases the higher concentration of ES to the outside (f).

Initially let us assume that at the moment a ring has formed, γ_C and γ_O are equal and both larger than γ_R (gradients: $\frac{\gamma_C}{\gamma_R} = \frac{\gamma_O}{\gamma_R} > 1$) (Figure IV.47a). If we also assume that deposition rate of ES from the droplet ring is equal in both directions, $\frac{\gamma_C}{\gamma_R}$ starts to decrease while on the smaller area, the deposition rate of ES will become larger than the rate of removal through dissolution (Figure IV.47b, no evaporation as stated in (i)). Now $\frac{\gamma_O}{\gamma_R} > \frac{\gamma_C}{\gamma_R}$ and the ring will expand as long as there are enough droplets around to be incorporated. As the expansion continues, the area inside the circle increases while the area outside decreases so $\frac{\gamma_C}{\gamma_R}$ is increasing towards the value of $\frac{\gamma_O}{\gamma_R}$ (Figure IV.47c-d). Once all of the droplets are incorporated into a single-chained ring, the two gradients are close enough to each other for a while that the capillary attraction of the droplet chain can withstand the pressure of the difference between the two gradients. But the two gradients depend on the area (in an experiment with 50x20ul droplets on a 90mm dish the inside area is approximately 40% smaller than the

outside area) and there may be some evaporation of ES near the edge. As soon as the expansion stops when all the droplets are in use, the inside gradient starts to decrease again (Figure IV.47e) until capillary attraction is insufficient to keep the ring together and the ring opens up. Now ES can flow from the inside to the outside of the ring, which collapses it (Figure IV.47f).

Stage V: Rapid formation and breaking of rings which are not fully unilamellar.
Atmosphere fully saturated and bulk close to saturation. During the ring stage (which can in some cases last for several hours, a lot of ES is being dissolved in the bulk. As the bulk is approaching saturation with ES, the dissolution reaction rate decreases further. This leads to more rapid destabilization of the rings as low ST states (ES+SDS) in the middle are obtained faster. Simultaneously the surface becomes more and more saturated with ES such that the short-range repulsion gradients of the droplets become so small that capillary attraction is stronger than the repulsion by the ever-decreasing surface tension gradients (fusion is prohibited by the surfactant stabilizing the droplets) such that clusters containing droplets with more than two links.

Stage VI: crystallization/death
Once the bulk becomes fully saturated with ES, all droplets are caught in capillary attraction and are not able to create any ST-gradients. The surface at this point is permanently saturated with ES+SDS such that ST-gradients occur only seldom.

Stage VII: Post death revival
If lid is lifted, ES can evaporate from the surface (increases surface tension), breaking the close packed structure (Figure two snaps before and after lift). Droplets can once again deposit ES to the surface. This creates a renewed repulsive surface tension gradient. Activity is low because no or very low dissolution to the bulk.

This proposed mechanism based on the saturation of atmosphere in bulk and ethyl salicylate flow geometry also explains all of the other behaviors of ES-droplets that were presented in this part. However, it should be emphasized that some mechanisms mentioned here still lack good experimental evidence such as the dissolution reaction between SDS and ethyl salicylate and the suggested anisotropic deposition of material from "immobilized" ES-droplets.
Population density and area coverage by droplets: at low population density and coverage we observed no ring formation because the system is not limited by size and the bulk phase has

a larger volume (longer time to get saturated), so droplets will be more spread out which leads to smaller clusters along with much longer experiment times until close packed stage. In fact, the behavior is very similar to a reference experiment performed without a lid at R=90mm and N=50 at which configuration e normally would observe ring formation. Without the lid, the air acts as an infinite sink for ES instead of the finite sink in bulk as described for the large dish. With an open lid we did observe close packed structures but not in one single cluster indicating that the bulk was almost saturated (more than one link) but some gradient could be maintained due to the evaporation. In the very densely populated experiment, we did see rings forming and due to the limited space, the remaining droplets would form secondary rings along the outer ring resulting in the observed two-dimensional soap bubble. It indicates, that the ring structure is an optimized geometry if space and ES-deposition is limited. That symmetry plays an important role was also shown during initial experiments with the two different dyes where we observed a difference in the time of first occurrence and stability of rings formed. At slightly higher numbers of droplets the system matures quicker and the more crowded environment promotes formation of larger clusters. With more droplets in the ring the difference between the surface inside the ring and outside becomes more equal thus keeping the ring stable for much longer times.

The difference between red and blue droplets, considering all of the performed experiments, comes down to a difference in ES-deposition rate and geometry. We were not able to determine the exact difference and mechanism for this but we showed that the two used dyes have a different influence on the interface between the droplet and the bulk surfactant solution, with Sudan black B decreasing interfacial tension more than Oil red O. This decreased interfacial tension would also explain why blue droplets were more likely to fuse and would extend further down into the bulk (higher density along with lower interfacial tension results in higher curvature according to Young-Laplace equation and Pascals law as curvature of a droplet is determined by interfacial tension and gravity.

The reduced Laplace pressure resulting from the reduced interfacial tension could also be responsible for the decreased emission of ES from the droplets containing Sudan black B.

With this we have obtained an improved picture of the collective ES-droplet behavior although the ongoing digitization of the experiments described here could reveal more information. Nevertheless, there is still need for continued experimentation along with modeling of the system to fully understand what is happening. This could include a series of experiments where all the parameters are kept constant except for the number of droplets, volume of the bulk or the concentration of the dye. Another useful experiment would be to find a dye that does not influence the behavior or attempt capturing the movement of droplets without dye,

using polarized light. Also investigating the side profile of droplets over time may be very interesting. We did perform such an experiment with both blue and red droplets together in a reservoir and saw that the contact angle changed significantly over time (Figure IV.48). It also seems from those initial results that the blue droplet over time is getting larger than the red one.

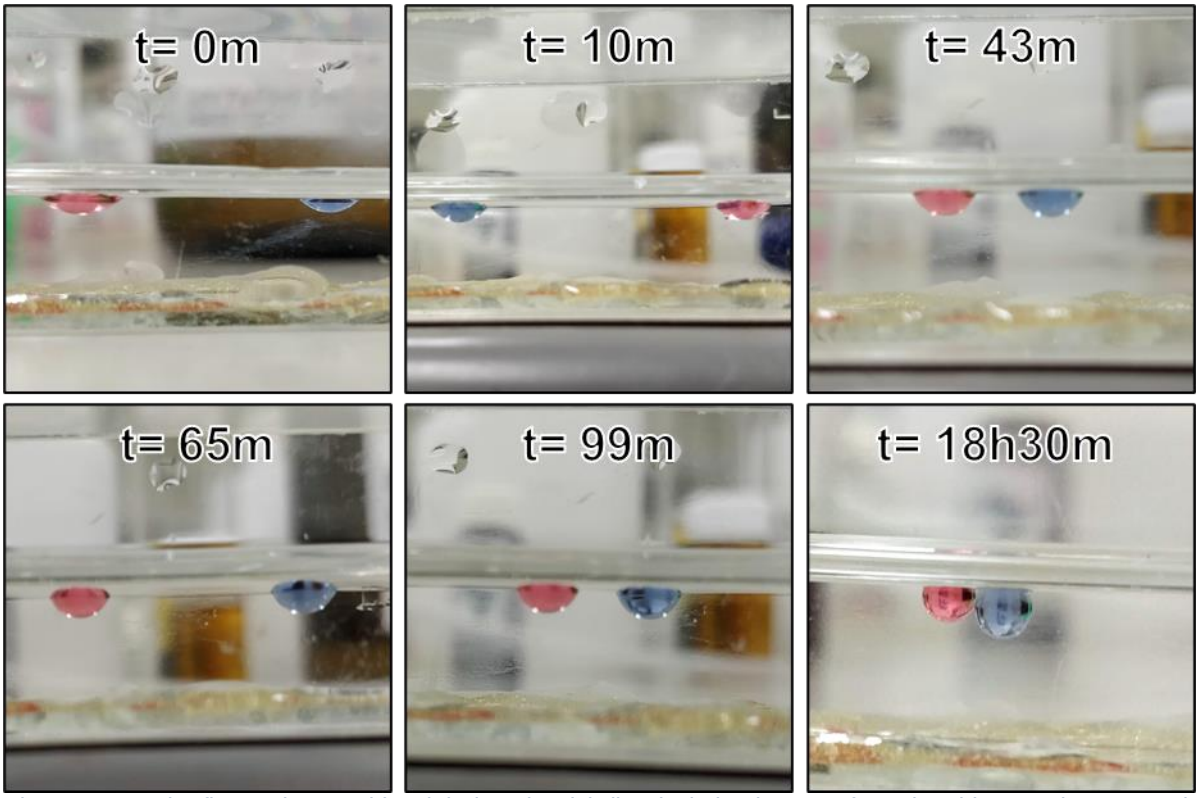

Figure IV.48: The figure shows a blue (SbB) and red (Oil red O) droplet seen from the side over time. It can be seen that the contact angle does change considerably over time. Furthermore, there may be some change in volume of the droplets with the blue droplet growing over time which could indicate some mass transport from droplet to droplet.

This is either due to perspective (as the droplets could move slightly towards or away from the perspective) or possibly due to ES or paraffin transport through the bulk and surface, combined with the different Laplace pressures of the droplets (in the last picture in Figure IV.48 after 18h it seems to be larger regardless of perspective). While this is an interesting result, we need to investigate the droplets individually and have a more controlled setup so this should be considered a very preliminary result. We have also begun to do preliminary experiments with hybrid droplets containing multiple dyes as well as changing the geometry of the boundary but this will have to wait until we have fully analyzed the data we have so far.

IV. 4 Ethyl salicylate droplet interaction with other surface-active droplets

During experiments discovered that ES is a strong solvent for amphiphilic weak surfactants on the water surface. Ethyl salicylate deposited onto pure water surface will not form droplets but instead violently dissipate. However, if a drop of an amphiphilic oil is placed first to form a monolayer, the es drop will be stable. At that point and additional droplet of the amphiphilic substance can be added to the surface. For example, this can be done using decanol where the ES-droplet dissolves decanol from the surface which results in chemical gradient that triggers a surface flow. This surface flow attracts the decanol drop to the ES drop (presumably due to different densities and drag forces). As the droplets approach the ES droplet will move away from the decanol droplet. This sort of interaction was first observed on a one-dimensional channel (see Figure IV.49 and Movie 41) and later in an open 2D-system (Movie 42). Previously this had been attempted using oleic acid mixed with paraffin however in such a case, the ES-droplet would catch the oil-droplet and fuse with it immediately. Using decanol this does not occur and thus the chase lasts for a much longer time. These preliminary results provide a strongly responsive systems that can be used for experimental studies on so called wolf and sheep or predator prey models and is arguably much more simple and easy to work with than others [58,61,126]. I plan to study this type of system extensively in my future work.

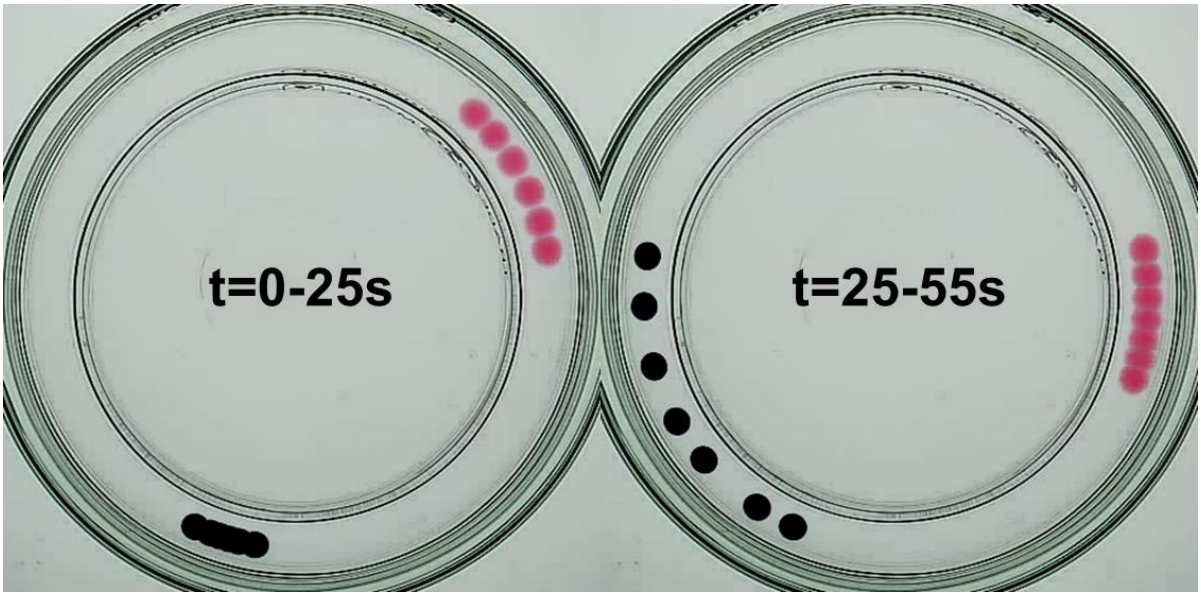

Figure IV.49: Predator and prey droplets on a 1D periodic channel. It can be seen how the red decanol droplet moves towards the black ES-droplet. At a certain distance the ES-droplet accelerates away from the decanol droplet.

IV. 5 Conclusions

The projects presented in this part show how curiosity combined with unexpected discoveries can lead to new interesting questions and projects. In the first part, a new soft matter self-propelled system was introduced which in essence is a soft matter version of a camphor particle. During this work I made the accidental discovery that the dye Oil red O has an effect on certain oil-water interfaces. This is a very important result because Oil red O is one of the most commonly used dyes for the coloring of self-propelled droplets[73,79,127]. We found that for paraffin, the magnitude of the effect on the interfacial tension with water scales with the concentration of the dye. Thus, we could control and predict droplet behavior by changing parameters such as camphor and Oil red O concentrations. The exact mechanism that occurs at the oil-water interface and leads to the reduction of the interfacial tension remains unknown and should be further investigated since it is not expected based on a common chemical intuition.

I was also able to further investigate the ethyl salicylate droplet behavior on a surfactant solution. During that project I investigated the collective behavior of such droplets depending on factors such as crowdedness, type of dye and concentration of dye. This gave further insight into the mechanism that governs the time evolution of such systems. I was able to make a good case for my suggestion that it is governed by the slow saturation of the closed atmosphere as well as the bulk surfactant solution with ethyl salicylate. However, several aspects of this need to be further investigated in the future. By measuring surface tensions at the various interface involved in the system I discovered that unlike for the paraffin-droplet system, the ethyl salicylate droplets interfacial tension with the surfactant solution is influence more strongly by Sudan black B than by Oil red O. In fact, it turns out that Oil red O only had an effect on the interface when paraffin present in the droplet as well. For Sudan black B the effect was present for the interface between ethyl salicylate and the surfactant solution and was increased when the oil phase consisted of an ES-paraffin mixture. This dye-dependent interfacial tension results in different individual droplet activity as it presumably affects the mechanism of ES supply from the droplet to the bulk and the surface of the surfactant solution. By combining the two types of droplets at different ratios, the collective behavior could change significantly as there occurred a phase separation between the two based on their motility. Also, in this case further study of the dyes acting as "interfactants" is warranted.

By combining the ethyl salicylate droplets with other known droplet systems like decanol droplets, I discovered a new responsive system of active matter in which one droplet chases another that moves away. This system has only been subject of very preliminary studies thus

far but is of great interest to us as it displays a predator prey mechanism which ah not been shown for macroscopic droplet systems thus far and to the best of our knowledge.
All of the described systems have predictable behavior based on complex mechanisms. With the knowledge of which parameters affect the behavior, these droplet systems essentially become programmable and could thusly be of potential use in the field of soft robotics[13,78].

V Conclusions and Outlook to the Future

The goal of my Ph.D. project was to introduce new materials and experimental setups useful for studies on self-propelled active matter. This goal was achieved for the various projects described in this thesis. I have proposed new hybrid materials that seem to be perfectly suited for experiments with self-propelled objects, investigated the role of dyes in active matter and suggested new setups allowing for more precise measurements of far-from equilibrium evolution. The milestones include:

Rotational camphor boat

An improved setup was developed and tested for long term studies of camphor boat motion on a water surface depending on changing diffusion distances of camphor underneath the boat [36]. This setup consisted of fixing the boat motion on a 1D circular trajectory by attaching it to an arm that rotates on a fixed axis. The preliminary long-term motion experiments showed that modes of motion do depend on the distance between the camphor pill underneath the boat and the closes boat edge. These modes included standstill, continuous motion, intermittent motion, vibratory motion and inversive motion. However, the interesting additional information gained by the possibility to perform very long experiments over multiple hours was that the modes can change multiple times over longer time scales and could even go into modes of motion that were completely unexpected at given pill distances. This indicates that the mode of motion is tied to the pill position as a probability (for example: pill is close to the edge – highest probability is continuous motion). In the future we plan to gather enough experimental data to describe how the probability distribution of types of motion changes with the position of the pill. This will be done by further development of this setup by improving the precision of the pill positioning and boat geometry. Square instead of round pills will enable a better fit, when pressed into a boat, avoiding the use of glue which else is a potential source of error. The boats can be more precisely made by using machining tools to cut them out of different materials or though 3D-printing. The gathering of data can be improved by controlling the optics of capturing the motion better by removing light artefacts etc. Finally, the treatment of digitized data could be further optimized in regards to computation time (considering that the datasets for such long experiments become quite substantial)

Hybrid materials

With the camphor-camphene wax and the camphor-camphene-polypropylene plastic we found the perfect materials for inexpensive and simple investigation of self-propelled objects of different shapes on water surfaces. It enables theoreticians to rapidly test their models in a real environment[39,43,44]. Furthermore, systems that are easy to set up without sophisticated equipment or large budgets are giving broader access to researchers and innovators that are interested in the field of active matter. Due to the malleability, almost any shape can be fabricated from either material at any desired ratio of components. For the camphor-camphene wax the composition was found to influence the behavior in terms of velocity. This enables experiments investigating the trajectories of equivalent shapes with different speeds of self-propulsion which even could be applicable for experimental studies on hydrodynamic drag depending on shape (a very difficult phenomenon to model [128,129]). The camphor-camphene-polypropylene plastic on the other hand has improved ease of use since the added polymer removes the stickiness of the material. It also makes motion less dependent on the camphor/camphene ratio as it forms a microporous scaffold inside the material, which equilibrates the deposition of surface-active components to the water surface. Thus, the material allows for repeated investigations on trajectories of different shapes as the scaffold-passivating effect counteracts inaccuracies that can occur during production of the material.

For future work we plan to use these hybrid materials to fabricate higher-order hybrid materials. As we can control the shape, stickiness and speed, both materials in combination with each other or any other object could be combined to make objects that have local differences in their interaction with the water surface. By including other materials and possibly chemistries, the plan is to enhance these materials to become responsive to their environment, similarly to some self-propelled droplet systems [59,68]. Such objects would be similar to Braitenberg vehicles[113] and therefore be applicable in the area of soft robotics [13,75,77].

With the discovery of a microporous polymer foam as a side product from the camphor-camphene-polypropylene material, we have come up with an inexpensive method for the production of microporous foams in large quantities that can enable innovators to search for possible applications in a cheap and facile way. As all of the components involved in the production in those foams are volatile it even enables a partial or complete recovery of the reagents: camphor, camphene, ethanol and acetone by simple distillation. This would make

the production a green process which are of great interest to industrial entities[130]. The foam itself has very beneficial properties as the microporous rough surface is superhydrophobic [103,105] and strongly absorbent towards non-polar liquids which has obvious potential applications such as cleaning contaminated water surfaces or in filtering processes. Furthermore, keeping closer to the topic of self-propelled materials, the absorbent ability could be exploited to obtain a new type of self-propelled object that similarly to filter papers[31] can be "loaded" with a surface active liquid or act as a sink for deposited chemicals on the water surface. Especially in combination with for example sticky camphor-camphene wax it could provide a multifunctional hybrid material for soft robotics applications.

Self-propelled droplets

During my foray into the world of self-propelled oil droplets, I was able to experience a chain of discoveries leading to new projects. By simple dissolution of the surface-active camphor in paraffin oil I discovered a new self-propelled droplet that moves on a water surface. The experiments performed on this new droplet system, led to the discovery that the dye Oil red O (which is commonly used as way to better visualize self-propelled droplets) can have a significant effect on the interfacial tension between the droplet and the water phase. We were able to map out the behavior of paraffin droplets depending on changing concentrations of camphor and Oil red O giving us the ability to produce a droplet with a certain behavior within those parameters.

The discovery of the dye influence of Oil red O on the interface between oil and water was a surprising one since a glance at the chemical structure of the dye does not suggest such interactions. This led me to work on the self-propelled ethyl-salicylate droplet on a surfactant solution system as there were indications that the dye would also influence the individual and collective behavior of such droplets[125]. Existing results[10,79,125] were confirmed, showing that the collective behavior of droplets follows a more or less fixed evolution of free movement turning into the formation of droplet chains and eventually hexagonal close-packed clusters. During the chain-cluster stage the shapes of clusters appear to influenced by the crowdedness and boundary conditions of the system. The two different dyes, Oil red O and Sudan black B, which were investigated, were shown to have an influence on the individual activity of the droplets which lead to a temporal shift of the stages in the time evolution of collective droplet behavior. It was also found that mixing the systems led to activity induced segregation of blue and red droplets (Sudan black B and Oil red O, respectively). I suggest a mechanism of the collective droplet behavior, based on the phenomenological observations and the investigation

of interfaces of the aqueous phase with the droplets and the atmosphere. According to this, the collective behavior is a result of a gradual saturation of the closed atmosphere and bulk surfactant solution with ethyl salicylate. In the future we want to further investigate the behavioral landscape of this system for example by mixing several dyes in a single droplet and changing the geometry of the system boundary. Furthermore, we want to investigate how these dyes influence the oil/water interface on a molecular level as such "interfactants" (influence oil/water interface but not surface of the oil or water) are not well studied and could have real world applications[131,132].

Working on the ethyl salicylate system also led me to the discovery of a new predator-prey droplet system where a decanol- and an ES-droplet were placed on a pure water surface (in that order). The decanol droplet in this interaction is attracted to the ES-droplet which on the other hand is repulsed by the decanol droplet as it approaches. This a very interesting system that we want to further study in the future as it, to my knowledge, is the first macroscopic artificial system with such a predator prey interaction[58] and is therefore expected generate interest in the active matter[2], artificial life[75] and soft-robotics[77] communities.

Final remarks

As the goal was to discover new materials for studies on nanostructures and spatio-temporal patterns self-organized by surface phenomena, the work done for this thesis was on a broad spectrum within the area of self-propelled materials. I was able to build up a repertoire of simple but fascinating experimental systems that inspire a wealth of future research projects involving active matter with life-like behavior.

VI **Experimental**

VI. 1 Analysis methods

VI. 1.1 Digital recording of system time evolution

Instrumentation and Materials: Three types of cameras were used to obtain video footage of the different self-propelled systems presented in this thesis. The main shooter used for experiments at ICHF laboratory was a NEX VG20EH from SONY with which experiments were filmed from above at 25 frames per second. For experiments performed at the University of Trento two different cameras were used: A Logitech C920 Webcam (30 fps from above) and Baumer VCXU-04C USB-3 camera (Also used for some experiments performed at Hiroshima University) with a 16 mm fixed focal length (Edmond Optics 33-304) which could be mounted to film experiments from above or below using a transparent polycarbonate box. Experiments were in some cases lit from above or below (depending on camera position) using a flat panel LED. Footage was either saved on the camera on SD-card or directly recorded to a laptop.
Processing of movies and data: Raw footage was concatenated, cropped and compressed to .mkv format using the FFMPEG distribution[133]. FFMPEG was also used to edit the footage in any additional way as well as to extract individual frames from the footage. Additional image processing and object tracking was done using the ImageJ software[134]. All extracted data was further processed and quantified using Mathematica[135] which also could be used to do some image processing.

VI. 1.2 SEM-Microscopy

Instrumentation and Materials: Zeiss FESEM-Supra 40 Field emission scanning electron microscope, sample mount, conductive carbon adhesive tape and plasma sputtering coater.
Measurement procedure: Polypropylene foam samples (see Section VI. 3.3 for preparation procedure) were cut into small cubes, mounted to the specimen mount using conductive carbon adhesive tape, placed in the plasma sputter coater and coated with a thin layer of platinum. The prepared samples were then imaged at different moderate magnifications.
Remarks: Special thanks to Lorenzo Moschini from the Department of Industrial Engineering and Biotech Centre at the University of Trento for supervising the sample preparation and performing the measurements with me.

VI. 1.3 Tensiometry

VI. 1.3.1 Wilhelmy plate method

Principle: If a plate (usually made of platinum which has a high wettability) of known perimeter is fully wetted around the perimeter (contact angle θ is zero), the surface tension γ of the liquid will be equal to the downward pulling force (F measured in mN/m) divided by the length of the plate perimeter ($l = 2 * width + 2 * length$) (see equation 1 and Figure VI.1):

$$\gamma = \frac{F}{l * \cos\theta} \quad (1)$$

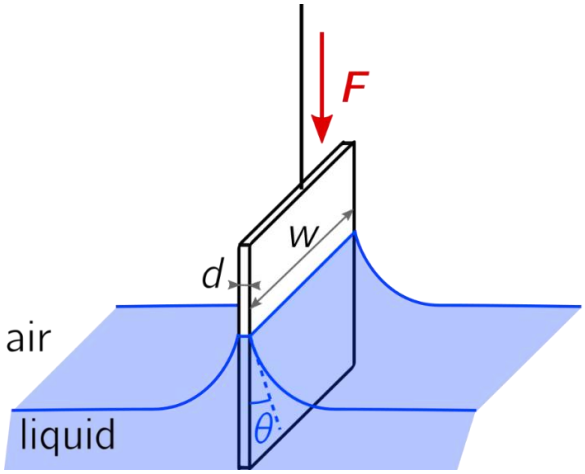

Figure VI.1: Graphical representation of Wilhelmy plate method. Image from Wikipedia[136]

Instrumentation and materials: Microbalance attached to Langmuir-Blodgett trough (Langmuir BAM 601 scale (Nima Technology Ltd., UK) using PS-4 surface pressure sensor), platinum plate, filter paper and 5cm Petri dish.

Measurement procedure: The microbalance was calibrated using a precise calibration weight and factoring in of the Wilhelmy-plate (Platinum plate or cut filter paper) contact perimeter. Samples of liquid in question were added to a 5cm Petri dish located underneath the balance. The plate was lowered until it was wetted around the perimeter and then raised until it released from the liquid. The highest measured force (at the point when the contact angle is 0) is taken as the surface tension. In between measurements (at least three per sample) the plate was then either washed with chloroform and burned off.

VI. 1.3.2 Pendant droplet method

Principle:

The pendant droplet method is an optical method to investigate surface and interfacial

tensions. For this method a hanging droplet suspended in a lighter phase (usually air) is photographed, backlit at a fixed distance to obtain a strong contrast. From this information about the shape and curvature of a droplet with a known density and volume the surface tension can be determined. This shape analysis is based on the Young-Laplace equation which put into relation the pressure difference between areas inside and outside a curved interface (Laplace pressure, ΔP)with the interfacial tension (γ) and the principal radii of curvature (R_i)[137]:

$$\Delta P = \gamma \left(\frac{1}{R_1} + \frac{1}{R_2} \right) \tag{2}$$

Since in the case of a hanging droplet, the shape is determined by gravity elongating the droplet and surface tension counteracting this by minimizing the surface area (the higher the surface tension, the higher curvature). From this, the surface tension can eb expressed as:

$$\gamma = \frac{\Delta \rho g R_0}{\beta} \tag{3}$$

Where $\Delta\rho$ is the difference in densities of the two phases, g is the gravitational constant, R_0 is the radius of curvature at the drop apex (at apex: $R_0 = R_1 = R_2$). Finally, β is the shape factor which can be determined from the Young-Laplace equation parameterized through the arc length s and expressed as three dimensionless first-order differential equations as can be seen in Figure VI.2[138].

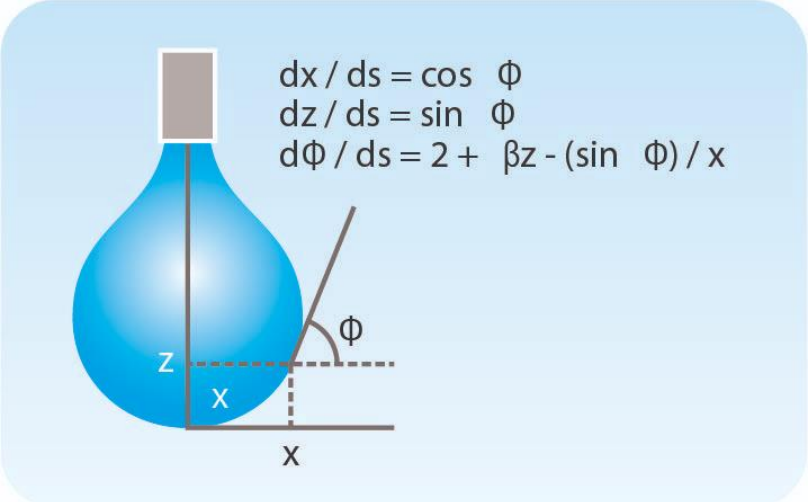

Figure VI.2: Graphical representation of a pendant droplet along with the Young-Laplace equation expressed as 3 dimensionless first-order differential equations parameterized by the arc length, s, of the drop. Figure from [138].

This can be numerically solved by the tensiometer software, fitting a curve to the droplet image. With known densities and volume, this yields the surface or interfacial tension.

Instrumentation: Biolin Scientific Theta Life pendant droplet tensiometer, cuvette, Syringe pump, syringe, tubing, straight needle and inverted needle (both 2mm in diameter).

Measurement procedure: For air-liquid surface tension measurements, the sample was loaded into the syringe to which one attaches the tubing and the needle was mounted in the instrument. Using the controller software by Biolin, a drop of a controlled appropriate volume was extruded and the measurement is made over time. For multiple measurements, the drop was fully extruded and a new one at equivalent volume was extruded. For interfacial tensions, a cuvette was filled with the lower density phase and the same procedure was performed. If the lighter phase was not transparent, an inverted needle with an opening pointing upwards could be used. When exchanging samples, the needle, tubing and syringe were thoroughly flushed with ethanol, acetone and chloroform.

VI. 1.3.3 Langmuir-Blodgett trough surface pressure Isotherm of different dyes

Instrumentation and materials: Langmuir-Blodgett trough with surface pressure meter (Kyowa Interface Science Co. Ltd., HMB, Saitama, Japan), Wilhelmy plate, syringe.
Solvent: Chloroform
Measurement procedure: The dye in question was diluted at a known precise concentration (0.32mg/ml) from a stock solution. 31.5 µl of the solution was dropped a pure MilliQ water surface in the trough such that the number of molecules is known. The barrier was then moved to decrease the area from 210 to 21cm^2 at a scanning speed of 16.5 cm^2/min while the surface pressure was measured continuously. The water temperature was 24 ± 1℃. Three measurements were performed to confirm results.
Remarks: Special thanks to Yuta Yamaguchi from Hiroshima University for assisting with obtaining the surface pressure isotherms.

VI. 2 Experimental setups

VI. 2.1 Rotating camphor boat

Materials: Aluminium sheet, plastic sheet, 20cm Petri dish, needle, metal standoff, LOCTITE 454 glue, 3mm pill press.
Instruments: Camera (digital camera NEX VG20EH, SONY)
Chemicals: (1R)-(+)-camphor (98% purity, CAS: 464-49-3, Sigma-Aldrich), water (Purified using Millipore ELIX5 system)
Procedure: An aluminium or plastic film sheet of dimensions 0.2x6x10mm or 0.2x6x15mm was folded on two sides to obtain either a 10mm or 15 mm long rectangular boat. A 70mm arm with a hole in one end made of plastic film was glued to the boat. A metal standoff with

a thin metal needle was glued to the middle of a 20cm Petri dish. Using a pill press, a round pill of camphor with a height of 1mm and a diameter of 3mm was prepared. For each experiment such a pill was glued underneath the boat at different distanced from the edge. The dish was filled with MilliQ water to gain a 4mm thick water layer. Then the boat arm was stuck on the needle-axis. The boat rotation was filmed with a top mounted digital camera NEX VG20EH, SONY for up to 5 hours. A black marker was placed on the boat to aid the later tracking of positions in post. For the analysis of the data see Section VI. 1.1. All experiments were performed at room temperature (22 ± 2 ℃).

VI. 2.2 Self-propelled shapes on a water surface

Materials and instrumentation: Sony or Baumer camera (See Section VI. 1.1), LED flat panel, Petri dishes (9, 11, 12 and 14cm), 4mm pill press, nitrile gloves, scalpel, syringe, hot water bath.

Chemicals: (1R)-(+)-camphor (98% purity, CAS: 464-49-3, Sigma-Aldrich), camphene (95% purity, CAS: 79-92-5, Sigma Aldrich), polypropylene pellets (CAS:9003-07-0, Sigma Aldrich), MilliQ purified water.

Procedure: For simple pill preparation, the material (camphor, camphene, camphor-camphene-wax or camphor-camphene-polypropylene plastic, see preparation of wax and plastic in Sections VI. 3.1 and VI. 3.2 respectively) was pressed into a pill using a 4mm pill press. In the case of pure camphene or wax/plastic with high camphene content, the press and the material were cooled down to -18℃ prior to pressing it into shape.

Non-trivial shapes were prepared either by forming the material (wax or plastic material) by hand while wearing rubber gloves (ellipse, crescent, sphere, spoon, rotator etc.). More precise shapes (crescent, triangle, rhomboid) were prepared by rolling the material of choice into a thin sheet and cutting out the desired shape with the help of a scalpel and a template.

Rods of the material (wax or plastic) were prepared by melting the material in a hot water bath, pulling it into a syringe with a 2mm opening and extruding it at the solidification point. The resulting long rod can be cut into sections of desired length.

The object was then placed onto a ca. 0.4mm thick water layer inside a Petri dish with diameter of choice. The Petri dish was lit from below to improve contrast. Footage was obtained using a top mounted camera. In some cases, tracker marks were placed on objects to either improver tracking detection or multiple in order to obtain information about orientation. For footage processing see Section VI. 1.1. All experiments were performed at room temperature (22 ± 2 ℃).

VI. 2.3 Camphor-paraffin droplets on a water surface

Materials and instrumentation: Camera (Sony NEX VG20EH), Petri dish (19 cm), Micropipette

Chemicals: (1R)-(+)-camphor (98% purity, CAS: 464-49-3, Sigma-Aldrich), paraffin oil (puriss., CAS-Number: 8012-95-1, Sigma-Aldrich), Oil red O (BioReagent, Sigma-Aldrich) and MilliQ purified water.

Procedure: Either 50 or 200μl of camphor-paraffin-dye solution at different concentrations of camphor and Oil red O (See Section VI. 3.4) were placed onto a water surface (ca. 4mm thick) inside a 19cm Petri dish. The behavior was captured with a top mounted camera for at least 20 minutes. The entire system, including experiment and camera, was enclosed to eliminate confounding effects from air flow in the laboratory. All experiments were performed at room temperature $(22 \pm 2\ ℃)$.

VI. 2.4 Ethyl salicylate droplets on a surfactant solution

Materials and instrumentation: Camera (Logitech or Baumer, see section VI. 1.1), LED flat panel, Petri dish (9 or 14 cm), Micropipette

Chemicals: Ethyl salicylate (Sigma Aldrich (CAS: 118-61-6), paraffin oil (puriss., CAS-Number: 8012-95-1, Sigma-Aldrich), sodium dodecyl sulfate (SDS, Sigma Aldrich, CAS: 151-21-3), Oil red O (BioReagent, Sigma-Aldrich), Sudan black B (certified by the Biological Stain Commission, Sigma Aldrich) and MilliQ purified water.

Procedure: The desired number of 20μl droplets (see preparation procedure in Section VI. 3.5 were placed onto a Petri dish containing a 4mm layer of 10g/l solution of sodium dodecyl sulfate using a micropipette. The parameters that could be varied were: number of droplets, the size of the dish, the type of dye (SbB or OrO), concentration of the dye (0.0025 wt% or 0.005 wt%), population ratio of different types of droplets (red or blue). The Petri dish was placed onto or underneath a LED flat panel prior to addition of aqueous SDS-solution and the droplets and covered with a glass cover. The behavior was filmed for between 3 and 20 hours. All experiments were performed at room temperature $(22 \pm 2\ ℃)$.

VI. 2.5 Polypropylene absorption test

Materials and instrumentation: Camera (Sony NEX VG20EH), LED flat panel, Petri dish (5 cm), Micropipette and polypropylene foam sample.

Chemicals: (1R)-(+)-camphor (98% purity, CAS: 464-49-3, Sigma-Aldrich), camphene (95% purity, CAS: 79-92-5, Sigma Aldrich), Polypropylene (CAS:9003-07-0, Sigma Aldrich), paraffin oil (puriss., CAS-Number: 8012-95-1, Sigma-Aldrich) Oil red O (BioReagent, Sigma-Aldrich) and MilliQ purified water.

Procedure: A 5cm Petri dish was filled with water to have a layer of ca. 5mm. A 200µl paraffin oil droplet containing 1.5mg/ml Oil red O was added to the water surface. A foam sample made from 45% camphor, 45% camphene and 10% polypropylene mixture (the camphor and camphene have been removed, see Section VI. 3.3) with the dimensions 0.5x1x1.5cm was placed in close proximity to the oil droplet. The absorption of the oil was filmed from above while lit form below. After most of the oil was absorbed, the light was turned off to show that the foam sample had been stained red by the dye in the absorbed oil.

VI. 2.6 Predator-prey droplets on a circular channel

Materials and instrumentation: Camera (Baumer VCXU-04C USB-3), Petri dish (5cm dish glued into 9cm dish), Micropipette

Chemicals: Ethyl salicylate (Sigma Aldrich (CAS: 118-61-6), 1-Decanol (Wako Pure Chemical), Oil red O (BioReagent, Sigma-Aldrich) and MilliQ purified water.

Procedure: The Petri dish with a 2m circular channel was filled with a 4mm layer of purified water. Then a 50μl droplet of 1-decanol (stained with Oil red O) was added to the water surface slowly to let a decanol layer form on the water surface along with the droplet. The next step was to add a 50 μl droplet of ethyl salicylate (stained with Sudan black B) to the water surface as well. The dish was then covered with a glass cover and a LED flat panel was placed above. The droplet behavior was filmed for 2 hours from below.

VI. 3 Sample preparation

VI. 3.1 Preparation of camphor-camphene wax

Materials: Laboratory scales, Hot plate with magnetic stirrer, 100ml beaker, glass cover, magnet, 50ml flat beaker, nitrile rubber sheet

Chemicals: (1R)-(+)-camphor (98% purity, CAS: 464-49-3, Sigma-Aldrich), camphene (95% purity, CAS: 79-92-5, Sigma Aldrich), polypropylene pellets (CAS:9003-07-0, Sigma Aldrich)

Procedure: Camphor and camphene were weighed off at the desired weight ratio (up to 70% camphor) and added to a beaker containing a stirrer magnet. The beaker was then covered with a glass cover and placed on a hot plate set to 140℃. Once some of the camphene had melted, the magnetic stirrer was activated and left stirring until all of the camphor had been

dissolved in the liquid camphene. At this point a dye could be added to the mixture if so desired. The liquid mixture was then transferred into a flat beaker, lined with a sheet of nitrile rubber to prevent the material from sticking to the glass. Once solidified the material could be stored in an airtight container or in the freezer to prevent it from evaporating. From this point on it could be used for further processing.

VI. 3.2 Preparation of camphor-camphene-polypropylene plastic

Materials: Laboratory scales, Hot plate with magnetic stirrer, 100ml beaker, glass cover, magnet, 50ml flat beaker, nitrile rubber sheet

Chemicals: (1R)-(+)-camphor (98% purity, CAS: 464-49-3, Sigma-Aldrich), camphene (95% purity, CAS: 79-92-5, Sigma Aldrich), polypropylene pellets (CAS:9003-07-0, Sigma Aldrich)

Procedure: Camphor, camphene and polypropylene were weighed off at the desired weight ratio (up to 45% camphor) and added to a beaker containing a stirrer magnet. The beaker was then covered with a glass cover and placed on a hot plate set to 250℃. Once some of the camphene had melted, the magnetic stirrer was activated and left stirring until all of the camphor and polypropylene had been dissolved in the liquid camphene. At this point a dye could be added to the mixture if so desired. The liquid mixture was then transferred into a flat beaker, lined with a sheet of nitrile rubber to prevent the material from sticking to the glass. Once solidified the material could be stored in an airtight container or in the freezer to prevent it from evaporating. From this point on it could be used for further processing.

VI. 3.3 Preparation of polypropylene plastic foam

Materials: camphor-camphene-polypropylene plastic, 50ml beaker, scalpel

Chemicals: (1R)-(+)-camphor (98% purity, CAS: 464-49-3, Sigma-Aldrich), camphene (95% purity, CAS: 79-92-5, Sigma Aldrich), polypropylene pellets (CAS:9003-07-0, Sigma Aldrich), camphor 96% and camphor.

Procedure: A block of camphor-camphene-polypropylene plastic at the desired component ratio is cut into a desired shape. Two beakers were prepared, filled with ethanol and acetone respectively. The sample was then left to soak 30s in ethanol, followed by 10s in camphor. After that the sample is placed on a piece of absorbent paper to let the solvents evaporate. This process was repeated until all of the camphor and camphene were removed, leaving behind a microporous polypropylene foam.

VI. 3.4 Preparation of camphor-paraffin-Oil red O droplets

Materials: Precision scales, 100ml conical flask, hot plate, magnetic stirrer, vortexer,

sonicator bath, 15ml Falcon centrifuge tubes, 50ml falcon tubes, micropipette

Chemicals: (1R)-(+)-camphor (98% purity, CAS: 464-49-3, Sigma-Aldrich), paraffin oil (puriss., CAS-Number: 8012-95-1, Sigma-Aldrich), Oil red O (BioReagent, Sigma-Aldrich)

Procedure: Stock solution of 150mg/ml of camphor in paraffin oil was prepared by adding the appropriate amount of camphor granules to 50ml paraffin oil in a conical flask. It was set on a hot plate stirring at 50℃ until all of the camphor was dissolved. A stock solution of 1.5 mg/ml of Oil red O in paraffin oil was prepared by adding the appropriate amount of Oil red O to 50ml of paraffin oil in a 50ml Falcon tube. The dye was dissolved by sonicating the mixture for 30 seconds followed by 30 seconds of vortexing. This procedure was repeated until all of the dye was dissolved. From these two stock solutions samples, of different camphor and OrO concentrations were prepared my mixing and diluting with paraffin oil inside of 15ml Falcon tubes using the sonicator and vortexer to mix them.

VI. 3.5 Preparation of ethyl salicylate droplets

Materials: Precision scales, vortexer, sonicator bath, 15ml Falcon centrifuge tubes, 50ml falcon tubes, micropipette

Chemicals: Ethyl salicylate (Sigma Aldrich (CAS: 118-61-6), paraffin oil (puriss., CAS-Number: 8012-95-1, Sigma-Aldrich), Oil red O (BioReagent, Sigma-Aldrich), Sudan black B (certified by the Biological Stain Commission, Sigma Aldrich).

Procedure: Two stock solutions of 0.1 wt% Oil red O and Sudan black B in ethyl salicylate respectively were prepared by weighing off appropriate amounts of dyes and adding them to a 15ml Falcon tube and adding 10ml of ethyl salicylate. Mixing was done by sonication followed by vortexing. Samples were prepared by mixing appropriate amounts of ethyl salicylate, paraffin oil and dye stock solution in order to obtain stock solutions of ethyl salicylate with 20wt% paraffin oil, with either 0.0025 or 0.005 wt% of dye. For tensiometric investigations, samples without paraffine oil were prepared.

VII **List of Movies**

Movie 1. Single Camphor disk motion, URL: https://youtu.be/AdKQhWIyeDQ

Movie 2. Simple boat motion, URL: https://youtu.be/2wX-jtezSHg

Movie 3. Flapboat motion, URL: https://youtu.be/yojzNE10ZBY

Movie 4. Continuous motion of circular setup, URL: https://youtu.be/aNVmk8bTva4

Movie 5. Multiple bursts of boat on circular setup, URL: https://youtu.be/-dWjSGyCWHQ

Movie 6. Vibratory motion of circular motion boat, URL: https://youtu.be/iy-fVskMPA0

Movie 7. Inversive motion of circular motion boat, URL: https://youtu.be/72n9cm3MU1A

Movie 8. Packman – non-trivial self-propelled shapes, URL: https://youtu.be/rChsiUTW-QA

Movie 9. Marble – self-propelled motion, URL: https://youtu.be/jdobpCO1hz4

Movie 10. Single rod movie, URL: https://youtu.be/vHv6SJe9wSQ

Movie 11. Spoon shape motion, URL: https://youtu.be/H-OHx9L3ATE

Movie 12. Ellipsoid shape motion, URL: https://youtu.be/vRCxOrFuUgw

Movie 13. Rotator shape motion, URL: https://youtu.be/Bp22FcVuqZg

Movie 14. Triangle, URL: https://youtu.be/YS8eTwwx7RM

Movie 15. Rhomboid, URL: https://youtu.be/bW8mJw5i3XM

Movie 16. Crescent, URL: https://youtu.be/GYwzWRlfiwo

Movie 17. Rods wax collective, URL: https://youtu.be/uGalSavY_6E

Movie 18. Marbles wax collective, URL: https://youtu.be/k4ahu6iL8K8

Movie 19. Rod plastic single, URL: https://youtu.be/roLRiuoRsuQ

Movie 20. Rods plastic collective, URL: https://youtu.be/VUKqqNAtsz8

Movie 21. Foam absorbs oil, URL: https://youtu.be/u211XpR5ou8

Movie 22. Droplet high complexity, URL: https://youtu.be/7KEv9vUwQLk

Movie 23. A, droplet expansion, URL: https://youtu.be/lvfIObj6IDM

Movie 24. B type continuous URL: https://youtu.be/vuAy3ebsOho

Movie 25. B type intermittent, URL: https://youtu.be/QDnCwxbrPJ4

Movie 26. C const, URL: https://youtu.be/ZjCjpL4Jrwg

Movie 27. C intermittent, URL: https://youtu.be/Nwbq5WJ6U_M

Movie 28. D type, URL: https://youtu.be/ex8FmDTnZhA

Movie 29. E type (fission), URL: https://youtu.be/J7vyL0FQciI

Movie 30. F type, URL: https://youtu.be/qHephOG4F6A

Movie 31. G type, URL: https://youtu.be/TkUxz3rrz2g

Movie 32. ES-drop 59 red low [OrO], URL: https://youtu.be/AmuNaqSpf0Q

Movie 33. Stage VII, URL: https://youtu.be/cvbTVFd5__A

Movie 34. Long term low crowdedness, URL: https://youtu.be/JuaQfz3BHkM

Movie 35. High crowdedness, URL: https://youtu.be/BY29NsfYtfc

Movie 36. Comparison of red and blue early stage, URL: https://youtu.be/D1VwtPDPDwM

Movie 37. 1 red 49 blue, URL: https://youtu.be/_lG7DAF2624

Movie 38. 10 to 40 red majority, URL: https://youtu.be/VsbMlUFI-xU

Movie 39. 10 to 40 blue majority, URL: https://youtu.be/6JLznMQ5ns8

Movie 40. 25 to 25, URL: https://youtu.be/TX6ofqs_Duo

Movie 41. Channel chase, URL: https://youtu.be/myh6wRchFw0

Movie 42. Open chase, URL: https://youtu.be/limWPImQwXo

VIII **Bibliography**

1. Newman, M.E.J. Complex Systems: A Survey. *Am. J. Phys.* **2011**, *79*, 800–810, doi:10.1119/1.3590372.
2. Gompper, G.; Winkler, R.G.; Speck, T.; Solon, A.; Nardini, C.; Peruani, F.; Löwen, H.; Golestanian, R.; Kaupp, U.B.; Alvarez, L.; et al. The 2020 motile active matter roadmap. *J. Phys. Condens. Matter* **2020**, *32*, doi:10.1088/1361-648X/ab6348.
3. Siegenfeld, A.F.; Bar-Yam, Y. An Introduction to Complex Systems Science and Its Applications. *Complexity* **2020**, *2020*, 1–16, doi:10.1155/2020/6105872.
4. Kaneko, K. *Life: An Introduction to Complex Systems Biology*; Understanding Complex Systems; Springer Berlin Heidelberg: Berlin, Heidelberg, 2006; ISBN 978-3-540-32666-3.
5. Chen, I.A.; Walde, P. From Self-Assembled Vesicles to Protocells. *Cold Spring Harb. Perspect. Biol.* **2010**, *2*, a002170–a002170, doi:10.1101/cshperspect.a002170.
6. Saha, T.; Galic, M. Self-organization across scales: From molecules to organisms. *Philos. Trans. R. Soc. B Biol. Sci.* **2018**, *373*, doi:10.1098/rstb.2017.0113.
7. Peruani, F.; Deutsch, A.; Bär, M. Nonequilibrium clustering of self-propelled rods. *Phys. Rev. E - Stat. Nonlinear, Soft Matter Phys.* **2006**, *74*, 1–4, doi:10.1103/PhysRevE.74.030904.
8. Baskaran, A.; Marchetti, M.C. Hydrodynamics of self-propelled hard rods. *Phys. Rev. E - Stat. Nonlinear, Soft Matter Phys.* **2008**, *77*, 1–9, doi:10.1103/PhysRevE.77.011920.
9. Nakata, S.; Nagayama, M.; Kitahata, H.; Suematsu, N.J.; Hasegawa, T. Physicochemical design and analysis of self-propelled objects that are characteristically sensitive to environments. *Phys. Chem. Chem. Phys.* **2015**, *17*, 10326–10338, doi:10.1039/c5cp00541h.
10. Tanaka, S.; Nakata, S.; Kano, T. Dynamic ordering in a swarm of floating droplets driven by solutal Marangoni effect. *J. Phys. Soc. Japan* **2017**, *86*, 1–9, doi:10.7566/JPSJ.86.101004.
11. Ebata, H.; Sano, M. Swimming droplets driven by a surface wave. *Sci. Rep.* **2015**, *5*, 8546, doi:10.1038/srep08546.
12. Nakata, S.; Pimienta, V.; Kitahata, H.; Lagzi, I. *Self-organized Motion: Physicochemical Design Based on Non-linear Dynamics*; Nakata, S., Pimienta, V., Lagzi, I., Kitahata, H., Suematsu, N.J., Eds.; Theoretical and Computational Chemistry Series; Royal Society

of Chemistry: Cambridge, 2019; ISBN 978-1-78801-166-2.
13. Čejková, J.; Banno, T.; Hanczyc, M.M.; Štěpánek, F. Droplets As Liquid Robots. *Artif. Life* **2017**, *23*, 528–549, doi:10.1162/ARTL_a_00243.
14. Satoh, Y.; Sogabe, Y.; Kayahara, K.; Tanaka, S.; Nagayama, M.; Nakata, S. Self-inverted reciprocation of an oil droplet on a surfactant solution. *Soft Matter* **2017**, *13*, 3422–3430, doi:10.1039/C7SM00252A.
15. SCRIVEN, L.E.; STERNLING, C. V. The Marangoni Effects. *Nature* **1960**, *187*, 186–188, doi:10.1038/187186a0.
16. Tadmor, R. Marangoni flow revisited. *J. Colloid Interface Sci.* **2009**, *332*, 451–454, doi:10.1016/j.jcis.2008.12.047.
17. Bangham, A.D. Membrane models with phospholipids. *Prog. Biophys. Mol. Biol.* **1968**, *18*, 29–95, doi:10.1016/0079-6107(68)90019-9.
18. Casagrande, C.; Fabre, P.; Raphaël, E.; Veyssié, M. "Janus Beads": Realization and Behaviour at Water/Oil Interfaces. *Europhys. Lett.* **1989**, *9*, 251–255, doi:10.1209/0295-5075/9/3/011.
19. Brown, A.; Poon, W. Ionic effects in self-propelled Pt-coated Janus swimmers. *Soft Matter* **2014**, *10*, 4016–4027, doi:10.1039/C4SM00340C.
20. Tomlinson, C. On the Motions of Camphor on the Surface of Water. *Proc. R. Soc. London* **1862**, *11*, 575–577, doi:10.1098/rspl.1860.0124.
21. Lord Rayleigh Measurements of the amount of oil necessary in order to check the motions of camphor upon water. *Proc. R. Soc. London* **1890**, *47*, 364–367, doi:10.1098/rspl.1889.0099.
22. CambridgeSoft Chembiodraw.
23. Nakata, S.; Iguchi, Y.; Ose, S.; Kuboyama, M.; Ishii, T.; Yoshikawa, K. Self-Rotation of a Camphor Scraping on Water : New Insight into the Old Problem. *Langmuir* **1997**, *13*, 4454–4458, doi:10.1021/la970196p.
24. Nakata, S.; Hayashima, Y. Spontaneous Dancing of a camphor scraping. *Faraday Trans.* **1998**, *94*, 3655–3658, doi:10.1039/a806281a.
25. Karasawa, Y.; Oshima, S.; Nomoto, T.; Toyota, T.; Fujinami, M. Simultaneous Measurement of Surface Tension and Its Gradient around Moving Camphor Boat on Water Surface. *Chem. Lett.* **2014**, *43*, 1002–1004, doi:10.1246/cl.140201.
26. Hayashima, Y.; Nagayama, M.; Doi, Y.; Nakata, S.; Kimura, M.; Iida, M. Self-motion of a camphoric acid boat sensitive to the chemical environment. *Phys. Chem. Chem. Phys.* **2002**, *4*, 1386–1392, doi:10.1039/b108686c.
27. Nagayama, M.; Nakata, S.; Doi, Y.; Hayashima, Y. A theoretical and experimental study

on the unidirectional motion of a camphor disk. *Phys. D Nonlinear Phenom.* **2004**, *194*, 151–165, doi:10.1016/j.physd.2004.02.003.

28. Suematsu, N.J.; Sasaki, T.; Nakata, S.; Kitahata, H. Quantitative Estimation of the Parameters for Self-Motion Driven by Difference in Surface Tension. *Langmuir* **2014**, *30*, 8101–8108, doi:10.1021/la501628d.
29. Maryadele J. O'Neil; O'Neil, M.J. (ed.). The Merck Index - An Encyclopedia of Chemicals, Drugs, and Biologicals. In; O'Neil, M.J., Ed.; Royal Society of Chemistry: Cambridge, 2013 ISBN 9781849736701.
30. Nanzai, B.; Ban, T. Chapter 6: Physical Chemistry of Energy Conversion in Self-propelled Droplets Induced by Dewetting Effect. In *Self-organized Motion: Physicochemical Design based on Nonlinear Dynamics*; Nakata, S., Pimienta, V., Lagzi, I., Kitahata, H., Suematsu, N.J., Eds.; Theoretical and Computational Chemistry Series; Royal Society of Chemistry: Cambridge, 2019; Vol. 2019-Janua, pp. 139–166 ISBN 978-1-78801-166-2.
31. Ikura, Y.S.; Heisler, E.; Awazu, A.; Nishimori, H.; Nakata, S. Collective motion of symmetric camphor papers in an annular water channel. *Phys. Rev. E* **2013**, *88*, 012911, doi:10.1103/PhysRevE.88.012911.
32. Hayashima, Y.; Nagayama, M.; Nakata, S. A Camphor Grain Oscillates while Breaking Symmetry. *J. Phys. Chem. B* **2001**, *105*, 5353–5357, doi:10.1021/jp004505n.
33. Nakata, S.; Hayashima, Y.; Komoto, H. Spontaneous switching of camphor motion between two chambers. *Phys. Chem. Chem. Phys.* **2000**, *2*, 2395–2399, doi:10.1039/b000648n.
34. Kohira, M.I.; Hayashima, Y.; Nagayama, M.; Nakata, S. Synchronized self-motion of two camphor boats. *Langmuir* **2001**, *17*, 7124–7129, doi:10.1021/la010388r.
35. Nakata, S.; Hiromatsu, S. Intermittent motion of a camphor float. *Colloids Surfaces A Physicochem. Eng. Asp.* **2003**, *224*, 157–163, doi:10.1016/S0927-7757(03)00248-6.
36. Suematsu, N.J.; Ikura, Y.; Nagayama, M.; Kitahata, H.; Kawagishi, N.; Murakami, M.; Nakata, S. Mode-switching of the self-motion of a camphor boat depending on the diffusion distance of camphor molecules. *J. Phys. Chem. C* **2010**, *114*, 9876–9882, doi:10.1021/jp101838h.
37. Frenkel, M.; Multanen, V.; Grynyov, R.; Musin, A.; Bormashenko, Y.; Bormashenko, E. Camphor-Engine-Driven Micro-Boat Guides Evolution of Chemical Gardens. *Sci. Rep.* **2017**, *7*, 3930, doi:10.1038/s41598-017-04337-w.
38. Koyano, Y.; Gryciuk, M.; Skrobanska, P.; Malecki, M.; Sumino, Y.; Kitahata, H.; Gorecki, J. Relationship between the size of a camphor-driven rotor and its angular velocity.

Phys. Rev. E **2017**, *96*, 012609, doi:10.1103/PhysRevE.96.012609.

39. Koyano, Y.; Kitahata, H.; Gryciuk, M.; Akulich, N.; Gorecka, A.; Malecki, M.; Gorecki, J. Bifurcation in the angular velocity of a circular disk propelled by symmetrically distributed camphor pills. *Chaos An Interdiscip. J. Nonlinear Sci.* **2019**, *29*, 013125, doi:10.1063/1.5061027.
40. Koyano, Y.; Kitahata, H.; Nakata, S.; Gorecki, J. On a simple model that explains inversion of a self-propelled rotor under periodic stop-and-release-operations. *Chaos An Interdiscip. J. Nonlinear Sci.* **2020**, *30*, 023105, doi:10.1063/1.5140626.
41. Ei, S.I.; Kitahata, H.; Koyano, Y.; Nagayama, M. Interaction of non-radially symmetric camphor particles. *Phys. D Nonlinear Phenom.* **2018**, *366*, 10–26, doi:10.1016/j.physd.2017.11.004.
42. Kitahata, H.; Iida, K.; Nagayama, M. Spontaneous motion of an elliptic camphor particle. *Phys. Rev. E* **2013**, *87*, 010901, doi:10.1103/PhysRevE.87.010901.
43. Kitahata, H.; Koyano, Y. Spontaneous Motion of a Camphor Particle with a Triangular Modification from a Circle. *J. Phys. Soc. Japan* **2020**, *89*, 094001, doi:10.7566/JPSJ.89.094001.
44. Koyano, Y.; Kitahata, H. Imperfect bifurcation in the rotation of a propeller-shaped camphor rotor. *Phys. Rev. E* **2021**, *103*, 012202, doi:10.1103/PhysRevE.103.012202.
45. Löffler, R.J.G.; Hanczyc, M.M.; Gorecki, J. A hybrid camphor-camphene wax material for studies on self-propelled motion. *Phys. Chem. Chem. Phys.* **2019**, *21*, 24852–24856, doi:10.1039/c9cp04722k.
46. Boniface, D.; Cottin-Bizonne, C.; Kervil, R.; Ybert, C.; Detcheverry, F. Self-propulsion of symmetric chemically active particles: Point-source model and experiments on camphor disks. *Phys. Rev. E* **2019**, *99*, 62605, doi:10.1103/PhysRevE.99.062605.
47. Nakata, S.; Doi, Y.; Hayashima, Y. Intermittent motion of a camphene disk at the center of a cell. *J. Phys. Chem. B* **2002**, *106*, 11681–11684, doi:10.1021/jp021675m.
48. Nakata, S.; Iguchi, Y.; Ose, S.; Ishii, T. pH-Sensitive Self-Motion of a Solid Scraping on an Aqueous Phase. *J. Phys. Chem. B* **1998**, *102*, 7425–7427, doi:10.1021/jp981887c.
49. Akella, V.S.; Singh, D.K.; Mandre, S.; Bandi, M.M. Dynamics of a Camphoric Acid boat at the air-water interface. **2017**.
50. Sharma, R.; Chang, S.T.; Velev, O.D. Gel-Based Self-Propelling Particles Get Programmed To Dance. *Langmuir* **2012**, *28*, 10128–10135, doi:10.1021/la301437f.
51. Maass, C.C.; Krüger, C.; Herminghaus, S.; Bahr, C. Swimming Droplets. *Annu. Rev. Condens. Matter Phys.* **2016**, *7*, 171–193, doi:10.1146/annurev-conmatphys-031115-011517.

52. Tanaka, S.; Sogabe, Y.; Nakata, S. Spontaneous change in trajectory patterns of a self-propelled oil droplet at the air-surfactant solution interface. *Phys. Rev. E* **2015**, *91*, 032406, doi:10.1103/PhysRevE.91.032406.
53. Banno, T.; Toyota, T.; Asakura, K. Self-Propelled Motion of Micrometer-Sized Oil Droplets in Aqueous Solution of Surfactant. *Prop. Uses Microemulsions* **2017**, doi:10.5772/67249.
54. Tanaka, S.; Nakata, S.; Nagayama, M. A surfactant reaction model for the reciprocating motion of a self-propelled droplet. *Soft Matter* **2021**, *17*, 388–396, doi:10.1039/D0SM01500H.
55. Löffler, R.J.G.; Gorecki, J.; Hanczyc, M. Better red than dead: On the influence of Oil Red O dye on complexity of evolution of a camphor-paraffin droplet on the water surface. In Proceedings of the The 2018 Conference on Artificial Life; MIT Press: Cambridge, MA, 2018; pp. 574–579.
56. Hanczyc, M.M.; Toyota, T.; Ikegami, T.; Packard, N.; Sugawara, T. Fatty acid chemistry at the oil-water interface: Self-propelled oil droplets. *J. Am. Chem. Soc.* **2007**, *129*, 9386–9391, doi:10.1021/ja0706955.
57. Toyota, T.; Maru, N.; Hanczyc, M.M.; Ikegami, T.; Sugawara, T. Self-propelled oil droplets consuming "Fuel" surfactant. *J. Am. Chem. Soc.* **2009**, *131*, 5012–5013, doi:10.1021/ja806689p.
58. Meredith, C.H.; Moerman, P.G.; Groenewold, J.; Chiu, Y.J.; Kegel, W.K.; van Blaaderen, A.; Zarzar, L.D. Predator–prey interactions between droplets driven by non-reciprocal oil exchange. *Nat. Chem.* **2020**, *12*, 1136–1142, doi:10.1038/s41557-020-00575-0.
59. Čejková, J.; Novák, M.; Štěpánek, F.; Hanczyc, M.M. Dynamics of Chemotactic Droplets in Salt Concentration Gradients. *Langmuir* **2014**, *30*, 11937–11944, doi:10.1021/la502624f.
60. Kitahata, H.; Yoshinaga, N.; Nagai, K.H.; Sumino, Y. Spontaneous motion of a droplet coupled with a chemical wave. *Phys. Rev. E - Stat. Nonlinear, Soft Matter Phys.* **2011**, *84*, 3–6, doi:10.1103/PhysRevE.84.015101.
61. Cira, N.J.; Benusiglio, A.; Prakash, M. Vapour-mediated sensing and motility in two-component droplets. *Nature* **2015**, *519*, 446–450, doi:10.1038/nature14272.
62. Duursma, G.; Kennedy, R.; Sefiane, K.; Yu, Y. Leidenfrost Droplets on Microstructured Surfaces. *Heat Transf. Eng.* **2016**, *37*, 1190–1200, doi:10.1080/01457632.2015.1112610.
63. Von Rohr, P.R.; Poulikakos, D.; Stamatopoulos, C.; Milionis, A.; Ackerl, N.; Donati, M.; De La Vallée, P.L. Droplet self-propulsion on superhydrophobic microtracks. *ACS Nano*

2020, *14*, 12895–12904, doi:10.1021/acsnano.0c03849.

64. Čejková, J.; Hanczyc, M.M.; Štěpánek, F. Multi-Armed Droplets as Shape-Changing Protocells. *Artif. Life* **2018**, *24*, 71–79, doi:10.1162/ARTL_a_00255.
65. Launay, G.; Sadullah, M.S.; McHale, G.; Ledesma-Aguilar, R.; Kusumaatmaja, H.; Wells, G.G. Self-propelled droplet transport on shaped-liquid surfaces. *Sci. Rep.* **2020**, *10*, 1–8, doi:10.1038/s41598-020-70988-x.
66. Čejková, J.; Holler, S.; Nguyenová, T.Q.; Kerrigan, C.; Štěpánek, F.; Hanczyc, M.M. Chemotaxis and Chemokinesis of Living and Non-living Objects. In *Advances in Unconventional Computing*; Adamatzky, A., Ed.; Emergence, Complexity and Computation; Springer International Publishing: Cham, 2017; Vol. 23, pp. 245–260 ISBN 978-3-319-33920-7.
67. Toyota, T.; Banno, T.; Castro, J.M.; Imai, M. Locomotion and transformation of underwater micrometer-sized molecular aggregates under chemical stimuli. *J. Phys. Soc. Japan* **2017**, *86*, 1–11, doi:10.7566/JPSJ.86.101006.
68. Kaneko, S.; Asakura, K.; Banno, T. Phototactic behavior of self-propelled micrometer-sized oil droplets in a surfactant solution. *Chem. Commun.* **2017**, *53*, 2237–2240, doi:10.1039/c6cc09236e.
69. Swanson, J.A.; Lansing Taylor, D. Local and spatially coordinated movements in Dictyostelium discoideum amoebae during chemotaxis. *Cell* **1982**, *28*, 225–232, doi:10.1016/0092-8674(82)90340-3.
70. Caschera, F.; Rasmussen, S.; Hanczyc, M.M. An oil droplet division-fusion cycle. *Chempluschem* **2013**, *78*, 52–54, doi:10.1002/cplu.201200275.
71. Hanczyc, M.M.; Parrilla, J.M.; Nicholson, A.; Yanev, K.; Stoy, K. Creating and Maintaining Chemical Artificial Life by Robotic Symbiosis. *Artif. Life* **2015**, *21*, 47–54, doi:10.1162/ARTL_a_00151.
72. Faiña, A.; Nejati, B.; Stoy, K. Evobot: An open-source, modular, liquid handling robot for scientific experiments. *Appl. Sci.* **2020**, *10*, doi:10.3390/app10030814.
73. Gutierrez, J.M.P.; Hinkley, T.; Taylor, J.W.; Yanev, K.; Cronin, L. Evolution of oil droplets in a chemorobotic platform. *Nat. Commun.* **2014**, *5*, 1–8, doi:10.1038/ncomms6571.
74. Parrilla-Gutierrez, J.M.; Tsuda, S.; Grizou, J.; Taylor, J.; Henson, A.; Cronin, L. Adaptive artificial evolution of droplet protocells in a 3D-printed fluidic chemorobotic platform with configurable environments. *Nat. Commun.* **2017**, *8*, doi:10.1038/s41467-017-01161-8.
75. Cejkova, J. Habilitation thesis: Chemical engineering contribution to artificial life research, University of Chemistry and Technology Prague, 2019.

76. Palagi, S.; Fischer, P. Bioinspired microrobots. *Nat. Rev. Mater.* **2018**, *3*, 113–124, doi:10.1038/s41578-018-0016-9.
77. Lee, C.; Kim, M.; Kim, Y.J.; Hong, N.; Ryu, S.; Kim, H.J.; Kim, S. Soft robot review. *Int. J. Control. Autom. Syst.* **2017**, *15*, 3–15, doi:10.1007/s12555-016-0462-3.
78. Holler, S.; Porcelli, C.; Ieropoulos, I.A.; Hanczyc, M.M. Transport of Live Cells under Sterile Conditions Using a Chemotactic Droplet. *Sci. Rep.* **2018**, *8*, 1–9, doi:10.1038/s41598-018-26703-y.
79. Čejková, J.; Schwarzenberger, K.; Eckert, K.; Tanaka, S. Dancing performance of organic droplets in aqueous surfactant solutions. *Colloids Surfaces A Physicochem. Eng. Asp.* **2019**, *566*, 141–147, doi:10.1016/j.colsurfa.2019.01.027.
80. Giomi, L.; Hawley-Weld, N.; Mahadevan, L. Swarming, swirling and stasis in sequestered bristle-bots. *Proc. R. Soc. A Math. Phys. Eng. Sci.* **2013**, *469*, 20120637, doi:10.1098/rspa.2012.0637.
81. Scholz, C.; Engel, M.; Pöschel, T. Rotating robots move collectively and self-organize. *Nat. Commun.* **2018**, *9*, 1–8, doi:10.1038/s41467-018-03154-7.
82. Turing, A.M. The chemical basis of morphogenesis. *Philos. Trans. R. Soc. Lond. B. Biol. Sci.* **1952**, *237*, 37–72, doi:10.1098/rstb.1952.0012.
83. Nakata, S.; Nagayama, M. Chapter 1. Theoretical and Experimental Design of Self-propelled Objects Based on Nonlinearity. In; 2018; pp. 1–30.
84. Yoshinaga, N. Spontaneous motion and deformation of a self-propelled droplet. *Phys. Rev. E* **2014**, *89*, 012913, doi:10.1103/PhysRevE.89.012913.
85. Vicsek, T.; Czirók, A.; Ben-Jacob, E.; Cohen, I.; Shochet, O. Novel Type of Phase Transition in a System of Self-Driven Particles. *Phys. Rev. Lett.* **1995**, *75*, 1226–1229, doi:10.1103/PhysRevLett.75.1226.
86. Joel, L.S. *Cellular Automata: A Discrete View of the World*; 2012; ISBN 9780470168790.
87. Kitahata, H.; Hiromatsu, S.; Doi, Y.; Nakata, S.; Rafiqul Islam, M. Self-motion of a camphor disk coupled with convection. *Phys. Chem. Chem. Phys.* **2004**, *6*, 2409, doi:10.1039/b315672a.
88. Iida, K.; Kitahata, H.; Nagayama, M. Theoretical study on the translation and rotation of an elliptic camphor particle. *Phys. D Nonlinear Phenom.* **2014**, *272*, 39–50, doi:10.1016/j.physd.2014.01.005.
89. Allen, R.W. XL.—The maximum pressure of camphor vapour. *J. Chem. Soc., Trans.* **1900**, *77*, 413–416, doi:10.1039/CT9007700413.
90. Allen, R.W. XXXIX.—The maximum pressure of naphthalene vapour. *J. Chem. Soc., Trans.* **1900**, *77*, 400–412, doi:10.1039/CT9007700400.

91. Andrews, M.R. Vapor Pressure of Naphthalene at Low Temperatures. *J. Phys. Chem.* **1926**, *30*, 1497–1500, doi:10.1021/j150269a005.
92. Koyano, Y.; Suematsu, N.J.; Kitahata, H. Rotational motion of a camphor disk in a circular region. *Phys. Rev. E* **2019**, *99*, 022211, doi:10.1103/PhysRevE.99.022211.
93. Löffler, R.J.G.; Hanczyc, M.M.; Gorecki, J. A Perfect Plastic Material for Studies on Self-Propelled Motion on the Water Surface. *Molecules* **2021**, *26*, 3116, doi:10.3390/molecules26113116.
94. Sigma-Aldrich Illustration of camphor molecular structure Available online: https://www.sigmaaldrich.com/catalog/substance/dcamphor1522346449311.
95. Sigma-Aldrich Illustration of camphene molecular structure Available online: https://www.sigmaaldrich.com/catalog/product/aldrich/456055.
96. Limsathayourat, N.; Melchert, H.-U. Hochtemperatur-Capillar-Gas-Chromatographie von Kohlenwasserstoffen, Fettsäurederivaten, Cholesterin-, Wachsestern und Triglyceriden am Beispiel des Bienenwachses. *Fresenius' Zeitschrift für Anal. Chemie* **1984**, *318*, 410–413, doi:10.1007/BF00533223.
97. Ogino, K.; Onishi, M. Interfacial action of natural surfactants in oil/water systems. *J. Colloid Interface Sci.* **1981**, *83*, 18–25, doi:10.1016/0021-9797(81)90004-7.
98. Tsai, W.L.; Hwu, Y.; Chen, C.H.; Chang, L.W.; Je, J.H.; Lin, H.M.; Margaritondo, G. Grain boundary imaging, gallium diffusion and the fracture behavior of Al–Zn Alloy – An in situ study. *Nucl. Instruments Methods Phys. Res. Sect. B Beam Interact. with Mater. Atoms* **2003**, *199*, 457–463, doi:10.1016/S0168-583X(02)01533-1.
99. Barenfanger, J.; Drake, C.A. Interpretation of Gram Stains for the Nonmicrobiologist. *Lab. Med.* **2001**, *32*, 368–375, doi:10.1309/C55D-B4A8-M06V-2KK3.
100. Nichols, J.B. Nitrocellulose and Camphor. *J. Phys. Chem.* **1924**, *28*, 769–771, doi:10.1021/j150241a008.
101. Curran, K.; Strlič, M. Polymers and volatiles: Using VOC analysis for the conservation of plastic and rubber objects. *Stud. Conserv.* **2015**, *60*, 1–14, doi:10.1179/2047058413Y.0000000125.
102. Pyeon, H.B.; Park, J.E.; Suh, D.H. Non-phthalate plasticizer from camphor for flexible PVC with a wide range of available temperature. *Polym. Test.* **2017**, *63*, 375–381, doi:10.1016/j.polymertesting.2017.08.029.
103. Wang, S.; Jiang, L. Definition of Superhydrophobic States. *Adv. Mater.* **2007**, *19*, 3423–3424, doi:10.1002/adma.200700934.
104. CPLabSafety Polypropylene Solvent stability Available online: https://www.calpaclab.com/polypropylene-chemical-compatibility-chart/.

105. Marmur, A. The Lotus Effect: Superhydrophobicity and Metastability. *Langmuir* **2004**, *20*, 3517–3519, doi:10.1021/la036369u.
106. Tanaka, H.; Araki, T. Spontaneous double phase separation induced by rapid hydrodynamic coarsening in two-dimensional fluid mixtures. *Phys. Rev. Lett.* **1998**, *81*, 389–392, doi:10.1103/PhysRevLett.81.389.
107. Xu, Z.-M.; Jiang, X.-L.; Liu, T.; Hu, G.-H.; Zhao, L.; Zhu, Z.-N.; Yuan, W.-K. Foaming of polypropylene with supercritical carbon dioxide. *J. Supercrit. Fluids* **2007**, *41*, 299–310, doi:10.1016/j.supflu.2006.09.007.
108. Lloyd, D.R.; Kinzer, K.E.; Tseng, H.S. Microporous membrane formation via thermally induced phase separation. I. Solid-liquid phase separation. *J. Memb. Sci.* **1990**, *52*, 239–261, doi:10.1016/S0376-7388(00)85130-3.
109. Kim, S.S.; Lloyd, D.R. Microporous membrane formation via thermally-induced phase separation. III. Effect of thermodynamic interactions on the structure of isotactic polypropylene membranes. *J. Memb. Sci.* **1991**, *64*, 13–29, doi:10.1016/0376-7388(91)80074-G.
110. Yang, M.C.; Perng, J.S. Microporous polypropylene tubular membranes via thermally induced phase separation using a novel solvent - Camphene. *J. Memb. Sci.* **2001**, *187*, 13–22, doi:10.1016/S0376-7388(00)00587-1.
111. Pochivalov, K. V.; Basko, A. V.; Lebedeva, T.N.; Ilyasova, A.N.; Golovanov, R.Y.; Yurov, M.Y.; Shandryuk, G.A.; Artemov, V. V.; Ezhov, A.A.; Kudryavtsev, Y. V. Analysis of the Thermal Behavior of Polypropylene–Camphor Mixtures for Understanding the Pathways to Polymeric Membranes via Thermally Induced Phase Separation. *J. Phys. Chem. B* **2019**, *123*, 10533–10546, doi:10.1021/acs.jpcb.9b07475.
112. Liakos, I.L.; Salvagnini, P.; Scarpellini, A.; Carzino, R.; Beltran, C.; Mele, E.; Murino, V.; Athanassiou, A. Biomimetic Locomotion on Water of a Porous Natural Polymeric Composite. **2016**, 1–8, doi:10.1002/admi.201500854.
113. Braitenberg, V. *Vehicles*; MIT Press, 1986; ISBN 9780262521123.
114. Lagzi, I.; Soh, S.; Wesson, P.J.; Browne, K.P.; Grzybowski, B.A. Maze Solving by Chemotactic Droplets. *J. Am. Chem. Soc.* **2010**, *132*, 1198–1199, doi:10.1021/ja9076793.
115. Nagai, K.; Sumino, Y.; Kitahata, H.; Yoshikawa, K. Mode selection in the spontaneous motion of an alcohol droplet. *Phys. Rev. E* **2005**, *71*, 065301, doi:10.1103/PhysRevE.71.065301.
116. Hanczyc, M.M. Metabolism and motility in prebiotic structures. *Philos. Trans. R. Soc. B Biol. Sci.* **2011**, *366*, 2885–2893, doi:10.1098/rstb.2011.0141.

117. Banno, T.; Asami, A.; Ueno, N.; Kitahata, H.; Koyano, Y.; Asakura, K.; Toyota, T. Deformable Self-Propelled Micro-Object Comprising Underwater Oil Droplets. *Sci. Rep.* **2016**, *6*, 31292, doi:10.1038/srep31292.
118. Man, X.; Doi, M. Vapor-Induced Motion of Liquid Droplets on an Inert Substrate. *Phys. Rev. Lett.* **2017**, *119*, 044502, doi:10.1103/PhysRevLett.119.044502.
119. Nagai, K.H.; Takabatake, F.; Sumino, Y.; Kitahata, H.; Ichikawa, M.; Yoshinaga, N. Rotational motion of a droplet induced by interfacial tension. *Phys. Rev. E - Stat. Nonlinear, Soft Matter Phys.* **2013**, *87*, doi:10.1103/PhysRevE.87.013009.
120. Pimienta, V.; Brost, M.; Kovalchuk, N.; Bresch, S.; Steinbock, O. Complex shapes and dynamics of dissolving drops of dichloromethane. *Angew. Chemie - Int. Ed.* **2011**, *50*, 10728–10731, doi:10.1002/anie.201104261.
121. Sigma-Aldrich Sigma Aldrich: Paraffin liquid product page Available online: https://www.sigmaaldrich.com/catalog/product/sial/18512.
122. Wikipedia: Page of Oil red O dye Available online: https://en.wikipedia.org/wiki/Oil_Red_O.
123. Diego, X.; Marcon, L.; Müller, P.; Sharpe, J. Key Features of Turing Systems are Determined Purely by Network Topology. *Phys. Rev. X* **2018**, *8*, 021071, doi:10.1103/PhysRevX.8.021071.
124. Ender, H.; Kierfeld, J. From diffusive mass transfer in Stokes flow to low Reynolds number Marangoni boats. *Eur. Phys. J. E* **2021**, *44*, doi:10.1140/epje/s10189-021-00034-9.
125. Tanaka, S. Periodic collective behaviors of organic solvent droplets on the surface of aqueous surfactant solutions. In Proceedings of the The 2019 Conference on Artificial Life; MIT Press: Cambridge, MA, 2019; pp. 656–657.
126. Vicsek, T.; Zafeiris, A. Collective motion. *Phys. Rep.* **2012**, *517*, 71–140, doi:10.1016/j.physrep.2012.03.004.
127. Čejkova, J.; Štěpanek, F.; Hanczyc, M.M. Evaporation-Induced Pattern Formation of Decanol Droplets. *Langmuir* **2016**, *32*, 4800–4805, doi:10.1021/acs.langmuir.6b01062.
128. Tajfirooz, S.; Meijer, J.G.; Kuerten, J.G.M.; Hausmann, M.; Fröhlich, J.; Zeegers, J.C.H. Statistical-learning method for predicting hydrodynamic drag, lift, and pitching torque on spheroidal particles. *Phys. Rev. E* **2021**, *103*, 023304, doi:10.1103/PhysRevE.103.023304.
129. Elkafas, A.G.; Elgohary, M.M.; Zeid, A.E. Numerical study on the hydrodynamic drag force of a container ship model. *Alexandria Eng. J.* **2019**, *58*, 849–859, doi:10.1016/j.aej.2019.07.004.

130. de Marco, B.A.; Rechelo, B.S.; Tótoli, E.G.; Kogawa, A.C.; Salgado, H.R.N. Evolution of green chemistry and its multidimensional impacts: A review. *Saudi Pharm. J.* **2019**, *27*, 1–8, doi:10.1016/j.jsps.2018.07.011.
131. Macul Perez, F.; Corrales Ureña, Y.R.; Rischka, K.; Leite Cavalcanti, W.; Noeske, P.-L.M.; Safari, A.A.; Wei, G.; Colombi Ciacchi, L. Bio-interfactants as double-sided tapes for graphene oxide. *Nanoscale* **2019**, *11*, 4236–4247, doi:10.1039/C8NR08607A.
132. Corrales-Ureña, Y.R.; Souza-Schiaber, Z.; Lisboa-Filho, P.N.; Marquenet, F.; Michael Noeske, P.-L.; Gätjen, L.; Rischka, K. Functionalization of hydrophobic surfaces with antimicrobial peptides immobilized on a bio-interfactant layer. *RSC Adv.* **2020**, *10*, 376–386, doi:10.1039/C9RA07380A.
133. FFmpeg distribution Available online: https://www.ffmpeg.org/.
134. ImageJ distribution Available online: https://imagej.net/Welcome.
135. Wolfram Mathematica Software Available online: https://www.wolfram.com/mathematica/.
136. Wikipedia Wilhelmy Plate - Wikipedia Available online: https://en.wikipedia.org/wiki/Wilhelmy_plate.
137. DataPhysics Instruments GmbH Pendant drop 1 Available online: https://www.dataphysics-instruments.com/knowledge/understanding-interfaces/pendant-drop-method/.
138. Laurén, S.; Biolin Scientific Pendant drop 2 Available online: https://www.biolinscientific.com/blog/pendant-drop-method-for-surface-tension-measurements.

Institute of Physical Chemistry
Polish Academy of Sciences

Kasprzaka 44/52
01-224 Warsaw, Poland

www.ichf.edu.pl